UNIVERSITAT POLITÈCNICA DE VALÈNCIA

School of Aerospace Engineering and Industrial Design

Development of a Numerical Model for Jet Engine Operation and Performance Prediction: Comparative Study and Validation using Analytical and Experimental Results.

Master's Thesis

Master's Degree in Aeronautical Engineering

AUTHOR: Río Monleón, Álvaro del

Tutor: Bares Moreno, Pau

ACADEMIC YEAR: 2023/2024

UNIVERSITAT POLITÈCNICA DE VALÈNCIA

ETSI Aeroespacial y Diseño Industrial

Development of a Numerical Model for Jet Engine Operation and Performance Prediction:

Comparative Study and Validation using Analytical and Experimental Results

Master's Thesis

Master's Degree in Aeronautical Engineering

Author: Del Río Monleón, Álvaro

Supervisor: Bares Moreno, Pau

Academic Year: 2023/2024

Date: September 14, 2024

Abstract

English

Numerical methods are fundamental in modern-day engineering, due to their capability of rapidly and inexpensively predicting the behavior of complex non-linear systems, providing insight into the phenomena involved.

In this work, a modular *Python* code is developed to solve the 0-D thermodynamic approach to a generic jet engine operation problem, using component performance maps for this purpose. Single spool and dual spool turbojet engines are modeled. They are among the most common propulsive systems in today's military aviation industry.

Their corresponding characteristic curves and operating lines are obtained employing this method. A comparative study, where some component features are being modified, is hereby be carried out to determine and investigate the most relevant phenomena in this problem. In the process, both steady state and transient behaviors are also investigated. These are compared with an analytical approach, showing in the end a better accuracy in the solution provided.

Results are validated with the help of experimental data from a laboratory-scale single spool turbojet *AMT Netherlands Olympus HP* engine. This information is obtained from a test rig and complemented with external measurements. In the end, an extended Kalman filter is applied to the transient problem, to provide better insight into the internal mechanisms that drive the engine. It will help refining the predictions for the evolution of state variables, by combining the model results with experimental readings.

This study aims towards the development of better tools for designing, understanding and characterizing propulsive systems, thus allowing to produce more effective and efficient means of transportation in the future.

Spanish

Los métodos numéricos son fundamentales en la ingeniería actual, debido a su capacidad de modelar rápidamente y con bajo coste el comportamiento de sistemas complejos no lineales, proporcionando asimismo gran detalle en los fenómenos involucrados.

En este trabajo se desarrolla un código modular en Python para resolver el enfoque termodinámico 0-D del problema de las actuaciones de un aerorreactor genérico, utilizando mapas de componentes para este fin. Se modelan sistemas turbojet monoeje y bieje. Estos se encuentran entre los más comunes en la industria aeronáutica militar actual.

Se obtienen sus curvas características y líneas de operación correspondientes mediante este método. Asimismo, se lleva a cabo un estudio comparativo, donde se modifican algunas características de componentes, con el fin de determinar e investigar los fenómenos más relevantes de este problema. Al mismo tiempo, se analiza tanto su comportamiento estacionario como transitorio. Estos se comparan con un enfoque analítico, demostrando que se obtiene una mayor precisión en la solución.

Los resultados se validan con ayuda de datos experimentales de un motor turbojet monoeje AMT Netherlands Olympus HP, a escala de laboratorio. Esta información es obtenida del banco de ensayos y complementada con medidas externas. Para finalizar, se aplica un filtro extendido de Kalman al problema transitorio, aportando mayor claridad en los mecanismos internos que permiten el funcionamiento del motor. Este ayuda a refinar las predicciones sobre la evolución de los estados, combinando los resultados arrojados por el modelo con las medidas experimentales.

Este estudio tiene como objetivo el desarrollo de herramientas más efectivas para diseñar, comprender y caracterizar sistemas propulsivos, lo que en el futuro puede permitir producir medios de transporte más eficaces y eficientes.

Valencian

Els mètodes numèrics són fonamentals en l'enginyeria moderna, degut a la seua capacitat de predir ràpidament i econòmicament el comportament de sistemes complexos no lineals, proporcionant una visió més profunda dels fenòmens implicats.

En aquest treball, es desenvolupa un codi modular en Python per a resoldre l'enfocament termodinàmic 0-D d'un problema d'operació d'un motor de reacció genèric, utilitzant mapes de rendiment dels components per a aquest propòsit. Es modelen motors de turbojet de rotor únic i de rotor dual. Aquests estan entre els sistemes propulsius més comuns en la indústria de l'aviació militar actual.

Les seues corbes característiques corresponents i línies d'operació s'obtenen emprant aquest mètode. Es duu a terme un estudi comparatiu, on es modifiquen algunes característiques dels components per a determinar i investigar els fenòmens més rellevants en aquest problema. Durant el procés, també s'investiguen els comportaments en règim estacionari i transitori. Aquests es comparen amb un enfocament analític, mostrant al final una millor precisió en la solució proporcionada.

Els resultats es validen amb l'ajuda de dades experimentals d'un motor turbojet de rotor únic a escala de laboratori, el AMT Netherlands Olympus HP. Aquesta informació s'obté a partir d'un banc de proves i es complementa amb mesures externes. Finalment, s'aplica un filtre de Kalman estès al problema transitori per a proporcionar una millor comprensió dels mecanismes interns que fan funcionar el motor. Aquest ajudarà a refinar les prediccions per a l'evolució de les variables d'estat, combinant els resultats del model amb les lectures experimentals.

Aquest estudi té com a objectiu el desenvolupament de millors eines per a dissenyar, comprendre i caracteritzar els sistemes propulsius, permetent així produir mitjans de transport més efectius i eficients en el futur.

Index

List of Acronyms

ACC	Active Clearance Control
AFR	Air to Fuel Ratio
ARP	Aerospace Recommended Practice
CC	Combustion Chamber
DOF	Degrees Of Freedom
EASA	European Union Aviation Safety Agency
EEC	Electronic Engine Controller
EGT	Exhaust Gas Temperature
EKF	Extended Kalman Filter
EPR	Engine Pressure Ratio
FAA	Federal Aviation Administration
FADEC	Full Authority Digital Engine Control
FAR	Fuel to Air Ratio
HMU	Hydromechanical Unit
HPC	High Pressure Compressor
HPT	High Pressure Turbine
ICE	Internal Combustion Engine
ISA	International Standard Atmosphere
IVP	Initial Value Problem
LPC	Low Pressure Compressor
LPT	Low Pressure Turbine
NaN	Not a Number
NGV	Nozzle Guide Vanes
NPR	Nozzle Pressure Ratio
OAT	Outside Air Temperature

OPR	Overall Pressure Ratio
PLF	Pressure Loss Factor
RK	Runge-Kutta Methods
RNI	Reynolds Number Index
SAE	Society of Automotive Engineers
SDG	Sustainable Development Goal
SI	International System of Units
TET	Turbine Entry Temperature
TLA	Thrust Lever Angle
TSFC	Thrust Specific Fuel Consumption
UPV	Universidad Politécnica de Valencia
VAT	Value Added Tax
VATN	Variable Area Turbine Nozzle
VBV	Variable Bleed Valves
VSV	Variable Stator Vanes

Symbols

Symbol	**Description**
A_x	Flow perpendicular area in station x
b_x	Bleed fraction at station x
B	Greitzer's surge parameter
c_{E}^{*}	Corrected TSFC
C_{A}	Angularity correction factor
C_{D}	Discharge coefficient
C_{V}	Velocity coefficient
$C_{\mathrm{p,c}}$	Cold specific heat at constant pressure
$C_{\mathrm{p,h}}$	Hot specific heat at constant pressure
E^{*}	Corrected thrust
$\mathbb{E}$	Expected Value
f	Fuel to air ratio
$\mathbf{f}$	State time evolution function (EKF)
$\mathcal{F}$	Fourier Transform
$\mathbf{F}_k$	State time evolution function jacobian matrix in time step k (EKF)
$\mathbf{G}$	Continuous time control matrix (EKF)
$\mathbf{G}_k$	Control matrix in time step k (EKF)
$\boldsymbol{G}$	Laplace transform of $\mathbf{G}$ (EKF)
$\mathbf{h}$	Measurement function (EKF)
$\mathbf{H}_k$	Measurement function jacobian matrix in time step k (EKF)
i	Coupling transmission ratio (single spool)

i_{HP}	High pressure coupling transmission ratio (dual spool)
i_{LP}	Low pressure coupling transmission ratio (dual spool)
I^*	Corrected axis polar moment of inertia (single spool)
I^*_{HP}	High pressure coupling corrected polar axis moment of inertia (dual spool)
I^*_{LP}	Low pressure coupling corrected polar axis moment of inertia (dual spool)
I^*_{sp}	Corrected specific impulse
k_{HPT}	Analytical HPT inlet corrected mass flow (dual spool)
k_{LPT}	Analytical LPT inlet corrected mass flow (dual spool)
k_{N}	Analytical nozzle inlet corrected mass flow
k_{T}	Analytical turbine inlet corrected mass flow (single spool)
$\mathbf{K}_k$	Kalman gain in time step k (EKF)
L	Fuel lower heating value
$\dot{m}_{\mathrm{f}}$	Fuel mass flow
$\dot{m}_x$	Gas mass flow at station x
$\dot{m}^*_{\mathrm{C}}$	Compressor corrected inlet mass flow (single spool)
$\dot{m}^*_{\mathrm{HPC}}$	HPC corrected inlet mass flow (dual spool)
$\dot{m}^*_{\mathrm{HPT}}$	HPT corrected inlet mass flow (dual spool)
$\dot{m}^*_{\mathrm{LPC}}$	LPC corrected inlet mass flow (dual spool)
$\dot{m}^*_{\mathrm{LPT}}$	LPT corrected inlet mass flow (dual spool)
$\dot{m}^*_{\mathrm{T}}$	Turbine corrected inlet mass flow (single spool)
$\dot{m}^*_x$	Corrected mass flow at station x
$\dot{m}^*_{x,\mathrm{max}}$	Maximum corrected mass flow at station x
M_{r}	Blade relative Mach number
M_x	Mach number at station x
N	Shaft speed (single spool)
N_{HP}	High pressure shaft speed (dual spool)
N_{LP}	Low pressure shaft speed (dual spool)
N_{C}	Compressor speed (single spool)
N_{HPC}	HPC speed (dual spool)

N_{HPT}	HPT speed (dual spool)
N_{LPC}	LPC speed (dual spool)
N_{LPT}	LPC speed (dual spool)
N_{p}	Number of points in the time discretization scheme
$N_{\mathrm{ref,C}}$	Compressor reference speed (single spool)
$N_{\mathrm{ref,HPC}}$	HPC reference speed (dual spool)
$N_{\mathrm{ref,HPT}}$	HPT reference speed (dual spool)
$N_{\mathrm{ref,LPC}}$	LPC reference speed (dual spool)
$N_{\mathrm{ref,LPT}}$	LPT reference speed (dual spool)
$N_{\mathrm{ref,T}}$	Turbine reference speed (single spool)
N_{T}	Turbine speed (single spool)
N^*	Corrected shaft speed (single spool)
N^*_{C}	Compressor corrected relative speed (single spool)
N^*_{HP}	High pressure corrected shaft speed (dual spool)
N^*_{HPC}	HPC corrected relative speed (dual spool)
N^*_{HPT}	HPT corrected relative speed (dual spool)
N^*_{LP}	Low pressure corrected shaft speed (dual spool)
N^*_{LPC}	LPC corrected relative speed (dual spool)
N^*_{LPT}	LPT corrected relative speed (dual spool)
N^*_{T}	Turbine corrected relative speed (single spool)
p_{ref}	Reference static pressure
p_x	Static pressure at station x
$p_{x\mathrm{t}}$	Total pressure at station x
$\mathbf{P}_{k\|l}$	Filter covariance matrix after time step k and measurement l (EKF)
$\mathbf{Q}$	Process noise spectral power density matrix (EKF)
$\mathbf{Q}_k$	Process noise covariance matrix in time step k (EKF)
$\mathbf{r}_{k\|l}$	State evolution linearization term in time step k and measurement l (EKF)
$\boldsymbol{r}_{k\|l}$	Laplace transform of $\mathbf{r}_{k\|l}$
R	Ideal gas constant

$\mathbf{R}_k$	Measurement noise covariance matrix in time step k (EKF)
$\mathcal{R}$	Autocorrelation Function (EKF)
s	Laplace transform frequency
$\mathbf{s}_{k-1\|k-1}$	Measurement linearization constant in time step $k-1$ (EKF)
$\mathcal{S}$	Spectral Power Density Function (EKF)
S_{M}	Surge margin
t	Time
T_{ref}	Reference static temperature
T_x	Static temperature at station x
$T_{x\mathrm{t}}$	Total temperature at station x
$\mathbf{u}$	Continuous time control vector (EKF)
$\mathbf{u}_{k-1}$	Control vector in time step $k-1$ (EKF)
V_x	Flow velocity at station x
$\mathbf{v}$	Continuous time measurement noise vector (EKF)
$\mathbf{v}_k$	Measurement noise vector in time step k (EKF)
$\mathbf{w}$	Continuous time process noise vector (EKF)
$\mathbf{w}_k$	Process noise vector in time step k (EKF)
$\boldsymbol{w}$	Laplace transform of $\mathbf{w}$ (EKF)
$\mathbf{x}$	Continuous time true state vector (EKF)
$\mathbf{x}_k$	True state vector in time step k (EKF)
$\boldsymbol{x}$	Laplace transform of $\mathbf{x}$ (EKF)
$\hat{\mathbf{x}}$	Continuous time estimated state vector (EKF)
$\hat{\mathbf{x}}_{k\|l}$	Estimated state vector after time step k and measurement l (EKF)
$\widehat{\mathbf{x}}$	Continuous time state vector error (EKF)
$\widehat{\mathbf{x}}_k$	State vector error at time steo k (EKF)
$\mathbf{z}$	Continuous time true observables (EKF)
$\mathbf{z}_k$	True observables in time step k (EKF)
$\hat{\mathbf{z}}$	Continuous time estimated observables (EKF)
$\hat{\mathbf{z}}_{k\|l}$	Estimated observables after time step k and measurement l (EKF)

α_{E}	External coupling over-relaxation factor
α_{HP}	High pressure coupling over-relaxation factor
α_{I}	Internal coupling over-relaxation factor
α_{LP}	Low pressure coupling over-relaxation factor
β_{C}	Compressor performance map beta line
β_{HPC}	HPC performance map beta line
β_{LPC}	LPC performance map beta line
γ_{c}	Cold adiabatic index
γ_{h}	Hot adiabatic index
δ	Dirac delta functional
$\boldsymbol{\delta}_{k-1}$	User input control vector in time step $k-1$ (EKF)
Δt	Time increment between steps
ϵ_{E}	External coupling loop termination tolerance
ϵ_{HP}	High pressure coupling loop termination tolerance
ϵ_{I}	Internal coupling loop termination tolerance
ϵ_{LP}	Low pressure coupling loop termination tolerance
ζ_{CC}	Combustion chamber's PLF
$\zeta_{\mathrm{CC,c}}$	Cold losses in combustion chamber's PLF
$\zeta_{\mathrm{CC,h}}$	Hot losses in combustion chamber's PLF
η_{C}	Compressor isentropic efficiency (single spool)
η_{CC}	Combustion chamber efficiency
η_{D}	Diffuser isentropic efficiency
η_{m}	Mechanical transmission efficiency (single spool)
η_{HPC}	HPC isentropic efficiency (dual spool)
η_{HPT}	HPT isentropic efficiency (dual spool)
$\eta_{\mathrm{m,HP}}$	High pressure coupling mechanical transmission efficiency (dual spool)
$\eta_{\mathrm{m,LP}}$	Low pressure coupling mechanical transmission efficiency (dual spool)
η_{LPC}	LPC isentropic efficiency (dual spool)
η_{LPT}	LPT isentropic efficiency (dual spool)

η_{N}	Nozzle isentropic efficiency
η_{T}	Turbine isentropic efficiency (single spool)
μ	Momentum factor in NGV bleed injection
ξ_{E}	External coupling loop relative error estimate
ξ'_{E}	First derivative of ξ_{E} for Newton-Raphson/Halley's Method
ξ''_{E}	Second derivative of ξ_{E} for Newton-Raphson/Halley's Method
ξ_{LP}	Low pressure coupling loop relative error estimate (double spool)
ξ'_{LP}	First derivative of ξ_{LP} for Newton-Raphson method (double spool)
π_{C}	Compressor total pressure ratio (single spool)
π_{CC}	Combustion chamber total pressure ratio
$\pi_{\mathrm{C,OL}}$	Compressor pressure ratio at the operating line
$\pi_{\mathrm{C,SL}}$	Compressor pressure ratio at the surge line
π_{HPC}	HPC total pressure ratio (dual spool)
$1/\pi_{\mathrm{HPT}}$	HPT total pressure ratio (dual spool). Constant in analytical solution.
π_{LPC}	LPC total pressure ratio (dual spool)
$1/\pi_{\mathrm{LPT}}$	LPT total pressure ratio (dual spool). Constant in analytical solution.
$1/\pi_{\mathrm{NGV}}$	Analytical HPT total pressure ratio in the NGV cooling bleed stage
$1/\pi_{\mathrm{T}}$	Turbine total pressure ratio (single spool). Constant in analytical solution.
ρ_x	Density at station x
$\rho_{x\mathrm{t}}$	Total density at station x
τ_{HPT}	Analytical HPT total temperature ratio (dual spool)
τ_{LPT}	Analytical LPT total temperature ratio (dual spool)
τ_{NGV}	Analytical HPT total temperature ratio in the NGV cooling bleed stage
τ_{T}	Analytical turbine total temperature ratio (single spool)
$\mathbf{\Phi}$	Continuous time state transition matrix (EKF)
$\mathbf{\Phi}_k$	State transition matrix in time step $k-1$ (EKF)
ω	Shaft angular velocity in rad/s (single spool). Fourier frequency
ω_{HP}	High pressure coupling shaft angular velocity in rad/s (dual spool)
ω_{LP}	Low pressure coupling shaft angular velocity in rad/s (dual spool)

List of Figures

List of Tables

1. Objectives

The main focus of this work is to provide a model and a framework for calculating performance and behavior of propulsive systems, in off-design and transient scenarios. Its extent will be limited to single spool and dual spool turbojet engines, albeit the methods hereby presented can be generalized to several propulsive system typologies, as long as it they are consistent with the approach taken. This solution is aimed to be iterative, numerical and achieved by using turbomachinery performance maps. It will be coded in the *Python* programming language, in a *Visual Studio Code* environment.

Another global objective is, after the formulation of the aforementioned methods, to identify general trends and engage in description of these systems and their different variants, identifying their most relevant features as well as their advantages and disadvantages. Some more specific objectives to be achieved through the course of this work are the following:

- This document aims to describe, in first place and in an insightful way, the importance of considering the off-design functioning of aircraft jet engines. This dissertation will, as an opening, provide justification for the development of the tools and generation of results in subsequent parts of this project.

- Along the way, an analytical solution to the problem will be derived, with the goal of comparing the different approaches that can be taken to tackle this problem, and serving as a way of performing a brief pre-validation process of the main method.

- Concerning this validation step, it is deemed to be a fundamental goal in this work. It is executed for a steady state, by employing own measurements obtained in a test rig, which are complemented with external sources. Validating the model with experimentation is essential to ensure the applicability of the methods exposed here.

- With the purpose of demonstrating the functioning of the code in all possible scenarios, an analysis of trends and patterns in generic turbojet engines will be performed to help understand the behavior of these systems and indicate how to avoid possible phenomena that could compromise safety or efficiency.

- Finally, aiming to refine the devised procedures for calculating the internal states of turbojet engines, a state observer in the form of a Kalman Filter will be applied. Transient state simulations are intended to be enriched by combining measurements and models in this unbiased optimal estimator.

2. Introduction

Aeronautical propulsion is an essential topic in aerospace engineering. Thrusting systems have a considerable impact on the economic viability of commercial airlines, as well as the operational capabilities of military forces. Superior propulsion technology offers strategic advantages in terms of flight speed, range, fuel consumption, payload capacity and emissions, among others, making this a crucial area for designers.

This area is, furthermore, subject of strong certification restrictions that naturally affect its design, due to the criticality in the safety of these systems. Engine design is also normally coupled with customer and economic requirements. It is therefore difficult to comply with all these different requisites while releasing to the market innovating and effective designs.

However, to achieve this purpose, theoretical studies of engine behavior can be carried out, not only to preliminarily design a thrust system according to the aforementioned restrictions, but also to investigate the effects in its performance of varying engine parameters and adding control features without drawing upon expensive testing campaigns.

Propulsive systems represent a complex and wide area of study in aeronautics, not exclusively due to the large amount of certification restrictions present. Their operation is strongly coupled with other areas and phenomena relevant in aircraft.

It poses a challenge to balance a pure thermodynamic engine design with other aspects: maintenance, control and indication, aerodynamics, structure integrity, hydraulic and electrical systems, etc. This work is mainly focused on a thermodynamic approach to predicting its behavior and performance, as it is the main tool to do so. However, some key aspects affecting other areas will be taken into account to ensure the results shown here are applicable to real-world situations.

This thermodynamic approach is fundamental for a preliminary design of the system. It is necessary for developers to have an adequate framework for this purpose. There are many software applications dedicated to 0-D thermodynamic design, the most renowned being *GasTurb* or *GSP*. However, they tend to fall into a more simplified and educational category and sometimes do not allow the flexibility of implementing self-made models or, as in the case of this project, combine results with measurements in a state observer.

To better understand the extent of this work, it is necessary to establish the boundaries of applicability of the present study in terms of validity of the developed framework for different types of aeronautical engines.

2.1 Propulsive System Classification

To justify the goals to achieve in this work, it is worth noting that the vehicle's propulsive system can take many different forms, but the most successful means of propulsion are those that have a high power density, allowing to produce more thrust while weighing less, thus facilitating flight capabilities.

There is a broad spectrum of engines used for propelling civil and military vehicles, being Internal Combustion Engines (ICEs) their biggest and more commonly employed family in modern day aviation [1]. The following diagram shows a general classification these types of engines, according to their most relevant features.

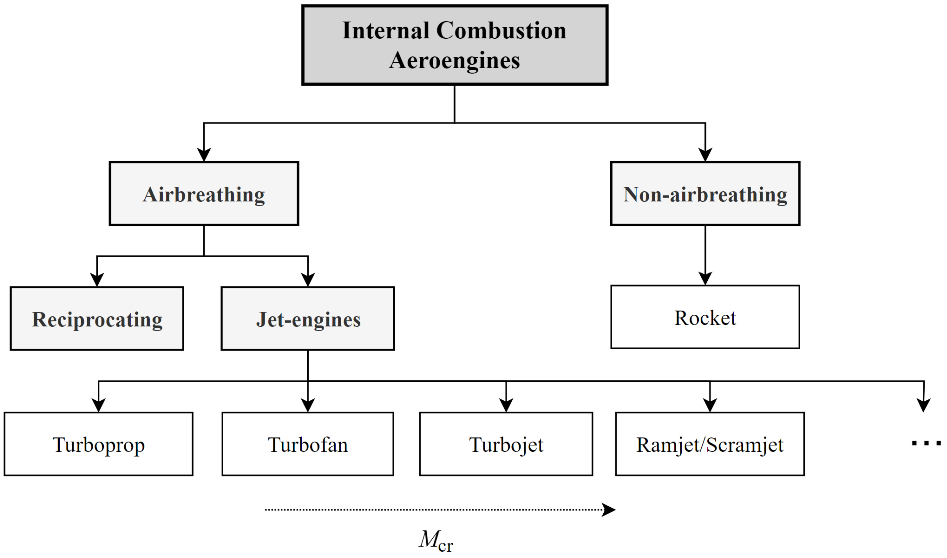

Figure 1: Classification of Internal Combustion of Aeronautical Engines. Adapted from [1].

Note that each internal combustion engine in Figure 1 is suited for a different flight condition, being the flight Mach number one of the deciding factors for their implementation in aviation.

Despite all of this, modern day propulsion system investigation no longer focuses mainly on ICEs, but often revolves around implementing electric propulsion in commercial aviation for achieving zero emissions, goal set to be accomplished in 2050 in the EU [10]. This is a difficult and distant-future task due to an intrinsic lack of power density, among with many other challenges these systems pose. This need for power density has been a historical trend in aviation. The paradigmatic example of this phenomenon is the replacement of reciprocating engines in favor of turbojet engines in commercial and military applications around the 1940s.

Due to their importance in present-day application, this work will revolve around the estimation of engine parameters in turbojet engines, one of the most employed of the latter, especially in military applications. Both single spool and dual spool turbojet engines will be considered in this study. The extension of the software to other typologies, such as separated flow turbofan engines can be easily accomplished and it is left for future improvements of the developed software.

2.2 Turbojet Architecture and Station Nomenclature

To understand the study that will be carried out in this document it is necessary to properly define the turbojet architecture considered, because many different variations can be contemplated.

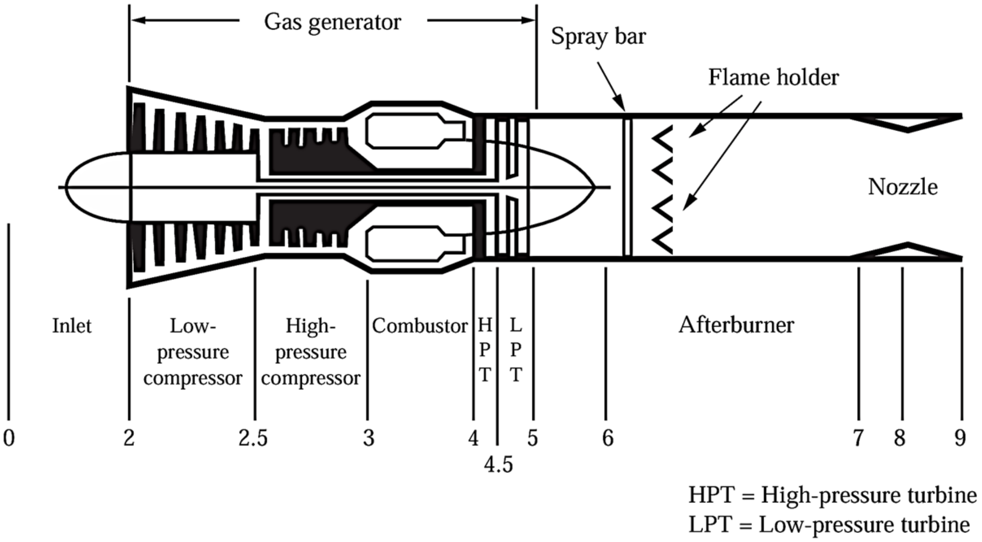

Figure 2: Schematic Dual Spool Turbojet Architecture and Nomenclature [2].

As many authors differ on the numbers used for each station, the nomenclature recommended in SAEs's ARP 755A is being followed in this work. The architecture considered for the modelling will be conventional, as shown in Figure 2. The only component that, in general, will not be modeled is the afterburner.

Additionally, a cooling bleed in the first NGV is considered, as it is a feature in many modern day engines. The following list describes the meaning of each station number and the components that they bound, with their respective functionalities.

- **Station 0: Far field Conditions**

  Extension of the engine control volume to the known far field conditions.

- **Station 1: Diffuser Inlet**

  Normally neglected in calculation as no relevant thermodynamic process takes place. Same process as Station 2.

- **Station 2: Diffuser Exit - Compressor Inlet (Single Spool) — Diffuser Exit - LPC Inlet (Dual Spool)**

  At the exit of the diffuser the working gas underwent a quasi-isentropic deceleration with almost constant total enthalpy.

- **Station 25: LPC Outlet - HPC Inlet (Dual Spool)**

  At the exit of the LPC the working gas has been quasi-isentropically compressed according to the compressor performance characteristics.

- **Station 3: Compressor Exit - Combustion Chamber Inlet (Single Spool) — HPC Exit - Combustion Chamber Inlet (Dual Spool)**

  The same process applies to this station, with the exception that LPC and HPC performance maps differ in the case of a dual spool engine. Furthermore, in this station it is common to have an engine bleed, when the working fluid can be injected in the combustion chamber due to a higher pressure.

- **Station 4: Combustion Chamber Outlet - NGV Bleed Injection**

  Fuel is injected in the combustion chamber, increasing the total enthalpy and entropy of the gas. This process is often modeled as an almost constant total pressure heat addition.

- **Station 41: NGV Bleed Injection - Turbine Inlet (Single Spool) — NGV Bleed Injection - HPT Inlet (Dual Spool)**

  A cooling bleed is injected to cope with the necessity that the total temperature in this region normally exceeds the melting temperature of the materials used in the construction of the turbine. It normally is extracted from Station 3 as mentioned.

- **Station 45: HPT Outlet - LPT Inlet (Dual Spool)**

  The gas is expanded in the HPT normally to power the LPC, as the speeds at which they work match closely. This expansion is quasi-isentropic.

- **Station 5: Turbine Outlet (Single Spool) — LPT Outlet (Dual Spool)**

  The gas has been expanded in the turbine to power the compressor (or LPT in the case of a dual spool engine to power the HPC). This process is again quasi-isentropic and turbine maps performance maps differ in the dual spool case.

- **Station 6: Afterburner Inlet**

  New heat addition to generate excess thrust in exchange of a lower TSFC. Not considered in this work, although it may be interesting for future investigations to study its interaction with a choked nozzle.

- **Station 7: Nozzle Inlet**

  Normally neglected in calculation as no relevant thermodynamic process takes place.

- **Station 8: Nozzle Throat**

  In a critical nozzle it defines the maximum corrected mass flow that can circulate through it. As this condition is often met in the normal operation of a turbojet engine, this station is relevant to be considered. In a convergent segment Station 8 and 9 coincide.

- **Station 9: Nozzle Exit**

  Normally modeled to either match ambient conditions if the nozzle is not choked or critical pressure. Exit of the gas in the control volume.

Having stated the nomenclature and architecture of a turbojet engine considered in this study, the off-design problem and models applied to each component are stated in further detail in the next Chapter.

2.3 Relevance of Off-design and Transient Engine Characterization

From a manufacturing point of view, off-design and transient engine behavior is considered during the middle stages of the process that defines the system. This, as a whole, requires a thorough and long iterative process. This process can be divided into different phases according to the detail achieved, while it is set to constantly receive feedback from all working areas to achieve the definition of the final product.

First off, a given specification is defined following a market research along with certification and commercial requirements. The final product has to comply with certification requisites (including certain performance metrics) defined in FAA FAR / EASA CS regulations as well as meeting client standards.

A conceptual design is necessary to define the objective global characteristics of the propulsive system in a design point. The engine Brayton cycle is often employed in this initial scratch work as a tool for developers to define the engine's objective design point parameters before delving into a more detailed analysis that includes the consideration of off-design and transient effects.

Engineers often define the necessary Turbine Entry Temperature (TET), Overall Pressure Ratio (OPR), objective thrust, bypass ratio (in the case of turbofan engines) and other fundamental parameters to optimize the engine's figures of merit in the point where it will be working most of its operative life. This point is normally considered to represent aircraft cruise conditions, especially if the engine is used in civil aviation applications. Many properties, like bypass ratio, TET and turbomachinery efficiency are initially estimated according to the level of the technology available to the manufacturer, since an increase in these values is beneficial for efficiency.

Preliminary design encompasses the study of component definition, transient and off-design behavior and control system design. Therefore, the core of this study will not focus on the conceptual design, given that developing a tool that facilitates **preliminary design** is one of the main points of this document.

Multiple different effects that occur in off-design and transient regimes are taken into consideration as well. Not only the kind of theoretical models employed in this phase are crucial for the final product definition, they will also allow to give a prediction of engine behavior as it is shown in this study by calculating an estimation of some engines' characteristic curves.

The last item of the design phase is a detailed definition of each component and feature that the final product is expected to have. These include, for example, a detailed definition of engine subsystems, necessary for engine operation but not directly related to thrust generation. Subsystems are, for example: fuel, lubrication, electrical, hydraulic (or servo fuel), air (bleeds, ventilation and sealing), pneumatic, health-monitoring systems, among many others.

In the following diagram, a sketch of the possible product definition phases that a generic jet engine must go through is shown.

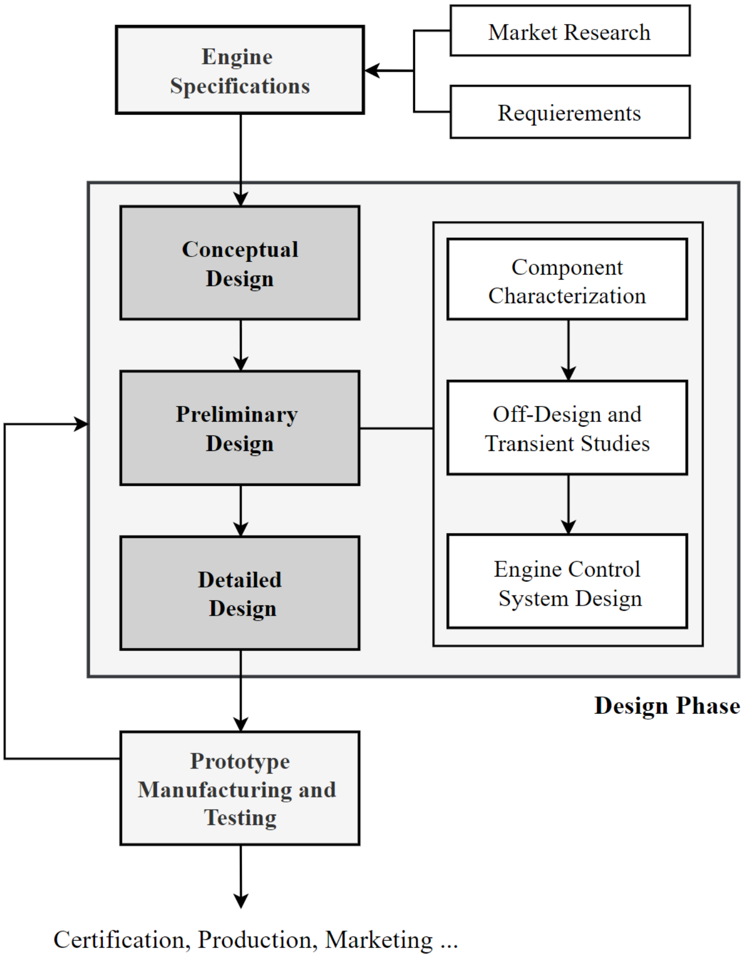

Figure 3: Final Product Definition Diagram.

As a remark, this project will not delve into some of the off-design phenomena as engine starting, engine windmilling or other similar processes that need to be addressed in this phase. It will rather focus on the fundamental behavior of the thrusting system, while it runs from idle phase to engine's operating limits.

The engine control system, that in many ways is set to command off-design and transient behavior is not going to be profusely studied in this document, where only several recommendations for control laws will be made, with the final goal of ensuring a safe operation.

Nowadays control systems are a vital part of the system, and are often integrated in a Full Authority Digital Engine Control (FADEC), running programmed commands from the Electronic Engine Controller (EEC) and then sending the information to the Hydromechanical Unit (HMU). This allows for a safe operation of the engine in case of unwanted commands that may lead to catastrophic results by modifying engine parameters. It also ensures the wellness, durability and efficient operation of the system.

Off-design and transient engine operation are necessary to be characterized a various number of reasons, including the following [11]:

- **Verifying Adequate Coupling Between the Compressor and the Turbine**

  This includes an efficiency as well as a safety motivation. The compressor and turbine projected to be installed in the system need to produce an adequate coupling, in the sense that the operation line stays within a path of high component efficiency, for both turbine a compressor. From a safety point of view, a bad coupling could result in certain concerns, most of them having a structural nature.

  - **Compressor Surge**

    Compressor surge is an aerodynamic instability, followed by destructive mechanical vibration with low a frequency (approximately 10 Hz) oscillation. This phenomenon is caused because of an initial stall of the blades. The decrease in blade loading leads to the reversal of upstream high pressure air. When the the stall is recovered the process starts again, forcing the flow to oscillate back and forth through the machine.

    Interestingly, the frequency and amplitude of the oscillation is more dependent on the plenum volume upstream, rather than compressor architecture. This lead to many researchers connecting this effect to an equivalent Helmholtz resonator.

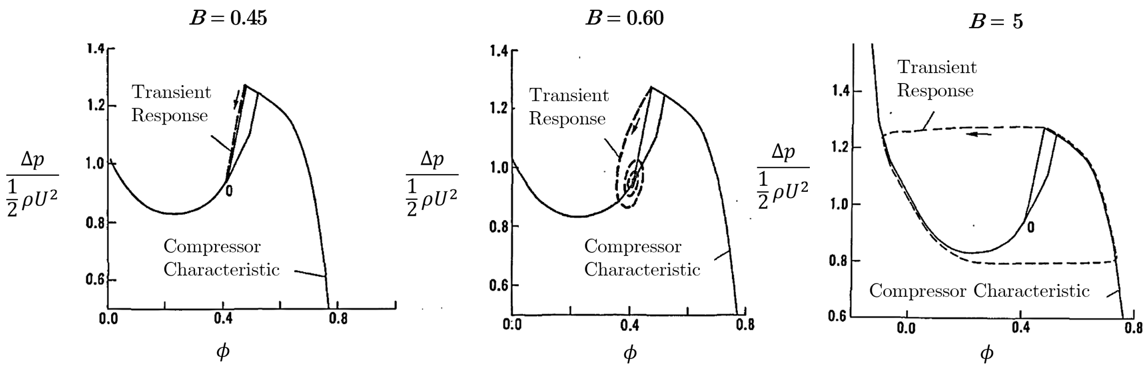

Figure 4: Axial Compressor Surge Behavior Dependent on Greitzer's B parameter. Adapted from [3].

Figure 4, representing non-dimensional compressor pressure increment and flow coefficient (axial velocity opposed to blade velocity), illustrates the process depending on Greitzer's B parameter [3], which is inversely proportional to the Helmholtz resonator frequency and proportional to blade speed. $B = 5$ is the case of deep surge.

Blade stall tends to be generalized across the whole intake area (in many cases this is in turn preceded by a phenomenon known as rotating compressor stall which is rather localized). It thus occurs at high blade incidences and often comes along with subsonic or supersonic stall flutter.

Compressors are perhaps the most critical component in these engines, because of their tendency to enter a stall, due to an adverse pressure gradient of the flow. For safety reasons, a surge margin S_{M} is defined. This is generally taken to be the relative distance to the operating line in terms of compressor pressure ratio at constant corrected intake mass flow. Needless to say, it varies with the engine operating point.

$$S_{\mathrm{M}} = \left. \frac{\pi_{\mathrm{C,SL}} - \pi_{\mathrm{C,OL}}}{\pi_{\mathrm{C,OL}}} \right|_{\dot{m}^*_{\mathrm{C}}} \tag{1}$$

Where OL and SL indicate Operating Line and Surge Line, respectively. Sometimes the coupling of both elements doesn't allow a sufficient surge margin, especially during transient maneuvers. When necessary, additional devices are employed to avoid this situation. These devices are comprised mainly of:

- Variable Stator Vanes (VSV)

  Stator blades are mechanically actuated to diminish rotor incidence angle with the purpose of ensuring a sufficient stall margin. They are also widely used in starting applications and to improve compressor efficiency along thr operating regimes the engine may encounter.

- Variable Bleed Valves (VBV)

  These bleed valves are commonly located in intermediate stages, so pressurized air can be evacuated in case of entering a compressor stall. In dual spool engines they tend to be installed between the LPC and HPC. As its name states, its opening is variable and actuated through the engine's control system.

- Handling Bleed Valves.

  These valves are actuated especially in cases of low shaft speed or engine start procedures. They are thus not especially relevant in the analysis conducted in this document.

In the present approach to calculate off-design behavior, none of these devices are considered. In dedicated software, VSV systems are many times modeled as a variable compressor map according to the stator blade angle chosen. VBV devices are in turn difficult to model and seldom used.

- **Temperature or Pressure Difference Excess**

  Extreme temperature or cycle OPR can force to define limits to the working space of a jet engine. Both of these conditions can generally happen at a high shaft speed, where the Fuel to Air Ratio (FAR) has a higher value.

  Newly developed turbofan engines can reach core OPR values of 60:1, with the future objective of reaching 80:1. This is a clear challenge, not only because of the difficulty of designing a light structure capable of resisting that amount of pressure difference (peaking at high altitudes), but also due to the difficulty of maintaining proper sealing in critical fuel or lubrication subsystems.

  This trend is coupled with incrementing the TET, as it is beneficial for achieving better a cycle thermal efficiency. The turbine is a critical component, due to the extreme temperature conditions it is submitted to.

  Due to this fact, TET temperature distributions are designed to avoid compromising structural integrity (one common choice is projecting the peak TET at 3/4 blade height from its root), as well as adding intricate cooling systems and ceramic coatings to protect the material, not quite from reaching its melting point, but to avoid phenomena like creep, thermal fatigue or corrosion.

  Note that certain engine modes, for example a take-off mode, can allow the engine TET can be increased above the continuous TET projected limit for several minutes. In this following graph this eventual temperature limit is shown to increase during the years.

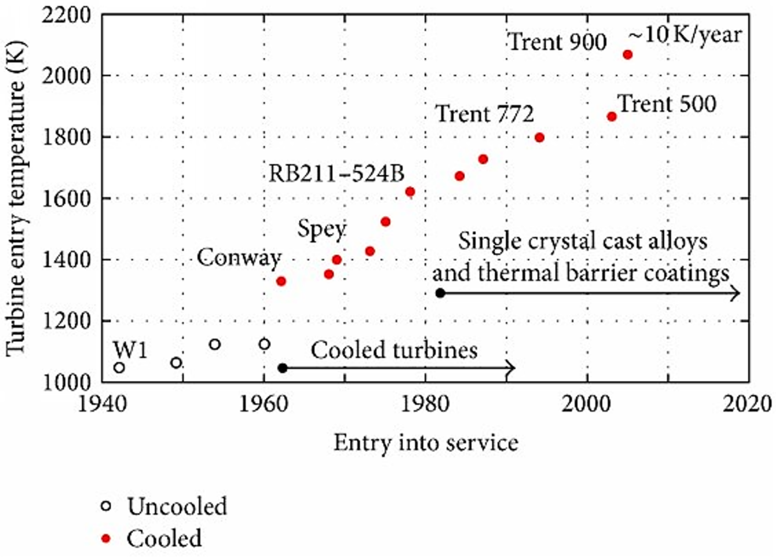

Figure 5: Trend in Take-off TET Values [4].

In many engines, control systems are responsible for cutting off fuel flow to the system accordingly, in order not to exceed these limits and preserve engine health throughout time.

– **Aeroelastic Phenomena**

These effects are particularly critical in compressors, where stall is one of the main causes of the structure-fluid coupling, causing flutter.

Buffeting is also a common aeroelastic phenomenon in compressors, appearing when the relative flow in the rotor achieves supersonic speeds. It generally tends to manifest itself near the tips, although the location of its appearance depends on the torsion law used in the design of the compressor.

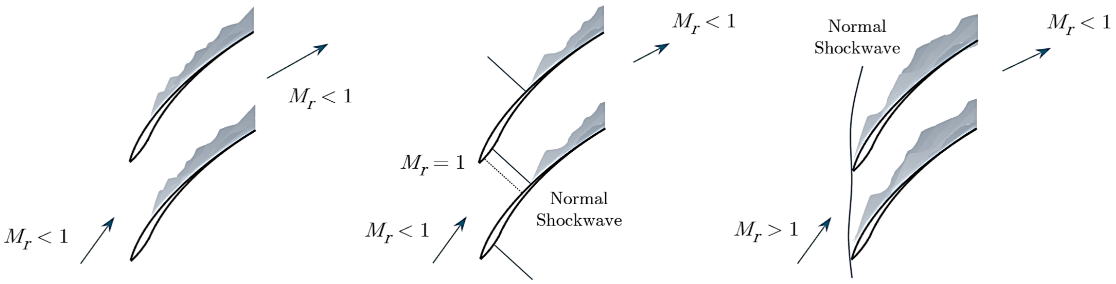

I. Subsonic Stall Flutter II. Choke Stall Flutter III. Supersonic Stall Flutter

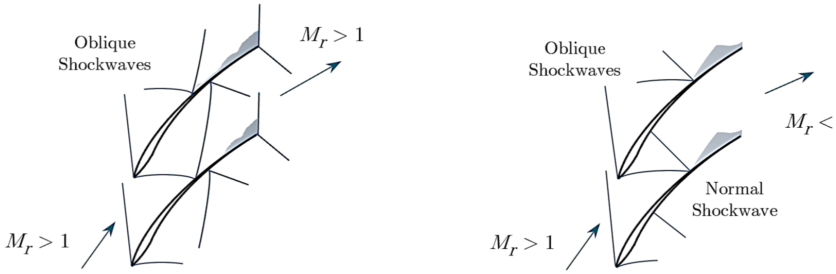

IV. Supersonic Flutter (Low Back Pressure) V. Supersonic Flutter (High Back Pressure)

Figure 6: Scheme of Different Compressor Aeroelastic Phenomena.

The first three of the stated phenomena are equivalent to stall flutter, while the last two are more related to shock buffeting. The nature of this circumstances is hereby briefly explained:

- I. Subsonic Stall Flutter

  As mentioned before, stall also happens near the surge line of the compressor map carrying with itself possible blade flutter before surge. In this case the flow remains subsonic at all times.

- II. Choke Stall Flutter

  Blade stall also tends to happen near the compressor choke line. In choke stall flutter a normal shockwave is generated to decelerate the flow and adapt to the upstream pressure after the conduct between blades is choked.

- III. Supersonic Stall Flutter

  When the surge line is approached at high blade speeds, normal shockwaves tend to envelop the blade tips, forming separation bubbles and leading to this aeroelastic effect.

- IV. Supersonic Flutter (Low back pressure)

  Also happening at relatively higher blade speeds, the relative flow is in many situations supersonic. If the back pressure is low, then the internal shockwaves tend to be weaker to cause less deceleration of the flow, thus, oblique shockwaves form and buffeting occurs.

- V. Supersonic Flutter (High back pressure)

  As in the last case, supersonic flow needs to adapt to back pressure condition. This leads to a higher deceleration of the flow, followed by the formation of internal oblique and normal shockwaves. It can cause blade buffeting.

Each region of the compressor map is associated with one of the effects shown above. Figure 7 represents schematically over a compressor performance map which region is related to the aforementioned phenomena. The described effects apply mostly to axial compressors, while radial and helico-centrifugal machines need not necessarily possess some of these problems.

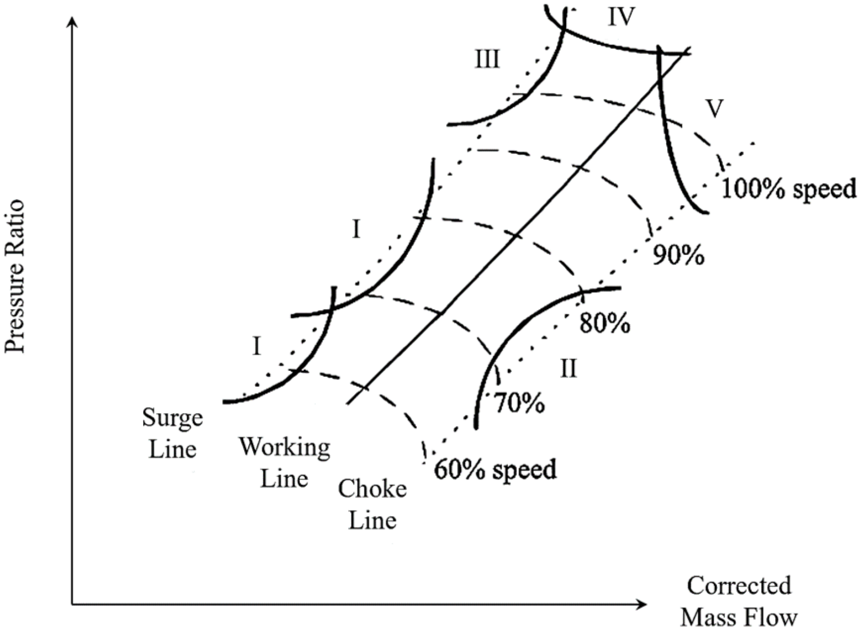

Figure 7: Schematic Location of Relevant Aeroelastic Phenomena on Axial Compressor Map. Adapted from [5].

Turbine cascades also can experience aeroelastic effects, especially in the last stages. These are often addressed by adding damping properties to the system, either by shrouding the cascade [12], adding mass damping and joint viscous damping devices, or fitting a damper wire between blades. This last technique is known as lacing, more common in steam turbines.

Another important reason behind shrouding turbine blades, which is especially done for ceramic blades, is to reduce gap clearance losses [13]. It is also important for avoiding the problems in the next point, as impact of rotors with the carcass pose a critical safety concern in shroudless machines.

– **High Shaft Speed or Shaft Speed near Idle**

Shaft speed can become critical if it exceeds a certain limit, where structural integrity can be compromised, mainly due to centrifugal forces. These range from static to fretting-fatigue issues and creep affecting blades and blade joints. Bearings, lubrication and the air subsystem can also operate outside of their admissible design range.

In compressors, these effects are not as critical as in turbines, because of two main reasons. As seen before, other destructive phenomena as flutter and shock buffeting tend to appear at high blade speed. Therefore, the engine EEC is forced to restrain the flow of fuel to avoid these problems and further compromising operative safety by overspeed.

Furthermore, compressors are not subject to high temperatures and corrosion as in the case of the turbine, although tip-clearance and blade static integrity keep being an important factor to take into account. In these machines fluid-excited vibration is generally a more relevant issue.

Turbines on the other hand often show signs of thermomechanical fatigue. It can have a different behavior compared with classical metal fatigue, because of the fact that modern turbine blades tend to be made from single crystal alloys.

Apart from these issues, if the shaft speed is low enough, engine stall can occur (do not confuse with aerodynamic stall). This effect generally happens when the turbine is no longer capable of powering the compressor, thus that energy imbalance causes deceleration in the system.

This effect can be seen in the present study (although a better modeling of bleeds and shaft viscous losses is needed to accurately predict it) when the steady power balance equations between compressor and turbine can no longer be satisfied in the calculation on the running line.

The control system is then in charge of maintaining a constant fuel flow at idle speed, or when Thrust Lever Angle (TLA) is at rest to avoid stalling the engine. This is done after engine start-up and lighting.

- **Tip Clearance in Sudden Accelerations**

In shroudless cascades, both for compressor and turbine, it is possible to overcome the tip clearance between blades and casing, provoking an impact between them. This phenomenon should always be taken into account in preliminary design because of the risk it poses.

It is commonly more critical in turbine cascades, where blade thermal expansion combined with stretching due to centrifugal effects can lead to this situation. This expansion is more notable during accelerations, where temperatures are higher than in steady state. As mentioned earlier, this is one of the main reasons why blade shrouding is often fitted, sometimes throughout all turbine stages.

Including these feature is not always possible, because it implies adding more weight to the blade tips, worsening centrifugal force effects throughout the blade span. This explains why it tends to be fitted in ceramic HPT cascades. Ceramic blades have a lower density compared with metal alloy ones, alleviating these stresses and making possible their inclusion.

One of other means of avoiding this issue is employing ACC, a computer controlled system, where the HMU is constantly measuring tip clearance to actuate the system.

ACC is based on thermal effects to avoid the impact of the blades against the case. Bleed air from the compressor/fan is directed towards this turbine casing to achieve blade tip cooling. It also allows for improving tip clearance margins, improving turbine efficiency.

For example, during take-off it can be even used to heat to avoid this problem. In deceleration, as the rotor contracts more than the case, the latter is further cooled to improve tip clearance without the tips bruising it. Figure 8 shows schematically the effect of ACC during flight.

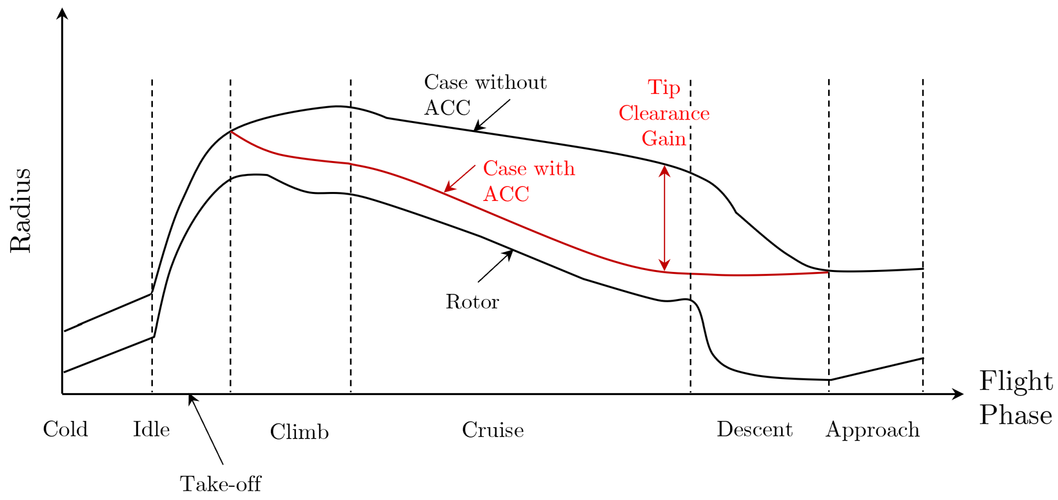

Figure 8: Scheme of the Effect of Active Clearance Control (ACC) on Case Radius in each Flight Phase. Adapted from [6].

- **Combustion Chamber Lean Blowout**

  Another possible effect during off-design operation is engine flameout. The combustion chamber thus has to be restarted. This can occur due to a low AFR and high FAR (Rich Limit) or due to a high AFR or low FAR (Weak Limit). The latter is also known as lean blowout [2].

  This effect is not as critical in practice, as many new engines feature the capability of lighting off the system after a sudden flameout. Nevertheless, it is not desirable and should be avoided when possible.

  The rich limit is typically not achieved in modern jet-engines, as they tend to work with a FAR lower than stoichiometric. Thus, the flame in the combustion chamber can be put out due to excess air, if the flame is not well locked in place. There are swirling devices for this purpose.

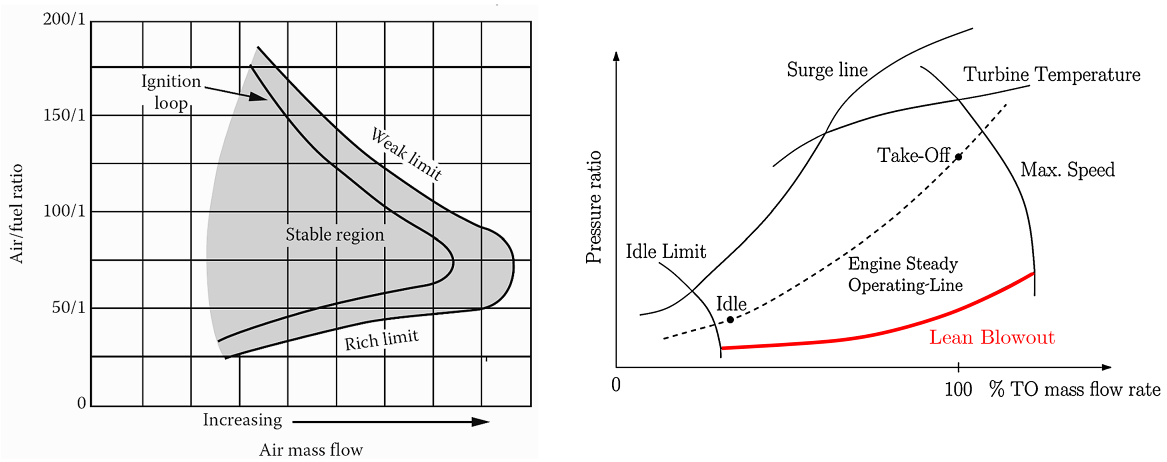

Figure 9: Schemes of Combustion Chamber Operation Limits (left) and Lean Blowout Line on Compressor Map (right). Adapted from [2] and [7], respectively.

  Figure 9 shows, on the left, an outline of combustion chamber operation limits. The weak limit (high AFR) is the one corresponding to the phenomenon hereby described.

  On the right, it shows a scheme of where the lean blowout line on a compressor map tends to be. It is near the compressor choke line, so possible blowout may not necessarily be achieved if the engine happened to function near this region. Instead, choke stall flutter may appear, which is undesirable as well.

  Transient engine dynamics can lead to a lean blowout if the off-design behavior is not well understood and if the coupling between compressor and turbine is not well achieved.

These off-design and transient effects, among many other that can affect other subsystems need to be taken into account to ensure a safe and efficient operation.

- **Complementing Existent Engine Data**

  Off-design analyses can help predict non-observable variables, allowing to complement experimental measurements. If a sensor has failed or is not showing sensible readings, a theoretical model can be a good substitute for these.

  There are also other quantities that sometimes can not be measured with some particular equipment. Take, for example, the measurement of the TET, which in some cases can reach 2000 K (see Figure 5). There are very few and specialized sensors that can perform this task. In onboard applications, for example, it is not common to have this measure available. In this case, the usage of the Exhaust Gas Temperature (EGT) and other parameters may be enough to provide a good estimation of the TET.

  This is actually the how thrust is estimated during flight. Thrust is a quantity that can not be reliably measured during the aircraft operation. It is common for manufacturers to estimate thrust onboard by employing one or a combination of the two following figures and a simple 0-D thermodynamic estimation:

  - **Low Pressure Corrected Shaft Speed:**

    Applying a thrust estimator based on corrected shaft speed has some advantages. First, this quantity is easily measurable. It is closely related to the turbomachinery blades' Mach number. The correction is also not dependent on the exterior pressure since this parameter is $N_{\text{LP}}^{*} = N_{\text{LP}}/\sqrt{T_0/T_{\text{ref}}}$.

    Its use has some disadvantages too. It needs to be corrected according to the humidity present in the air, which has some influence in the production of thrust. This fact will not be considered in this study, although it is necessary to note this effect. It also tends to vary considerably with respect to engine wear. This parameter is used commonly by manufacturers like CFM and General Electric.

  - **Engine Pressure Ratio (EPR)**

    EPR is defined to be the ratio of the total pressure after the turbine (or approximately at the nozzle inlet, 7) and the total pressure at the exit of the diffuser/entry of the compressor: p_{5t}/p_{2t}.

    The models that apply EPR are mostly independent of exterior conditions, although they involve more variables, hence it is more sensor-dependent. Rolls-Royce and Pratt and Whitney are more prone to the usage of this figure.

  As a final remark, note that complimenting measurements by applying a theoretically valid model can predict unexpected results if paired with data considered trustworthy. This may mean that some unforeseen phenomena, not present in the model, are occurring inside the engine, which may be problematic.

- **Analysis of Test Rig/Flight Acquired Data**

  Experimental results obtained in a test rig (or even in-flight) can allow validating an off-design and transient model when applied to the system under measurement. This is generally achieved by means of a statistical approach. A simple validation will be addressed in this present work to confirm the validity of the generated engine model with measurements from a small sensor-equipped gas turbine.

  Having two different sources of information can enrich data analyses, providing a much deeper understanding of the processes that may be involved during off-design or transient engine operation.

  Furthermore, a state observer can be applied to mix known states and measurements and predictions from the theoretical off-design and transient model. This kind of process will be studied in more detail in this work, where an Extended Kalman Filter (EKF, which is a linear-quadratic state estimator) will be applied. This mixing between data and theory can be a very good estimator of the real process, hence greatly improving the model accuracy.

  Having a better understanding of a system, for example, can lead to lower (but certifiable) safety margins in design, as well as ensuring a good final product quality, less prone to develop undesired effects.

- **Guaranteeing Safe Operation During Preliminary Design Phase**

  During the preliminary design stage (Figure 3), it is convenient to estimate engine behavior before testing, to later create a safe testing environment using the knowledge provided by a raw off-design and transient analyses.

  Ensuring a good selection of components and their coupling is fundamental for operative safety during testing. Therefore, having a first estimate of the engine's behavior can supply a prediction for the appearance of several of the aforementioned destructive effects beforehand.

  For example, if the system component interaction is not well addressed, surge can appear during start-up or normal operation, not only endangering those present at the test rig, but also possibly destroying an expensive prototype if the stall is not quickly recovered. Note that many physical processes are present in these systems and the many intricate subsystems they are comprised of. This fact can sometimes lead to unpredictable results or unexpected failures.

  A better understanding can generally be achieved if, again, a state observer is considered to be applied to real-time measurements. Safety concerns in the sensor readings and the yielded results of this model can be foreseen, leading to an improved overall safety when testing.

- **Control System Definition and Tuning**

  The engine's control system, as it has been reiterated many times in this Chapter, is a fundamental equipment for correct engine operation. It is necessary and indispensable in modern jet engines. Off-design and transient studies are needed for their correct definition and tuning.

  Historically different types of control devices have been used in aircraft propulsive systems, depending on their basic principle of acting on them. Many of these systems were initially used for supervisory purposes of the functioning of the system. They were soon replaced by FADEC devices with mechanical control over the system. Nowadays, these FADEC systems are fully electronic, which provides quick and more precise response with a simpler architecture.

  The engine control system is used to actuate many possible features. The basic parameter controlled by it is the fuel flow required (measured and supplied by the HMU). Apart from it, several components can receive inputs from the control system to modify their behavior. Many of these do not have a direct impact in the generation of thrust like, for example, incrementing the flow rate in the lubrication system in a need of a surge of power.

  Some possible control features that have a more clear impact in the generation of thrust are the following:

  - **Variable Stator Vanes, Variable Bleed Valves and Blow Off Valves**

    As mentioned earlier, these devices are control actuated and share a common purpose of avoiding compressor surge among other uses, like aiding in start-up or improving efficiency, which is the case of the VSV.

  - **Active Clearance Control**

    It is also comprised of control-actuated bleed valves, that can extract air from multiple stages to adjust the objective case cooling.

  - **Nozzle Geometry and Variable Area Turbine Nozzle (VATN)**

    In many applications, especially military ones, the nozzle geometry is variable. It allows to adjust the gas conditions at the exit to match those of the ambient when choked, hence maximizing thrust generation. This is not commonly done in civil applications due to low nozzle NPR, which results in low thrust losses. It also is used to aid with engine start-up. In some other cases, turbine nozzle stators (VATN) are movable too, to offer a direct control to the power balance in the shaft.

  Many different subsystems can be control-actuated in these engines, these latter are common examples of these devices. Another common device in turbojet engines are movable supersonic inlets. Either way, controlling fuel flow is the most important task the control system has, to provide a quick, precise and safe response to the commands.

- **Providing Models to Aircraft Manufacturers and Final Users**

  Normally, when a product of this kind is purchased, its operative and maintenance manual and other relevant data are offered to client so they use it according to safety standards and as intended by the manufacturer.

  The engine's characteristic curves, as well as its operative limits are stated after their estimation in off-design testing and modeling. They are provided as it is an essential information for its integration with the rest of the vehicle. The common thrust-corrected shaft speed curve is an illustrative example of a characteristic curve, among many other that describe steady state operation.

  The generated thrust is typically limited either by temperature or pressure difference by the control unit, as stated in the first of these points. It, in turn, depends on exterior conditions, so it is important for aircraft manufacturers to take into account the behavior of the engine according to these atmospheric variables.

  This leads to the creation of derated take-off thrust curves with respect to Outside Air Temperature (OAT) and other corrections to the models, like the aforementioned humidity correction for N_{LP}^{*}. These curves vary with respect to engine mode, and are especially important for take-off conditions.

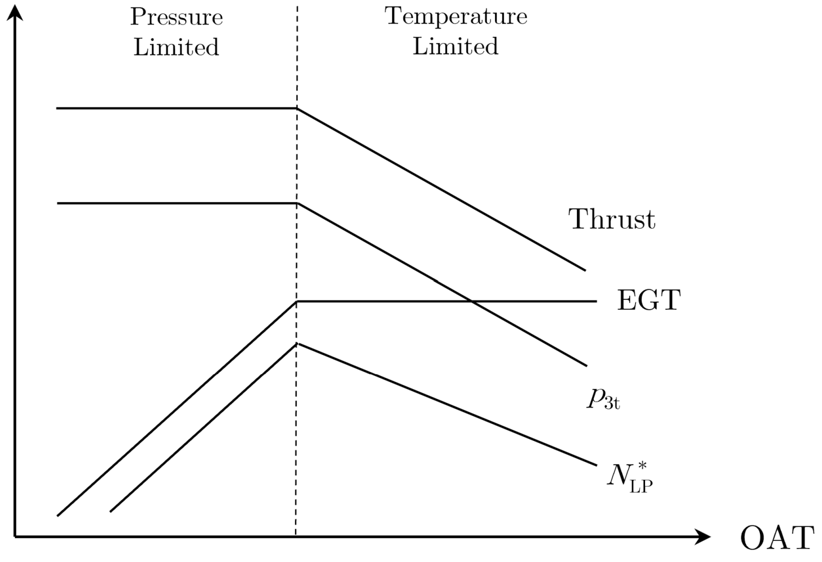

Figure 10: Sketch of Derated Thrust at 100 % TLA - OAT Curves.

Figure 10 is a schematic drawing of the aspect of these thrust derated curves. For values under a critical OAT the control system acts to prevent surpassing maximum pressure difference limits. Furthermore, maximum thrust is kept independent of exterior temperature so the aircraft operator detects having the same amounts of thrust each take-off operation. Above that critical OAT, the control system is triggered to avoid a temperature excess.

Generated thrust in these conditions is inferior to the one in the pressure limited region. If the OAT is high, air density decreases, and hence a greater amount of thrust is needed to overcome this issue. However, as seen in Figure 10 thrust needs to be derated even more, which is detrimental for completing the take-off maneuver.

- **Integration in the FADEC for Maneuver Prediction, Health Diagnosis and Failure Prognosis**

  These type of off-design and transient analyses are also employed for onboard engine parameter estimation, as mentioned. It is common to integrate fast models to predict the response of the engine under certain maneuvers in real time. The engine's control system then actuates if necessary, correcting it.

  Engine health diagnosis is also carried in many modern engines. Taking profit of the onboard sensing equipment and an off-transient model the EEC can predict, for example, turbomachinery performance map degradation over time or possible irregularities in the cycle.

  It has been proven to be essential for the economical and safe operation of the engine. This is due to the prediction of component efficiency degradation as well as the early diagnostics of component breakdown. This last case allows in turn to reduce the cost of maintenance programs, reducing both required predictive and corrective maintenance time.

  On another hand, prognosis refers the techniques that try to predict the moment in which the product will lose its capability of functioning as it must. Of course, it is effective when the mechanisms that are involved in the engine failure are known [6]. The models for those physical mechanisms have to be accurate enough to correctly predict possible component failure, otherwise there is a risk that the system ends up operating in dangerous conditions.

  It is nonetheless difficult to predict engine failure with accuracy, as it generally occurs after a long process of wear after usage and multiple phenomena are involved in the process. These are not always visible in the sensor data.

- **Integration in Flight Simulators**

  Off-design fast-prediction models are sometimes integrated in flight simulators to provide accurate estimations of thrust production for simulating aircraft mechanics and other purposes.

  As an example, other magnitudes that are often indicated to the pilot can be calculated and displayed in the cockpit. State variables like N_{LP}^{*} or EPR (and N_{HP}^{*} if applicable), EGT, temperature and pressure of the lubrication system are indicated in the environment to provide a more accurate training for pilots.

3. Engine Modeling

In this chapter, the process employed to find a solution to the off-design and transient behavior is described. Throughout this work, for both the analytical and performance map solution, the engine will be modeled by means of a 0-D thermodynamic approach. Thus, the flow will be considered one-dimensional and thermodynamic states will be mass flow averaged in their corresponding station. Both will be formulated in the same kind of variables.

First off, the number of problem dependencies can be reduced my means of dimensional analysis, using for this purpose different types of variables. In the following table [11] several kinds are stated, among a brief description and an example.

Variable Type	Description	Example
Conventional	Conventional units Simple and physical interpretation Do not reduce problem dimensionality	$\dot{m}$
Nondimensional	Do not have units Physical, more intricate interpretation Reduce the number of equations	$\frac{V}{\sqrt{\gamma R T}}$
Quasi-nondimensional	Have nonstandard units Lack a clear physical interpretation Reduce the number of equations	$\frac{N}{\sqrt{T_\mathrm{t}}}$
Corrected	Conventional units Lack a clear physical interpretation Reduce the number of equations	$\frac{\dot{m}\sqrt{T_\mathrm{t}/T_\mathrm{ref}}}{p_\mathrm{t}/p_\mathrm{ref}}$

Table 1: Variable Types According to Problem Dimensionality and Units.

The problem will be formulated in **corrected variables**, with the consequent appearance of many nondimensional variables. This election is motivated by the fact that they reduce the problem's dimensionality while maintaining conventional units. Their interpretation, although many times nonphysical because of the correction terms, is simpler for the reader.

3.1 General Solution Employing Performance Maps

The solution based on compressor and turbine performance maps is one of the principal goals in this work. The analytical solution on the other hand, is a simplification of this problem and will be considered to compare both proceedings.

3.1.1 Assumptions

Several assumptions must be made in order to have a viable model and set of equations to solve. First, the problem will be considered in both steady and transient state. Compressor and turbine performance maps are scalable, whose Reynolds Number Index (RNI) is high enough to ensure validity of the map throughout the analysis. Air is assumed to behave as an ideal gas (constant R), but not a perfect gas (variable C_{p}). These particular properties are divided according to the cold and hot region of the cycle. This cold part is defined to span stations 0 to 3, while the hot one is considered to start from 4 up to station 8 or 9.

Furthermore, combustion model needs to be simple. A frozen flow, simple thermodynamic heat addition at almost constant total pressure is the model chosen in this component. Better models, like considering chemical equilibrium, provide a more exact estimation of combustion chamber operation.

It is also reasonable to model components as adiabatic, as flow velocity is often too high to have noticeable losses due to heat transfer. Of course, this applies to all components except the combustion chamber, where not only heat is injected into the system, but also heat losses will be considered, at least for this component's pressure ratio. Also, regarding mass and heat transfer, no leakage in mass or enthalpy flows are considered to be relevant. In transient analysis, secondary effects like mass or heat pocketing are left out of the model. Thermodynamic properties are supposed to change infinitely faster than the axis angular velocity, so steady state component equations can be used. Table 2 summarizes what has been exposed in the last paragraphs.

Property	Description
Analysis Type	Exact 0D with turbomachinery performance maps
Time Dependence	Steady state and transient
Gas Model	Ideal, semiperfect with cold/hot zone differentiation
Combustion Model	Simple heat addition, frozen flow
Mass/Energy Transfer	Adiabatic parts (except CC), no leaks or pocketing
Miscellanea	Diffuser, nozzle isentropic efficiencies considered to be constant Shaft power transmission efficiency and bleed percentages also remain unchanged during operation

Table 2: Summary of Assumptions for the Off-design Problem Employing Performance Maps.

3.1.2 Problem Variables

The off-design problem is hereby detailed. The goal of this subchapter is to reach a full thermodynamic description of the system, in corrected variables, after imposing the corresponding Degrees Of Freedom (DOF) associated to it.

This means that, for each of the components that make up the system, there are 4 thermodynamic variables to be solved. They are detailed in the following tables for both single spool turbojet and dual spool turbojet.

These are, in general, the corrected mass flow at the station corresponding to the component inlet, total pressure ratio (although not in the case of the diffuser and nozzle, where one of the components is static), total temperature ratio (again not applicable to these two for the same reason) and a specific variable corresponding to the nature of each component. The only exception to this rule is the NGV bleed injection, corresponding to span stations 4 and 41, that adds only 3 variables.

- **Single Spool Turbojet**

  The model employed for a single spool turbojet has a total of **23 variables**, expressed in the following Table 3. The special variables for diffuser and nozzle are the inlet Mach number and exit Mach number, respectively. For compressor and turbine these variables represent the relative corrected shaft speed. Note that N_C and N_T do not necessarily have to be equal, as they could be coupled through a gearbox. Finally, the combustion chamber introduces the fuel parameter $\frac{\eta_\mathrm{CC} f L}{C_\mathrm{p} T_\mathrm{3t}}$.

Component	**Variables**
Diffuser	$\frac{T_\mathrm{2t}}{T_0}, \frac{p_\mathrm{2t}}{p_0}, \frac{\dot{m}_0\sqrt{T_0/T_\mathrm{ref}}}{p_0/p_\mathrm{ref}}, \frac{V_0}{\sqrt{\gamma_\mathrm{c} R T_0}}$
Compressor	$\frac{T_\mathrm{3t}}{T_\mathrm{2t}}, \frac{p_\mathrm{3t}}{p_\mathrm{2t}}, \frac{\dot{m}_2\sqrt{T_\mathrm{2t}/T_\mathrm{ref}}}{p_\mathrm{2t}/p_\mathrm{ref}}, \frac{N_\mathrm{C}/N_\mathrm{ref,C}}{\sqrt{T_\mathrm{2t}/T_\mathrm{ref}}}$
Combustion Chamber	$\frac{T_\mathrm{4t}}{T_\mathrm{3t}}, \frac{p_\mathrm{4t}}{p_\mathrm{3t}}, \frac{\dot{m}_3\sqrt{T_\mathrm{3t}/T_\mathrm{ref}}}{p_\mathrm{3t}/p_\mathrm{ref}}, \frac{\eta_\mathrm{CC} f L}{C_\mathrm{p} T_\mathrm{3t}}$
NGV Bleed Injection	$\frac{T_\mathrm{41t}}{T_\mathrm{4t}}, \frac{p_\mathrm{41t}}{p_\mathrm{4t}}, \frac{\dot{m}_4\sqrt{T_\mathrm{4t}/T_\mathrm{ref}}}{p_\mathrm{4t}/p_\mathrm{ref}}$
Turbine	$\frac{T_\mathrm{5t}}{T_\mathrm{41t}}, \frac{p_\mathrm{5t}}{p_\mathrm{41t}}, \frac{\dot{m}_{41}\sqrt{T_\mathrm{41t}/T_\mathrm{ref}}}{p_\mathrm{41t}/p_\mathrm{ref}}, \frac{N_\mathrm{T}/N_\mathrm{ref,T}}{\sqrt{T_\mathrm{41t}/T_\mathrm{ref}}}$
Nozzle	$\frac{T_9}{T_{5t}}, \frac{p_9}{p_{5t}}, \frac{\dot{m}_5\sqrt{T_\mathrm{5t}/T_\mathrm{ref}}}{p_\mathrm{5t}/p_\mathrm{ref}}, \frac{V_9}{\sqrt{\gamma_\mathrm{h} R T_9}}$

Table 3: Problem Variables for the Single Spool Turbojet.

- **Dual Spool Turbojet**

  The model devised for a dual spool turbojet brings a total of **31 variables** to solve for. Since the compressor and turbines are divided into two different low pressure and high pressure components to achieve the coupling, these add 8 new variables to the system. Again the cooling bleed is considered to add 3 new variables because the bleed percentage is known. These are shown in Table 4.

Component	**Variables**
Diffuser	$\frac{T_{2t}}{T_0}, \frac{p_{2t}}{p_0}, \frac{\dot{m}_0\sqrt{T_0/T_{\mathrm{ref}}}}{p_0/p_{\mathrm{ref}}}, \frac{V_0}{\sqrt{\gamma_c R T_0}}$
Low Pressure Compressor	$\frac{T_{25t}}{T_{2t}}, \frac{p_{25t}}{p_{2t}}, \frac{\dot{m}_2\sqrt{T_{2t}/T_{\mathrm{ref}}}}{p_{2t}/p_{\mathrm{ref}}}, \frac{N_{\mathrm{LPC}}/N_{\mathrm{ref,LPC}}}{\sqrt{T_{2t}/T_{\mathrm{ref}}}}$
High Pressure Compressor	$\frac{T_{3t}}{T_{25t}}, \frac{p_{3t}}{p_{25t}}, \frac{\dot{m}_{25}\sqrt{T_{25t}/T_{\mathrm{ref}}}}{p_{25t}/p_{\mathrm{ref}}}, \frac{N_{\mathrm{HPC}}/N_{\mathrm{ref,HPC}}}{\sqrt{T_{25t}/T_{\mathrm{ref}}}}$
Combustion Chamber	$\frac{T_{4t}}{T_{3t}}, \frac{p_{4t}}{p_{3t}}, \frac{\dot{m}_3\sqrt{T_{3t}/T_{\mathrm{ref}}}}{p_{3t}/p_{\mathrm{ref}}}, \frac{\eta_{\mathrm{CC}} f L}{C_{\mathrm{p,c}} T_{3t}}$
NGV Bleed Injection	$\frac{T_{41t}}{T_{4t}}, \frac{p_{41t}}{p_{4t}}, \frac{\dot{m}_4\sqrt{T_{4t}/T_{\mathrm{ref}}}}{p_{3t}/p_{\mathrm{ref}}}$
High Pressure Turbine	$\frac{T_{45t}}{T_{41t}}, \frac{p_{45t}}{p_{41t}}, \frac{\dot{m}_{41}\sqrt{T_{41t}/T_{\mathrm{ref}}}}{p_{41t}/p_{\mathrm{ref}}}, \frac{N_{\mathrm{HPT}}/N_{\mathrm{ref,HPT}}}{\sqrt{T_{41t}/T_{\mathrm{ref}}}}$
Low Pressure Turbine	$\frac{T_{5t}}{T_{45t}}, \frac{p_{5t}}{p_{45t}}, \frac{\dot{m}_{45}\sqrt{T_{45t}/T_{\mathrm{ref}}}}{p_{45t}/p_{\mathrm{ref}}}, \frac{N_{\mathrm{LPT}}/N_{\mathrm{ref,LPT}}}{\sqrt{T_{45t}/T_{\mathrm{ref}}}}$
Nozzle	$\frac{T_9}{T_{5t}}, \frac{p_9}{p_{5t}}, \frac{\dot{m}_5\sqrt{T_{5t}/T_{\mathrm{ref}}}}{p_{5t}/p_{\mathrm{ref}}}, \frac{V_9}{\sqrt{\gamma_h R T_9}}$

Table 4: Problem Variables for the Dual Spool Turbojet.

The variables introduced by these systems are sometimes interchanged by other quantities, to facilitate the resolution. This is the case of beta lines, that are used as a more efficient way to enter information when accessing compressor and turbine maps, as they tend to be more orthogonal to characteristics than, for example, corrected mass flow.

Beta lines will be decisive to achieve an efficient solution algorithm, which will be described in following subchapters. Either way, these latter will be the considered variables of the problem, although other 23 in the case of the single spool or 31 in the case of the dual spool could be defined.

3.1.3 Problem Equations

The variables that form the problem are then complemented with a series of equations for it to be solved. The difference of free variables and equations yields the problem's DOFs, which must be imposed to provide a solution. These will allow for parametric studies too, given other quantities considered constant are modified and counted as DOFs, like bleed fractions or nozzle area. In the following equations these will not be counted as such.

Component Modeling and Mass Flow Continuity at their Inlet

To start off, the equations provided by the components are stated for both kinds of turbojet engines. Many of these equations are shared, so component equations will be described in general and later counted. Generally, components introduce 3 new equations to the system, with the exceptions of the diffuser and nozzle. All relations are expressed in **steady state** and, through various assumptions, will be used in a forthcoming transient analysis too.

- **Diffuser**

  Diffusers introduce 2 new equations. These are, respectively, energy conservation (in the form of constant total enthalpy) and total pressure evolution, coming from the definition of diffuser isentropic efficiency. They are represented in the following Equation 2 and 3.

  $$\frac{T_{2\mathrm{t}}}{T_0} = 1 + \frac{\gamma_\mathrm{c} - 1}{2} M_0^2 \tag{2}$$

  $$\frac{p_{2\mathrm{t}}}{p_0} = \left(1 + \frac{\gamma_\mathrm{c} - 1}{2} \eta_\mathrm{D} M_0^2\right)^{\frac{\gamma_\mathrm{c} - 1}{\gamma_\mathrm{c}}} \tag{3}$$

  As stated in Table 2, diffuser isentropic efficiency η_D is considered constant and near 1, as in general subsonic inlets do not generally introduce great total pressure losses. The corrected inlet mass flow $\dot{m}_0^*$ and flight Mach number M_0 are also part of the introduced component variables, stated in Table 3 and Table 4. These take the following abbreviations:

  $$\dot{m}_0^* = \frac{\dot{m}_0 \sqrt{T_0 / T_\mathrm{ref}}}{p_0 / p_\mathrm{ref}} \tag{4}$$

  $$M_0 = \frac{V_0}{\sqrt{\gamma_\mathrm{c} R T_0}} \tag{5}$$

  Supersonic inlets' behavior is totally opposite to the former. Due to the appearance of compressibility effects that greatly increment entropy, their efficiency is generally lower and more dependent on Mach number or even aircraft angle of attack.

  Furthermore, these inlets are more prone to flow separation, affecting components downstream. They are generally modeled through performance curves and sometimes control-actuated. They will not be considered in the present study. It is not desired to add further complexity unless necessary.

- **Compressor**

  One of the main point of this study is achieved through the modeling of compressors employing their performance maps, which achieves a much more precise solution than other methods. Off-design undesired effects involving compressor instabilities can be predicted if their location in compressor map is known (see Figure 7).

  Performance maps take two real inputs (commonly β lines or inlet corrected mass flow $\dot{m}^*$ and compressor characteristic N_{C}^*) and return two parameters, in this present analysis compressor total pressure ratio π_{C} and isentropic efficiency η_{C} .

  In general, these are empirically measured mappings relating two or more dependence parameters with the outputs. These input parameters can include RNI or even engine diameter, blade chord, height and angle if the geometry is variable. As said, only two inputs are going to be considered, thus defining a mapping $\mathcal{M} : \mathbb{R}^2 \longrightarrow \mathbb{R}^2$ that generates 2 new equations to solve the system. These relations are the following, depending if the considered engine is a single spool or dual spool turbojet:

  - **Single Spool Turbojet**

    For a single spool engine there is only one compressor, providing 2 new equations for the thermodynamic variables and 1 for continuity of mass flow. Therefore, it introduces 3 relations, stated in Equation 6, 7 and 9.

$$\frac{T_{3\mathrm{t}}}{T_{2\mathrm{t}}} = 1 + \frac{1}{\eta_{\mathrm{C}}}\left(\left(\frac{p_{3\mathrm{t}}}{p_{2\mathrm{t}}}\right)^{\frac{\gamma_{\mathrm{c}}-1}{\gamma_{\mathrm{c}}}} - 1\right) \tag{6}$$

$$\frac{p_{3\mathrm{t}}}{p_{2\mathrm{t}}} = \pi_{\mathrm{C}}(\dot{m}_2^*, N_{\mathrm{C}}^*) \tag{7}$$

    Efficiency is the second variable given by the performance maps:

$$\eta_{\mathrm{C}} = \eta_{\mathrm{C}}(\dot{m}_2^*, N_{\mathrm{C}}^*) \tag{8}$$

    Compressor isentropic efficiency in Equation 8 is not considered a new equation, just a transition one. It links the component's total pressure ratio with total temperature ratio. Equation 6 is derived from the definition of isentropic efficiency. Continuity equation reads the following, assuming there are no bleeds between stations 0 and 2:

$$\dot{m}_2^* = \frac{\dot{m}_2\sqrt{T_{2\mathrm{t}}/T_{\mathrm{ref}}}}{p_{2\mathrm{t}}/p_{\mathrm{ref}}} = \dot{m}_0^*\frac{\sqrt{T_{2\mathrm{t}}/T_0}}{p_{2\mathrm{t}}/p_0} \tag{9}$$

    Relative corrected compressor shaft speed N_{C}^* is expressed in the following form:

$$N_{\mathrm{C}}^* = \frac{N_{\mathrm{C}}/N_{\mathrm{ref,C}}}{\sqrt{T_{2\mathrm{t}}/T_{\mathrm{ref}}}} \tag{10}$$

- **Dual Spool Turbojet**

  In the case of a dual spool turbojet, 6 new equations are included: 4 component equations and 2 mass conservation ones, given that it is divided into two sections, both having different performance maps and shaft connections. For the LPC:

$$\frac{T_{25\mathrm{t}}}{T_{2\mathrm{t}}} = 1 + \frac{1}{\eta_{\mathrm{LPC}}}\left(\left(\frac{p_{25\mathrm{t}}}{p_{2\mathrm{t}}}\right)^{\frac{\gamma_{\mathrm{c}}-1}{\gamma_{\mathrm{c}}}} - 1\right) \tag{11}$$

$$\frac{p_{25\mathrm{t}}}{p_{2\mathrm{t}}} = \pi_{\mathrm{LPC}}(\dot{m}_2^*, N_{\mathrm{LPC}}^*) \tag{12}$$

  For the HPC the set of component equations is identical to the LPC, with the exception of depending on the latter's exit mass flow and thermodynamic properties, which coincides with the one in its inlet. It also spins at a different relative shaft speed because of its connection with the HPT. These relations are:

$$\frac{T_{3\mathrm{t}}}{T_{25\mathrm{t}}} = 1 + \frac{1}{\eta_{\mathrm{HPC}}}\left(\left(\frac{p_{3\mathrm{t}}}{p_{25\mathrm{t}}}\right)^{\frac{\gamma_{\mathrm{c}}-1}{\gamma_{\mathrm{c}}}} - 1\right) \tag{13}$$

$$\frac{p_{3\mathrm{t}}}{p_{25\mathrm{t}}} = \pi_{\mathrm{HPC}}(\dot{m}_{25}^*, N_{\mathrm{HPC}}^*) \tag{14}$$

  Isentropic efficiencies are also considered transition equations given in each performance map. Note their dependence on the component maps:

$$\eta_{\mathrm{LPC}} = \eta_{\mathrm{LPC}}(\dot{m}_2^*, N_{\mathrm{LPC}}^*), \quad \eta_{\mathrm{HPC}} = \eta_{\mathrm{HPC}}(\dot{m}_{25}^*, N_{\mathrm{HPC}}^*) \tag{15}$$

  On the other hand, taking into account bleed fractions b_{25} and b_3 expressed with respect to inlet air mass flow, continuity equations for station 2 coincides with Equation 9, while in station 25 a bleed is applied:

$$\dot{m}_{25}^* = \frac{\dot{m}_{25}\sqrt{T_{25\mathrm{t}}/T_{\mathrm{ref}}}}{p_{25\mathrm{t}}/p_{\mathrm{ref}}} = \dot{m}_2^*(1 - b_{25})\frac{\sqrt{T_{25\mathrm{t}}/T_{2\mathrm{t}}}}{p_{25\mathrm{t}}/p_{2\mathrm{t}}} \tag{16}$$

  This time, relative corrected shaft speed for both components is expressed as:

$$N_{\mathrm{LPC}}^* = \frac{N_{\mathrm{LPC}}/N_{\mathrm{ref,LPC}}}{\sqrt{T_{2\mathrm{t}}/T_{\mathrm{ref}}}} \tag{17}$$

$$N_{\mathrm{HPC}}^* = \frac{N_{\mathrm{HPC}}/N_{\mathrm{ref,HPC}}}{\sqrt{T_{25\mathrm{t}}/T_{\mathrm{ref}}}} \tag{18}$$

  Note that neither N_{LPC} or N_{HPC} have to be equal to N_{LPT} and N_{HPT} respectively, because a gearbox with a certain transmission ratio can be considered in their coupling. Thus, the 6 equations introduced in this modeling of the systems are Equation 9, 11, 12, 13, 14 and 16.

- **Combustion Chamber**

  This component's effect on the working gas is modeled by a simple almost constant total pressure process. With a simple energy balance (reiterating, in steady state frozen flow and mass averaged properties) it is possible to arrive at Equation 19. To derive this, an approximated value for the FAR f is assumed. This value is expressed with respect to combustion chamber inlet mass flow $\dot{m}_3$. Also, the aforementioned cold and hot differentiated zones have been included, assuming air properties in the hot zone are those of the gas after combustion.

  $$\frac{T_{4\mathrm{t}}}{T_{3\mathrm{t}}} \approx \frac{1}{1+f} \frac{C_{\mathrm{p,c}}}{C_{\mathrm{p,h}}} \left(1 + \frac{\eta_{\mathrm{CC}} f L}{C_{\mathrm{p,c}} T_{3\mathrm{t}}}\right) \tag{19}$$

  Note the simple relation between the total temperature ratio and the fuel parameter $(\eta_{\mathrm{CC}} f L)/(C_{\mathrm{p,c}} T_{3\mathrm{t}})$. This is the reason why this variable has been chosen to represent the phenomena occurring in this component. It denotes the power injected to the system as fuel (where η_{CC} is the combustion chamber efficiency and L is its heating value) with respect to the enthalpic power of the inlet flow in the combustion chamber.

  Total pressure losses in this component are not going to be considered constant as many of the component efficiencies of the analysis. It will be modeled according to the Pressure Loss Factor (PLF) denoted here as ζ_{CC}. This model is often employed and constitutes an empirical estimation of the total pressure ratio.

  $$\zeta_{\mathrm{CC}} = \frac{p_{3\mathrm{t}} - p_{4\mathrm{t}}}{\frac{1}{2}\rho_3 V_3^2} \approx \zeta_{\mathrm{CC,c}} + \zeta_{\mathrm{CC,h}} \left(\frac{T_{4\mathrm{t}}}{T_{3\mathrm{t}}} - 1\right) \tag{20}$$

  Where $\zeta_{\mathrm{CC,c}}$ represents the cold pressure losses, due to irreversibilities within the turbulent flow and $\zeta_{\mathrm{CC,h}}$ denotes the hot total pressure losses due to heat transfer through the component. Both values depend on the type of combustion chamber, $\zeta_{\mathrm{CC,c}}$ ranging from 18 to 35 and $\zeta_{\mathrm{CC,h}}$ from 1 to 2, suggesting that total pressure drop is are fundamentally generated by cold losses.

  $$\frac{p_{4\mathrm{t}}}{p_{3\mathrm{t}}} = \pi_{\mathrm{CC}} = 1 - \zeta_{\mathrm{CC}} \frac{\frac{1}{2}\rho_3 V_3^2}{p_{3\mathrm{t}}} \approx 1 - \frac{\zeta_{\mathrm{CC}}}{2} \frac{R T_{\mathrm{ref}}}{p_{\mathrm{ref}}^2 A_3^2} \left(m_3^*\right)^2 \tag{21}$$

  After assuming that densities $\rho_{3\mathrm{t}} \approx \rho_3$. Finally, all component relations are given in Equation 19, 21 and 22 or 23 to complete a total of 3 relations. Mass conservation at the outlet is, for both kinds of turbojet engines considered:

  - **Single Spool Turbojet**

    $$\dot{m}_3^* = \frac{\dot{m}_3 \sqrt{T_{3\mathrm{t}}/T_{\mathrm{ref}}}}{p_{3\mathrm{t}}/p_{\mathrm{ref}}} = \dot{m}_2^* (1 - b_3) \frac{\sqrt{T_{3\mathrm{t}}/T_{2\mathrm{t}}}}{p_{3\mathrm{t}}/p_{2\mathrm{t}}} \tag{22}$$

  - **Dual Spool Turbojet**

    $$\dot{m}_3^* = \frac{\dot{m}_3 \sqrt{T_{3\mathrm{t}}/T_{\mathrm{ref}}}}{p_{3\mathrm{t}}/p_{\mathrm{ref}}} = \dot{m}_{25}^* \frac{1 - b_{25} - b_3}{1 - b_{25}} \frac{\sqrt{T_{3\mathrm{t}}/T_{25\mathrm{t}}}}{p_{3\mathrm{t}}/p_{25\mathrm{t}}} \tag{23}$$

- **NGV Cooling Bleed**

  Although this cannot really be considered an engine component, a cooling bleed between stations 4 and 41 is included to model the injection of a low temperature gas coming from the last compressor stages, as it is done in the vast majority of modern day engines. These relations are gathered in Equation 24, 25, and 26 for a single spool engine and Equation 25, 27, and 28 for a dual spool one.

  This system introduces 3 new equations and 3 new variables, hence doesn't affect the number of problem DOFs. Despite all of this, it will affect engine behavior, as the effective TET will be reduced, having an impact in the power generated by subsequent turbine components.

  The total temperature ratio is considered through an enthaplic power balance of the gases between stations 4 and 41, where the inlet air bleed fraction b_3 is fed into the system. Total pressure ratio will not be considered to change, since $p_{4t}/p_{3t} \approx 1$ and $b_3 << 1$.

  Turbine refrigeration is actually a very complicated and fundamental topic in engine design. The model employed is actually very simplified, assuming that he injected gas acts as a perfect heat exchanger. Nonetheless, considering it will be useful for the purposes of this study. If more resolution is needed, more accurate bleed and cooling models should be considered but, to reiterate, it is not the goal of this study. The aforementioned enthalpy balance is reordered to be expressed in total temperature ratio.

  - **Single Spool Turbojet**

    For a single spool turbojet only one extracted bleeding air is considered during the compression stage. The three equations have the following form:

$$\frac{T_{41\mathrm{t}}}{T_{4\mathrm{t}}} = \frac{(1-b_3)(1+f) + b_3 \frac{C_{\mathrm{p,c}}}{C_{\mathrm{p,e}}} \left(\frac{T_{3\mathrm{t}}}{T_{4\mathrm{t}}}\right)}{(1-b_3)(1+f) + b_3} \tag{24}$$

$$\frac{p_{41\mathrm{t}}}{p_{4\mathrm{t}}} \approx 1 \tag{25}$$

$$\dot{m}_4^* = \frac{\dot{m}_4 \sqrt{T_{4\mathrm{t}}/T_{\mathrm{ref}}}}{p_{4\mathrm{t}}/p_{\mathrm{ref}}} = \dot{m}_3^* \frac{(1-b_3)(1+f)}{1-b_3} \frac{\sqrt{T_{4\mathrm{t}}/T_{3\mathrm{t}}}}{p_{4\mathrm{t}}/p_{3\mathrm{t}}} \tag{26}$$

  - **Dual Spool Turbojet**

    For a dual spool turbojet an additional bleed air is considered to be extracted from the system at station 25. Note the validity of Equation 25.

$$\frac{T_{41\mathrm{t}}}{T_{4\mathrm{t}}} = \frac{(1-b_{25}-b_3)(1+f) + b_3 \frac{C_{\mathrm{p,c}}}{C_{\mathrm{p,e}}} \left(\frac{T_{3\mathrm{t}}}{T_{4\mathrm{t}}}\right)}{(1-b_{25}-b_3)(1+f) + b_3} \tag{27}$$

$$\dot{m}_4^* = \frac{\dot{m}_4 \sqrt{T_{4\mathrm{t}}/T_{\mathrm{ref}}}}{p_{4\mathrm{t}}/p_{\mathrm{ref}}} = \dot{m}_3^* \frac{(1-b_{25}-b_3)(1+f)}{1-b_{25}-b_3} \frac{\sqrt{T_{4\mathrm{t}}/T_{3\mathrm{t}}}}{p_{4\mathrm{t}}/p_{3\mathrm{t}}} \tag{28}$$

- **Turbine**

  The behavior of turbines will also be modeled accessing component performance maps, due to the need of a more precise solution. These are more complicated to work with, due to the limited region of corrected mass flow $\dot{m}^*_{\mathrm{T}}$ and turbine total pressure ratio π_{T} they work in. Furthermore, turbine characteristics tend to lack orthogonality with respect to corrected inlet mass flow near choke conditions.

  They pose a numerical challenge for these multiple reasons, which lead to develop an analytical solution avoiding performance maps, among other approximations that use this fact. This is done by assuming choke conditions and its corresponding mass and thermodynamic properties in the turbine along the whole operating line. As it will be seen in following chapters, this is many times not far from reality, given some additional conditions are met.

  Beta lines are also sometimes used in these performance maps to increase orthogonality with turbine characteristics. Similarly to the assumptions made with compressor maps, control operated devices like VATN will not be considered. High RNI ensures map reproducibility as well as possible scaling.

  - **Single Spool Turbojet**

    Again, for a single spool engine there is only one turbine, providing 2 new equations for the thermodynamic variables and 1 for continuity of mass flow. 3 relations are then introduced, stated in Equation 29, 30 and 32.

$$\frac{T_{5\mathrm{t}}}{T_{41\mathrm{t}}} = 1 - \eta_{\mathrm{T}} \left(1 - \left(\frac{p_{5\mathrm{t}}}{p_{41\mathrm{t}}} \right)^{\frac{\gamma_{\mathrm{h}}-1}{\gamma_{\mathrm{h}}}} \right) \tag{29}$$

$$\frac{p_{5\mathrm{t}}}{p_{41\mathrm{t}}} = \frac{1}{\pi_{\mathrm{T}}(\dot{m}^*_{41}, N^*_{\mathrm{T}})} \tag{30}$$

    Turbine isentropic efficiency is recovered for performance maps too, and considered a side relation that does not add any new equations:

$$\eta_{\mathrm{T}} = \eta_{\mathrm{T}}(\dot{m}^*_{41}, N^*_{\mathrm{T}}) \tag{31}$$

    The only mass conservation relation in this component is formulated in station 41, where μ is the momentum factor. It is the fraction of bleed air b_3 that injects momentum in the turbine rotors, causing an influence in its generated power:

$$\dot{m}^*_{41} = \frac{\dot{m}_{41}\sqrt{T_{41\mathrm{t}}/T_{\mathrm{ref}}}}{p_{41\mathrm{t}}/p_{\mathrm{ref}}} = \dot{m}^*_4 \frac{(1-b_3)(1+f)+\mu b_3}{(1-b_3)(1+f)} \frac{\sqrt{T_{41\mathrm{t}}/T_{4\mathrm{t}}}}{p_{41\mathrm{t}}/p_{4\mathrm{t}}} \tag{32}$$

    Relative corrected turbine shaft speed N^*_{C} is expressed in the following form:

$$N^*_{\mathrm{T}} = \frac{N_{\mathrm{T}}/N_{\mathrm{ref,T}}}{\sqrt{T_{41\mathrm{t}}/T_{\mathrm{ref}}}} \tag{33}$$

- **Dual Spool Turbojet**

As it happened with both compressors in the dual spool case, 6 equations are provided with intrinsic turbine equations, given two different couplings occur. In the case of the HPT:

$$\frac{T_{45\mathrm{t}}}{T_{41\mathrm{t}}} = 1 - \eta_{\mathrm{HPT}} \left(1 - \left(\frac{p_{45\mathrm{t}}}{p_{41\mathrm{t}}}\right)^{\frac{\gamma_{\mathrm{h}}-1}{\gamma_{\mathrm{h}}}}\right) \tag{34}$$

$$\frac{p_{45\mathrm{t}}}{p_{41\mathrm{t}}} = \frac{1}{\pi_{\mathrm{HPT}}(\dot{m}_{41}^{*}, N_{\mathrm{HPT}}^{*})} \tag{35}$$

For the LPT thermodynamic evolution relations are formulated the same way as in the HPT, according to its performance maps, noting once more their different coupling. In the case of the former these relations are:

$$\frac{T_{5\mathrm{t}}}{T_{45\mathrm{t}}} = 1 - \eta_{\mathrm{LPT}} \left(1 - \left(\frac{p_{5\mathrm{t}}}{p_{45\mathrm{t}}}\right)^{\frac{\gamma_{\mathrm{h}}-1}{\gamma_{\mathrm{h}}}}\right) \tag{36}$$

$$\frac{p_{5\mathrm{t}}}{p_{45\mathrm{t}}} = \frac{1}{\pi_{\mathrm{LPT}}(\dot{m}_{45}^{*}, N_{\mathrm{LPT}}^{*})} \tag{37}$$

Note that the adiabatic index is considered in hot conditions, due to the region of application. Also, take into account the dependence of both isentropic efficiencies on their respective component maps, which have different inputs:

$$\eta_{\mathrm{HPT}} = \eta_{\mathrm{HPT}}(\dot{m}_{41}^{*}, N_{\mathrm{HPT}}^{*}), \quad \eta_{\mathrm{LPT}} = \eta_{\mathrm{LPT}}(\dot{m}_{45}^{*}, N_{\mathrm{LPT}}^{*}) \tag{38}$$

The additional equations, referring to mass conservation, are stated here. In the LPT the injected cooling bleed is considered to fully exert work in this turbine, thus $\mu = 1$ here:

$$\dot{m}_{41}^{*} = \frac{\dot{m}_{41}\sqrt{T_{41\mathrm{t}}/T_{\mathrm{ref}}}}{p_{41\mathrm{t}}/p_{\mathrm{ref}}} = \dot{m}_{4}^{*}\frac{(1-b_{25}-b_{3})(1+f)+\mu b_{3}}{(1-b_{25}-b_{3})(1+f)}\frac{\sqrt{T_{41\mathrm{t}}/T_{4\mathrm{t}}}}{p_{41\mathrm{t}}/p_{4\mathrm{t}}} \tag{39}$$

$$\dot{m}_{45}^{*} = \frac{\dot{m}_{45}\sqrt{T_{45\mathrm{t}}/T_{\mathrm{ref}}}}{p_{45\mathrm{t}}/p_{\mathrm{ref}}} = \dot{m}_{41}^{*}\frac{(1-b_{25}-b_{3})(1+f)+b_{3}}{(1-b_{25}-b_{3})(1+f)+\mu b_{3}}\frac{\sqrt{T_{45\mathrm{t}}/T_{41\mathrm{t}}}}{p_{45\mathrm{t}}/p_{41\mathrm{t}}} \tag{40}$$

The relative corrected shaft speed for both of the turbines has the expressions detailed below:

$$N_{\mathrm{HPT}}^{*} = \frac{N_{\mathrm{HPT}}/N_{\mathrm{ref,HPT}}}{\sqrt{T_{41\mathrm{t}}/T_{\mathrm{ref}}}} \tag{41}$$

$$N_{\mathrm{LPT}}^{*} = \frac{N_{\mathrm{LPT}}/N_{\mathrm{ref,LPT}}}{\sqrt{T_{45\mathrm{t}}/T_{\mathrm{ref}}}} \tag{42}$$

Finally, the 6 new equations coming from turbine components and proposed for the model are Equation 34, 35, 36, 37, 39 and 40.

- **Nozzle**

The nozzle is a fundamental component in these types of engines, because it allows the flow to gradually accelerate to adapt to exterior conditions, maximizing the generation of thrust. As it will be studied throughout this document, nozzle geometry haves a great impact in off-design characteristics.

Nozzle area will be considered a known parameter, thus the corresponding equation associated to its relation to thermodynamic variables will also be added to the model, producing a total of 4 equations. This parameter can be used to adapt the functioning line if the component is choked.

Several correction coefficients are used in the calculation of nozzles [2], like the angularity C_{A}, discharge C_{D}, or velocity coefficient C_{V}. This last one is closely related to nozzle isentropic efficiency η_{N}, so the latter will be the coefficient used for most of the analysis. C_{A} will be taken to be 1, while the effect of C_{D} is only going to be considered in the validation study. Energy conservation is consistently considered in this component, thus $T_{5\mathrm{t}} = T_{8\mathrm{t}} = T_{9\mathrm{t}}$. Convergent and convergent-divergent nozzle segments are also considered in the present study. A control actuated variable area law (A_9/A_8) is applied to the convergent-divergent one system to adapt it to the outer static pressure. Depending on the nozzle geometry, the models used for this study vary significantly.

First off, due to energy conservation, the temperature ratio can be easily calculated if the Mach number is known in the exit:

$$\frac{T_9}{T_{5\mathrm{t}}} = \frac{1}{1 + \frac{\gamma_{\mathrm{h}}-1}{2} M_9^2} \tag{43}$$

The component's pressure ratio can be calculated by means of the definition of nozzle isentropic efficiency:

$$\frac{p_9}{p_{5\mathrm{t}}} = \left(1 - \frac{1}{\eta_{\mathrm{N}}}\left(1 - \frac{1}{1 + \frac{\gamma_{\mathrm{h}}-1}{2} M_9^2}\right)\right)^{\frac{\gamma_{\mathrm{h}}}{\gamma_{\mathrm{h}}-1}} \tag{44}$$

Regarding the mass conservation equation, its form can depend on the typology of engine considered, like in other components. In station 5 the momentum factor μ is disregarded for the single spool engine, since the bleed air b_3 is considered to be thoroughly mixed with the rest of the flow.

- **Single Spool Turbojet**

$$\dot{m}_5^* = \dot{m}_{41}^* \frac{(1-b_3)(1+f)+b_3}{(1-b_3)(1+f)+\mu b_3} \frac{\sqrt{T_{5\mathrm{t}}/T_{41\mathrm{t}}}}{p_{5\mathrm{t}}/p_{41\mathrm{t}}} \tag{45}$$

- **Dual Spool Turbojet**

$$\dot{m}_5^* = \dot{m}_{45}^* \frac{\sqrt{T_{5\mathrm{t}}/T_{45\mathrm{t}}}}{p_{5\mathrm{t}}/p_{45\mathrm{t}}} \tag{46}$$

An additional equation is provided in this component. Let $C_\mathrm{D}A_9$ be the effective nozzle area at the exit. Then the corrected mass flow circulating the component $\dot{m}_5^*$ is given by Equation 47:

$$\begin{aligned}
\dot{m}_5^* &= \frac{\dot{m}_5\sqrt{T_{5\mathrm{t}}/T_\mathrm{ref}}}{p_{5\mathrm{t}}/p_\mathrm{ref}} \\
&= \frac{C_\mathrm{D}A_9 p_\mathrm{ref}}{\sqrt{RT_\mathrm{ref}}}\sqrt{\gamma_\mathrm{h}}M_9\left(1+\left(1-\frac{1}{\eta_\mathrm{N}}\right)\frac{\gamma_\mathrm{h}-1}{2}M_9^2\right)^{\frac{\gamma_\mathrm{h}}{\gamma_\mathrm{h}-1}}\left(1+\frac{\gamma_\mathrm{h}-1}{2}M_9^2\right)^{-\frac{\gamma_\mathrm{h}+1}{2(\gamma_\mathrm{h}-1)}} \\
&= \frac{C_\mathrm{D}A_9 p_\mathrm{ref}}{\sqrt{RT_\mathrm{ref}}}\left(\frac{p_9}{p_{5\mathrm{t}}}\right)\left(1-\eta_\mathrm{N}\left(1-\left(\frac{p_9}{p_{5\mathrm{t}}}\right)^{\frac{\gamma_\mathrm{h}-1}{\gamma_\mathrm{h}}}\right)\right)^{-1} \\
&\quad\cdot\sqrt{\frac{2\gamma_\mathrm{h}\eta_\mathrm{N}}{\gamma_\mathrm{h}-1}\left(1-\left(\frac{p_9}{p_{5\mathrm{t}}}\right)^{\frac{\gamma_\mathrm{h}-1}{\gamma_\mathrm{h}}}\right)}
\end{aligned} \tag{47}$$

Where the dependence can be put in terms of the exit Mach number or the component pressure ratio. Therefore, without loss of generality, the relations provided by this component can be summarized in Equation 43, 44, 45 or 46, and 47. The exit Mach number in this formulae is one of the free variables in Table 3 and 4, reading:

$$M_9 = \frac{V_9}{\sqrt{\gamma_\mathrm{h}RT_9}} \tag{48}$$

This series of equations must be treated carefully, as their nature changes when the nozzle is choked. This behavior depends fundamentally on nozzle geometry. When this happens, the maximum corrected mass flow $\dot{m}_5^*$ is given by the throat area, where flow conditions become critical. Equation 47 reads the following for station 8:

$$\dot{m}_{5,\max}^* = \frac{C_\mathrm{D}A_8 p_\mathrm{ref}}{\sqrt{RT_\mathrm{ref}}}\sqrt{\gamma_\mathrm{h}}\left(1+\left(1-\frac{1}{\eta_\mathrm{N}}\right)\frac{\gamma_\mathrm{h}-1}{2}\right)^{\frac{\gamma_\mathrm{h}}{\gamma_\mathrm{h}-1}}\left(\frac{2}{\gamma_\mathrm{h}+1}\right)^{\frac{\gamma_\mathrm{h}+1}{2(\gamma_\mathrm{h}-1)}} \tag{49}$$

- **Convergent Nozzle**

  In a convergent nozzle stations 8 and 9 coincide, then $A_8 = A_9$. Thermodynamic critical conditions are present at the exit of the component.

$$M_8 = M_9 = 1 \tag{50}$$

$$\frac{T_8}{T_{5\mathrm{t}}} = \frac{T_9}{T_{5\mathrm{t}}} = \frac{2}{\gamma_\mathrm{h}+1} \tag{51}$$

$$\frac{p_8}{p_{5\mathrm{t}}} = \frac{p_9}{p_{5\mathrm{t}}} = \left(1-\frac{1}{\eta_\mathrm{N}}\frac{\gamma_\mathrm{h}-1}{\gamma_\mathrm{h}+1}\right)^{\frac{\gamma_\mathrm{h}}{\gamma_\mathrm{h}-1}} \tag{52}$$

- **Convergent-Divergent Nozzle**

  In a convergent-divergent nozzle sonic conditions are met at the throat, but it allows for an acceleration by increasing exit area A_9. Then M_9 is unknown at the exit and given by a certain area law. Equation 43, 44 and 47 are still valid, with the last one normally used after dividing it by mass flow at sonic conditions (Equation 49), yielding the relation between the area law and the exit Mach Number (after also assuming $p_{8t}/p_{9t} \approx 1$):

$$\frac{A_9}{A_8} = \frac{1}{M_9}\left(\frac{2}{\gamma_h + 1}\left(1 + \frac{\gamma_h - 1}{2}M_9^2\right)\right)^{\frac{\gamma_h+1}{2(\gamma_h-1)}} \tag{53}$$

The aforementioned correcting coefficients are important to be taken into account, as multiple effects can differ from the relations presented here, based on one-dimensional compressible flow. This will be taken into account in this work's validation step, as the tested engine mounts a conical nozzle, where two-dimensional effects happen to be important.

In two-dimensional flow, the generation of a sonic region at the nozzle throat doesn't imply the choking of the device. After the appearance of sonic conditions, flow characteristic waves can still influence this sonic region, allowing for it to curve and allow a greater amount of mass flow through the component [8], see Figure 11.

This phenomenon is generally quantified through the use of the discharge coefficient C_D, which accounts for the equivalent one-dimensional flow area that the working gas must go through. In subsonic conditions it is also important to be taken into account, because of *vena contracta* effects where the flow reaches ambient conditions. C_D depends strongly on geometry and Nozzle Pressure Ratio (NPR) p_{5t}/p_9.

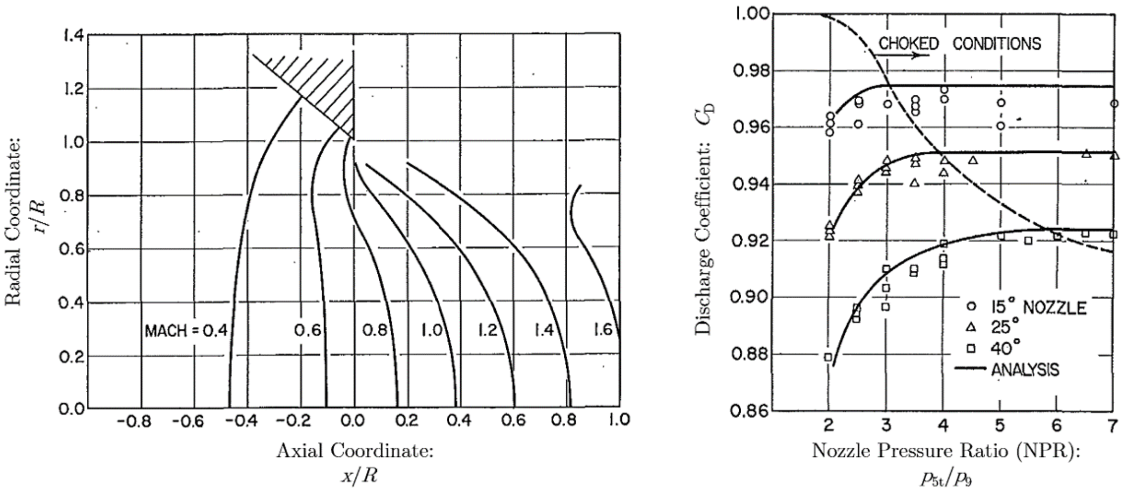

Figure 11: Constant Mach Lines in 40° Conical Nozzle at NPR = 4 (left) and Experimental and Theoretical Discharge Coefficient vs. NPR (right). Adapted from [8].

Compatibility Relations and Power Balance

This section will revolve around the equations provided by the power transmission between the turbomachinery of the engine.

On one hand, compatibility equations are those that allow to relate the angular velocity of the turbines and compressors connected through a shaft in the engine. As mentioned earlier, a gear transmission ratio between components is possible. This lead to be considered in the off-design and transient analysis. However, in many situations, fitting a reducer gearbox is not necessary.

On the other hand, a power balance between this component is necessary, as the turbines' fundamental goal in most of the propulsive applications is to power the compressors to achieve generating power in a Brayton cycle. Other types of turbines fitted in this systems can be used to generate power for other purposes. This type of problem adds more DOFs to the system, and will not be considered in this work. Also, these equations' formulation depends on the typology of engine, as usually happened with many of the components.

- **Single Spool Turbojet**

  A total of 2 compatibility and power balance equations are provided in a single spool engine. The only shaft is given a transmission ratio of i. Equation 54 relates Equation 10 with 33. As expressed, normally $i = 1$:

  $$N_{\mathrm{C}} = iN_{\mathrm{T}} \tag{54}$$

  Power balance with mechanical transmission efficiency η_{m}, angular velocity ω [rad/s] $N_{\mathrm{T}} = N_{\mathrm{C}} = N$ [rpm], and axis moment of inertia I, before expressing the balance equations in nondimensional and corrected variables (see Table 1), reads the following in a general transient state, with the former set of assumptions:

  $$\eta_{\mathrm{m}}\dot{m}_{41}C_{\mathrm{p,h}}\left(T_{41\mathrm{t}} - T_{5\mathrm{t}}\right) - \dot{m}_2 C_{\mathrm{p,c}}\left(T_{3\mathrm{t}} - T_{2\mathrm{t}}\right) = I\omega\frac{d\omega}{dt} = \left(\frac{2\pi}{60}\right)^2 IN\frac{dN}{dt}$$

  After nondimensionalization, the equation becomes the following:

  $$\begin{aligned}\frac{dN^*}{dt} = \frac{\dot{m}_0^* C_{\mathrm{p,c}} T_{\mathrm{ref}}}{\left(2\pi/60\right)^2 I^* N^*}\frac{T_{2\mathrm{t}}}{T_0}\Bigg(&\frac{C_{\mathrm{p,e}}}{C_{\mathrm{p,c}}}\eta_{\mathrm{m}}\left(\left(1+f\right)\left(1-b_3\right)+\mu b_3\right)\\ &\cdot\left(1-\frac{T_{5\mathrm{t}}}{T_{41\mathrm{t}}}\right)\frac{T_{41\mathrm{t}}}{T_{4\mathrm{t}}}\frac{T_{4\mathrm{t}}}{T_{3\mathrm{t}}}\frac{T_{3\mathrm{t}}}{T_{2\mathrm{t}}} - \left(\frac{T_{3\mathrm{t}}}{T_{2\mathrm{t}}} - 1\right)\Bigg)\end{aligned} \tag{55}$$

  Where N^* and I^* are a new parameters, the corrected axis speed and corrected axis moment of inertia, respectively:

  $$N^* = \frac{N}{\sqrt{T_0/T_{\mathrm{ref}}}}, \quad I^* = I\frac{\sqrt{T_0/T_{\mathrm{ref}}}}{\left(p_0/p_{\mathrm{ref}}\right)} \tag{56}$$

- **Dual Spool Turbojet**

  In a dual spool engine, one the other hand, a total of four compatibility and power balance relations arise. The respective transmission ratio of the low pressure coupling and high pressure coupling is, respectively: i_{LP} and i_{HP}. Equation 54 then relates Equation 17 with 42 and 18 with 41. Again, in normal conditions $i_{\mathrm{LP}} = 1$ and $i_{\mathrm{HP}} = 1$:

  $$N_{\mathrm{LPC}} = i_{\mathrm{LP}} N_{\mathrm{LPT}} \tag{57}$$

  $$N_{\mathrm{HPC}} = i_{\mathrm{HP}} N_{\mathrm{HPT}} \tag{58}$$

  There are also two power balances for the high pressure and low pressure coupling, with their respective parameters. These are, respectively: mechanical transmission efficiency $\eta_{\mathrm{m,LP}}$ and $\eta_{\mathrm{m,HP}}$, axis angular velocity ω_{LP} and ω_{HP} [rad/s] or N_{LP} and N_{HP} [rpm] (with $N_{\mathrm{LPC}} = N_{\mathrm{LPT}} = N_{\mathrm{LP}}$ and $N_{\mathrm{HPC}} = N_{\mathrm{HPT}} = N_{\mathrm{HP}}$ in the following formulae), and axis moment of inertia I_{LP} and I_{HP} [kgm^2]. To expose the context from which Equation 59 and 60 come from, the low pressure and high pressure balances are presented:

  $$\eta_{\mathrm{m,LP}} \dot{m}_{45} C_{\mathrm{p,h}} \left(T_{45\mathrm{t}} - T_{5\mathrm{t}}\right) - \dot{m}_2 C_{\mathrm{p,c}} \left(T_{25\mathrm{t}} - T_{2\mathrm{t}}\right) = I_{\mathrm{LP}} \omega_{\mathrm{LP}} \frac{d\omega_{\mathrm{LP}}}{dt} = \left(\frac{2\pi}{60}\right)^2 I_{\mathrm{LP}} N_{\mathrm{LP}} \frac{dN_{\mathrm{LP}}}{dt}$$

  $$\eta_{\mathrm{m,HP}} \dot{m}_{41} C_{\mathrm{p,h}} \left(T_{41\mathrm{t}} - T_{45\mathrm{t}}\right) - \dot{m}_{25} C_{\mathrm{p,c}} \left(T_{3\mathrm{t}} - T_{25\mathrm{t}}\right) = I_{\mathrm{HP}} \omega_{\mathrm{HP}} \frac{d\omega_{\mathrm{HP}}}{dt} = \left(\frac{2\pi}{60}\right)^2 I_{\mathrm{HP}} N_{\mathrm{HP}} \frac{N_{\mathrm{HP}}}{dt}$$

  Which become, after variable correction and nondimensionalization:

  $$\begin{aligned} \frac{dN^*_{\mathrm{LP}}}{dt} = \frac{\dot{m}^*_0 C_{\mathrm{p,c}} T_{\mathrm{ref}}}{(2\pi/60)^2 I^*_{\mathrm{LP}} N^*_{\mathrm{LP}}} \frac{T_{2\mathrm{t}}}{T_0} \Bigg(& \frac{C_{\mathrm{p,e}}}{C_{\mathrm{p,c}}} \eta_{\mathrm{m,LP}} \left((1+f)\left(1 - b_{25} - b_3\right) + b_3\right) \\ & \cdot \left(1 - \frac{T_{5\mathrm{t}}}{T_{45\mathrm{t}}}\right) \frac{T_{45\mathrm{t}}}{T_{41\mathrm{t}}} \frac{T_{41\mathrm{t}}}{T_{4\mathrm{t}}} \frac{T_{4\mathrm{t}}}{T_{3\mathrm{t}}} \frac{T_{3\mathrm{t}}}{T_{25\mathrm{t}}} \frac{T_{25\mathrm{t}}}{T_{2\mathrm{t}}} - \left(\frac{T_{25\mathrm{t}}}{T_{2\mathrm{t}}} - 1\right) \Bigg) \end{aligned} \tag{59}$$

  $$\begin{aligned} \frac{dN^*_{\mathrm{HP}}}{dt} = \frac{\dot{m}^*_0 C_{\mathrm{p,c}} T_{\mathrm{ref}}}{(2\pi/60)^2 I^*_{\mathrm{HP}} N^*_{\mathrm{HP}}} \frac{T_{25\mathrm{t}}}{T_{2\mathrm{t}}} \frac{T_{2\mathrm{t}}}{T_0} \Bigg(& \frac{C_{\mathrm{p,e}}}{C_{\mathrm{p,c}}} \eta_{\mathrm{m,HP}} \left((1+f)\left(1 - b_{25} - b_3\right) + \mu b_3\right) \\ & \cdot \left(1 - \frac{T_{45\mathrm{t}}}{T_{41\mathrm{t}}}\right) \frac{T_{41\mathrm{t}}}{T_{4\mathrm{t}}} \frac{T_{4\mathrm{t}}}{T_{3\mathrm{t}}} \frac{T_{3\mathrm{t}}}{T_{25\mathrm{t}}} - \left(1 - b_{25}\right) \left(\frac{T_{3\mathrm{t}}}{T_{25\mathrm{t}}} - 1\right) \Bigg) \end{aligned} \tag{60}$$

  Where the corrected speed and inertia in each one is expressed as in Equation 56. A system of differential equations describes the evolution of the dual spool system. As assumed, mechanical efficiencies and bleed fractions remain constant through time.

This whole section's equation have been derived for a general transient case, where there is an infinite rate of change of the thermodynamic variables with respect to axis speed, with no mass pocketing or heat sinks/sources or other secondary effects. Therefore, component equations can be used as if they were in steady state each time step.

Boundary Conditions

Finally, the problem is closed with an additional equation, which is a boundary condition (do not confuse with the transient problem's initial condition). The boundary condition applied will depend on the nozzle being choked (critical) or not.

- **Non-critical Nozzle**

  If the nozzle is not choked, pressure perturbations can travel downstream from the nozzle outlet, propagating information about the ambient conditions outside of this component. In this situation, pressure will equalize at the exit to match that of the ambient air.

  To simulate in-flight operation the following condition is imposed. Again, the thermodynamic evolution depends on engine kind:

  - **Single Spool Turbojet**

  $$\frac{p_9}{p_0} = \frac{p_9}{p_{5\mathrm{t}}}\frac{p_{5\mathrm{t}}}{p_{41\mathrm{t}}}\frac{p_{41\mathrm{t}}}{p_{4\mathrm{t}}}\frac{p_{4\mathrm{t}}}{p_{3\mathrm{t}}}\frac{p_{3\mathrm{t}}}{p_{2\mathrm{t}}}\frac{p_{2\mathrm{t}}}{p_0} = 1 \tag{61}$$

  - **Dual Spool Turbojet**

  $$\frac{p_9}{p_0} = \frac{p_9}{p_{5\mathrm{t}}}\frac{p_{5\mathrm{t}}}{p_{45\mathrm{t}}}\frac{p_{45\mathrm{t}}}{p_{41\mathrm{t}}}\frac{p_{41\mathrm{t}}}{p_{4\mathrm{t}}}\frac{p_{4\mathrm{t}}}{p_{3\mathrm{t}}}\frac{p_{3\mathrm{t}}}{p_{25\mathrm{t}}}\frac{p_{25\mathrm{t}}}{p_{2\mathrm{t}}}\frac{p_{2\mathrm{t}}}{p_0} = 1 \tag{62}$$

  This can also happen if the expansion in a convergent-divergent nozzle is not adequate and compression shockwaves form inside, decelerating the flow to subsonic speeds before reaching the exit. Nonetheless, a perfect area rule, and thus, an isentropic expansion to supersonic conditions is assumed at all engine operating points when the nozzle is choked. This phenomenon will not be considered.

- **Critical Nozzle**

  When the nozzle is critical, the imposed boundary condition is that the corrected mass flow at its inlet $\dot{m}_5^*$ is maximum and given by Equation 49. Thus:

  $$\dot{m}_5^* = \dot{m}_{5,\mathrm{max}}^* \tag{63}$$

  If moreover a convergent-divergent nozzle is considered to be equipped, the area relation, given by 53 is control-actuated to ensure at all times that $p_9/p_0 = 1$, in other words, conditions given in Equation 61 and 62.

With this, a total of **21 equations** for the single spool turbojet and **29 equations** for the dual spool are given. As the problem is divided in multiple subproblems, their respective DOFs will be counted next.

The steady state problem is divided into an internal and engine coupling problem. In the case of the dual spool turbojet, the internal one is further divided into a high pressure coupling and low pressure coupling. Its resolution poses an intermediate step of calculating the off-design problem.

On the one hand, internal coupling refers to the interaction and common mechanisms that link compressors, starting from their inlet station, up until the outlet stations of the turbines they are coupled with. Engine coupling, on another hand, refers to the resolution of the whole system and its interaction with the ambient conditions, including components like diffuser and nozzle.

Subproblem	**Single Spool**	**Dual Spool**	
Internal Coupling	2	**HP**	2
		LP	2
Engine Coupling	2	2	
Transient	3	4	

Table 5: Number of Subproblem Degrees of Freedom.

In Table 5 the number of subproblem DOF is counted by means of subtracting the adequate number of equations from problem variables (stated in Table 3 and 4, considering the bounds of each subproblem.

This division into subproblems is due to the fact that many times some parameter needs to be iterated to find the engine operating point in a component map, thus forcing the compartmentalization of algorithms to be able to access them.

Note that in the steady state solution every subproblem has 2 DOF. Although many parameters (like bleed percentages or nozzle area) can be considered extra DOF they will remain considered as parameters, and modified as necessary in further parametric studies. The reason behind this is that they are considered to remain constant throughout engine operation, hence they are not considered variables.

These two necessary parameters will then generally be those that allow for entering the component maps (thus β or $\dot{m}^*$ and N^*) as will be described in the following section. This is true for both the internal coupling in a single spool as well as a low pressure and high pressure internal coupling in the case of a dual spool engine.

The transient problem considers the solution to the differential equations in Equation 55, 59 and 60 to obtain the time evolution of the system variables. Thus, an extra DOF is added because of the need of imposing initial conditions, which are characteristic of an Initial Value Problem (IVP).

3.1.4 Steady State Solution Strategy

The steady state solution of the problem requires applying the aforementioned equations to the problem while employing performance maps for achieving it. These performance maps must to be accessed through a pair of parameters $(\dot{m}^*, N^*)$ or (β, N^*), therefore, the algorithm must be built around this fact.

Internal Coupling

The following algorithms have been developed according to engine type, as the architecture greatly influences the resolution of the problem.

- **Single Spool Turbojet**

  The 2 DOF of the internal coupling problem for a single spool turbojet are initially imposed in the compressor map. Given β_{C} and N^*_{C} it is possible to determine the associated $\dot{m}^*_2$. Also, Equation 6 and 7 are applied to determine the conditions at the combustion chamber inlet.

  Then, because of the need of having 2 parameters with which the turbine map can be entered, a load parameter $(T_{4\mathrm{t}}/T_{2\mathrm{t}})_0$ is initially guessed and fed into the system. Thus, the combustion chamber can be prematurely calculated, according to this guess. In it Equation 21 and 22 are applied. To illustrate the process, the total temperature ratio is calculated in iteration $k-1$:

$$\frac{T_{4\mathrm{t}}}{T_{3\mathrm{t}}} = \left(\frac{T_{4\mathrm{t}}}{T_{2\mathrm{t}}}\right)_{k-1} \Big/ \left(\frac{T_{3\mathrm{t}}}{T_{2\mathrm{t}}}\right), \quad k \in \mathbb{N}_{\geq 0} \tag{64}$$

  The air then goes through the refrigeration bleed, where Equation 24, 25 and 26 determine the evolution of the system. It is after this point when the turbine map can be accessed, as $\dot{m}^*_{41}$ is calculated from Equation 32 and N^*_{T} is estimated as:

$$\begin{aligned} N^*_{\mathrm{T}} &= \frac{1}{i\sqrt{(T_{41\mathrm{t}}/T_{4\mathrm{t}})(T_{4\mathrm{t}}/T_{3\mathrm{t}})(T_{3\mathrm{t}}/T_{2\mathrm{t}})}} \frac{N_{\mathrm{ref,C}}}{N_{\mathrm{ref,T}}} \frac{N_{\mathrm{C}}/N_{\mathrm{ref,C}}}{\sqrt{T_{2\mathrm{t}}/T_{\mathrm{ref}}}} \\ &= \frac{1}{i\sqrt{(T_{41\mathrm{t}}/T_{4\mathrm{t}})(T_{4\mathrm{t}}/T_{3\mathrm{t}})(T_{3\mathrm{t}}/T_{2\mathrm{t}})}} \frac{N_{\mathrm{ref,C}}}{N_{\mathrm{ref,T}}} N^*_{\mathrm{C}} \end{aligned} \tag{65}$$

  If no gearbox in the connection is considered, $i = 1$. After accessing the turbine map, the rest of the thermodynamic conditions at the end of the internal coupling are calculated in Equation 29 and 30.

  This is not the end of the algorithm, as the load parameter comes from a guess and is being iterated. The iteration consists on correcting the k-th value with the value of the load parameter obtained in the equilibrium stated in Equation 55 for $dN^*/dt = 0$. An over-relaxation coefficient is needed, as the algorithm tends to fluctuate if the initial guess is not precise enough.

This results in the following direct linear interpolation procedure:

$$\left(\frac{T_{4\mathrm{t}}}{T_{2\mathrm{t}}}\right)_k = \alpha_\mathrm{I}\left(\frac{T_{4\mathrm{t}}}{T_{2\mathrm{t}}}\right)_{k-1} + (1-\alpha_\mathrm{I})\frac{(T_{3\mathrm{t}}/T_{2\mathrm{t}})-1}{\frac{C_{\mathrm{p,e}}}{C_{\mathrm{p,c}}}\eta_\mathrm{m}\left((1+f)(1-b_3)+\mu b_3\right)\left(1-\frac{T_{5\mathrm{t}}}{T_{41\mathrm{t}}}\right)\frac{T_{41\mathrm{t}}}{T_{4\mathrm{t}}}} \tag{66}$$

Where $\alpha_\mathrm{I} \in (0,1)$ is the aforementioned over-relaxation factor, which interpolates the new and old guesses for the load parameter. A first guess for $(T_{4\mathrm{t}}/T_{2\mathrm{t}})_0$ is $(T_{4\mathrm{t}}/T_{3\mathrm{t}})$, and, as it can not be lower than this value, it is gradually incremented until the algorithm enters a loop for the calculation. While there is no engaging in the solution the method returns a Not a Number (NaN) value. If it is too high or the time it consumes reaches a certain threshold, the process is shut down and a warning is shown.

The algorithm is finished when the L_1 error ϵ_I in this same variable between iteration k and $k-1$ considered to be low enough (throughout further analyses $\epsilon_\mathrm{I} = 10^{-6}$).

$$\left|\left(\frac{T_{4\mathrm{t}}}{T_{2\mathrm{t}}}\right)_k - \left(\frac{T_{4\mathrm{t}}}{T_{2\mathrm{t}}}\right)_{k-1}\right| < \epsilon_\mathrm{I} \tag{67}$$

It returns all the variables calculated during the process (rows 2 to 5 in Table 3). The following flowchart in Figure 12 illustrates the process.

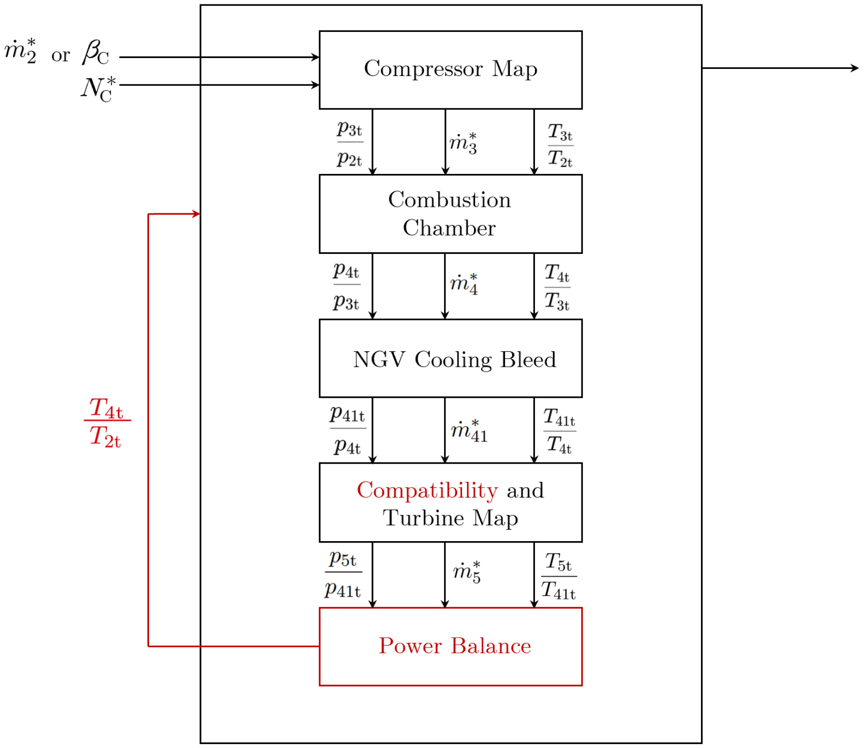

Figure 12: Internal Coupling Algorithm Flowchart for the Single Spool Turbojet. Equations and Variables Iterated to Achieve the Solution (red).

- **Dual Spool Turbojet**

The dual spool problem also has 2 DOF. The high pressure internal coupling in this type of engine is almost identical to the one described for a single spool. Here, given β_{LPC} and N^*_{LPC}, the HPC corrected mass flow at the inlet $\dot{m}^*_{25}$ is first calculated . Again, Equation 13 and 14 determine the conditions at the combustion chamber inlet.

As in the single spool internal coupling, 2 parameters are needed to input to the HPT. A new load parameter $(T_{4\mathrm{t}}/T_{25\mathrm{t}})_0$ is initially guessed and added as a known parameter. Thus, the combustion chamber can be prematurely calculated, according to this guess. The combustion chamber is again calculated through Equation 21 and 23. The total temperature ratio is then shown for iteration $k-1$:

$$\frac{T_{4\mathrm{t}}}{T_{3\mathrm{t}}} = \left(\frac{T_{4\mathrm{t}}}{T_{25\mathrm{t}}}\right)_{k-1} \Big/ \left(\frac{T_{3\mathrm{t}}}{T_{25\mathrm{t}}}\right), \quad k \in \mathbb{N}_{\geq 0} \tag{68}$$

The cooling bleed predicts the evolution of the system through Equation 25, 27 and 28. The turbine map can be accessed by applying compatibility, after $\dot{m}^*_{41}$ has been calculated from Equation 39. N^*_{HPT} has now the following expression:

$$\begin{aligned} N^*_{\mathrm{HPT}} &= \frac{1}{i_{\mathrm{HP}}\sqrt{(T_{41\mathrm{t}}/T_{4\mathrm{t}})(T_{4\mathrm{t}}/T_{3\mathrm{t}})(T_{3\mathrm{t}}/T_{25\mathrm{t}})}} \frac{N_{\mathrm{ref,HPC}}}{N_{\mathrm{ref,HPT}}} \frac{N_{\mathrm{HPC}}/N_{\mathrm{ref,HPC}}}{\sqrt{T_{25\mathrm{t}}/T_{\mathrm{ref}}}} \\ &= \frac{1}{i_{\mathrm{HP}}\sqrt{(T_{41\mathrm{t}}/T_{4\mathrm{t}})(T_{4\mathrm{t}}/T_{3\mathrm{t}})(T_{3\mathrm{t}}/T_{25\mathrm{t}})}} \frac{N_{\mathrm{ref,HPC}}}{N_{\mathrm{ref,HPT}}} N^*_{\mathrm{HPC}} \end{aligned} \tag{69}$$

If no gearbox in the high pressure coupling is considered, $i_{\mathrm{HP}} = 1$. Finally, equations Equation 34 and 35. The algorithm follows again by iterating with the high pressure power equilibrium, given by Equation 60 with $dN^*_{\mathrm{HP}}/dt = 0$. Remember bleed air fraction b_{25} at the HPC inlet is considered.

$$\begin{aligned} \left(\frac{T_{4\mathrm{t}}}{T_{25\mathrm{t}}}\right)_k &= \alpha_{\mathrm{HP}} \left(\frac{T_{4\mathrm{t}}}{T_{25\mathrm{t}}}\right)_{k-1} \\ &\quad + (1-\alpha_{\mathrm{HP}}) \frac{(1-b_{25})\,(T_{3\mathrm{t}}/T_{25\mathrm{t}}) - 1}{\frac{C_{\mathrm{p,e}}}{C_{\mathrm{p,c}}}\eta_{\mathrm{m,HP}}\left((1+f)\,(1-b_{25}-b_3) + \mu b_3\right)\left(1 - \frac{T_{45\mathrm{t}}}{T_{41\mathrm{t}}}\right)\frac{T_{41\mathrm{t}}}{T_{4\mathrm{t}}}} \end{aligned} \tag{70}$$

An over-relaxation coefficient $\alpha_{\mathrm{HP}} \in (0,1)$ is used, once more to ensure the convergence of the method. This step works identically as in the case of the single spool. The first taken guess for $(T_{4\mathrm{t}}/T_{25\mathrm{t}})_0$ is also $(T_{4\mathrm{t}}/T_{3\mathrm{t}})$. When the L_1 error ϵ_{HP} between iteration k and $k-1$ is below a certain threshold, iterations stop and the process is done.

$$\left| \left(\frac{T_{4\mathrm{t}}}{T_{25\mathrm{t}}}\right)_k - \left(\frac{T_{4\mathrm{t}}}{T_{25\mathrm{t}}}\right)_{k-1} \right| < \epsilon_{\mathrm{HP}} \tag{71}$$

It returns all the variables calculated during the process (rows 3 to 6 in Table 4). The following flowchart in Figure 13 illustrates the process.

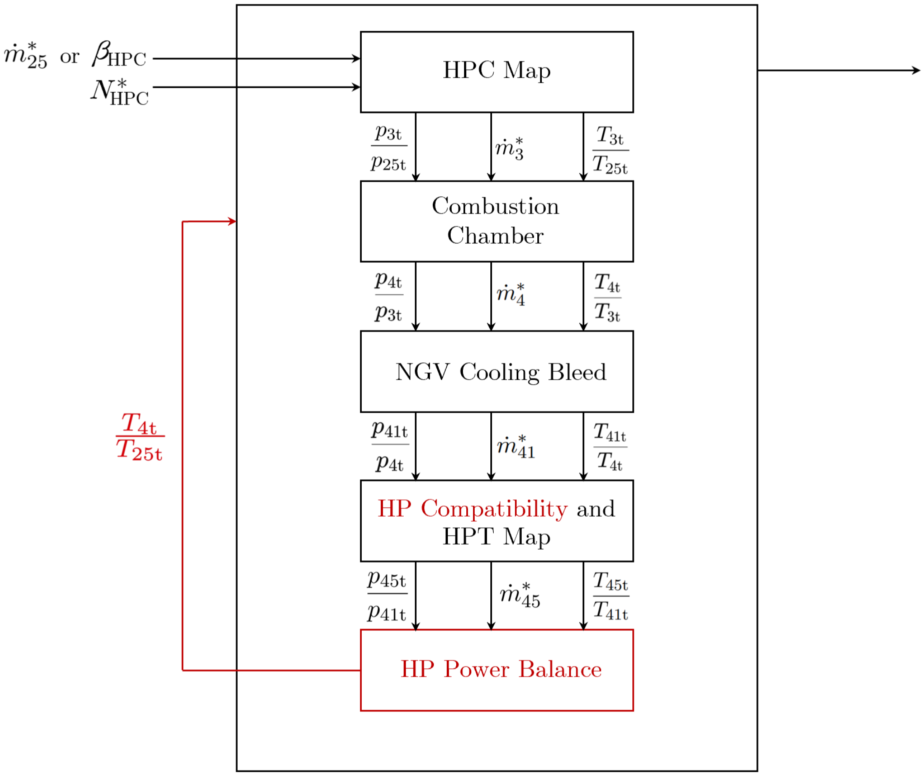

Figure 13: High Pressure Internal Coupling Algorithm Flowchart for the Dual Spool Turbojet. Equations and Variables Iterated to Achieve the Solution (red).

The difference that the dual spool engine introduces is now a low pressure internal coupling, where the high pressure one is acting as a component. It needs to be resolved iteratively too. As the 2 DOF of the problem are imposed at the compressor map, because the need to be accessed with those.

Again, the imposed variables are β_{LPC} or $\dot{m}^*_2$ (preferably the former because of a better orthogonality to compressor characteristics) and N^*_{LPC}. Evaluating the compressor map yields the thermodynamic variables in Equation 11 and 12 and it is possible to know the corrected mass flow at the inlet $\dot{m}^*_2$ in Equation 9.

Those variables are then passed to the high pressure internal coupling algorithm described moments ago. Of course, as it includes evaluating the HPC compressor map in the first place, it is necessary to impose an extra variable with which is possible to iterate. It will be corrected once equilibrium is granted.

For this purpose the HPC beta lines will be used. Imposing β_{HPC} at the high pressure internal coupling as well as $\dot{m}^*_{25}$ (calculated with Equation 16 at the HPC entry) grants access to the map and thus continues to loop. Finally, when all intermediate properties in the high pressure coupling are calculated, the necessary ones are passed to the LPT to apply compatibility and evaluate its performance map.

Properties like $T_{45\mathrm{t}}/T_{41\mathrm{t}}$ and $p_{45\mathrm{t}}/p_{41\mathrm{t}}$ and $\dot{m}^*_{41}$ are passed to the LPT, where Equation 40 is applied to yield $\dot{m}^*_{45}$. Compatibility reads:

$$\begin{aligned} N^*_{\mathrm{LPT}} &= \frac{1}{i_{\mathrm{LP}}\sqrt{(T_{45\mathrm{t}}/T_{41\mathrm{t}})(T_{41\mathrm{t}}/T_{4\mathrm{t}})(T_{4\mathrm{t}}/T_{3\mathrm{t}})(T_{3\mathrm{t}}/T_{25\mathrm{t}})(T_{25\mathrm{t}}/T_{2\mathrm{t}})}}\frac{N_{\mathrm{ref,LPC}}}{N_{\mathrm{ref,LPT}}}\frac{N_{\mathrm{LPC}}/N_{\mathrm{ref,LPC}}}{\sqrt{T_{2\mathrm{t}}/T_{\mathrm{ref}}}} \\ &= \frac{1}{i_{\mathrm{LP}}\sqrt{(T_{45\mathrm{t}}/T_{41\mathrm{t}})(T_{41\mathrm{t}}/T_{4\mathrm{t}})(T_{4\mathrm{t}}/T_{3\mathrm{t}})(T_{3\mathrm{t}}/T_{25\mathrm{t}})(T_{25\mathrm{t}}/T_{2\mathrm{t}})}}\frac{N_{\mathrm{ref,LPC}}}{N_{\mathrm{ref,LPT}}}N^*_{\mathrm{LPC}} \end{aligned} \tag{72}$$

Where normally $i_{\mathrm{LP}} = 1$. With both corrected mass flow at the inlet and corrected speed the LPT map is evaluated, yielding $T_{5\mathrm{t}}/T_{45\mathrm{t}}$ which is necessary to impose equilibrium ($dN^*_{\mathrm{LP}}/dt = 0$) in Equation 59.

The variable in which the error will be measured is $T_{25\mathrm{t}}/T_{2\mathrm{t}}$, as it is possible to be evaluated at the LPC exit and from the power balance, which, after reordering is:

$$\left(\frac{T_{25\mathrm{t}}}{T_{2\mathrm{t}}}\right)_k = \frac{1}{1-\eta_{\mathrm{m,LP}}\frac{C_{\mathrm{p,e}}}{C_{\mathrm{p,c}}}\left((1+f)\left(1-b_{25}-b_3\right)+b_3\right)\left(1-\frac{T_{5\mathrm{t}}}{T_{45\mathrm{t}}}\right)\frac{T_{45\mathrm{t}}}{T_{41\mathrm{t}}}\frac{T_{41\mathrm{t}}}{T_{4\mathrm{t}}}\frac{T_{4\mathrm{t}}}{T_{3\mathrm{t}}}\frac{T_{3\mathrm{t}}}{T_{25\mathrm{t}}}} \tag{73}$$

Where the subindex $k \in \mathbb{N}_{\geq 0}$ denotes an estimated state after imposing β_{HPC} in iteration k. The algorithm flowchart is detailed in Figure 14.

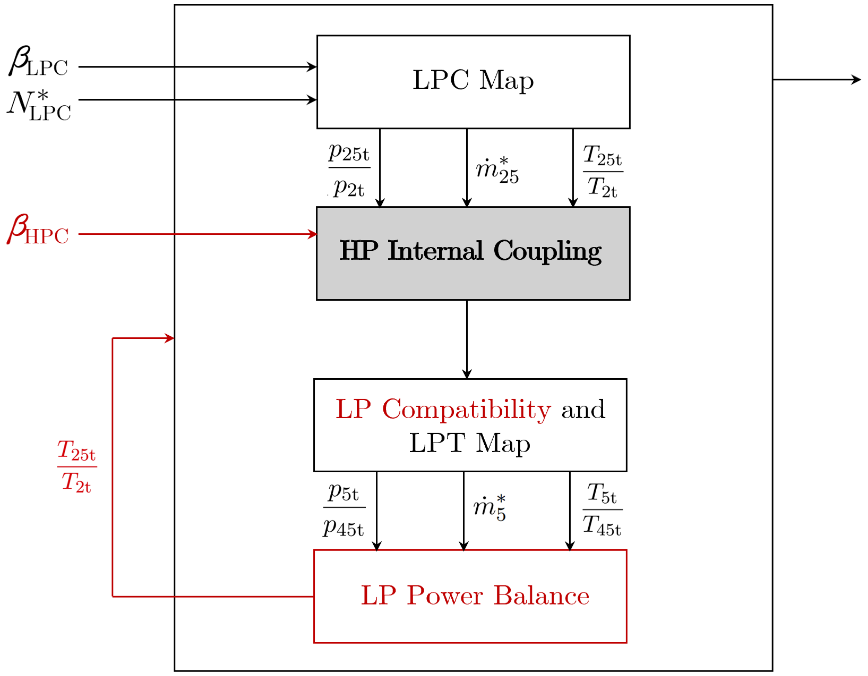

Figure 14: Low Pressure Internal Coupling Algorithm Flowchart for the Dual Spool Turbojet. Equations and Variables Iterated to Achieve the Solution (red).

The L_1 relative error $\xi_{\mathrm{LP},k}$ of the estimate, after imposing $\beta_{\mathrm{HPC},k}$ in iteration k has the following expression:

$$\xi_{\mathrm{LP}}(\beta_{\mathrm{HPC},k}) = \xi_{\mathrm{LP},k} = \frac{\left|(T_{25\mathrm{t}}/T_{2\mathrm{t}})_k - T_{25\mathrm{t}}/T_{2\mathrm{t}}\right|}{T_{25\mathrm{t}}/T_{2\mathrm{t}}} < \epsilon_{\mathrm{LP}} \tag{74}$$

The error is reduced through a Newton-Raphson method [14], again including over-relaxation $\alpha_{\mathrm{LP}} \in (0,1)$ to facilitate convergence, as this problem is many times not well-posed. If the latter algorithm is created to be a function of the inserted β_{HPC} returning the error ξ_{LP} and including its sign (otherwise it can fluctuate because of the jump in the absolute value function derivative):

$$\begin{gathered} \widehat{\beta_{\mathrm{HPC}}}_{k-1} = \beta_{\mathrm{HPC},k-1} - \frac{\xi_{\mathrm{LP},k-1}}{\xi'_{\mathrm{LP},k-1}} \\ \beta_{\mathrm{HPC},k} = \alpha_{\mathrm{LP}}\beta_{\mathrm{HPC},k-1} + (1-\alpha_{\mathrm{LP}})\widehat{\beta_{\mathrm{HPC}}}_{k-1} \end{gathered} \tag{75}$$

The hat sign represents the intermediate step of the Newton-Raphson method, where over-relaxation still has not been included. $\xi'_{\mathrm{LP},k-1}$ is the numerical derivative of the signed error function in iteration $k-1$, it can be estimated by finite differences by a forward increment:

$$\xi'_{\mathrm{LP},k-1} = \left(\frac{d\xi_{\mathrm{LP}}}{d\beta_{\mathrm{HPC}}}\right)_{k-1} \approx \frac{\xi_{\mathrm{LP}}(\beta_{\mathrm{HPC},k-1} + \Delta\beta_{\mathrm{HPC}}) - \xi_{\mathrm{LP}}(\beta_{\mathrm{HPC},k-1})}{\Delta\beta_{\mathrm{HPC}}} \tag{76}$$

Where an increment $\Delta\beta_{\mathrm{HPC}}$ in the input variable has generally been taken to be around 10^{-7} to preserve precision. The effectiveness of considering the derivative like a finite difference depends on the actual precision of the methods and the resolution of the performance maps.

Other methods with lower order of convergence have been tested, like, for example the secant method or *regula falsi* method. Nevertheless, although they were sometimes more efficient because they do not involve estimating a derivative, the problem is not well posed and the Newton-Raphson method ended up being more effective in most of the situations tested. Note that the order of this method is $\mathcal{O}(\beta^2_{\mathrm{HPC}})$

This algorithm finishes when the error is below ϵ_{LP} as shown in Equation 74. After that, all variables calculated during the process are returned by the algorithm. This details the calculation of the internal coupling for a dual spool turbojet engine.

The described processes correspond to the internal coupling for both types of turbojet engines. Nonetheless, if the whole engine were to be modeled, the coupling between it and exterior conditions must be taken into account.

Engine Coupling

After devising an algorithm for the internal coupling in both types of turbojet engines, the exterior coupling algorithm is developed to contain it. The resolution process is also equivalent for both single spool and dual spool.

The 2 imposed DOF will be the flight Mach number M_0 and the LPC relative corrected shaft speed N_{C}^* or N_{LPC}^* if the engine in single spool or dual spool, respectively. The algorithm is very similar to that developed for the low pressure part of the internal coupling in a dual spool turbojet engine.

First off, with the fight Mach number Equation 2 and 3 are applied, yielding the corresponding thermodynamic ratio in the component. With those, it is not possible to access the internal coupling solver algorithm, so a new iteration variable is considered. This will be β_{C} or β_{LPC}, depending on the type of engine described.

Imposing β_{C} or β_{LPC} and N_{C}^* or N_{LPC}^* allows for the calculation of the mass flow corrected with exterior conditions $\dot{m}_0^*$ as follows from Equation 9:

$$\dot{m}_0^* = \dot{m}_2^* \frac{p_{2\mathrm{t}}/p_0}{\sqrt{T_{2\mathrm{t}}/T_0}} \tag{77}$$

After the internal coupling procedure, the necessary variables are available to calculate the nozzle, first by applying Equation 45 or 46 to have an estimate of $\dot{m}_5^*$ and comparing with the maximum possible corrected mass flow $\dot{m}_{5,\mathrm{max}}^*$ Equation 49. The nature of the solution will depend on the nozzle being choked or not.

This algorithm has two different lines of action depending on the value of the corrected mass flow and its associated boundary conditions:

- **Case 1:** $\dot{m}_5^* < \dot{m}_{5,\mathrm{max}}^*$

  If the maximum allowed corrected mass flow is bigger than the actual calculated corrected mass flow after imposing the estimate β_{LPC}, then the nozzle is considered not to be choked. This implies complying with the boundary condition given in Equation 61 or 62, which forces the pressure at the engine outlet to be the ambient pressure.

  Then, Equation 47 is solved for M_9, knowing $\dot{m}_5^*$. This is the plugged into Equation 44 to yield the NPR, so that an error in the estimate of $p_{2\mathrm{t}}/p_0$ can be considered. In iteration k. Notice that $p_{2\mathrm{t}}/p_0$ is known, as it is an exact value from solving the diffuser equations with M_0. This relative error estimate is ξ_{E}.

  $$\xi_{\mathrm{E},k} = \frac{\left| (p_{2\mathrm{t}}/p_0)_k - p_{2\mathrm{t}}/p_0 \right|}{p_{2\mathrm{t}}/p_0} < \epsilon_{\mathrm{E}} \tag{78}$$

  The algorithm is finished when ξ_{E} is less than a given error tolerance ϵ_{E}, generally taken to be around 10^{-3}.

- **Case 2:** $\dot{m}_5^* > \dot{m}_{5,\max}^*$

  In this case the estimate of the error must be changed, as the nozzle is now considered to be choked. In that case it is known that $\dot{m}_5^* = \dot{m}_{5,\max}^*$. The error estimate is now considered to be in iteration k:

$$\xi_{\mathrm{E},k} = \frac{\left| m_{5,k}^* - \dot{m}_{5,\max}^* \right|}{\dot{m}_{5,\max}^*} < \epsilon_{\mathrm{E}} \tag{79}$$

Another Newton-Raphson method in the same fashion as that exposed for the low pressure coupling in a dual spool engine. Although it is presented with abuse of notation, consider from now on β to be either β_{C} or β_{LPC}, depending on the engine that is being modeled. Then the method is the following:

$$\begin{gathered} \widehat{\beta}_{k-1} = \beta_{k-1} - \frac{\xi_{\mathrm{E},k-1}}{\xi'_{\mathrm{E},k-1}} \\ \beta_k = \alpha_{\mathrm{E}}\beta_{k-1} + (1-\alpha_{\mathrm{E}})\widehat{\beta}_{k-1} \end{gathered} \tag{80}$$

Where again, the hat sign represents the intermediate step of the method. The numerical derivative $\xi'_{\mathrm{E},k-1}$ is calculated in the fashion exposed by Equation 76. α_{E} denotes the relaxation factor of the method in this iteration step. Once the conditions in Equation 78 or 79 are met the loop stops. The method is illustrated in Figure 15.

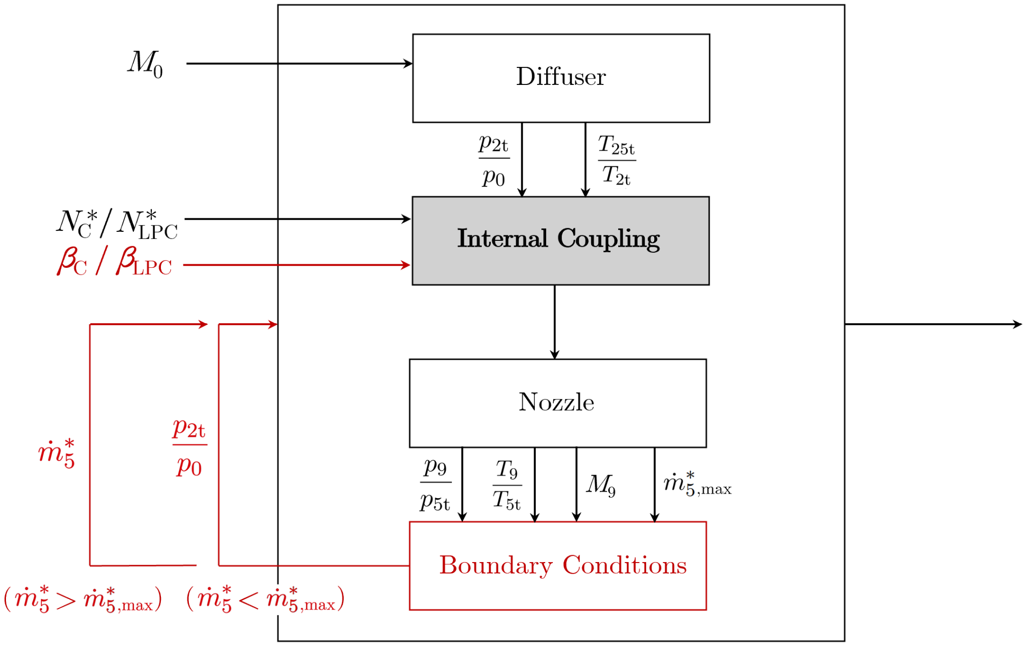

Figure 15: Engine Coupling Algorithm Flowchart. Equations and Variables Iterated to Achieve the Solution (red).

The final iteration allows to calculate the actual nozzle equations (with a small error), so in the end $T_9/T_{5\mathrm{t}}$ Equation 43, $p_9/p_{5\mathrm{t}}$ 44 and M_9 in 47 are calculated with the found nozzle inlet corrected mass flow $\dot{m}_5^*$.

This not only allows to calculate the mass flow averaged thermodynamic evolution of the air inside of the engine, it also provides a way to estimate the corrected thrust E^* and other figures of merit of the engine, like corrected specific impulse $I_{\mathrm{sp}}^* = (E/\dot{m}_0)^*$ and corrected Thrust Specific Fuel Consumption (TSFC), denoted as $c_{\mathrm{E}}^* = (\dot{m}_f/E)^*$.

The corrected thrust comes initially from a momentum balance in the system's control volume. This expression reads, before correction:

$$E = (\dot{m}_9 V_9 - \dot{m}_0 V_0) + (p_9 - p_0)\, A_9$$

After expressing it in nondimensional and corrected variables, considering through the process all bleeds and the assumed value for f, the aforementioned corrected thrust and figures of merit is the following:

- **Single Spool Turbojet**

  The difference between both types of engine is basically the number of stations and bleed fractions. In the case of a single spool engine, the corrected thrust is:

$$\begin{aligned} E^* = \frac{E}{p_0/p_{\mathrm{ref}}} = \dot{m}_0^* \Bigg(&\left((1+f)\,(1-b_3) + b_3\right) \sqrt{\gamma_{\mathrm{h}} R T_{\mathrm{ref}}}\, M_9 \sqrt{\frac{T_9}{T_0}} \\ &- \sqrt{\gamma_{\mathrm{c}} R T_{\mathrm{ref}}}\, M_0 \Bigg) + \left(\frac{p_9}{p_0} - 1\right) p_{\mathrm{ref}} A_9 \end{aligned} \tag{81}$$

  Where the cycle static temperature ratio T_9/T_0 is:

$$\frac{T_9}{T_0} = \frac{T_9}{T_{5\mathrm{t}}} \frac{T_{5\mathrm{t}}}{T_{41\mathrm{t}}} \frac{T_{41\mathrm{t}}}{T_{4\mathrm{t}}} \frac{T_{4\mathrm{t}}}{T_{3\mathrm{t}}} \frac{T_{3\mathrm{t}}}{T_{2\mathrm{t}}} \frac{T_{2\mathrm{t}}}{T_0} \tag{82}$$

  Then, the corrected specific impulse of the engine is simply obtained with the corrected inlet mass flow and corrected thrust:

$$I_{\mathrm{sp}}^* = \frac{I_{\mathrm{sp}}}{\sqrt{T_0/T_{\mathrm{ref}}}} = \frac{E}{p_0/p_{\mathrm{ref}}} \Bigg/ \frac{\dot{m}_0 \sqrt{T_0/T_{\mathrm{ref}}}}{p_0/p_{\mathrm{ref}}} = \frac{E^*}{\dot{m}_0^*} \tag{83}$$

  Finally, to estimate of the TSFC it needs to be corrected with the fuel parameter, making it independent of the characteristics of the combustion chamber. It is necessary to take into account that f is the FAR with respect to combustion chamber inlet mass flow:

$$c_{\mathrm{E}}^* = \frac{\eta_{\mathrm{CC}} c_{\mathrm{E}} L}{\sqrt{T_0/T_{\mathrm{ref}}}} = C_{\mathrm{p,c}} T_{\mathrm{ref}}\,(1-b_3)\, \frac{T_{3\mathrm{t}}}{T_{2\mathrm{t}}} \frac{T_{2\mathrm{t}}}{T_0} \left((1+f)\, \frac{C_{\mathrm{p,h}}}{C_{\mathrm{p,c}}} \frac{T_{4\mathrm{t}}}{T_{3\mathrm{t}}} - 1\right) \Bigg/ I_{\mathrm{sp}}^* \tag{84}$$

- **Dual Spool Turbojet**

  For a dual spool engine, as said, the thrust corrected parameter only varies in considering other bleed fractions and more stations, but its operation behaves quite differently in comparison with a single spool:

$$E^* = \frac{E}{p_0/p_{\mathrm{ref}}} = \dot{m}_0^* \Bigg(\left((1+f)\left(1 - b_{25} - b_3\right) + b_3 \right) \sqrt{\gamma_{\mathrm{h}} R T_{\mathrm{ref}}} M_9 \sqrt{\frac{T_9}{T_0}} - \sqrt{\gamma_{\mathrm{c}} R T_{\mathrm{ref}}} M_0 \Bigg) + \left(\frac{p_9}{p_0} - 1 \right) p_{\mathrm{ref}} A_9 \tag{85}$$

  Now the cycle static temperature ratio T_9/T_0 is:

$$\frac{T_9}{T_0} = \frac{T_9}{T_{5\mathrm{t}}} \frac{T_{5\mathrm{t}}}{T_{45\mathrm{t}}} \frac{T_{45\mathrm{t}}}{T_{41\mathrm{t}}} \frac{T_{41\mathrm{t}}}{T_{4\mathrm{t}}} \frac{T_{4\mathrm{t}}}{T_{3\mathrm{t}}} \frac{T_{3\mathrm{t}}}{T_{25\mathrm{t}}} \frac{T_{25\mathrm{t}}}{T_{2\mathrm{t}}} \frac{T_{2\mathrm{t}}}{T_0} \tag{86}$$

  Then, the corrected specific impulse has the same expression as in Equation 83. The corrected parameter for the TSFC is now, considering bleeds and stages:

$$c_{\mathrm{E}}^* = \frac{\eta_{\mathrm{CC}} c_{\mathrm{E}} L}{\sqrt{T_0/T_{\mathrm{ref}}}} = C_{\mathrm{p,c}} T_{\mathrm{ref}} \left(1 - b_{25} - b_3\right) \frac{T_{3\mathrm{t}}}{T_{25\mathrm{t}}} \frac{T_{25\mathrm{t}}}{T_{2\mathrm{t}}} \frac{T_{2\mathrm{t}}}{T_0} \left((1+f) \frac{C_{\mathrm{p,h}}}{C_{\mathrm{p,c}}} \frac{T_{4\mathrm{t}}}{T_{3\mathrm{t}}} - 1 \right) \Big/ I_{\mathrm{sp}}^* \tag{87}$$

Calculating an estimation for steady-state, off-design operation, not only leads to obtaining these last estimations of corrected thrust and several figures of merit. If the problem is calculated for a fixed flight Mach number M_0 while varying the compressor or LPC relative corrected speed, the steady-state **operating lines** can be plotted in both the compressor and turbine maps.

As seen in chapter 2 1, this can predict the appearance of multiple destructive off-design effects. However, a better model would be needed to estimate when they will appear and their intensity. The operating lines over the turbine and compressor will be plotted in next analyses, to prove that the developed algorithms return coherent results, and also observe how the components should be modified so the operating lines are adjusted properly to high-efficiency regions of the performance maps.

In general, engine **characteristic curves** for the steady state can be generated from this present method. If the developed code is proven to be a correct approximation of the problem, it can pose a noteworthy alternative to other more expensive methods of designing and testing an engine of this kind.

Moreover, through this method, it is possible to predict the value of other variables that can lead to failure of the system. For example, maximum pressure ratio in the engine $p_{3\mathrm{t}}/p_0$, cycle OPR $p_{3\mathrm{t}}/p_{2\mathrm{t}}$, and maximum temperature ratio in the engine $T_{4\mathrm{t}}/T_0$. The engine's shaft speed corrected with outside conditions N_{LP}^* is also an interesting parameter to plot, and present in many examples of characteristic curves.

3.1.5 Transient Solution Strategy

As mentioned in the assumptions made in the development of the models, the transient solution will be based upon many simplifications so an estimation of transient engine behavior can be found.

These assumptions hereby summarized and detailed, including some other important effects to take into account that have not yet been mentioned:

- The change in angular momentum of the axis is the most relevant time-varying effect, having an higher order of magnitude than the rest mentioned in following points.
- There are no heat "soakage" or volume packing effects, therefore changes in thermodynamic properties and mass flow are considered immediate, so the presented steady state component equations can be used.
- The turbine and compressor maps remain unchanged through transient effects. This involves assuming there are no noticeable changes in tip clearance with respect to steady state operation or unsteady aerodynamic effects.
- The process of combustion remains similar to frozen flow, and although some chemical kinetic effects can be important and can cause delays in the reaction, those will not be taken into account. The effects in thermodynamic conditions are immediate after the injection of fuel.
- Except in the case of having a variable area nozzle if a convergent-divergent segment is considered to be fitted, the rest of control-actuated devices do not operate in the transient process. This first one responds immediately to changes in ambient pressure and is always adapted.

The transient problem involves solving the IVP stated in Equation 55, or the system of equations in Equation 59 and 60. Therefore, an initial condition for the problem is always needed, which represents one of the problem DOF.

Then, the rest of the problem's DOF will be covered, first, by imposing a constant flight Mach number M_0 during the transient maneuver. In fact, exterior conditions are modeled to be time-independent. The second one is imposed by feeding the method a time-dependent fuel parameter $(\eta_{\mathrm{CC}} f L)/(C_{\mathrm{p,c}} T_0)$.

This fuel parameter is closely related to the engine's FAR and it is a forcing term in the aforementioned differential equations, fundamental for controlling the engine's acceleration. Likewise, in following analyses, it is assumed that the engine is controlled through a known FAR at every moment, considering that the rest of terms in the fuel parameter don't vary through operation.

There is an alternative to using the fuel parameter as a control variable. It can be multiplied by inlet corrected mass flow $\dot{m}_0^*$ to yield another parameter in which almost every other term is constant through operation, except for the injected fuel mass flow. Note that, with the way the FAR is defined in this model: $\dot{m}_0 f \neq \dot{m}_f$, but instead $\dot{m}_3 f = \dot{m}_f$. Then the engine's bleed values are considered part of this new fuel parameter. All considerations aside, the code will be schematized for imposing simply $(\eta_{\mathrm{CC}} f L)/(C_{\mathrm{p,c}} T_0)$.

The process of the algorithms designed to solve this problem are more straightforward than those devised for achieving a steady state solution, because the equilibrium equations are unbalanced due to axis acceleration.

Nonetheless, as compressor and turbine maps need to be accessed by employing certain parameters, again β_C or β_LPC is imposed. It will be iterated to satisfy the boundary conditions, in a similar fashion to what has been done in the engine coupling for the steady state. This followed process depends on the engine being single spool or dual spool.

- **Single Spool Turbojet**

  First off, time is discretized into $N_p \in \mathbb{N}$ points. Then, a constant Mach number M_0 is imposed, thus thermodynamic ratios at the compressor inlet are known. Here, the first estimate of β_C is imposed too. Given the last time estimate (consider a generic discretized form $n-1 \in \{0, 1, 2, ..., N_p\}$), with shaft corrected speed it is possible to access the map, because it is known from the previous time marching step:

  $$N_\text{C}^* = \frac{{}^{n-1}N^*/N_\text{ref,C}}{\sqrt{T_\text{2t}/T_0}} = \frac{N_\text{C}/N_\text{ref,C}}{\sqrt{T_0/T_\text{ref}}\sqrt{T_\text{2t}/T_0}} = \frac{N_\text{C}/N_\text{ref,C}}{\sqrt{T_\text{2t}/T_\text{ref}}} \tag{88}$$

  This allows to calculate $\dot{m}_2^*$ and $\dot{m}_0^*$ with Equation 77 and advance the solution towards the combustion chamber, where the fuel parameter in time step $n-1$ is known. Here, Equation 19, 21 and 22 are applied to continue the process.

  The NGV Cooling Bleed is reached, where again Equation 24, 25 and 26 continues the process. The turbine is accessed through the application of Equation 32 and the turbine relative corrected speed, which is calculated identically to Equation 54.

  The power balance is not considered in this step, ignored up until the algorithm in β_C finished adjusting the current state to the boundary conditions. For that, the nozzle is summoned, and again the boundary condition depends on the value of $\dot{m}_5^*$, as in Equation 78 and 79.

  These iterations are done through Halley's method, a higher order ($\mathcal{O}(\beta_\text{C})^3$) variant of root finding methods like Newton-Raphson. This will later be described as it is a common subject for both single spool and dual spool turbojets.

  When the iterations of this method reached convergence for the current time step ($n-1$), the solution is advanced by considering the power balance between compressor and turbine, given in Equation 55, but discretized in an forward Euler method. A higher order temporal or implicit temporal scheme like backwards Euler or Runge-Kutta Methods (RK) have not been considered, as it has been deemed that the algorithm instabilities do not generally come from the numerical solution of the differential equation, unless the chosen time increments are relatively large.

Equation 89 shows the discretized version of the power balance, where the thermodynamic properties have been iterated to comply with the boundary conditions and evaluated in the instant $n-1$.

$$\begin{aligned} {}^{n}N^* = {}^{n-1}N^* + \Delta t \frac{\dot{m}_0^* C_{\mathrm{p,c}} T_{\mathrm{ref}}}{(2\pi/60)^2 \, I^*({}^{n-1}N^*)} \frac{T_{2\mathrm{t}}}{T_0} \left(\frac{C_{\mathrm{p,e}}}{C_{\mathrm{p,c}}} \eta_{\mathrm{m}} \left((1+f)(1-b_3) + \mu b_3 \right) \cdot \right. \\ \left. \cdot \left(1 - \frac{T_{5\mathrm{t}}}{T_{41\mathrm{t}}} \right) \frac{T_{41\mathrm{t}}}{T_{4\mathrm{t}}} \frac{T_{4\mathrm{t}}}{T_{3\mathrm{t}}} \frac{T_{3\mathrm{t}}}{T_{2\mathrm{t}}} - \left(\frac{T_{3\mathrm{t}}}{T_{2\mathrm{t}}} - 1 \right) \right) \end{aligned} \tag{89}$$

After finishing, time is advanced according to the current discretization and the process is restarted again:

$$t_n = t_{n-1} + \Delta t \tag{90}$$

This process describes the simplified time behavior of a single spool engine. Each time step all variables are stored to later be processed to create operating lines in the compressor and turbine map or unsteady characteristic curves. The process for current a time step $n-1$ is illustrated in Figure 16.

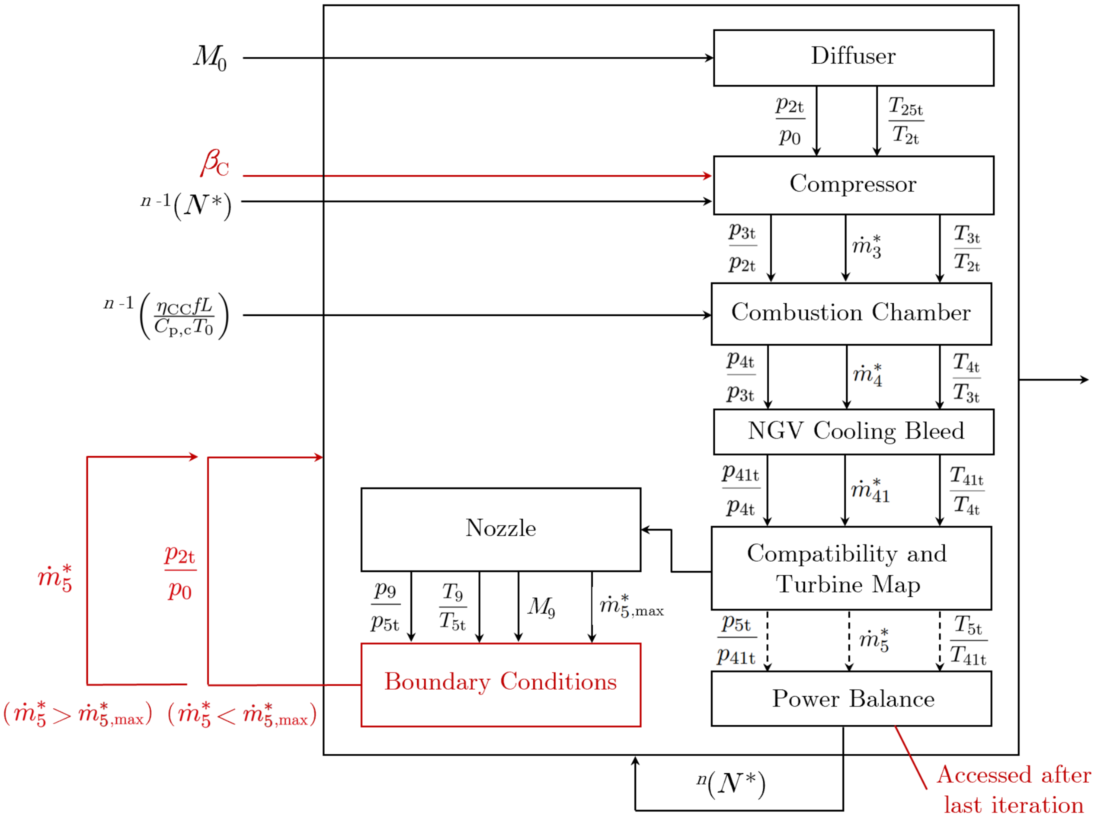

Figure 16: Transient Solver Algorithm Flowchart for the Single Spool Turbojet. Equations and Variables Iterated to Achieve the Solution (red).

- **Dual Spool Turbojet**

In a dual spool engine, time is discretized the same way as in a single spool, hence, into $N_p \in \mathbb{N}$ points. Consider the current iteration $n-1,\ n \in \{1, 2, ..., N_p\}$. Again, a constant Mach number M_0 is imposed. The thermodynamic variables at the compressor inlet together with an estimate of β_{LPC} allow to continue the process. The LPC shaft corrected speed in the current time step makes it possible to access the map:

$$N^*_{\text{LPC}} = \frac{{}^{n-1}N^*_{\text{LP}}/N_{\text{ref,LPC}}}{\sqrt{T_{\text{2t}}/T_0}} = \frac{N_{\text{LPC}}/N_{\text{ref,LPC}}}{\sqrt{T_0/T_{\text{ref}}}\sqrt{T_{\text{2t}}/T_0}} = \frac{N_{\text{LPC}}/N_{\text{ref,LPC}}}{\sqrt{T_{\text{2t}}/T_{\text{ref}}}} \tag{91}$$

Once more this allows to calculate $\dot{m}^*_2$ and $\dot{m}^*_0$ with Equation 77, together with $T_{\text{25t}}/T_{\text{2t}}$ and $p_{\text{25t}}/p_{\text{2t}}$. Now the solution is advanced to the HPC. As the current time high pressure shaft corrected speed is also known from a previous calculation in the process:

$$\begin{aligned} N^*_{\text{HPC}} &= \frac{{}^{n-1}N^*_{\text{HP}}/N_{\text{ref,HPC}}}{\sqrt{(T_{\text{25t}}/T_{\text{2t}})(T_{\text{2t}}/T_0)}} \\ &= \frac{N_{\text{HPC}}/N_{\text{ref,HPC}}}{\sqrt{T_0/T_{\text{ref}}}\sqrt{(T_{\text{25t}}/T_{\text{2t}})(T_{\text{2t}}/T_0)}} = \frac{N_{\text{HPC}}/N_{\text{ref,HPC}}}{\sqrt{T_{\text{25t}}/T_{\text{ref}}}} \end{aligned} \tag{92}$$

The solution is again advanced towards the combustion chamber. The fuel parameter in the current time step is known. Equation 19, 21 and 23 are applied. The NGV Cooling Bleed introduces Equation 27, 25 and 28. The HPT is accessed through the application of Equation 39 and the HPT relative corrected speed compatibility relation, which is identical to Equation 69.

The same is done with the LPT, after the calculation of the thermodynamic ratios before and after the HPT. These are evaluated through Equation 34 and 35 the corrected mass flow to access the LPT is calculated in Equation 40. The compatibility relation is given in Equation 72.

Both power balances are ignored until the algorithm in β_{LPC} is finished adjusting the engine's states to the ambient conditions. Once more the boundary condition is different depending on $\dot{m}^*_5$, as in Equation 78 and 79.

Just when the algorithm has finished adjusting β_{LPC}, the power balance in Equation 60 is summoned, once again discretized in an forward Euler method. This reads the following:

$$\begin{aligned} &{}^{n}N^*_{\text{HP}} = {}^{n-1}N^*_{\text{HP}} + \Delta t \frac{\dot{m}^*_0 C_{\text{p,c}} T_{\text{ref}}}{(2\pi/60)^2\, I^*_{\text{HP}}({}^{n-1}N^*_{\text{HP}})} \frac{T_{\text{25t}}}{T_{\text{2t}}} \frac{T_{\text{2t}}}{T_0} \Bigg(\frac{C_{\text{p,e}}}{C_{\text{p,c}}} \eta_{\text{m,HP}} \cdot \\ &((1+f)(1-b_{25}-b_3)+\mu b_3)\left(1-\frac{T_{\text{45t}}}{T_{\text{41t}}}\right)\frac{T_{\text{41t}}}{T_{\text{4t}}}\frac{T_{\text{4t}}}{T_{\text{3t}}}\frac{T_{\text{3t}}}{T_{\text{25t}}} - (1-b_{25})\left(\frac{T_{\text{3t}}}{T_{\text{25t}}}-1\right)\Bigg) \end{aligned} \tag{93}$$

For the case of the low pressure side, the balance is also discretized and time marching is applied after calculating all variables in the $(n-1)$-th step.

$$\begin{aligned}
{}^{n}N^*_{\mathrm{LP}} = {}^{n-1}N^*_{\mathrm{LP}} + \Delta t \frac{\dot{m}^*_0 C_{\mathrm{p,c}} T_{\mathrm{ref}}}{(2\pi/60)^2\, I^*_{\mathrm{LP}}({}^{n-1}N^*_{\mathrm{LP}})} \frac{T_{2\mathrm{t}}}{T_0} & \left(\frac{C_{\mathrm{p,e}}}{C_{\mathrm{p,c}}} \eta_{\mathrm{m,LP}} \cdot \right. \\
\left. ((1+f)(1-b_{25}-b_3)+b_3) \left(1-\frac{T_{5\mathrm{t}}}{T_{45\mathrm{t}}}\right) \frac{T_{45\mathrm{t}}}{T_{41\mathrm{t}}} \frac{T_{41\mathrm{t}}}{T_{4\mathrm{t}}} \frac{T_{4\mathrm{t}}}{T_{3\mathrm{t}}} \frac{T_{3\mathrm{t}}}{T_{25\mathrm{t}}} \frac{T_{25\mathrm{t}}}{T_{2\mathrm{t}}} - \left(\frac{T_{25\mathrm{t}}}{T_{2\mathrm{t}}} - 1\right)\right) &
\end{aligned} \tag{94}$$

The process for a dual spool engine is summarized in a flowchart in Figure 17.

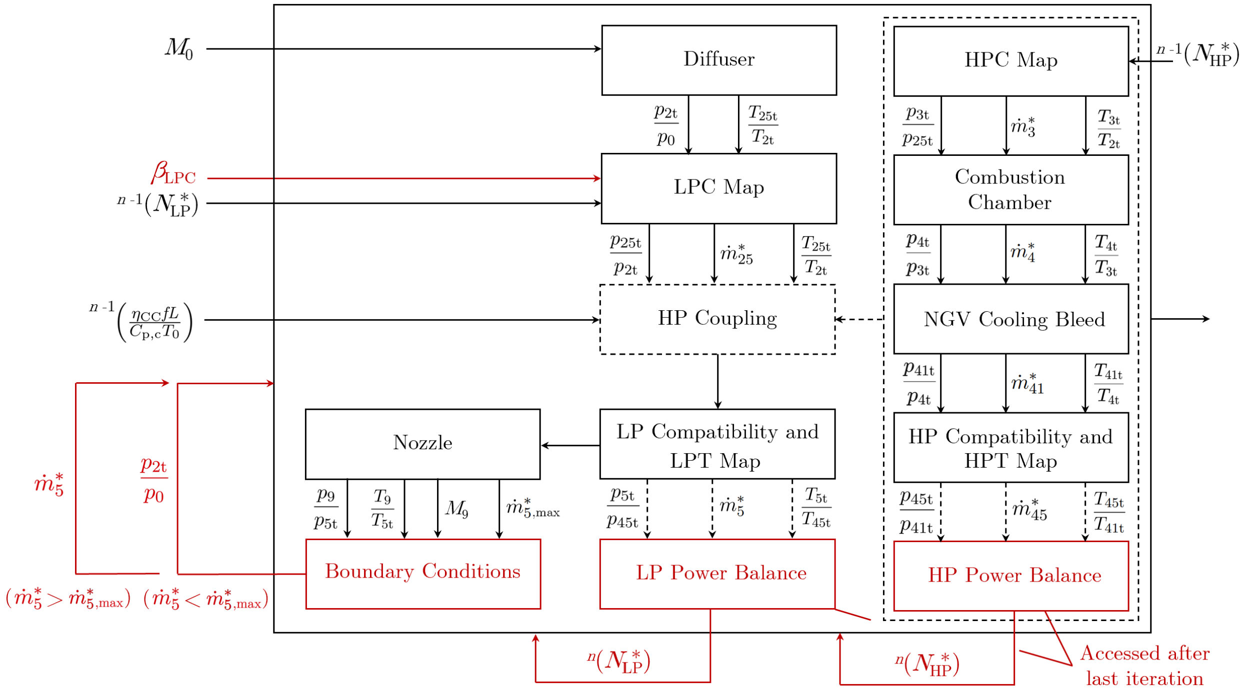

Figure 17: Transient Solver Algorithm Flowchart for the Dual Spool Turbojet. Equations and Variables Iterated to Achieve the Solution (red).

The iteration steps in a generic β follow the same structure as described in Equation 78 and 79. Given the error estimate in iteration $k-1$ for time step $n-1$, ${}^{n-1}\xi_{\mathrm{E},k-1}$, Halley's method including over-relaxation $\alpha_{\mathrm{E}} \in (0,1)$ is, where ${}^{n-1}\xi'_{\mathrm{E},k-1}$ is estimated like in Equation 76:

$$\begin{aligned}
\widehat{\beta}_{k-1} &= \frac{2({}^{n-1}\xi_{\mathrm{E},k-1})}{{}^{n-1}\xi'_{\mathrm{E},k-1} \pm \sqrt{({}^{n-1}\xi'_{\mathrm{E},k-1})^2 - 2({}^{n-1}\xi_{\mathrm{E},k-1})({}^{n-1}\xi''_{\mathrm{E},k-1})}} \\
{}^{n-1}\xi''_{\mathrm{E},k-1} &\approx \frac{{}^{n-1}\xi_{\mathrm{E},k-1}(\beta_{k-1}+\Delta\beta) - 2({}^{n-1}\xi_{\mathrm{E},k-1}(\beta_{k-1})) +{}^{n-1} \xi_{\mathrm{E},k-1}(\beta_{k-1}-\Delta\beta)}{(\Delta\beta)^2} \\
\beta_k &= \alpha_{\mathrm{E}}\beta_{k-1} + (1-\alpha_{\mathrm{E}})\widehat{\beta}_{k-1}
\end{aligned} \tag{95}$$

3.2 Analytical Solution

The analytical solution is a simplified version of the off-design problem that allows to have a make a quick calculation of the operating lines and characteristic curves by linearizing the conditions at the engine design point, as well as making more assumptions about engine behavior. It will be used in this study as a reference method of resolution of the off-design problem only in a **steady state**. Hence, this solution will allow to compare with the more elaborate and less simplified algorithms, which employ turbomachinery performance maps.

There is also a transient analytical solution, which makes similar assumptions about the unsteady behavior of this engines. However, this last one will not be considered, as it is deemed too unrealistic to linearize the engine design point when the operating line greatly diverges from the high-efficiency regions of the map.

3.2.1 Assumptions

Many of the assumptions made for the general solution are shared with the analytical one, only this time the problem is further simplified. The main new assumption of this analysis is supposing that the conditions at the design point can be extended along the operating line. This includes considering constant isentropic efficiencies in compressors and turbines, even though the corrected mass flow and component pressure ratio can vary. This is the main purpose of the linearization, which allows to discard the usage of component maps.

Common assumptions include considering a cold and hot zone in the cycle, adiabatic components except for the combustion chamber, where a simple frozen flow model is applied, and constant efficiencies and bleed fractions in the rest of the engine parts. Intrinsic assumptions of this method is considering the turbines choked in every operating point.

Property	Description
Analysis Type	0-D linearized design point
Time Dependence	Steady state
Gas Model	Ideal, semiperfect with cold/hot zone differentiation
Combustion Model	Simple heat addition, frozen flow
Mass/Energy Transfer	Adiabatic parts (except CC), no leaks or pocketing
Miscellanea	Constant diffuser and nozzle isentropic efficiencies Constant power transmission efficiency and bleed fractions Constant compressor and turbine efficiencies Constant CC and 4-41 pressure drop, and NGV cooling ratio Both turbines remain in critical conditions during operation

Table 6: Assumptions for the Analytical Solution.

3.2.2 Problem Variables

The problem's variables are expressed in the same way as the general solution. Their nomenclature coincides to what has been shown in Table 3 and 4, with a few exceptions. Among these exceptions are the turbines' inlet corrected mass flow, which, due to them being critical, are considered constants. Their nomenclature will be modified to reinforce the knowledge of this fact. Then, for a single spool and dual spool this implies:

- **Single Spool Turbojet**

  For a single spool engine the turbine inlet corrected mass flow is renamed as k_{T}:

$$k_{\mathrm{T}} = \dot{m}_{41}^{*} = \frac{\dot{m}_{41}\sqrt{T_{41\mathrm{t}}/T_{\mathrm{ref}}}}{p_{41\mathrm{t}}/p_{\mathrm{ref}}} \tag{96}$$

  Notice that, as long as the nozzle is choked, the total temperature and total pressure ratio between stations 41 and 5 are constants too, because the turbine isentropic efficiency is assumed not to change during operation. Thus, calling the nozzle corrected mass flow k_{N}, which is also constant in this context:

$$\begin{aligned} \frac{k_{\mathrm{T}}}{k_{\mathrm{N}}} = \frac{\dot{m}_{41}^{*}}{\dot{m}_{5}^{*}} &= \frac{\dot{m}_{41}\sqrt{T_{41\mathrm{t}}/T_{\mathrm{ref}}}}{p_{41\mathrm{t}}/p_{\mathrm{ref}}} \Bigg/ \frac{\dot{m}_{5}\sqrt{T_{5\mathrm{t}}/T_{\mathrm{ref}}}}{p_{5\mathrm{t}}/p_{\mathrm{ref}}} \\ &= \frac{(1+f)(1-b_3)+\mu b_3}{(1+f)(1-b_3)+b_3}\sqrt{\frac{T_{41\mathrm{t}}}{T_{5\mathrm{t}}}}\frac{p_{5\mathrm{t}}}{p_{41\mathrm{t}}} \\ &= \frac{(1+f)(1-b_3)+\mu b_3}{(1+f)(1-b_3)+b_3}\frac{1}{\sqrt{\tau_{\mathrm{T}}}\pi_{\mathrm{T}}} \end{aligned} \tag{97}$$

  While Equation 29, that relates total temperature ratio and total pressure ratio through turbine isentropic efficiency, holds true. Again, a nomenclature change carried out to remark the fact that those parameters are constant given these conditions. The total temperature ratio in the turbine is called τ_{T} while the total pressure ratio in it is, from now on, $1/\pi_{\mathrm{T}}$.

  This allows to have an additional equation in the internal coupling of the engine, subtracting a DOF from this subproblem. This makes the running lines independent of the flight Mach number M_0 when the nozzle is choked.

  That same phenomenon is also present in the general solution through compressor and turbine maps, but it is not visualized in Table 5 because the solving strategy consisted in dividing the problem into an internal coupling subproblem with 2 DOF, which did not have access to what happens in the nozzle. This will be visualized when analyzing results obtained through the general solver.

  Either way, those total temperature and pressure ratios cannot be considered constant in the problem, as the nozzle is not choked all the time during operation. They are still considered problem variables, while the corrected mass flow in station 41 is not.

Take into account that now component maps are not part of the analysis, thus the shaft speed variables associated to them disappear from the approach. This fact greatly reduces the complexity of the solution.

Component	Variables
Diffuser	$\frac{T_{2t}}{T_0}, \frac{p_{2t}}{p_0}, \frac{\dot{m}_0\sqrt{T_0/T_{\mathrm{ref}}}}{p_0/p_{\mathrm{ref}}}, \frac{V_0}{\sqrt{\gamma_c R T_0}}$
Compressor	$\frac{T_{3t}}{T_{2t}}, \frac{p_{3t}}{p_{2t}}, \frac{\dot{m}_2\sqrt{T_{2t}/T_{\mathrm{ref}}}}{p_{2t}/p_{\mathrm{ref}}}$
Combustion Chamber	$\frac{T_{4t}}{T_{3t}}, \frac{\dot{m}_3\sqrt{T_{3t}/T_{\mathrm{ref}}}}{p_{3t}/p_{\mathrm{ref}}}, \frac{\eta_{\mathrm{CC}} f L}{C_{\mathrm{p}} T_{3t}}$
NGV Bleed Injection	$\frac{\dot{m}_4\sqrt{T_{4t}/T_{\mathrm{ref}}}}{p_{4t}/p_{\mathrm{ref}}}$
Turbine	$\frac{T_{5t}}{T_{41t}}, \frac{p_{5t}}{p_{41t}}$
Nozzle	$\frac{T_9}{T_{5t}}, \frac{p_9}{p_{5t}}, \frac{\dot{m}_5\sqrt{T_{5t}/T_{\mathrm{ref}}}}{p_{5t}/p_{\mathrm{ref}}}, \frac{V_9}{\sqrt{\gamma_h R T_9}}$

Table 7: Problem Variables for the Single Spool Turbojet.

Table 7 summarizes this problem's variables. Note the reduction in measurable quantities inside of the engine. This hints towards a lower resolution of the method compared to the general solution. In the end there are **17 variables**.

- **Dual Spool Turbojet**

In a dual spool turbojet engine, both turbines' inlet corrected mass flow remains constant. These are renamed k_{HPT} and k_{LPT}:

$$k_{\mathrm{HPT}} = \dot{m}^*_{41} = \frac{\dot{m}_{41}\sqrt{T_{41t}/T_{\mathrm{ref}}}}{p_{41t}/p_{\mathrm{ref}}} \tag{98}$$

$$k_{\mathrm{LPT}} = \dot{m}^*_{45} = \frac{\dot{m}_{45}\sqrt{T_{45t}/T_{\mathrm{ref}}}}{p_{45t}/p_{\mathrm{ref}}} \tag{99}$$

Now, despite the nozzle not being critical, the total temperature and total pressure ratios between station 41 to 45 are known and always constant, so in fact, these do not contribute in the addition of new problem variables.

The constant values for the thermodynamic ratios in the HPT, which are denoted as τ_{HPT} in the case of the total temperature and $1/\pi_{\mathrm{HPT}}$ in the case of the total pressure, come from mixing Equation 100 with 34. The first one yields the following:

$$\begin{aligned}\frac{k_{\mathrm{HPT}}}{k_{\mathrm{LPT}}}=\frac{\dot{m}_{41}^{*}}{\dot{m}_{45}^{*}}&=\frac{\dot{m}_{41}\sqrt{T_{41\mathrm{t}}/T_{\mathrm{ref}}}}{p_{41\mathrm{t}}/p_{\mathrm{ref}}}\Bigg/\frac{\dot{m}_{45}\sqrt{T_{45\mathrm{t}}/T_{\mathrm{ref}}}}{p_{45\mathrm{t}}/p_{\mathrm{ref}}}\\&=\frac{(1+f)\left(1-b_{25}-b_{3}\right)+\mu b_{3}}{(1+f)\left(1-b_{25}-b_{3}\right)+b_{3}}\sqrt{\frac{T_{41\mathrm{t}}}{T_{45\mathrm{t}}}\frac{p_{45\mathrm{t}}}{p_{41\mathrm{t}}}}\\&=\frac{(1+f)\left(1-b_{25}-b_{3}\right)+\mu b_{3}}{(1+f)\left(1-b_{25}-b_{3}\right)+b_{3}}\frac{1}{\sqrt{\tau_{\mathrm{HPT}}\pi_{\mathrm{HPT}}}}\end{aligned}\qquad(100)$$

After subtracting other DOF that were included because of working with performance maps, Table 8 collects all problem variables. To reiterate, the problem is greatly reduced after disregarding shaft speeds and assuming constant many values of corrected mass flow or component total temperature and pressure ratios, which in the end will allow to reach a closed form for the analytical approach. This is seen in Table 8.

Component	Variables
Diffuser	$\frac{T_{2\mathrm{t}}}{T_0},\ \frac{p_{2\mathrm{t}}}{p_0},\ \frac{\dot{m}_0\sqrt{T_0/T_{\mathrm{ref}}}}{p_0/p_{\mathrm{ref}}},\ \frac{V_0}{\sqrt{\gamma_{\mathrm{c}}RT_0}}$
Low Pressure Compressor	$\frac{T_{25\mathrm{t}}}{T_{2\mathrm{t}}},\ \frac{p_{25\mathrm{t}}}{p_{2\mathrm{t}}},\ \frac{\dot{m}_2\sqrt{T_{2\mathrm{t}}/T_{\mathrm{ref}}}}{p_{2\mathrm{t}}/p_{\mathrm{ref}}}$
High Pressure Compressor	$\frac{T_{3\mathrm{t}}}{T_{25\mathrm{t}}},\ \frac{p_{3\mathrm{t}}}{p_{25\mathrm{t}}},\ \frac{\dot{m}_{25}\sqrt{T_{25\mathrm{t}}/T_{\mathrm{ref}}}}{p_{25\mathrm{t}}/p_{\mathrm{ref}}}$
Combustion Chamber	$\frac{T_{4\mathrm{t}}}{T_{3\mathrm{t}}},\ \frac{\dot{m}_3\sqrt{T_{3\mathrm{t}}/T_{\mathrm{ref}}}}{p_{3\mathrm{t}}/p_{\mathrm{ref}}},\ \frac{\eta_{\mathrm{CC}}fL}{C_{\mathrm{p,c}}T_{3\mathrm{t}}}$
NGV Bleed Injection	$\frac{\dot{m}_4\sqrt{T_{4\mathrm{t}}/T_{\mathrm{ref}}}}{p_{3\mathrm{t}}/p_{\mathrm{ref}}}$
High Pressure Turbine	–
Low Pressure Turbine	$\frac{T_{5\mathrm{t}}}{T_{45\mathrm{t}}},\ \frac{p_{5\mathrm{t}}}{p_{45\mathrm{t}}}$
Nozzle	$\frac{T_9}{T_{5\mathrm{t}}},\ \frac{p_9}{p_{5\mathrm{t}}},\ \frac{\dot{m}_5\sqrt{T_{5\mathrm{t}}/T_{\mathrm{ref}}}}{p_{5\mathrm{t}}/p_{\mathrm{ref}}},\ \frac{V_9}{\sqrt{\gamma_{\mathrm{h}}RT_9}}$

Table 8: Problem Variables for the Dual Spool Turbojet.

Again, if the nozzle is critical, the thermodynamic ratios from 45 to 5 are now known, as it happened in the last case. This also reduces 1 DOF from the internal coupling:

$$\begin{aligned}\frac{k_{\mathrm{LPT}}}{k_{\mathrm{N}}} &= \frac{\dot{m}^*_{45}}{\dot{m}^*_5} = \frac{\dot{m}_{45}\sqrt{T_{41\mathrm{t}}/T_{\mathrm{ref}}}}{p_{45\mathrm{t}}/p_{\mathrm{ref}}} \bigg/ \frac{\dot{m}_5\sqrt{T_{5\mathrm{t}}/T_{\mathrm{ref}}}}{p_{5\mathrm{t}}/p_{\mathrm{ref}}} \\ &= \sqrt{\frac{T_{45\mathrm{t}}}{T_{5\mathrm{t}}}}\frac{p_{5\mathrm{t}}}{p_{45\mathrm{t}}} = \frac{1}{\sqrt{\tau_{\mathrm{LPT}}}\pi_{\mathrm{LPT}}}\end{aligned} \tag{101}$$

While the thermodynamic ratios are also related through Equation 36 with a constant LPT isentropic efficiency. The nomenclature for the total temperature and pressure ratio are τ_{LPT} $1/\pi_{\mathrm{LPT}}$, respectively. These are again, not considered constant because the nozzle can transition to not be critical. In this case there is a total of **20 variables**.

Finally, for both kinds, let τ_{NGV} and $\pi_{\mathrm{NGV}} \approx 1$ refer to the total temperature ratio and total pressure ratio in the NGV Cooling Bleed stage. Also, π_{CC} refers to the constant total pressure drop in the combustion chamber.

3.2.3 Problem Equations

Many of the equations used for achieving analytical solution have been mentioned in former sections, thus their validity will be briefly stated here. They will also be counted to state the number of problem DOF.

Component Modeling and Mass Flow Continuity at their Inlet

The component equations presented before and are valid for the current analyses are hereby mentioned, as no new one is introduced.

- **Diffuser**

  Both Equation 2 and 3 are valid.

- **Compressor**

  The number of equations depends on the number of components of this type. Thus, depending on the typology of the engine:

  - **Single Spool Turbojet**

    Equation 6 and 9 are valid. The first one must be used with a constant isentropic efficiency, corresponding to the value at the engine's design point.

  - **Dual Spool Turbojet**

    Equation 9, 11, 13 and 16 are valid. Again, use constant isentropic efficiencies corresponding to the respective design points.

- **Combustion Chamber**

  Equation 19 is still valid. Now the total pressure losses are considered constant so no new equation is introduced.

  - **Single Spool Turbojet**

    Equation 22 is valid.

  - **Dual Spool Turbojet**

    Equation 23 is valid.

- **NGV Cooling Bleed**

  In this component the total temperature and total pressure ratio are considered constants. For the corrected mass flow in station 4, on the other hand:

  - **Single Spool Turbojet**

    Equation 26 is valid.

  - **Dual Spool Turbojet**

    Equation 28 is valid.

- **Turbine**

  The inlet corrected mass flow depends on engine type, as different bleed fractions comprise the problem. Not only that, also the total temperature ratio across the component.

  - **Single Spool Turbojet**

    Equation 29 is valid to be used with a constant design point turbine isentropic efficiency. Equation 32 described corrected mass flow evolution.

  - **Dual Spool Turbojet**

    Only Equation 36 is valid in the LPT, as the HPT properties are being considered constant. Also use along a constant isentropic efficiency. Equation 39 is the mass flow continuity equation in this case.

- **Nozzle**

  All 3 relations given in Equation 43, 44, 47 are valid in this context, while depending on the engine:

  - **Single Spool Turbojet**

    Equation 45 is valid.

  - **Dual Spool Turbojet**

    Equation 46 is valid.

Power Balance

Only power balance in steady state are considered, as compatibility is not modeled in this analysis. These depend on the type of engine once again:

- **Single Spool Turbojet**

  Equation 55 is valid with $dN^*/dt = 0$ because only steady state is considered.

- **Dual Spool Turbojet**

  Equation 59 and 60 are valid with $dN^*_{\text{LP}}/dt = 0$ and $dN^*_{\text{HP}}/dt = 0$, respectively, for the same reason.

Boundary Conditions

Boundary conditions coincide with the equations exposed before, depending on wheter the nozzle is critical or not:

- **Non-critical Nozzle**

  If the nozzle is not critical again the outlet pressure equalizes with the ambient one, thus $p_9/p_0 = 1$. This can be differently expanded:

  - **Single Spool Turbojet**

    Equation 61 in this case.

  - **Dual Spool Turbojet**

    Equation 62 which considers more stations.

- **Critical Nozzle**

  Equation 63 is the one to be applied to ensure that $\dot{m}_5^* = \dot{m}_{5,max}^*$ which in this case has been called k_{N}.

For a single spool engine there is a total of **15 equations**, while for a dual spool there is a total of **18 equations**. All these equations have been presented before and are valid in this case.

Again, the number of problem DOF is counted, subtracting from the number of variables appearing in each approach the number of available equations. Note the effect of diminishing 1 DOF in the internal coupling for the case of a critical nozzle. This will not be expressed in Table 9, as the nozzle can be non-critical too.

Subproblem	Single Spool	Dual Spool	
Internal Coupling	2	**HP**	2
		LP	2
Engine Coupling	2	2	

Table 9: Number of Subproblem Degrees of Freedom.

3.2.4 Solution Strategy

In this section the presented equations and variables will be combined to obtain the equations intrinsic to the analytical solution and that allow to solve the problem in a simplified way.

As a remark, the combustion chamber does not intervene in reaching the solution. It is calculated as a consequence of imposing power equilibrium. However, it is still considered a necessary component to be calculated. Hence, the variables in Table 7 and 8 and its intrinsic equations are considered in this analysis.

Once more, the problem is conveniently divided into an internal coupling and an engine coupling. These terms have the same meaning as previously described. Internal coupling refers to the study of the engine from the inlet of the first compressor to the outlet of the last turbine, without taking into account their relation to diffuser, nozzle and interaction with outside conditions.

Nonetheless some terms that need to be obtained in the whole engine coupling with the exterior conditions will be present in this derivation.

The nozzle being critical or not will include or exclude variables from the following analysis, so it is deemed to affect the study of the internal coupling. This is done because the boundary conditions change the nature of the solution, as commented. Hence, this is an illustrative phenomenon that is hereby described.

The formulation of the engine coupling problem will once more depend on the type of engine, thus once more a division into single spool and dual spool is considered. For solving the problem the 2 modified DOF chosen will be the flight Mach number M_0 and the compressor total pressure ratio p_{3t}/p_{2t} or the LPC total pressure ratio p_{25t}/p_{2t} when applicable.

- **Single Spool Turbojet**

  First of all, the evolution of thermodynamic variables is calculated in the diffuser. T_{2t}/T_0 and p_{2t}/p_0 are determined from Equation 2 and 3.

  Then, the relation between compressor total pressure ratio and inlet corrected mass flow is derived for the present case. For this, a combination of compressor and turbine equations is employed.

  Combine the corrected mass flow evolution equations from station 2 to 3, 3 to 4 and 4 to 41, given by Equation 22, 26 and 32. This gives an expression dependent on $\dot{m}_2^*$ with respect to $k_\mathrm{T} = \dot{m}_{41}^*$:

$$\dot{m}_2^* = \frac{k_\mathrm{T}\pi_\mathrm{NGV}\pi_\mathrm{CC}}{(1-b_3)(1+f)+\mu b_3}\frac{p_{3t}/p_{2t}}{\sqrt{T_{41t}/T_{2t}}}$$

  Finally, the total temperature ratio in the denominator needs to be isolated from the equilibrium equation. Hence, from Equation 55 in steady state, that fraction is, after substituting T_{3t}/T_{2t} with Equation 6:

$$\frac{T_{41t}}{T_{2t}} = \frac{(p_{3t}/p_{2t})^{\frac{\gamma_c-1}{\gamma_c}}-1}{\frac{C_{p,e}}{C_{p,c}}\eta_C\eta_m\left((1+f)(1-b_3)+\mu b_3\right)(1-T_{5t}/T_{41t})} \tag{102}$$

  Finally, joining both:

$$\dot{m}_2^* = k_\mathrm{T}\pi_\mathrm{NGV}\pi_\mathrm{CC}\sqrt{\frac{C_{p,e}}{C_{p,c}}\frac{\eta_C\eta_m(1-T_{5t}/T_{41t})}{(1+f)(1-b_3)+\mu b_3}}\frac{p_{3t}/p_{2t}}{\sqrt{(p_{3t}/p_{2t})^{\frac{\gamma_c-1}{\gamma_c}}-1}} \tag{103}$$

  It is possible to assess the corrected mass flow at the inlet of the compressor with one of the chosen DOF. Together with T_{2t}/T_0 and p_{2t}/p_0, the engine inlet corrected mass flow is derived $\dot{m}_0^*$. Note that there is still a term that does not allow for the precise calculation, that is T_{5t}/T_{41t}.

  For this, it is necessary to consider the boundary conditions, and find at which value of p_{3t}/p_{2t} the criticality threshold of the nozzle is reached. Note that from Equation 97 and 29, if the nozzle is choked, the thermodynamic ratios at the turbine are known. This value is calculated for a convergent nozzle as:

$$\left(\frac{p_{3t}}{p_{2t}}\right)_\mathrm{u} = \frac{1}{(p_{2t}/p_0)\pi_\mathrm{CC}\pi_\mathrm{NGV}(1/\pi_\mathrm{T})\left(1-\frac{1}{\eta_\mathrm{N}}\frac{\gamma_h-1}{\gamma_h+1}\right)^{\frac{\gamma_h}{\gamma_h-1}}} \tag{104}$$

Where it has been recognized that at this point: $p_9/p_0 = 1$ but the nozzle and turbine are still critical. If the nozzle is non-critical and convergent-divergent $p_9/p_{5\mathrm{t}}$ is known too and can be plugged into Equation 104 (not considered in this work). There are then 2 possible cases to look at:

- **Case 1:** $p_{3\mathrm{t}}/p_{2\mathrm{t}} < (p_{3\mathrm{t}}/p_{2\mathrm{t}})_{\mathrm{u}}$

  When the compressor total pressure ratio is below the threshold the nozzle is considered to be in non-critical conditions. In this case the inverse of the NPR is isolated, because it can relate to π_{T}, again with $p_9/p_0 = 1$:

  $$\left(\frac{p_9}{p_{5\mathrm{t}}}\right)(\pi_{\mathrm{T}}) = \frac{1}{(p_{2\mathrm{t}}/p_0)(p_{3\mathrm{t}}/p_{2\mathrm{t}})\pi_{\mathrm{CC}}\pi_{\mathrm{NGV}}(1/\pi_{\mathrm{T}})} \tag{105}$$

  Then, it is recognised that $\dot{m}_5^*$ is possible to be found through Equation 29 and 45, and show its dependence on π_{T}. After that, with the nozzle equation in Equation 47:

  $$\begin{aligned}\dot{m}_5^* &= k_{\mathrm{T}}\frac{(1-b_3)(1+f)+b_3}{(1-b_3)(1+f)+\mu b_3}\frac{\sqrt{T_{5\mathrm{t}}/T_{41\mathrm{t}}}}{p_{5\mathrm{t}}/p_{41\mathrm{t}}} \\ &= k_{\mathrm{T}}\pi_{\mathrm{T}}\frac{(1-b_3)(1+f)+b_3}{(1-b_3)(1+f)+\mu b_3}\sqrt{1-\eta_{\mathrm{T}}\left(1-\left(\frac{1}{\pi_{\mathrm{T}}}\right)^{\frac{\gamma_{\mathrm{h}}-1}{\gamma_{\mathrm{h}}}}\right)} \\ &= \frac{C_{\mathrm{D}}A_9 p_{\mathrm{ref}}}{\sqrt{RT_{\mathrm{ref}}}}\left(\frac{p_9}{p_{5\mathrm{t}}}\right)(\pi_{\mathrm{T}})\left(1-\eta_{\mathrm{N}}\left(1-\left(\frac{p_9}{p_{5\mathrm{t}}}(\pi_{\mathrm{T}})\right)^{\frac{\gamma_{\mathrm{h}}-1}{\gamma_{\mathrm{h}}}}\right)\right)^{-1} \\ &\quad\cdot\sqrt{\frac{2\gamma_{\mathrm{h}}\eta_{\mathrm{N}}}{\gamma_{\mathrm{h}}-1}\left(1-\left(\frac{p_9}{p_{5\mathrm{t}}}(\pi_{\mathrm{T}})\right)^{\frac{\gamma_{\mathrm{h}}-1}{\gamma_{\mathrm{h}}}}\right)}\end{aligned} \tag{106}$$

  Where π_{T} can be numerically solved. So is $p_9/p_{5\mathrm{t}}$, and with Equation 43 and 44 the nozzle is solved. $T_{5\mathrm{t}}/T_{41\mathrm{t}}$ can then be found to plug in Equation 103 and continue the process.

  Note that there is abuse of notation in the last equations for the sake of making the process more comprehensible to the reader, note that π_{T} is not a constant in this case, as it was said previously. It varies with operation and represents the variable $p_{41\mathrm{t}}/p_{5\mathrm{t}}$.

- **Case 2:** $p_{3\mathrm{t}}/p_{2\mathrm{t}} \geq (p_{3\mathrm{t}}/p_{2\mathrm{t}})_{\mathrm{u}}$

  For values of $p_{3\mathrm{t}}/p_{2\mathrm{t}}$ meeting this condition, the nozzle will be choked and $T_{5\mathrm{t}}/T_{41\mathrm{t}} = \tau_{\mathrm{T}}$, as well as $1/\pi_{\mathrm{T}} = p_{5\mathrm{t}}/p_{41\mathrm{t}}$ and $\dot{m}_5^* = k_{\mathrm{N}}$ are constant values. In this case, the variables at the critical nozzle are found by applying expressions Equation 50, 51 and 52 if it is convergent or Equation 43, 44 and 53 otherwise.

After plugging in the adequate T_{41t}/T_{5t} in Equation 103, $\dot{m}_3^*$ and T_{3t}/T_{2t} are found through Equation 22 and 6. Employing Equation 102 with the imposed p_{3t}/p_{2t} and the found T_{41t}/T_{5t}, T_{41t}/T_{2t} is returned, making it possible to solve the combustion chamber and NGV cooling bleed variables:

$$\frac{T_{4t}}{T_{3t}} = \frac{1}{\tau_{\mathrm{NGV}}} \frac{T_{41t}/T_{2t}}{T_{3t}/T_{2t}} \tag{107}$$

The corresponding fuel parameter $(\eta_{\mathrm{CC}} f L)/(C_{\mathrm{p,c}} T_{3t})$ and the corrected mass flow in station 4, $\dot{m}_4^*$, are found by invoking Equation 19 and 26, respectively. The mass flow at station 41, $\dot{m}_{41}^*$, is found also by Equation 32 with τ_{NGV} and π_{NGV}. The problem has then been analytically solved for a single spool engine.

- **Dual Spool Turbojet**

The first step of the process, once again, is the determination of the evolution of thermodynamic variables after the diffuser. T_{2t}/T_0 and p_{2t}/p_0 are calculated throughout Equation 2 and 3.

Now, the relation between the HPC total pressure ratio and inlet corrected mass flow is derived to continue the analysis. For this, combine the corrected mass flow evolution equations for $\dot{m}_3^*$, $\dot{m}_4^*$ and $k_{\mathrm{HPT}} = \dot{m}_{41}^*$; given by Equation 23, 28 and 39. This yields the following relation, dependent on $\dot{m}_{25}^*$, and put in terms of k_{HPT}:

$$\dot{m}_{25}^* = k_{\mathrm{HPT}} \pi_{\mathrm{NGV}} \pi_{\mathrm{CC}} \frac{1 - b_{25}}{(1 - b_{25} - b_3)(1 + f) + \mu b_3} \frac{p_{3t}/p_{25t}}{\sqrt{T_{41t}/T_{25t}}}$$

The total temperature fraction is again isolated from the high pressure equilibrium equation. This means that it is taken from Equation 60 in steady state, where T_{3t}/T_{25t} needs to be substituted from Equation 13, with $T_{45t}/T_{41t} = \tau_{\mathrm{HPT}}$ constant:

$$\frac{T_{41t}}{T_{25t}} = \frac{(1 - b_{25}) \left((p_{3t}/p_{25t})^{\frac{\gamma_c - 1}{\gamma_c}} - 1 \right)}{\frac{C_{\mathrm{p,e}}}{C_{\mathrm{p,c}}} \eta_{\mathrm{HPC}} \eta_{\mathrm{m,HP}} \left((1 + f)(1 - b_{25} - b_3) + \mu b_3 \right) (1 - \tau_{\mathrm{HPT}})} \tag{108}$$

The HPC inlet corrected mass flow is hereby stated, after substituting the last two relations derived above, yields an expression dependent on the still unknown HPC total pressure ratio. The rest of the parameters that shape the equation are indeed assumed to be constant:

$$\begin{aligned} \dot{m}_{25}^* = k_{\mathrm{HPT}} \pi_{\mathrm{NGV}} \pi_{\mathrm{CC}} & \sqrt{\frac{C_{\mathrm{p,e}}}{C_{\mathrm{p,c}}} \frac{\eta_{\mathrm{HPC}} \eta_{\mathrm{m,HP}} (1 - b_{25})(1 - \tau_{\mathrm{HPT}})}{(1 + f)(1 - b_{25} - b_3) + \mu b_3}} \\ & \cdot \frac{p_{3t}/p_{25t}}{\sqrt{(p_{3t}/p_{25t})^{\frac{\gamma_c - 1}{\gamma_c}} - 1}} \end{aligned} \tag{109}$$

Now the low pressure coupling power balance (Equation 59) is considered, knowing that the thermodynamic ratios in it are constant and known. Also, Equation 11 is plugged into it to yield:

$$\frac{T_{41\mathrm{t}}}{T_{2\mathrm{t}}} = \frac{\left(p_{25\mathrm{t}}/p_{2\mathrm{t}}\right)^{\frac{\gamma_\mathrm{c}-1}{\gamma_\mathrm{c}}} - 1}{\frac{C_\mathrm{p,e}}{C_\mathrm{p,c}} \eta_\mathrm{LPC} \eta_\mathrm{m,LP} \left(\left(1+f\right)\left(1-b_{25}-b_3\right)+b_3\right)\left(1-T_{5\mathrm{t}}/T_{45\mathrm{t}}\right)\tau_\mathrm{HPT}} \tag{110}$$

Now, the relation between the HPC and LPC is obtained by first considering the following identity, coming from Equation 11:

$$\frac{T_{41\mathrm{t}}}{T_{2\mathrm{t}}} = \frac{T_{41\mathrm{t}}}{T_{25\mathrm{t}}}\frac{T_{25\mathrm{t}}}{T_{2\mathrm{t}}} = \frac{T_{41\mathrm{t}}}{T_{25\mathrm{t}}}\left(1 + \frac{1}{\eta_\mathrm{LPC}}\left(\left(\frac{p_{25\mathrm{t}}}{p_{2\mathrm{t}}}\right)^{\frac{\gamma_\mathrm{c}-1}{\gamma_\mathrm{c}}} - 1\right)\right)$$

Substituting what has been found in Equation 108 and 110, then inverting to isolate $p_{3\mathrm{t}}/p_{25\mathrm{t}}$ it is found that it depends only on $p_{25\mathrm{t}}/p_{2\mathrm{t}}$ and $T_{5\mathrm{t}}/T_{45\mathrm{t}}$:

$$\begin{aligned}\frac{p_{3\mathrm{t}}}{p_{25\mathrm{t}}} = \Bigg(1 + &\frac{\eta_\mathrm{HPC}\eta_\mathrm{m,HP}}{\eta_\mathrm{LPC}\eta_\mathrm{m,LP}} \frac{(1+f)(1-b_{25}-b_3)+\mu b_3}{\left(1-b_{25}\right)\left((1+f)(1-b_{25}-b_3)+b_3\right)} \\ &\cdot \frac{1-\tau_\mathrm{HPT}}{\tau_\mathrm{HPT}\left(1-T_{5\mathrm{t}}/T_{45\mathrm{t}}\right)} \frac{\left(p_{25\mathrm{t}}/p_{2\mathrm{t}}\right)^{\frac{\gamma_\mathrm{c}-1}{\gamma_\mathrm{c}}} - 1}{1+\frac{1}{\eta_\mathrm{LPC}}\left(\left(p_{25\mathrm{t}}/p_{2\mathrm{t}}\right)^{\frac{\gamma_\mathrm{c}-1}{\gamma_\mathrm{c}}} - 1\right)}\Bigg)^{\frac{\gamma_\mathrm{c}}{\gamma_\mathrm{c}-1}}\end{aligned} \tag{111}$$

Then the corrected mass flow at the inlet of the LPC is going to be expressed with respect to the imposed LPC total pressure ratio $p_{25\mathrm{t}}/p_{2\mathrm{t}}$. This is done substituting the HPC total pressure ratio found in Equation 111 in Equation 109:

$$\begin{aligned}\dot{m}_2^* &= \frac{\dot{m}_{25}^*}{1-b_{25}}\sqrt{\frac{T_{2\mathrm{t}}}{T_{25\mathrm{t}}}}\frac{p_{25\mathrm{t}}}{p_{2\mathrm{t}}} \\ &= k_\mathrm{HPT}\pi_\mathrm{NGV}\pi_\mathrm{CC}\sqrt{\frac{C_\mathrm{p,e}}{C_\mathrm{p,c}}\eta_\mathrm{LPC}\eta_\mathrm{m,LP}\left((1+f)(1-b_{25}-b_3)+b_3\right)\tau_\mathrm{HPT}\left(1-\frac{T_{5\mathrm{t}}}{T_{45\mathrm{t}}}\right)} \\ &\quad\cdot \frac{1}{(1+f)(1-b_{25}-b_3)+\mu b_3}\frac{p_{25\mathrm{t}}/p_{2\mathrm{t}}}{\sqrt{\left(p_{25\mathrm{t}}/p_{2\mathrm{t}}\right)^{\frac{\gamma_\mathrm{c}-1}{\gamma_\mathrm{c}}} - 1}}\Bigg(1 + \frac{\eta_\mathrm{HPC}\eta_\mathrm{m,HP}}{\eta_\mathrm{LPC}\eta_\mathrm{m,LP}} \\ &\quad\cdot \frac{(1+f)(1-b_{25}-b_3)+\mu b_3}{\left(1-b_{25}\right)\left((1+f)(1-b_{25}-b_3)+b_3\right)}\frac{1-\tau_\mathrm{HPT}}{\tau_\mathrm{HPT}\left(1-T_{5\mathrm{t}}/T_{45\mathrm{t}}\right)} \\ &\quad\cdot \frac{\left(p_{25\mathrm{t}}/p_{2\mathrm{t}}\right)^{\frac{\gamma_\mathrm{c}-1}{\gamma_\mathrm{c}}} - 1}{1+\frac{1}{\eta_\mathrm{LPC}}\left(\left(p_{25\mathrm{t}}/p_{2\mathrm{t}}\right)^{\frac{\gamma_\mathrm{c}-1}{\gamma_\mathrm{c}}} - 1\right)}\Bigg)^{\frac{\gamma_\mathrm{c}}{\gamma_\mathrm{c}-1}}\end{aligned} \tag{112}$$

Note that this expression is dependent on the ratio $T_{5\mathrm{t}}/T_{45\mathrm{t}}$, which not always remains constant during operation. As explained, this only occurs when the nozzle is critical.

Therefore, in order for this formula to have any validity, it is necessary to consider the boundary conditions first, to find the value of p_{25t}/p_{2t} for which the criticality threshold of the nozzle is reached. Note that from Equation 101 and 36, if the nozzle is choked, the thermodynamic ratios at the turbine are known. This value is $(p_{25t}/p_{2t})_u$ and is calculated by the following method:

$$\frac{p_9}{p_0} = \frac{p_{2t}}{p_0}\left(\frac{p_{25t}}{p_{2t}}\right)_u \frac{p_{3t}}{p_{25t}}\pi_{CC}\left(\pi_{NGV}\right)\left(\frac{1}{\pi_{HPT}}\right)\left(\frac{1}{\pi_{LPT}}\right)\left(1-\frac{1}{\eta_N}\frac{\gamma_h-1}{\gamma_h+1}\right)^{\frac{\gamma_h}{\gamma_h-1}} = 1 \quad (113)$$

Where $p_9/p_0 = 1$ and now p_{3t}/p_{25t} depends on $(p_{25t}/p_{2t})_u$, so it is an intrinsic equation and needs to be resolved iteratively. The nozzle and turbines are critical in this point. Note again that p_{9t}/p_{5t} does not necessarily have to be the inverse of the critical NPR in a convergent-divergent nozzle, but with k_N and A_9/A_8 it can be calculated. However, throughout this document it is not considered to be viable to have a convergent-divergent segment in subcritical or limit nozzle scenarios, like this presented one. Note the 2 possible situations that can occur:

- **Case 1:** $p_{25t}/p_{2t} < (p_{25t}/p_{2t})_u$

  In case that the LPC total pressure ratio is below the calculated threshold. The inverse of the NPR is calculated and put in terms of π_{LPT}, again considering $p_9/p_0 = 1$:

  $$\left(\frac{p_9}{p_{5t}}\right)(\pi_{LPT}) = \frac{\pi_{HPT}\pi_{LPT}}{(p_{2t}/p_0)(p_{25t}/p_{2t})(p_{3t}/p_{25t}(\pi_{LPT}))\pi_{CC}\pi_{NGV}} \quad (114)$$

  Note that $\dot{m}_5^*$ can be estimated through Equation 36 and 46, depending on the constant parameter k_{LPT} and the variable π_{LPT} (abusing notation again). With the nozzle equation in Equation 47:

  $$\begin{aligned}\dot{m}_5^* &= k_{LPT}\frac{\sqrt{T_{5t}/T_{45t}}}{p_{5t}/p_{45t}} = k_{LPT}\pi_{LPT}\sqrt{1-\eta_{LPT}\left(1-\left(\frac{1}{\pi_{LPT}}\right)^{\frac{\gamma_h-1}{\gamma_h}}\right)} \\ &= \frac{C_D A_9 p_{ref}}{\sqrt{RT_{ref}}}\left(\frac{p_9}{p_{5t}}\right)(\pi_{LPT})\left(1-\eta_N\left(1-\left(\frac{p_9}{p_{5t}}(\pi_{LPT})\right)^{\frac{\gamma_h-1}{\gamma_h}}\right)\right)^{-1} \\ &\cdot\sqrt{\frac{2\gamma_h\eta_N}{\gamma_h-1}\left(1-\left(\frac{p_9}{p_{5t}}(\pi_{LPT})\right)^{\frac{\gamma_h-1}{\gamma_h}}\right)}\end{aligned} \quad (115)$$

  Once again, π_{LPT} can be numerically solved as done in the single spool case. p_9/p_{5t} can be solved too. With Equation 43 and 44 the jump in conditions through the nozzle is determined. T_{5t}/T_{45t} is determined and plugged in Equation 109 and 112.

- **Case 2:** $p_{25\text{t}}/p_{2\text{t}} \geq (p_{25\text{t}}/p_{2\text{t}})_\text{u}$

  If this condition is met, the nozzle will be critical and $T_{5\text{t}}/T_{45\text{t}} = \tau_\text{LPT}$ as well as $1/\pi_\text{T} = p_{5\text{t}}/p_{45\text{t}}$ are constant values, like happened to the HPT (note Equation 100 and 101). The variables at the critical nozzle are then calculated with Equation 50, 51 and 52 or, if it is the case of a convergent-divergent segment, Equation 43, 44 and 53.

Plugging in the adequate $T_{45\text{t}}/T_{5\text{t}}$ in Equation 109 and 112, together with with the thermodynamic ratios at the diffuser, the corrected inlet mass flow $\dot{m}_0^*$ can be found, because $\dot{m}_2^*$ is known. $\dot{m}_{25}^*$ can be determined by continuity Equation 16 or by Equation 109, while HPC total pressure ratio and total temperature ratio are determined using Equation 111 and 13. $\dot{m}_3^*$ is returned by Equation 23 after this.

With Equation 108 and the now known $T_{3\text{t}}/T_{25\text{t}}$ the conditions at the combustion chamber and NGV cooling bleed are possible to be solved:

$$\frac{T_{4\text{t}}}{T_{3\text{t}}} = \frac{1}{\tau_\text{NGV}} \frac{T_{41\text{t}}/T_{25\text{t}}}{T_{3\text{t}}/T_{25\text{t}}} \tag{116}$$

The fuel parameter $(\eta_\text{CC} f L)/(C_{\text{p,c}} T_{3\text{t}})$ and the corrected mass flow at the outlet of the combustion chamber, $\dot{m}_4^*$, are found by Equation 19 and 28. The mass flow at station 41, $\dot{m}_{41}^*$, is determined by Equation 39 with τ_NGV and π_NGV.

Finally, it is necessary to mention that, to obtain the characteristic constant parameters of the analytical solution, it is normally accepted to use the values correspondent to the engine's design point.

Taking into account that most jet engines are designed in component choke conditions, the characteristic total temperature ratios, τ in this analysis, and total pressure ratios, π, from the turbines and nozzles are obtained from this design point.

This is why many times the analytical solution is described as a design point linearization. Some other variables like the CC pressure drop or cooling in certain stations can be assumed to be constant, as it has been done in this analysis, although the derivation some times allows to implement simple models for calculating them.

It is many times deemed as a tool for approximating engine behavior near these design conditions, and to easily take into account the effect of varying some parameters of the system, so quick decisions can be made. However, it is not a tool for precision preliminary design, because several of the assumptions made do not hold in certain situations.

Reiterating, when speaking about an obtained solution in the rest of this study, it will refer y default to a solution obtained using the main method, based on the utilization of performance maps. The analytical solution will serve as a comparison tool, and it will be seen how it is a correct approximation near the design point conditions, but generally fails outside of that domain.

4. Validation

The results of the developed method are validated through data obtained by experimentation with a single spool laboratory-scale engine, the *AMT Netherlands Olympus HP*. It is often used in universities for educational purposes, as it is prepared with multiple accesses for sensor placement, thus allowing to measure multiple engine parameters.

The steady state validation of the current model is done through comparison with experimental data from measurements in Universidad Politécnica de Valencia (UPV), which in this case will only be used for nozzle calibration [9], among other sources that have tested this engine's properties [15], [16], [17], [18], [19], [20], [21], including the engine's datasheet. This decision has been taken after noticing that steady state results in UPV differ considerably from the cited sources and the model.

This datasheet tends to overestimate some parameters, such as thrust, and displays scarce amounts of data about some other variables like engine mass flow. It is hence complemented with own and external testing results to accomplish the validation.

Note that the small scale of the turbine introduces sometimes some unexpected effects that the code is not prepared to deal with. One of the most notable is the appearance of fuel reaction after the combustion chamber exit, sometimes all the way after the nozzle, this can be observed during one of the tests in Figure 18.

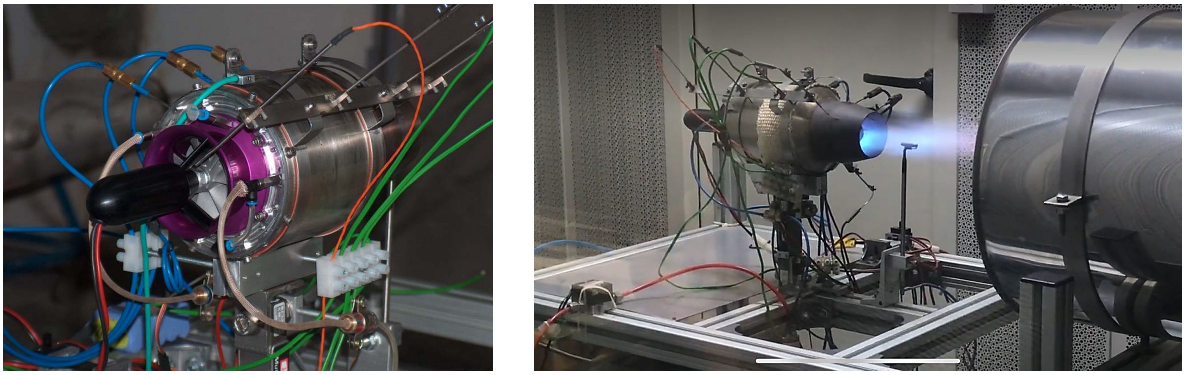

Figure 18: UPV Test Rig Sensor Equipment [9] (left) and Test Procedure Involving Uncontained Combustion (right).

The sensor equipment used in testing mainly consists of thermocouples for temperature sensing (as the engine easily allows for their introduction) as well as pressure gauges; whose acquisition frequency is considerably higher, together with a flow meter to estimate fuel consumption and a load cell to measure thrust directly. Air mass flow is estimated through the aforementioned nozzle calibration [9].

4.1 Model Parameters

The parameters chosen for the validation of the performance map solution model are hereby stated. First off, the compressor is radial, and its map is given in the engine's manual, and also stated by some authors [21]. It is digitized and incorporated to the code in *.csv* format to be interpolated.

The same will be done with the turbine map, after adapting it from a generic performance map in the program *GSP*, because there is no available information about it. Besides, is not extremely critical to predict behavior. The rest of constant parameters are stated in Table 10.

Parameter	**Value**	**Source**
T_{ref} [K]	288.15	ISA atmospheric temperature at 0 m elevation
p_{ref} [bar]	1.01325	ISA atmospheric pressure at 0 m elevation
$C_{\mathrm{p,c}}$ [J/kg/K]	1,004.5	Estimation at 288.15 K (ambient temperature)
$C_{\mathrm{p,h}}$ [J/kg/K]	1,121.0	Estimation at 900 K (mean hot part temperature)
R [J/kg/K]	287	Exhaust air estimated value
γ_{c} [-]	1.4	Estimation at 288.15 K (ambient temperature)
γ_{h} [-]	1.344	Estimation at 900 K (mean hot part temperature)
$N_{\mathrm{ref,C}}$ [rpm]	108,500	Datasheet (engine maximum corrected speed)
$N_{\mathrm{ref,T}}$ [rpm]	57,235	Fitting of the turbine performance map [16]
b_3 [-]	0	Blueprints and Datasheet. No bleed air.
$\zeta_{\mathrm{CC,c}}$ [-]	27	Tubular CC, reverse flow [11]
$\zeta_{\mathrm{CC,h}}$ [-]	2	Tubular CC, reverse flow [11]
μ [-]	0.5	Estimation
f [-]	0.02	Estimation using UPV test rig data
η_{m} [-]	0.99	Estimation
η_{D} [-]	0.99	Estimation using UPV test rig data
A_9 [m^2]	0.0032	Blueprints.

Table 10: Model Properties for the Validation Study. Value and Source.

Some properties that do not have a great influence on the final solution have been simply estimated, according to common values. These are, for example, diffuser efficiency η_{D}, shaft mechanical efficiency η_{m}, or engine FAR.

4.2 Results

Results obtained in steady state by employing the aforementioned parameter are presented. For simplification purposes, in Table 11 the chosen sources that appear in the following validation study result plots are stated.

	Ref. 1	Ref 2.	Ref 3.
Source	[15]	[16]	[17]

Table 11: Sources Chosen for Validation Study Graph Comparison.

First off, the engine's running lines are plotted over the compressor and turbine performance maps in Figure 19. No information about the design point is given by the manufacturer.

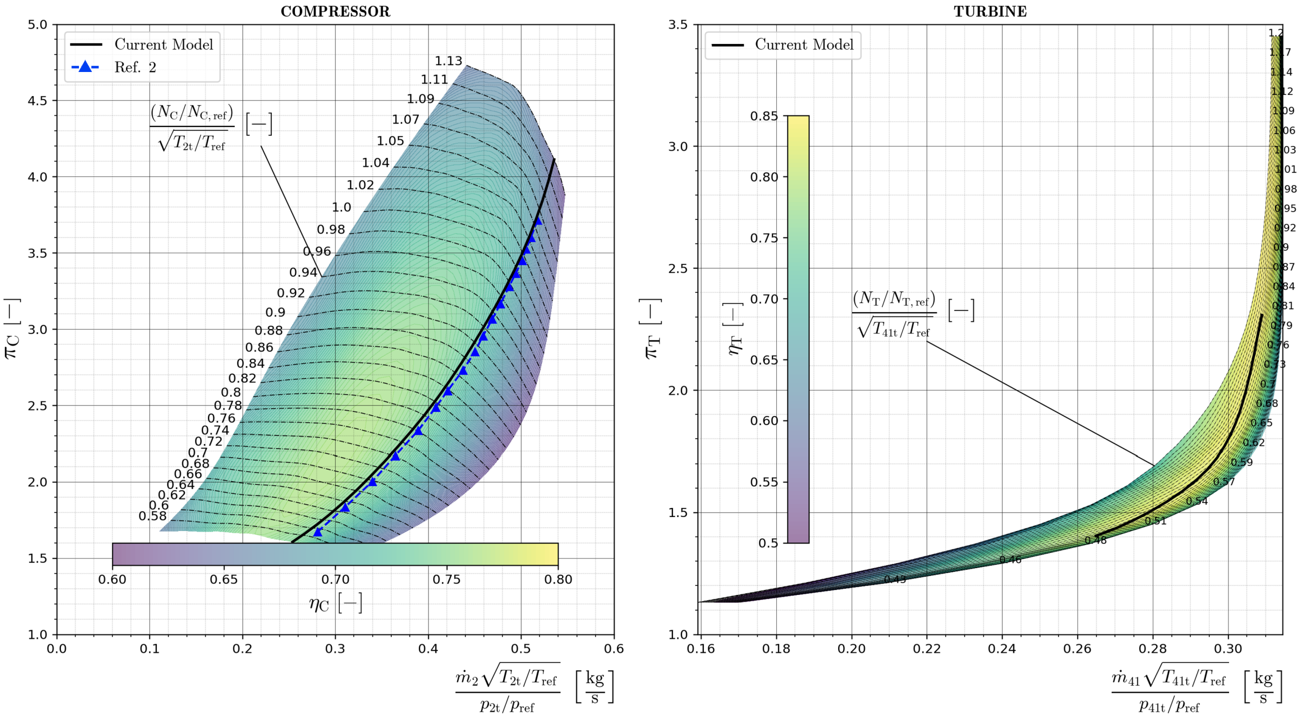

Figure 19: Operating Lines for the Engine's Compressor (left) and Turbine (right)

One the one hand, the operating line in the compressor is far away from the surge line given in the manual. Furthermore, the calculated values for the line are in concordance with those supplied in [16]. Note that the engine apparently does not run over regions of high efficiency. This might be due to a poor coupling or errors in measurements and model.

On the other hand the turbine performance map has been chosen to represent a generic axial one-stage machine. It is adjusted so the running line transits a high-efficiency region of around 0.85 [21].

Figure 20 and 21 describe the prediction for corrected thrust and corrected inlet mass flow and its dependence on engine relative corrected speed.

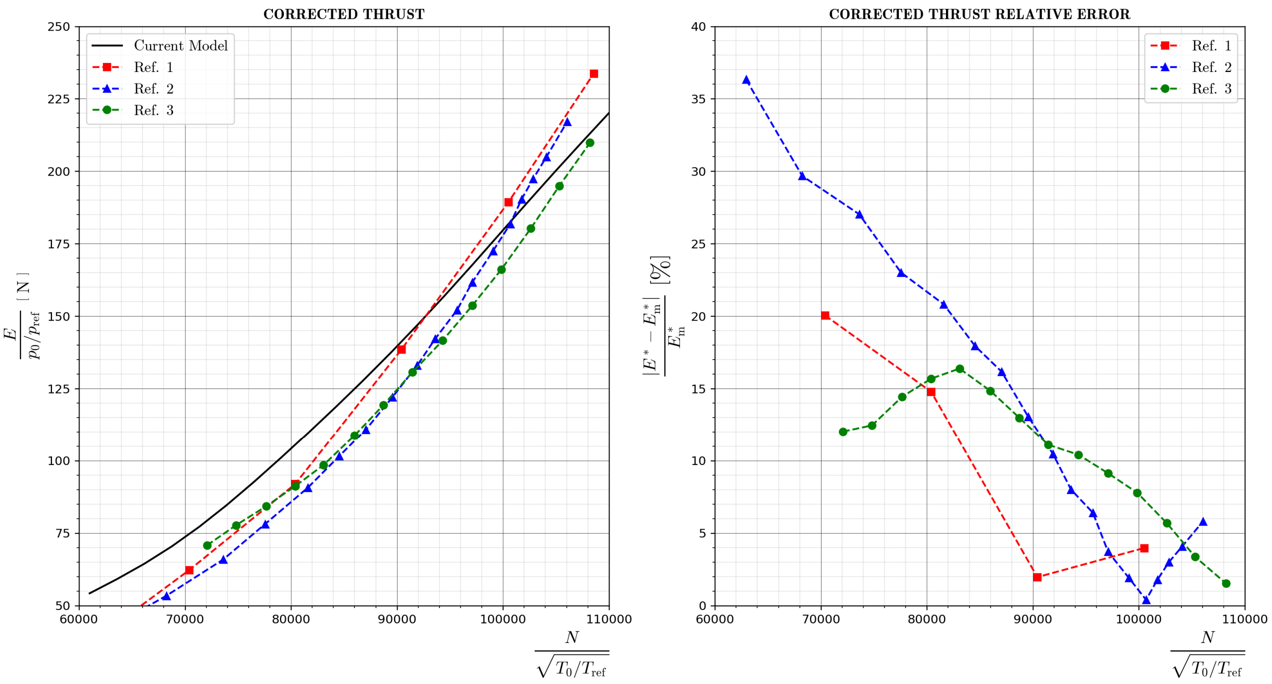

Figure 20: Corrected Thrust with Respect to Relative Corrected Engine Speed (left) and Relative Error to the Sources (right).

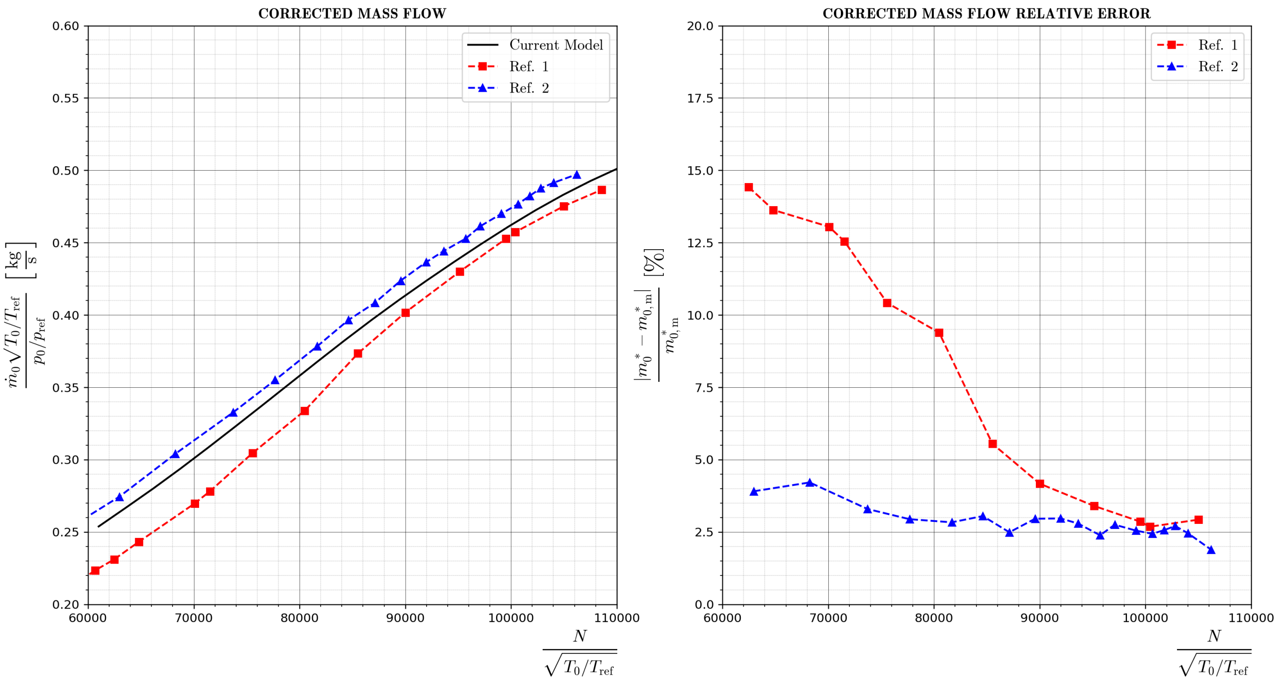

Figure 21: Corrected Inlet Mass Flow with Respect to Relative Corrected Engine Speed (left) and Relative Error to the Sources (right).

Figure 22 and 23 in turn describe the dependence of the injected fuel mass flow and and EGT, calculated with $\eta_{\mathrm{CC}} \approx 0.95$, $L \approx 42.8$ MJ/kg, $T_0/T_{\mathrm{ref}} \approx 1$ and $p_0/p_{\mathrm{ref}} \approx 1$.

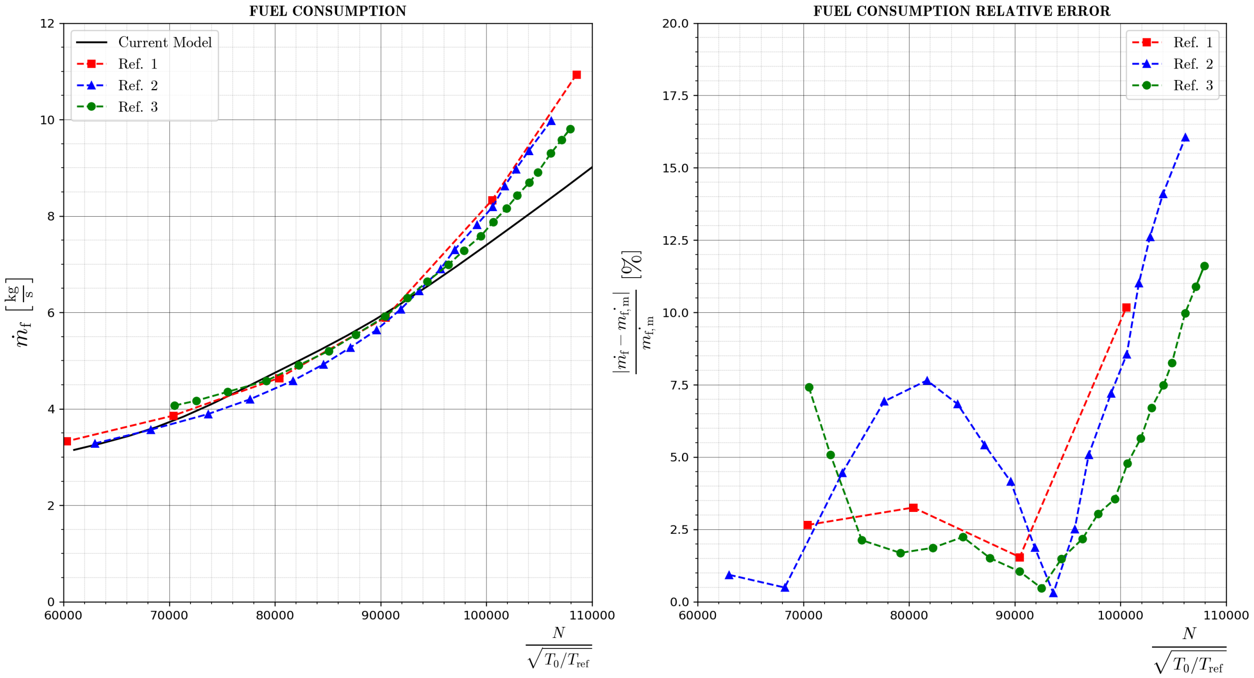

Figure 22: Corrected Fuel Mass Flow with Respect to Relative Corrected Engine Speed (left) and Relative Error to the Sources (right).

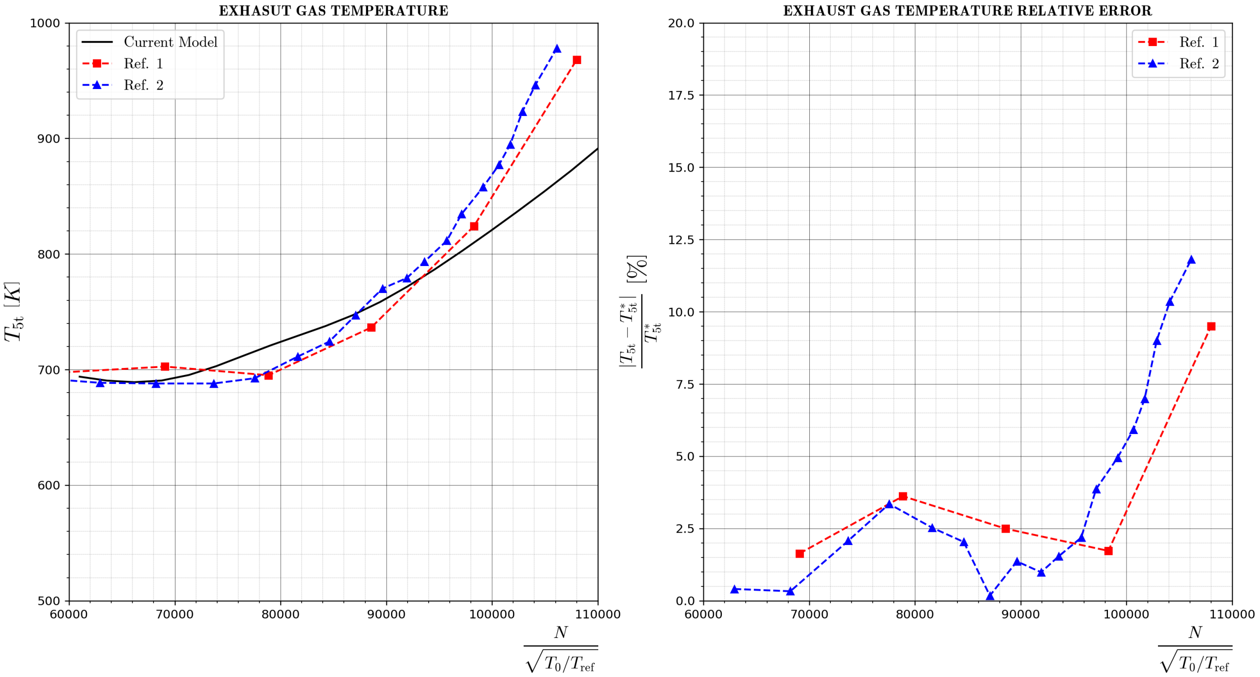

Figure 23: EGT with respect to Relative Corrected Engine Speed (left) and Relative Error to the Sources (right).

Notice the concordance of the model with many of the shown results. In Figure 20 there is a maximum discrepancy of a 35 % to what has been measured in [16], while it is precise near the maximum speeds of the device, where errors are less than 10 %. Corrected air mass flow is well represented by the model, according to both references [15] and [16]. The tendency with engine corrected speed is well captured.

The model overestimates thrust and noticeably underestimates EGT. Notice how retarded combustion mechanisms like those shown graphically in Figure 18 may be affecting the behavior of the engine as a whole, making the model fail to predict high gas temperatures at the outlet.

Nonetheless, fuel mass flow with the aforementioned combustion chamber parameters (where L corresponds to kerosene Jet A-1 lower heating value) is adequately represented by the model. In this case the maximum error occurs near the engine's maximum speed.

The validation has been completed after noting that the engine's nozzle is conical, with a prominent cone angle of about 35º. The presence of two-dimensional effects is evident when analyzing the data obtained in UPV, as it does not fit well with one-dimensional compressible flow theory.

For this reason, a correcting discharge coefficient C_D dependent on NPR is fitted to Equation 47, in accordance to what has been exposed in Figure 11. The corrected mass flow that circulates the component now is more correctly fitted and adequate to include in the model. It is shown in Figure 24.

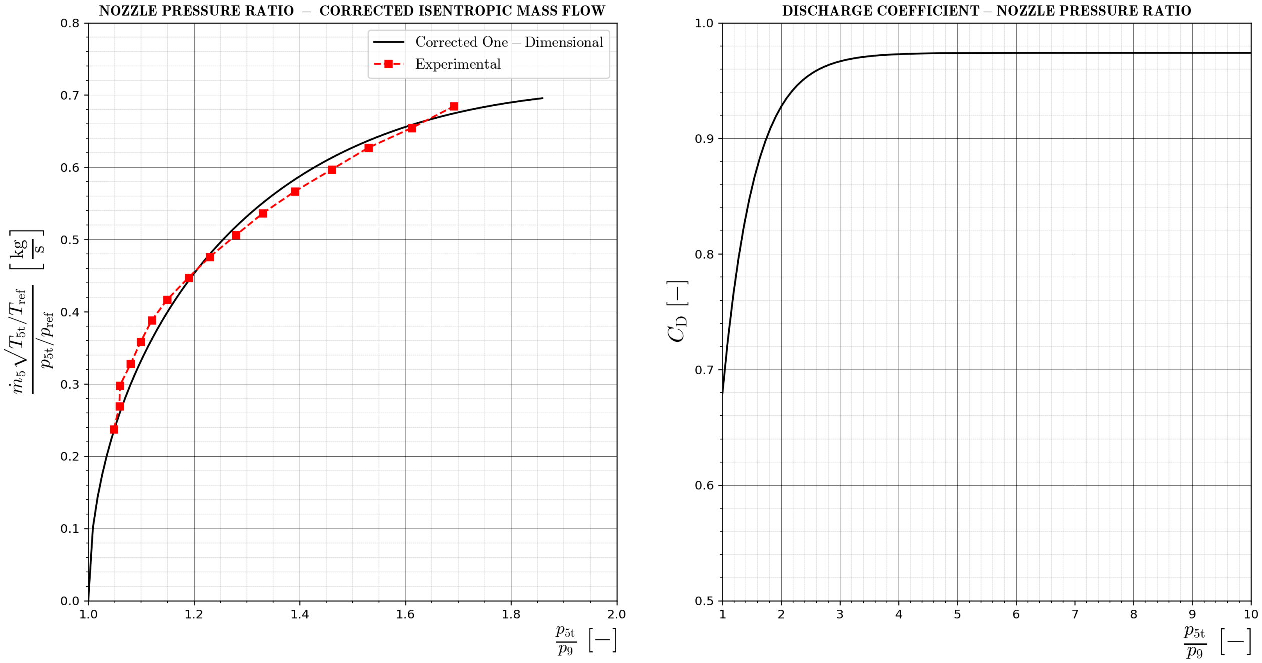

Figure 24: UPV Experimental [9] and Modeled Nozzle Corrected Mass Flow (left) and Discharge Coefficient (right) with Respect to NPR.

5. Generic Results

In this chapter, some results involving the modeling of a general single spool and dual spool engine will be shown. This will prove the validity of the code in various situations, as well as the adaptability to different turbojet typologies.

Comparison with analytical results will also be carried out here, as one of the main purposes of this study is contrasting the more elaborate results obtained employing performance maps with a simpler method, namely the analytical solution. As mentioned before, only the steady state analytical method of solution was presented here, so this comparison will only be present in the steady state results.

As there is no possibility of validating the method in some situations; in this case, for not having access to testing of engines of this kind, these following analyses will serve as a way of performing a test on the coherence of results, although its precision cannot be evaluated in this way.

For this purpose, scalable axial compressor and axial turbine maps obtained from commercial software (in particular *GSP*) will be fitted together to form the internal coupling. Recursively, they are adjusted to make their design point coincide. These maps are added to the code (in *.csv* format as before), read and interpolated through cubic splines, so the algorithms can access the maps as a function.

Solutions will be obtained for both steady state and transient state response, although, for convenience, many of the results obtained in steady state will not be reproduced in a transient scenario. This is because some properties, like characteristic curves, do not vary significantly from a steady to a transient state for the values of inertia considered. The parameters used for the following systems have been chosen to be similar, to compare the difference introduced by each one of them.

Steady state parametric studies are hereby carried out. They will focus on obtaining running lines for various flight Mach numbers and plotting characteristic curves for all kinds of considered systems, as well as stating the error between this solution and the analytically obtained method. Meanwhile, transient analyses will revolve around the engine's running line evolution and speed response curves, although the method allows to obtain more information about the evolution of the system.

When possible, the modification of some major engine features will be considered, like changing the nozzle type. This does not have a direct effect on running lines when the throat area is the same and the geometry is convergent while the nozzle is not critical. Thus, the obtained running line will be valid for both kinds of nozzle.

5.1 Single Spool Turbojet

For a single spool turbojet engine running lines and characteristic curves will be obtained, both for an engine equipping a convergent and a convergent-divergent nozzle. The nozzle throat are A_8 is common for both. The following parameters are the ones used in the simulations. The design parameters, denoted by a subscript d are sufficient to adjust the aforementioned performance maps:

Parameter	Value	Parameter	Value
T_{ref} [K]	288.15	$M_{0,\mathrm{d}}$ [-]	0.8
p_{ref} [bar]	1.01325	$\dot{m}^*_{0,\mathrm{d}}$ [kg/s]	80
$C_{\mathrm{p,c}}$ [J/kg/K]	1,004.5	$\pi_{\mathrm{C,d}}$ [-]	10.52
$C_{\mathrm{p,h}}$ [J/kg/K]	1,210.0	$\pi_{\mathrm{T,d}}$ [-]	2.45
R [J/kg/K]	287	$((\eta_{\mathrm{CC}} f L) / (C_{\mathrm{p,c}} T_0))_{\mathrm{d}}$ [-]	5.1216
γ_{c} [-]	1.4	b_3 [-]	0.05
γ_{h} [-]	1.309	$\zeta_{\mathrm{CC,c}}$ [-]	27
$N_{\mathrm{ref,C}}$ [rpm]	25,000	$\zeta_{\mathrm{CC,h}}$ [-]	2
$N_{\mathrm{ref,T}}$ [rpm]	10,833	A_8 [m^2]	0.1216
η_{D} [-]	0.98	μ [-]	0.5
η_{m} [-]	0.99	f [-]	0.025
η_{N} [-]	0.97		

Table 12: Properties for the Generic Single Spool Engine.

Note the inclusion of these design parameters, needed to scale the maps to the correct size. Reiterating, this can be done if the RNI of the turbomachinery is well over the cutoff RNI. Some constant bleed fractions have been included in the process to more accurately emulate real engine behavior, although it is assumed to be constant. It is not mentioned in Table 12, but no two-dimensional flow effects in the nozzle are considered, so $C_{\mathrm{D}} = 1$ in Equation 47.

A more complicated, although relatively simple for combustion chamber total pressure losses is implemented, shown in Equation 21 and whose coefficients are displayed in Table 12. The cooling effect before the turbine is also included with Equation 24. These are not included in the analytical solution, so their effect can be seen in following sections.

The nozzle throat area A_8 has been calculated to allow the running line in both compressor and turbine to cross the design point, allowing for a high-performance coupling of the system. As previously said, when considering a convergent-divergent nozzle, it is assumed to always be adapted to outside pressure (Equation 61), changing the area ratio to comply with this condition.

5.1.1 Steady State

Steady state results for a single spool engine are hereby presented. All parameters in Table 12 allow for a steady state representation, if the scalable compressor and turbine maps are known beforehand.

Operating Lines

First off, the corresponding engine operating lines (also called running lines in this document) are plotted for different values of the flight Mach number. See Figure 25.

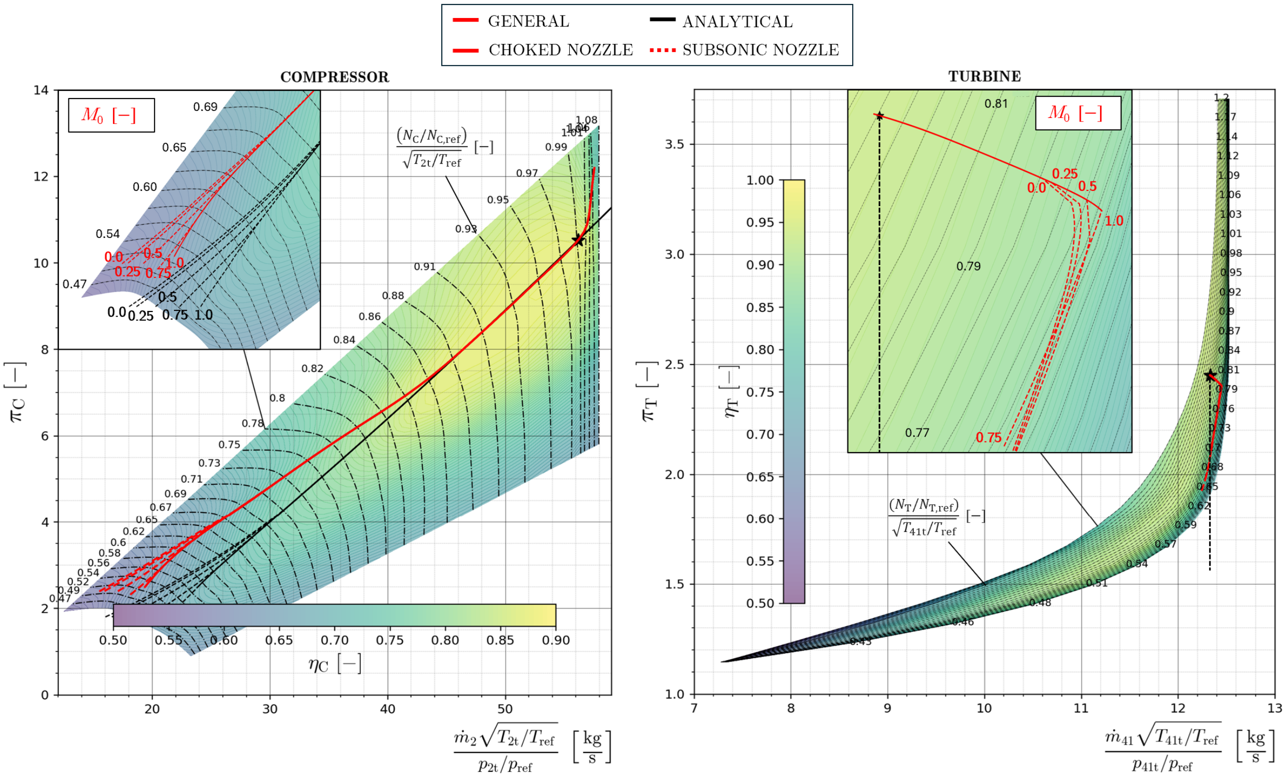

Figure 25: Operating Lines in a Single Spool Engine Estimated with the General (red) and Analytical Solution (black) for Different Values of Flight Mach Number. Compressor (left) and Turbine (right).

Note how the running lines in the compressor have been fitted to transit the performance map's high efficiency region, which is to be expected in the coupling design step. The analytical solution is a good linearization of the compressor operating line near the design point, after assuming a constant corrected mass flow in the turbine. This can be seen in Figure 25, as the pressure ratio when the nozzle is not critical (dashed line) is variable, while the turbine inlet corrected mass flow is assumed to be constant.

The importance of carrying more accurate analyses can also be seen here. Applying a more precise model has predicted that the running lines in the compressor are closer to the surge line than using an analytic approach. The operating lines for different Mach numbers do not differ by much between them in this setup, nonetheless, the nozzle chokes in noticeably different operating points.

Characteristic Curves

Steady state characteristic curves are plotted. Dashed lines indicate a non-critical nozzle.

- **Convergent Nozzle**

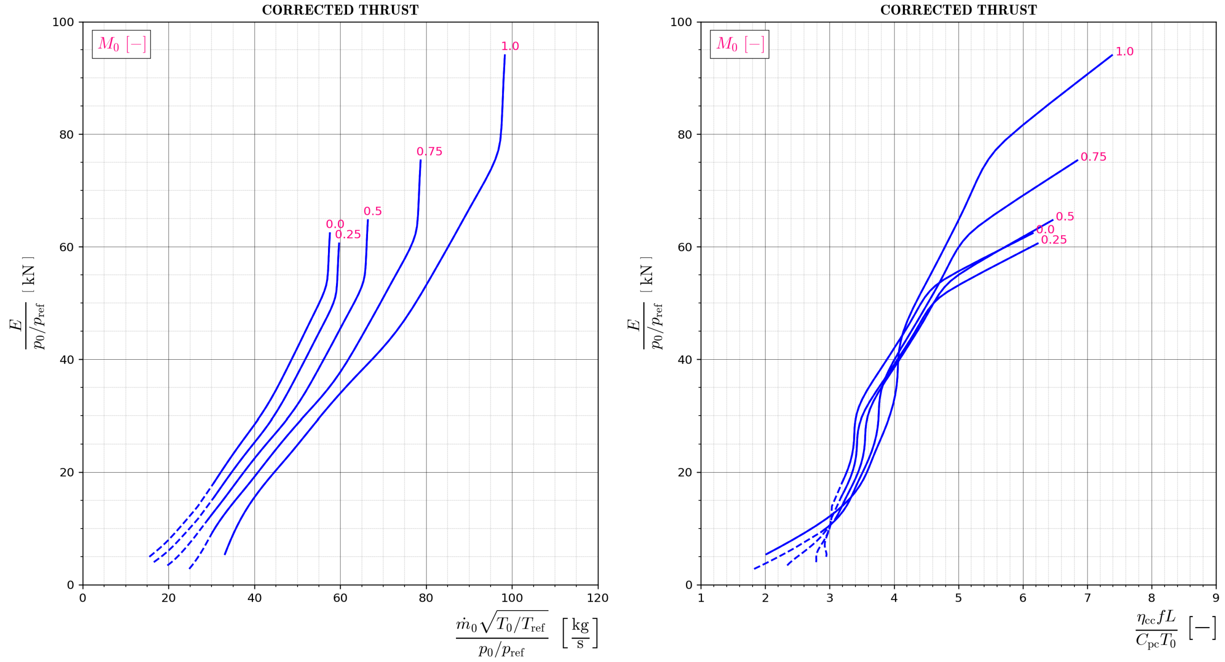

Figure 26: Single Spool Corrected Thrust vs. Inlet Corrected Mass Flow (left) and Fuel Parameter (right). Convergent Nozzle.

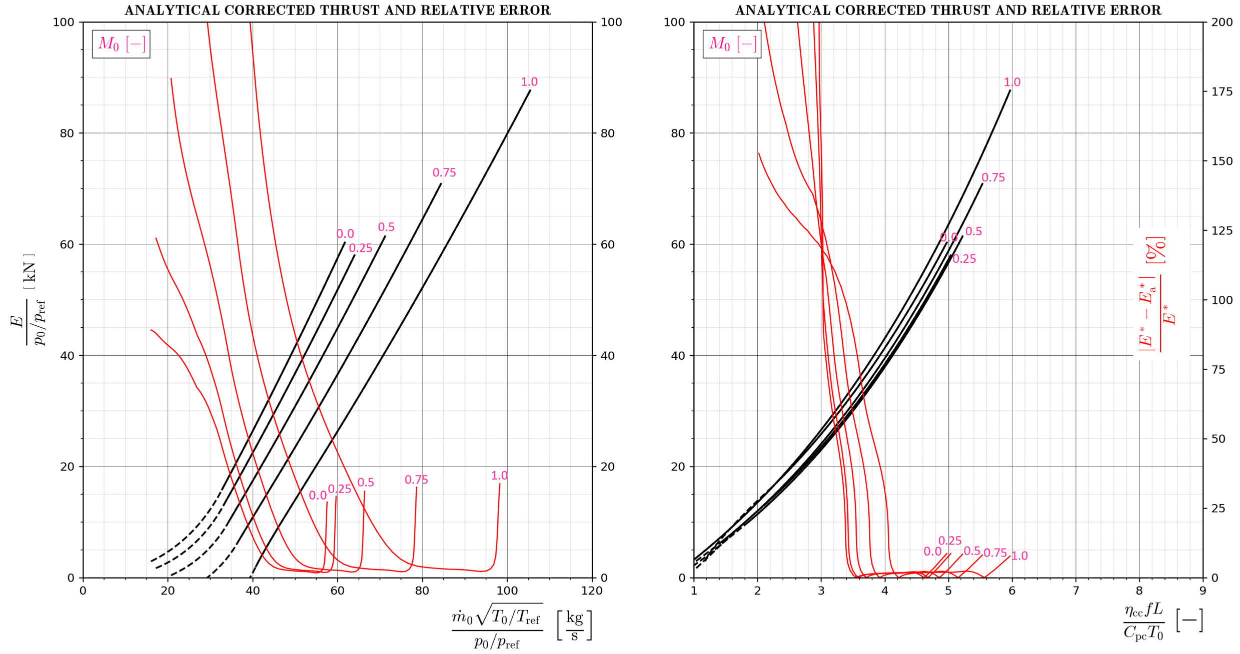

Figure 27: Single Spool Analytical Corrected Thrust vs. Inlet Corrected Mass Flow (left) and Fuel Parameter (right) Including Error to General Solution. Convergent Nozzle.

Corrected thrust has a region where it is almost independent of flight Mach number when plotted against fuel parameter (all curves collapse). Next up, specific impulse is represented. Note that it tends to be higher the lower the Mach number is.

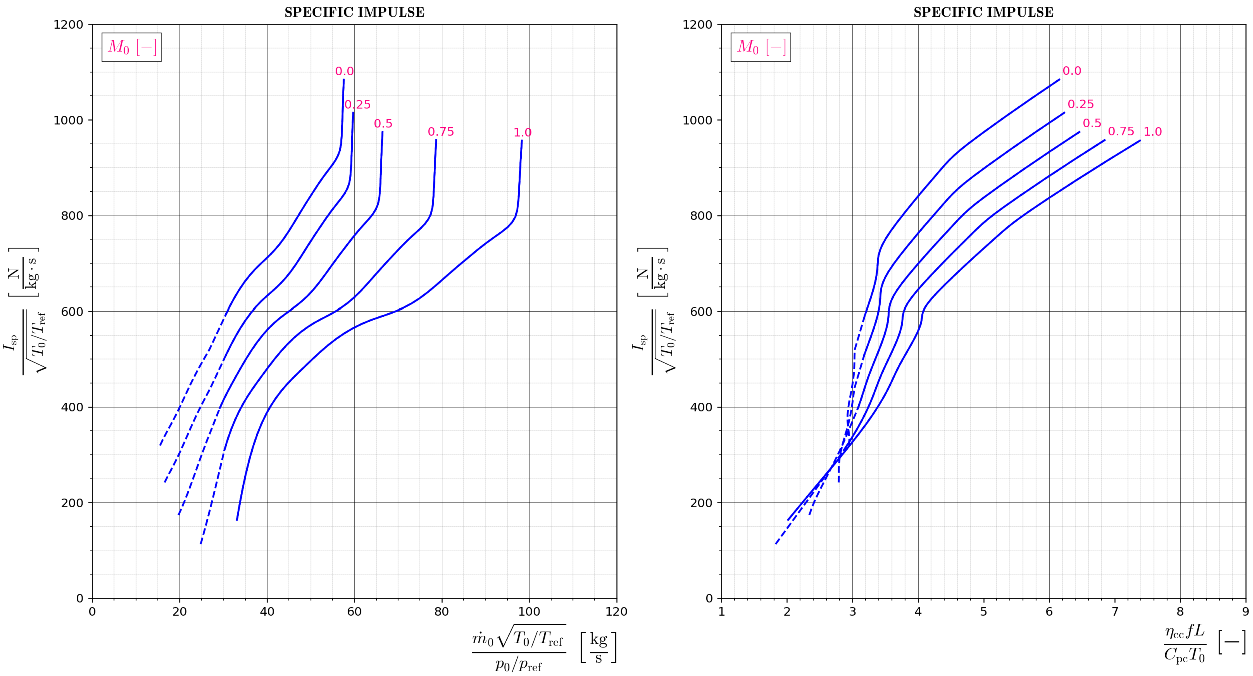

Figure 28: Single Spool Corrected Specific Impulse vs. Inlet Corrected Mass Flow (left) and Fuel Parameter (right). Convergent Nozzle.

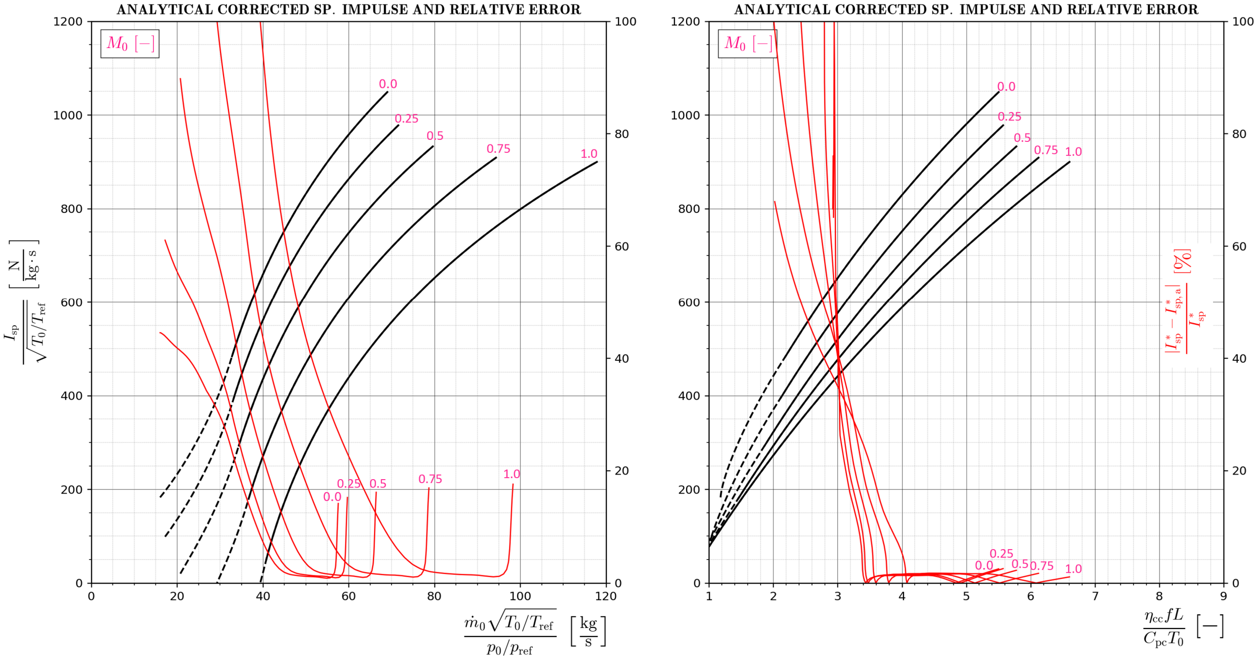

Figure 29: Single Spool Analytical Corrected Specific Impulse vs. Inlet Corrected Mass Flow (left) and Fuel Parameter (right) Including Error to General Solution. Convergent Nozzle.

Corrected TSFC is also sensitive to the Mach number and is closely related to overall performance. Notice how this engine efficiency decreases (high TSFC) for a high M_0, especially far away from the design conditions.

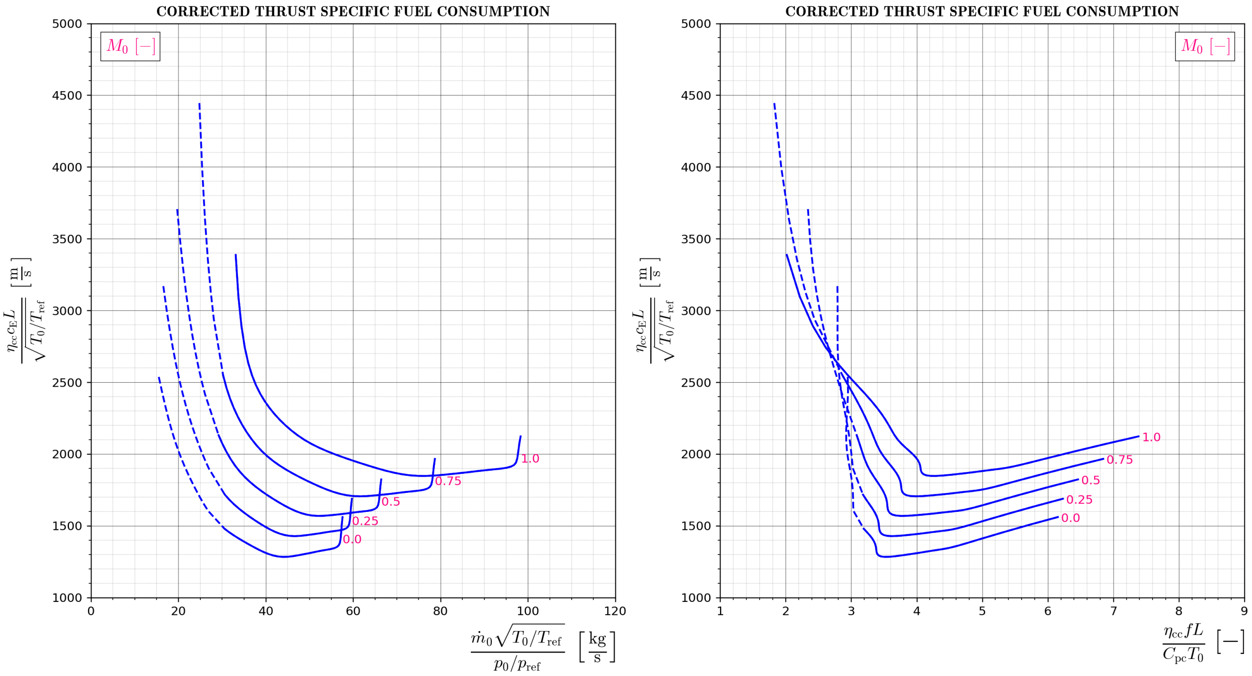

Figure 30: Single Spool Corrected TSFC vs. Inlet Corrected Mass Flow (left) and Fuel Parameter (right). Convergent Nozzle.

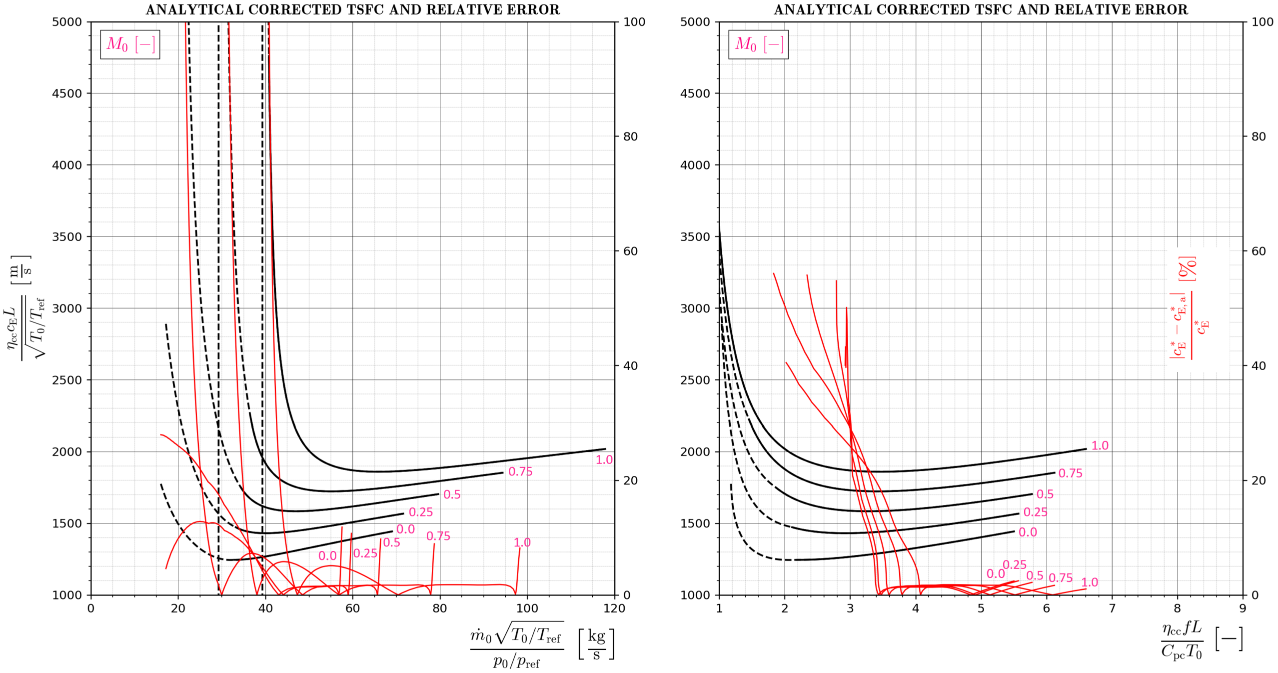

Figure 31: Single Spool Analytical Corrected TSFC vs. Inlet Corrected Mass Flow (left) and Fuel Parameter (right) Including Error to General Solution. Convergent Nozzle.

Engine corrected speed and inlet mass flow curves also tend to collapse to a single line when plotted against fuel parameter and Mach number. In this case, static and maximum temperature ratio across the engine has a linear trend. It is not the case of static pressure ratio and OPR.

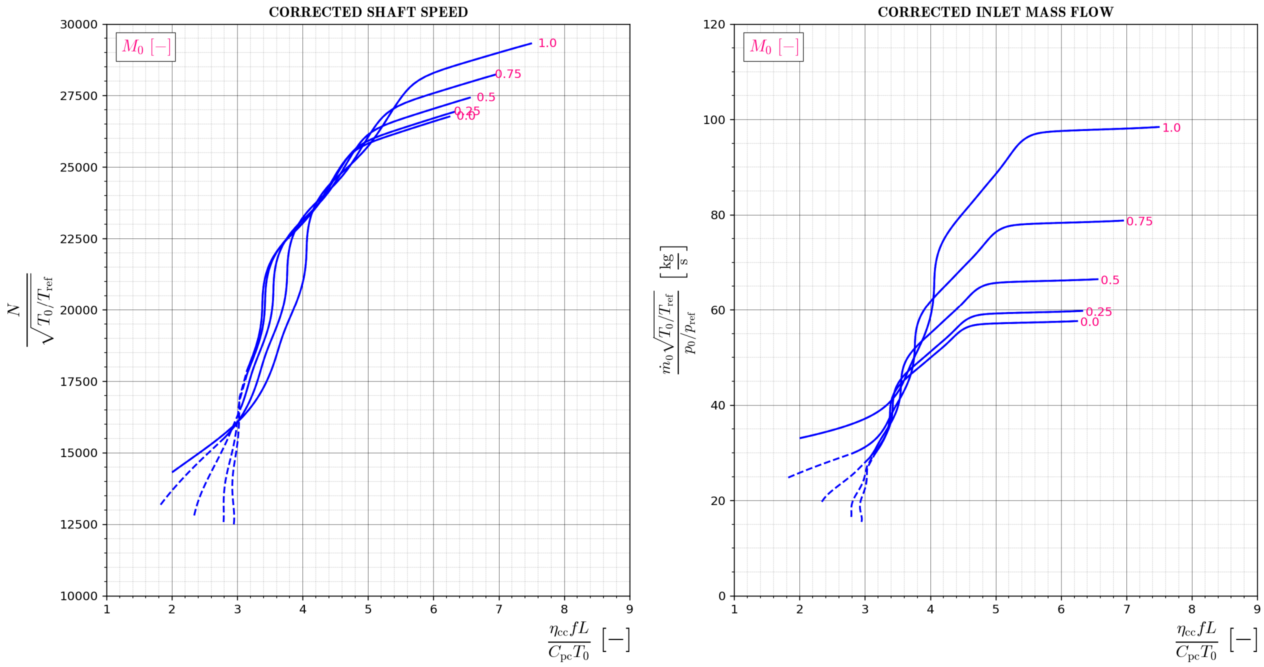

Figure 32: Single Spool Corrected Shaft Speed (left) and Inlet Corrected Mass Flow (right) vs. Fuel Parameter.

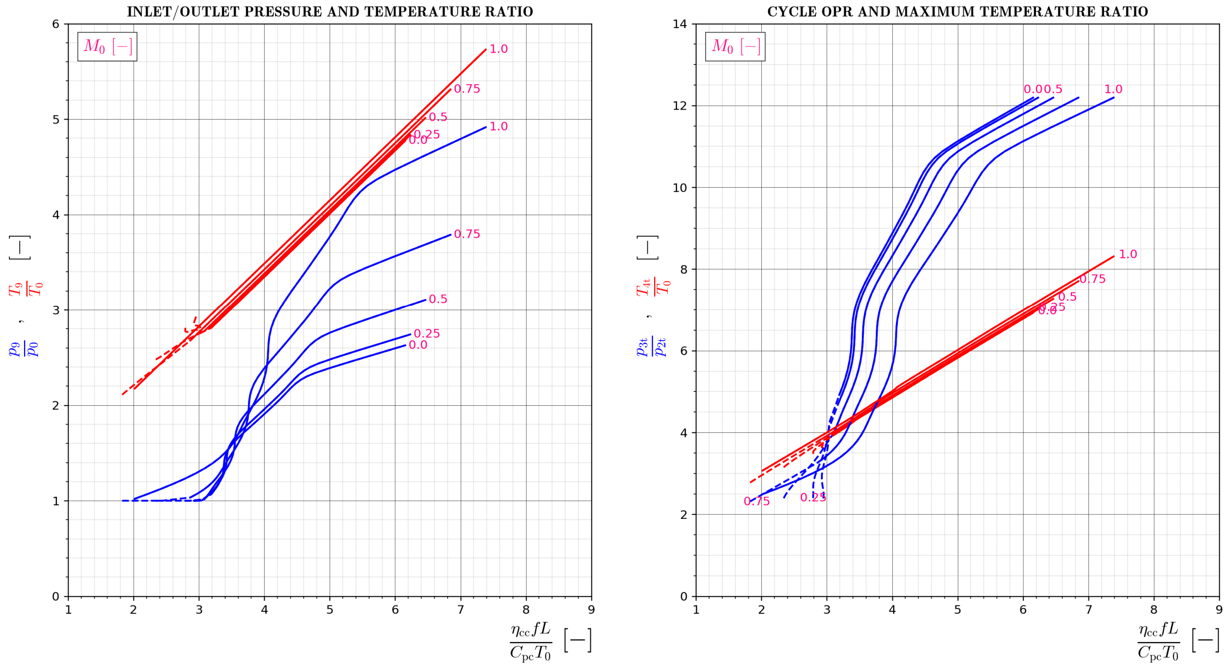

Figure 33: Single Spool Static Temperature and Pressure Ratio (left) and Maximum Temperature Ratio and OPR (right) vs. Fuel Parameter. Convergent Nozzle.

- **Convergent-Divergent Nozzle**

  The obtained results for a convergent-divergent nozzle are similar in trend as those plotted before. Some curves relating the internal coupling even coincide, as the same A_8 has been considered in both cases. See corrected thrust first:

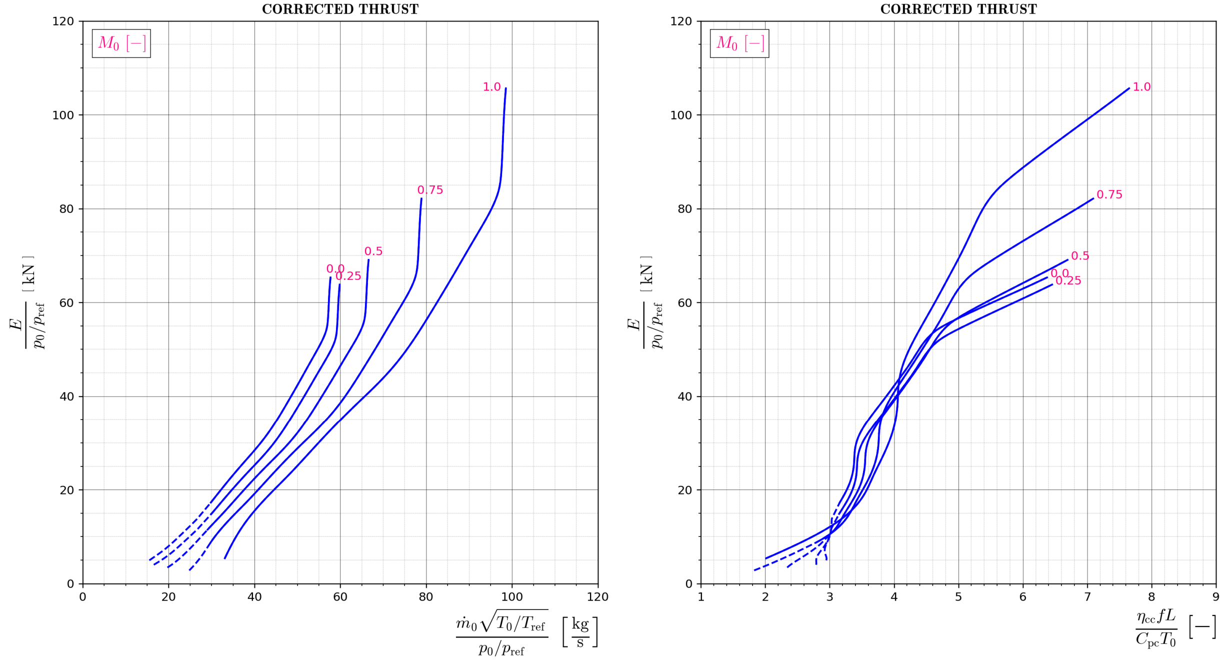

Figure 34: Single Spool Corrected Thrust vs. Inlet Corrected Mass Flow (left) and Fuel Parameter (right). Convergent-Divergent Nozzle.

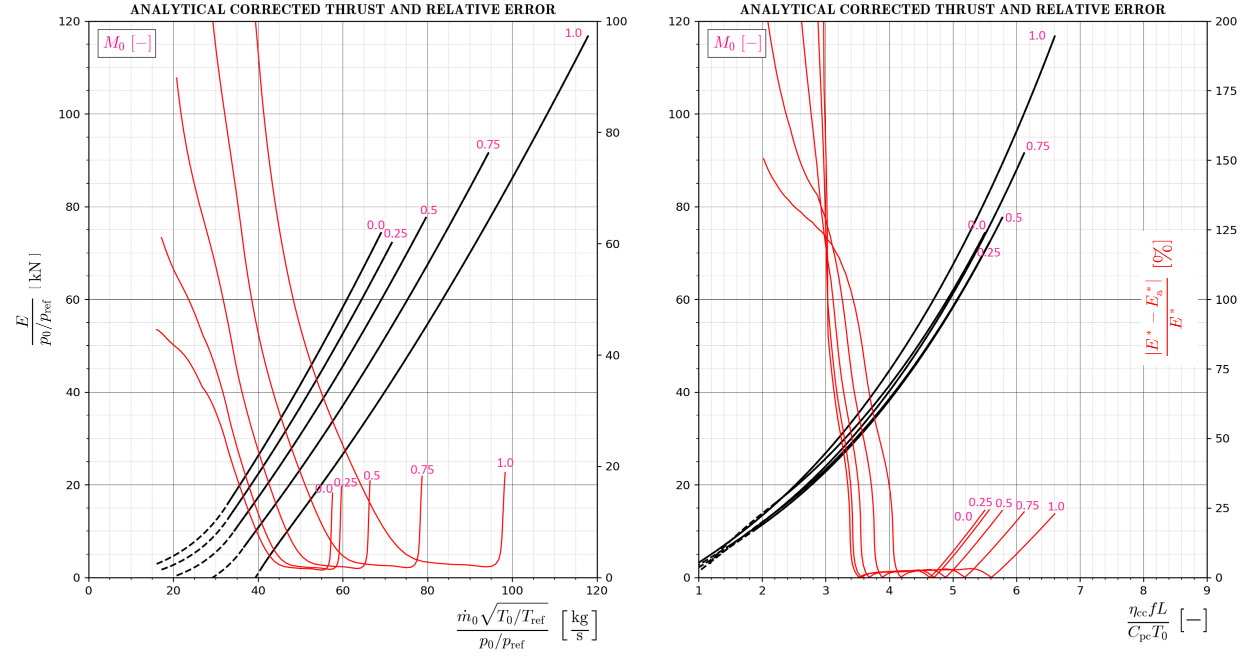

Figure 35: Single Spool Analytical Corrected Thrust vs. Inlet Corrected Mass Flow (left) and Fuel Parameter (right) Including Error to General Solution. Convergent-Divergent Nozzle.

Corrected specific impulse is generally higher after fitting a convergent-divergent segment, and so is corrected thrust. This means that adapting the nozzle to outside conditions improves engine efficiency.

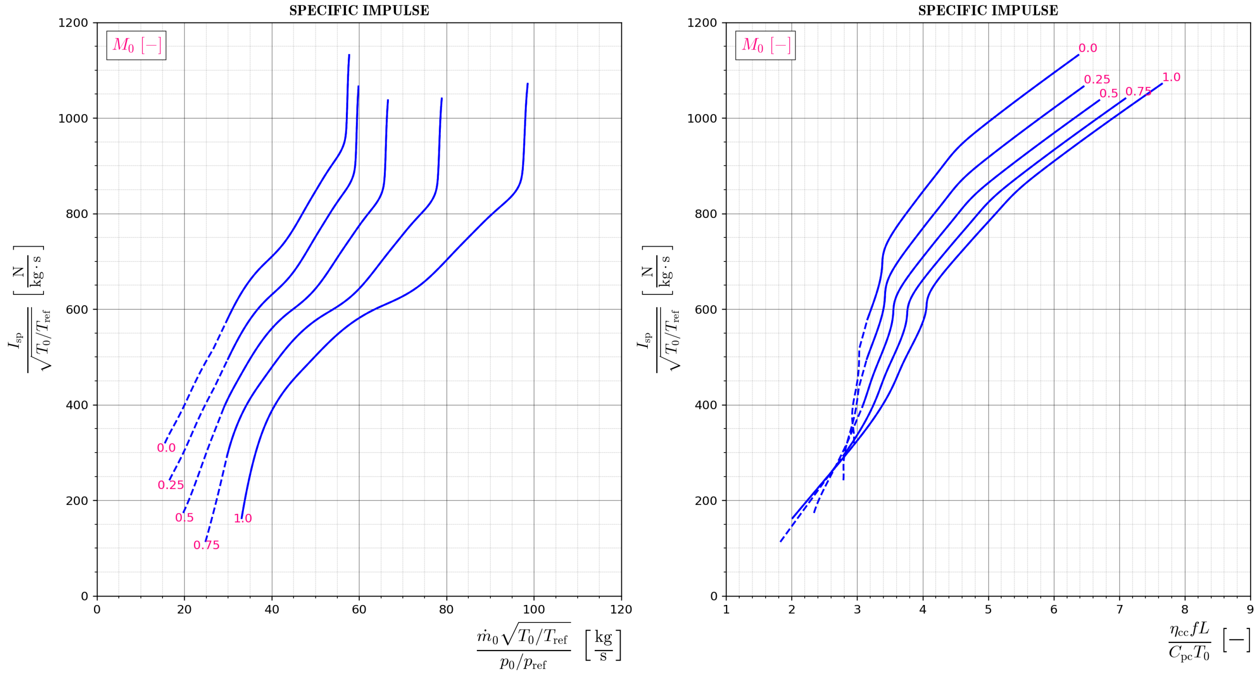

Figure 36: Single Spool Corrected Specific Impulse vs. Inlet Corrected Mass Flow (left) and Fuel Parameter (right). Convergent-Divergent Nozzle.

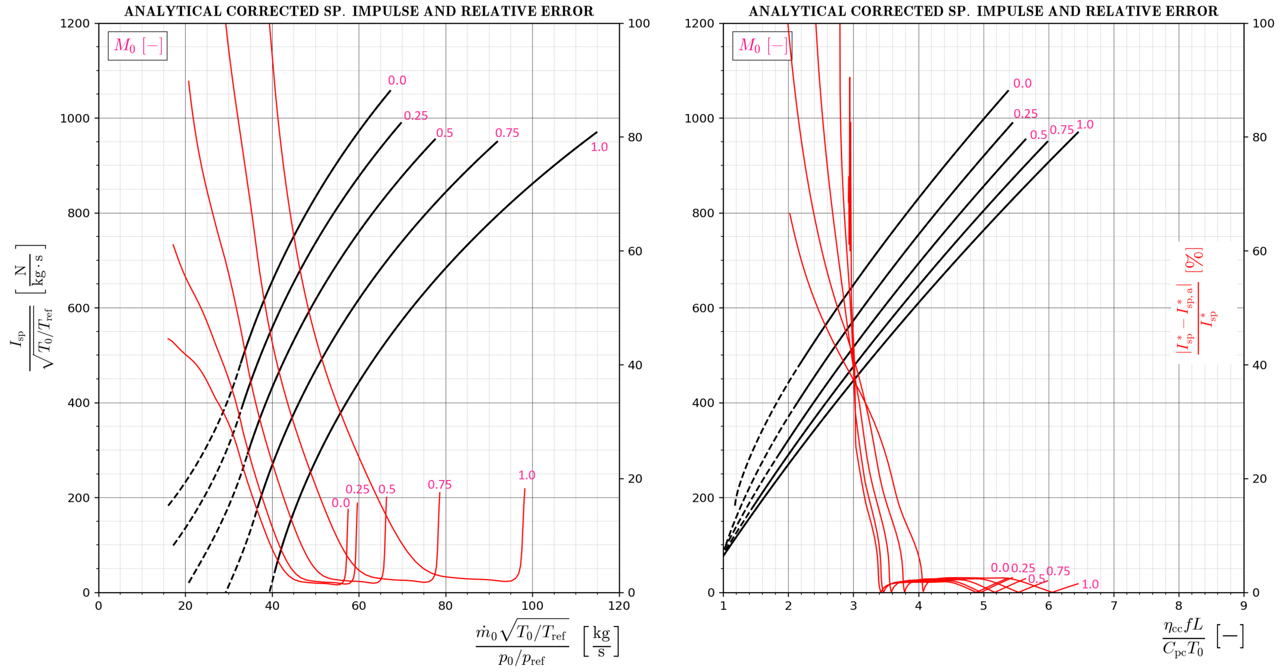

Figure 37: Single Spool Analytical Corrected Specific Impulse vs. Inlet Corrected Mass Flow (left) and Fuel Parameter (right) Including Error to General Solution. Convergent-Divergent Nozzle.

This general improvement in efficiency can be seen after comparing Figure 30 and 38, as well as Figure 31 and 39.

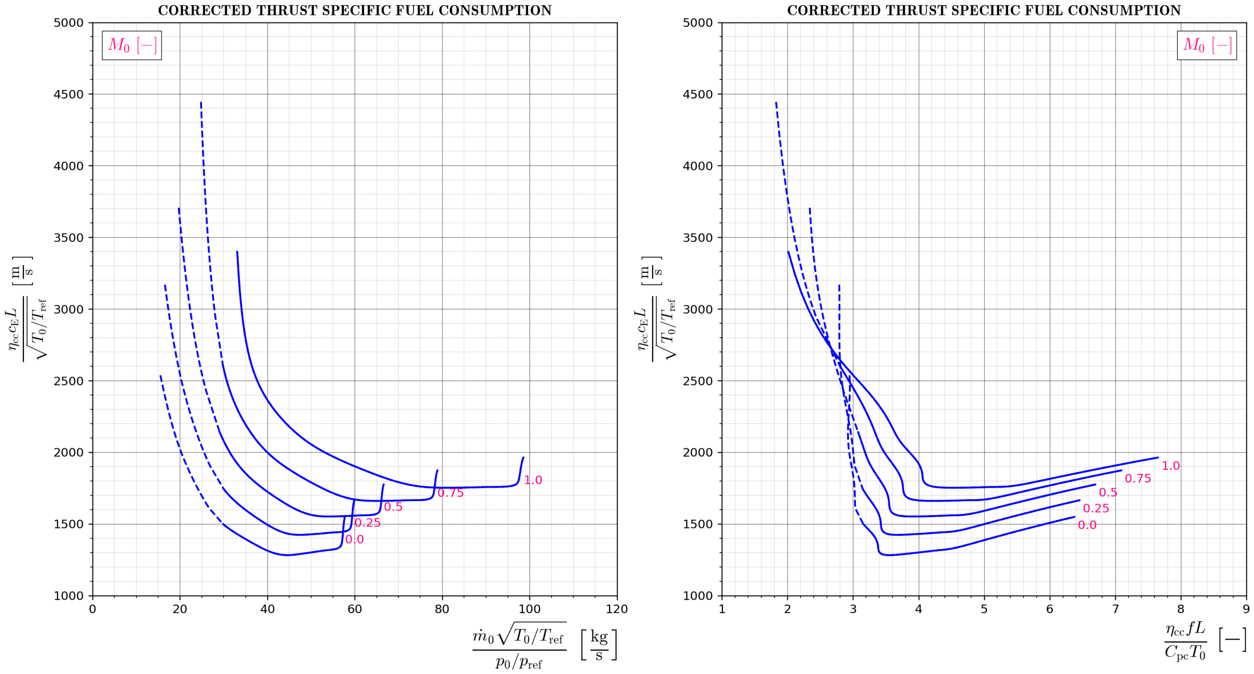

Figure 38: Single Spool Corrected TSFC vs. Inlet Corrected Mass Flow (left) and Fuel Parameter (right). Convergent-Divergent Nozzle.

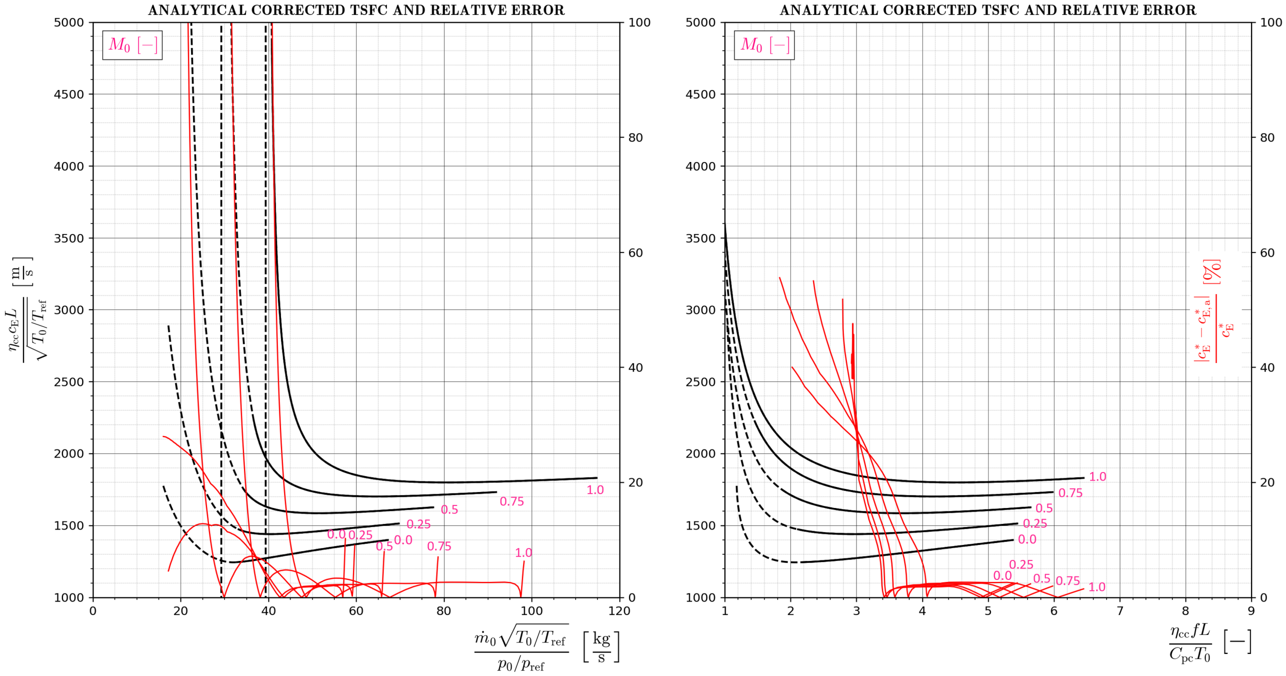

Figure 39: Single Spool Analytical Corrected TSFC vs. Inlet Corrected Mass Flow (left) and Fuel Parameter (right) Including Error to General Solution. Convergent-Divergent Nozzle.

Next up, due to the nature of the nozzle, it is interesting to plot the outlet Mach number M_9 at the exit, as well as the applied area law. Note the surprising capability of the analytical solution to predict this nozzle area ratio with a low error.

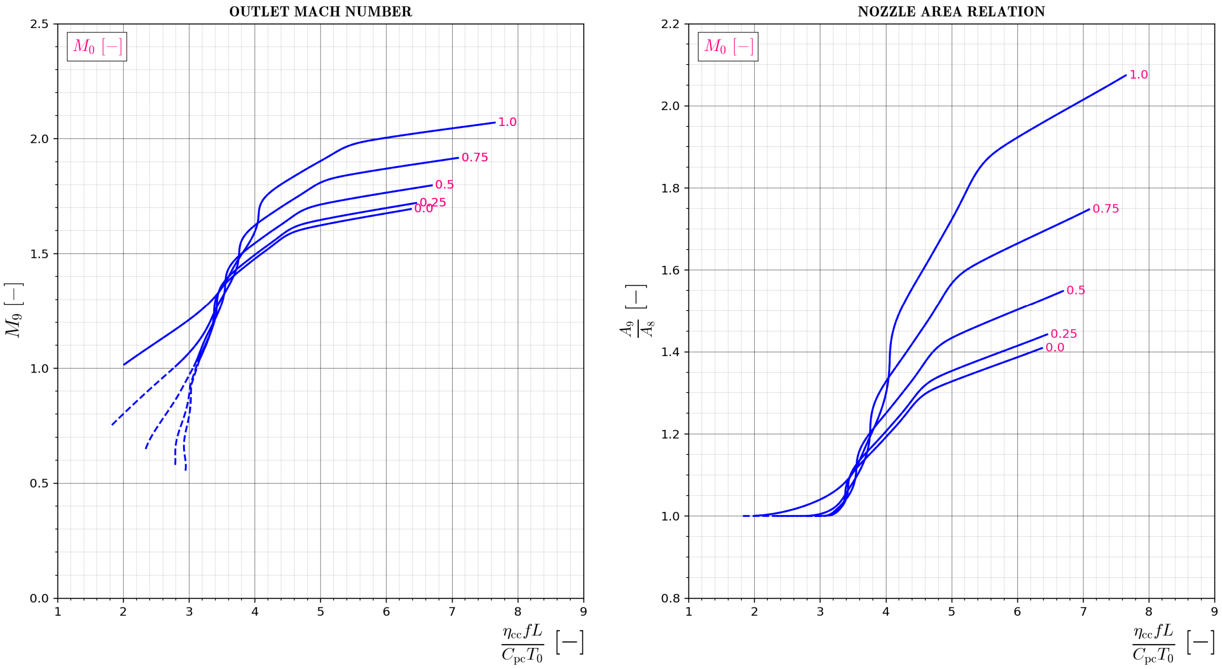

Figure 40: Single Spool Outlet Mach Number (left) and Nozzle Area Ratio (right) vs. Fuel Parameter.

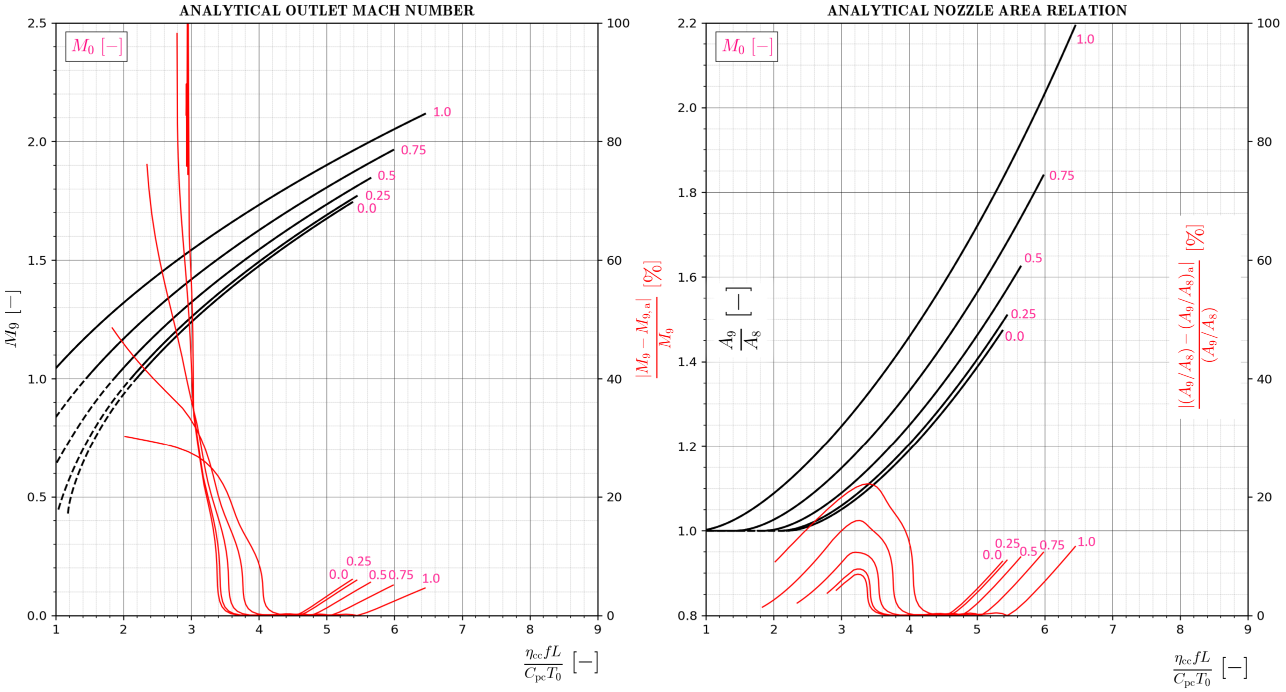

Figure 41: Single Spool Analytical Outlet Mach Number (left) and Nozzle Area Ratio (right) vs. Fuel Parameter Including Error to General Solution.

Finally, outlet thermodynamic properties, OPR and maximum temperature ratio are represented. The static temperature ratio no longer remains quasi-linear, as in Figure 33. Now $p_9/p_0 = 1$, as opposed to Figure 42.

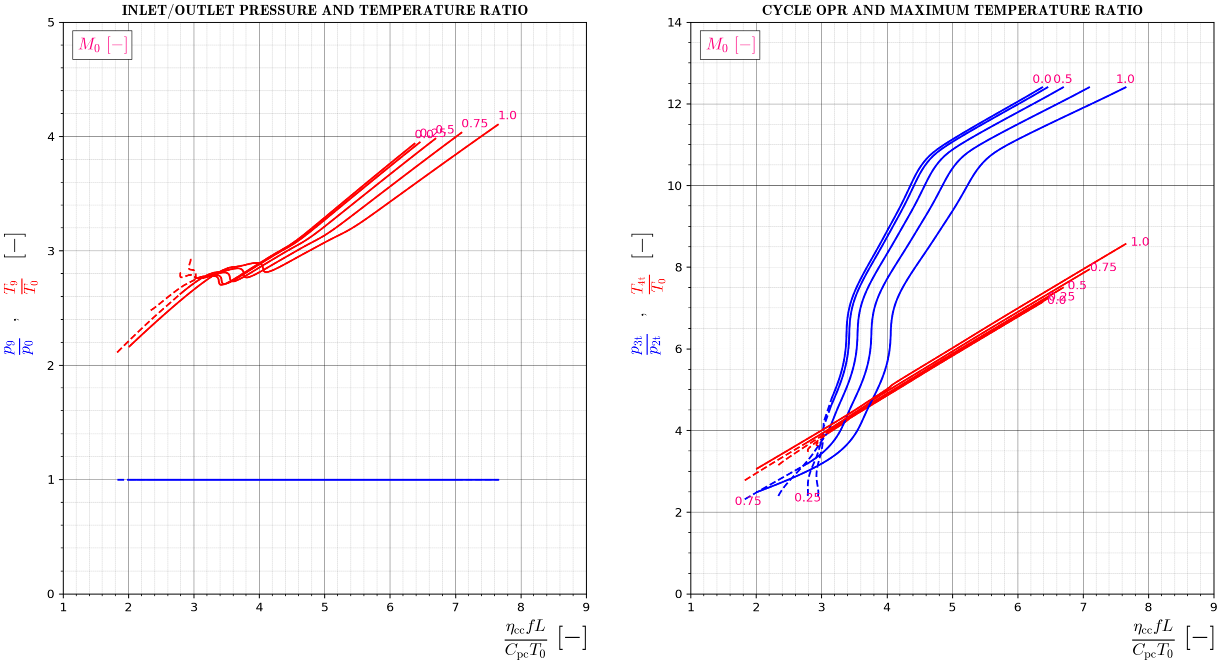

Figure 42: Single Spool Static Temperature and Pressure Ratio (left) and Maximum Temperature Ratio and OPR (right) vs. Fuel Parameter. Convergent-Divergent Nozzle.

Corrected shaft speed and corrected inlet mass flow curves do not change from those value shown in Figure 32 after considering a convergent-divergent nozzle with the same throat area A_8, that allows for the running line to pass through the engine's design point.

A general trend after comparing these curves with the ones obtained by means of the analytical solution is that the error is lower near regions close to the design point. This confirms what is to be expected, as it is a linearization of the conditions near this point.

Moreover, fitting a convergent-divergent nozzle improves some figures of merit like the corrected specific impulse and TSFC, while allowing to generate a bigger amount of thrust. However, the shown characteristic curves and their trends are similar.

This is why many times it is not economically viable to fit a variable area convergent-divergent nozzle in commercial aircraft. The improvement in efficiency and generation of thrust is not notable enough when the NPR near the design point is not high. Some authors [2] state that, as a heuristic rule, manufacturers implement them when the design NPR is greater than 5. In contrast, one-dimensional flow choking happens at a value of around 1.86, depending on the nozzle isentropic efficiency and gas properties at the exit.

These curves also serve their purpose in safe design of the engine. Maximum temperature ratio and OPR in steady state can be estimated, thus allowing to tune the control system adequately to permanently avoid this operating points. Also, steady state surge margin can be calculated (see Figure 25).

5.1.2 Transient State

A simple transient state analysis is also executed to prove the validity of the created solver. For this, the same component equations and parameters that have been stated in Table 12 are used in the method, with the addition of other necessary values to carry out this analysis of the system.

These additional values are gathered in Table 13. The time step Δt and number of points N_{p} chosen in the discretization make the total time of the simulation to be 30 s. The corrected inertia is chosen to be a generic value.

Parameter	**Value**
I^* [kgm^2]	0.935
N_{p} [-]	200
Δt [s]	0.15

Table 13: Additional Values for the Single Spool Transient Simulation.

In this transient state several cases will be studied. To better represent both acceleration and deceleration, *slam* fuel parameter inputs are taken to be the input to the model's forcing term. *Slam* will from now on refer to a sudden input of fuel, followed by a period of stabilization where a quasi-steady state is awaited, to then input a sudden deceleration with a steep reduction of this fuel parameter.

For this purpose, 4 different cases will be studied, both with different corrected speed initial conditions and flight Mach number, so the corrected speed response to the input and the running lines can be evaluated after it. They are gathered in Table 14.

Parameter	**Case 1**	**Case 2**	**Case 3**	**Case 4**
M_0 [-]	0	0.5	0.8	1
$^0\left(N^*_{\mathrm{C}}\right)$ [-]	0.65	0.7	0.7	0.65

Table 14: Different Cases Considered for the Single Spool Transient Simulations.

The fuel parameter inputs will be shown as a plot to facilitate the understanding of the fuel input, and will also be considered to happen in all cases from the initial condition steady state fuel parameter $^0\left(\left(\eta_{\mathrm{CC}} f L\right) / \left(C_{\mathrm{p,c}} T_0\right)\right)$ to the engine design point fuel parameter (stated as $\left(\left(\eta_{\mathrm{CC}} f L\right) / \left(C_{\mathrm{p,c}} T_0\right)_{\mathrm{d}}\right)$ in Table 12) to return back to the first one after achieving a quasi-steady state of the system.

Operating lines and shaft speed evolution curves will both be plotted next to each other for a better visualization, and time will be superposed to the transient running lines. Nonetheless, no transient characteristic plots have been deemed to be useful enough to be shown here, as they tend to almost coincide with steady state curves unless the model inertia is notably low. The time discretization is, as commented before, a forward Euler method.

- **Case 1**

  Notice the presence of bistable points, after the *slam* input in fuel parameter the corrected speed does not return to its initial value. This is due to the possibility of various points having the same FAR.

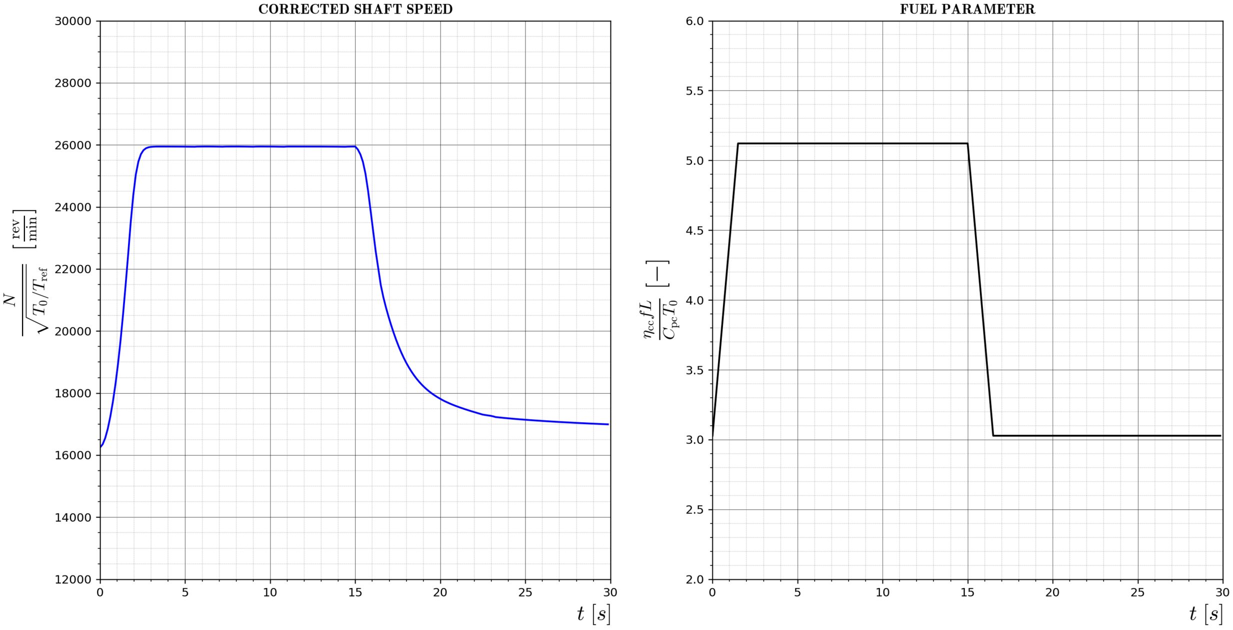

Figure 43: Case 1. Corrected Speed (left) and Input Fuel Parameter (right) in a Single Spool Engine Transient Simulation.

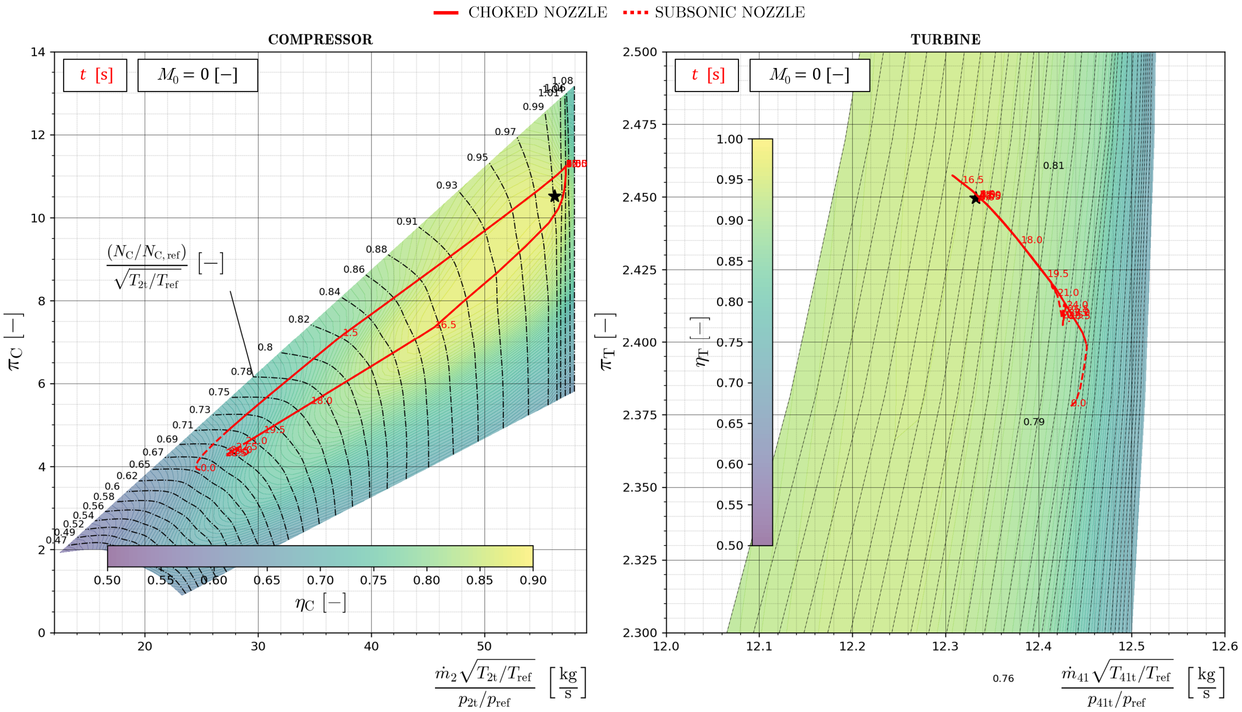

Figure 44: Case 1. Operating Lines in a Single Spool Engine Transient Simulation.

- **Case 2**

  This point bistability is an uncommon feature. In Case 2 this does not happen, and the corrected speed returns to the initial value after the *slam* input.

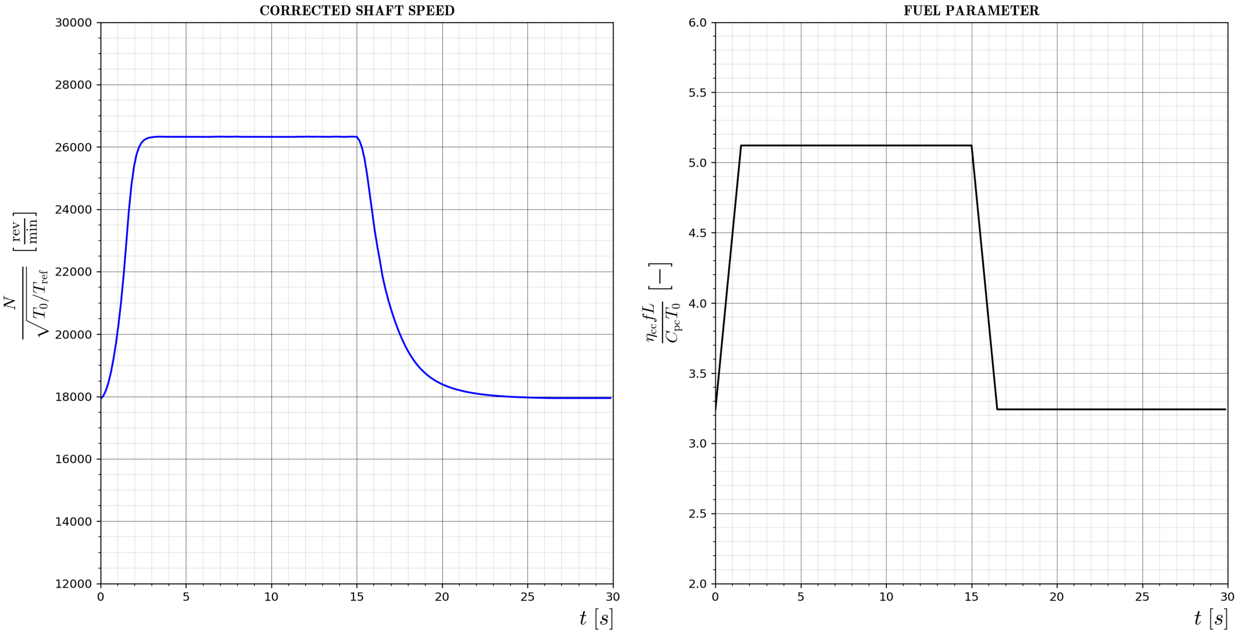

Figure 45: Case 2. Corrected Speed (left) and Input Fuel Parameter (right) in a Single Spool Engine Transient Simulation.

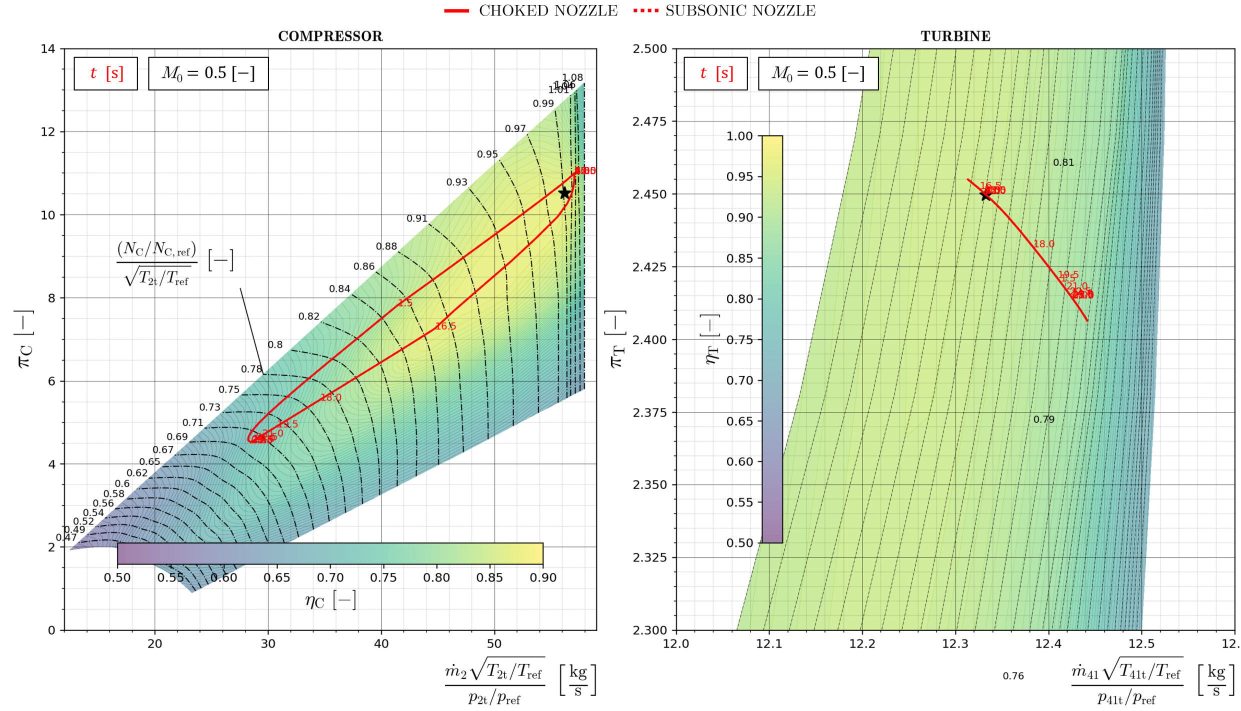

Figure 46: Case 2. Operating Lines in a Single Spool Engine Transient Simulation.

- **Case 3**

  Case 3 behaves almost the same as Case 2, this time the running line is farther from the surge line. The turbine running line in these cases almost coincides with the one calculated in steady state.

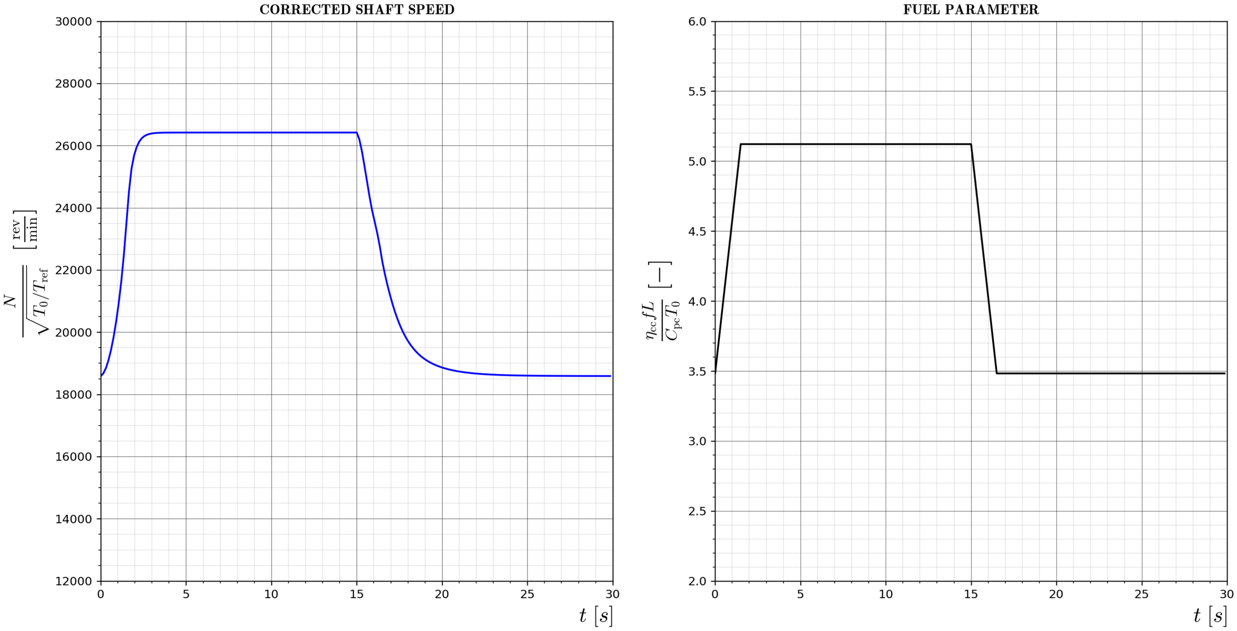

Figure 47: Case 3. Corrected Speed (left) and Input Fuel Parameter (right) in a Single Spool Engine Transient Simulation.

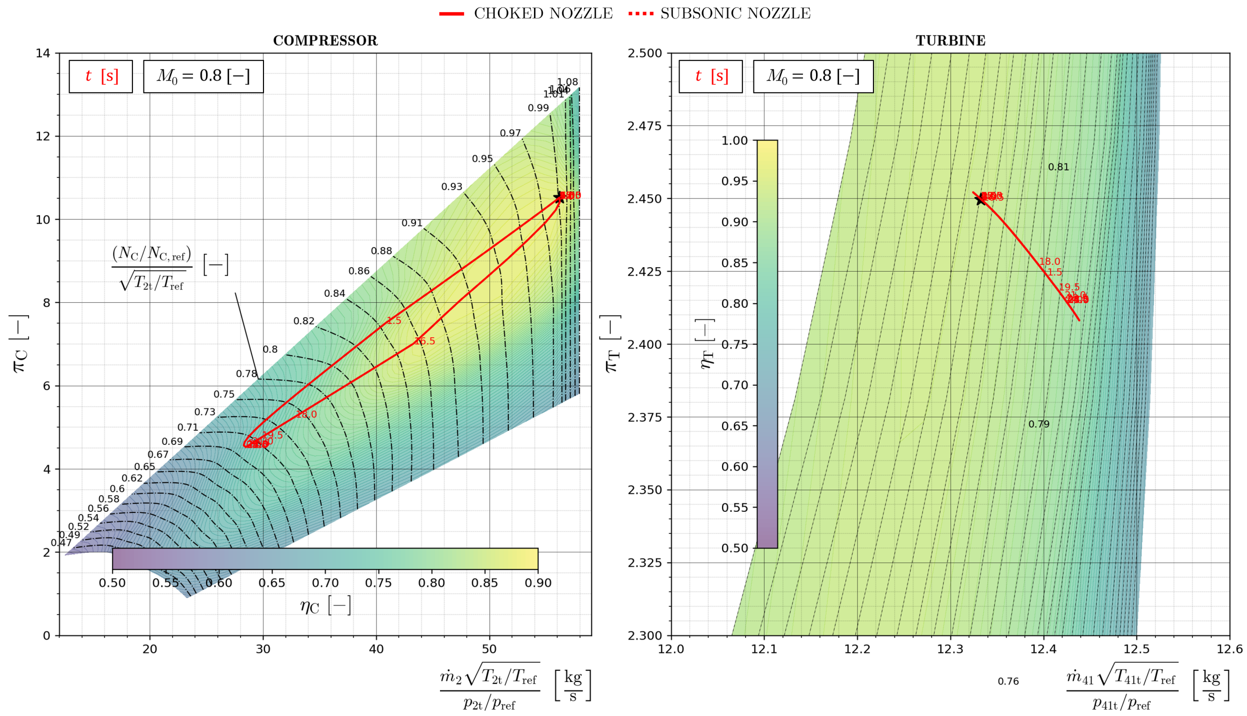

Figure 48: Case 3. Operating Lines in a Single Spool Engine Transient Simulation.

- **Case 4**

This final case also features and overdamped response on the system's corrected shaft speed. This does not mean that some harming effects could eventually appear. Because of the maximum imposed fuel parameter, the design point is now not reached.

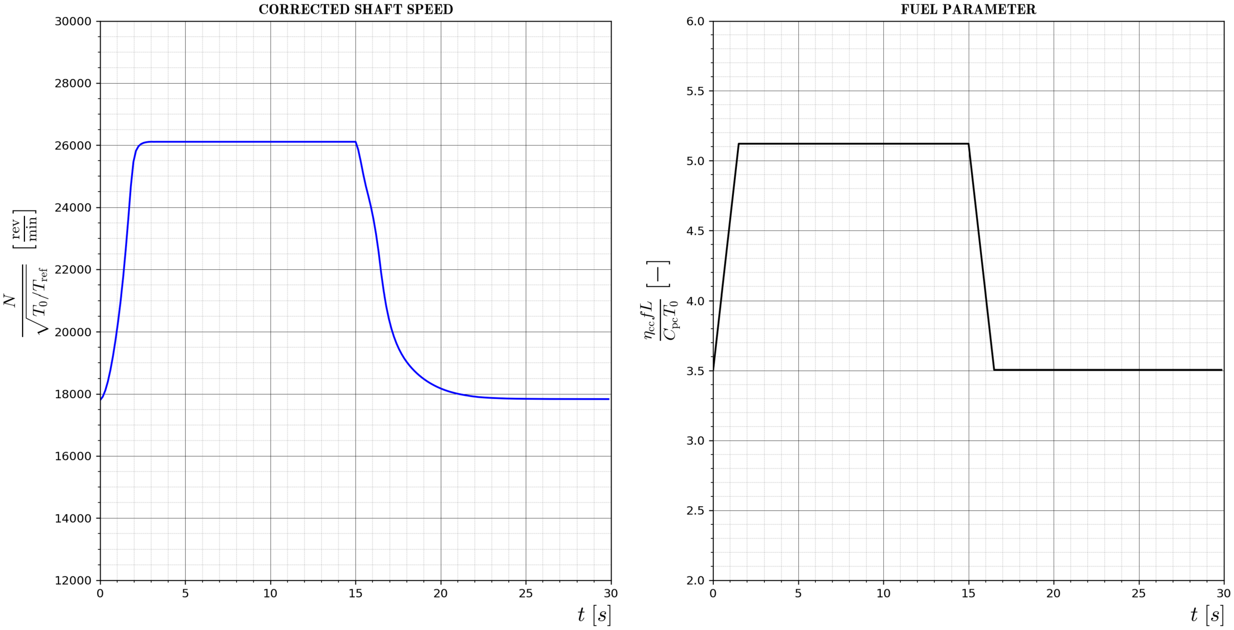

Figure 49: Case 4. Corrected Speed (left) and Input Fuel Parameter (right) in a Single Spool Engine Transient Simulation.

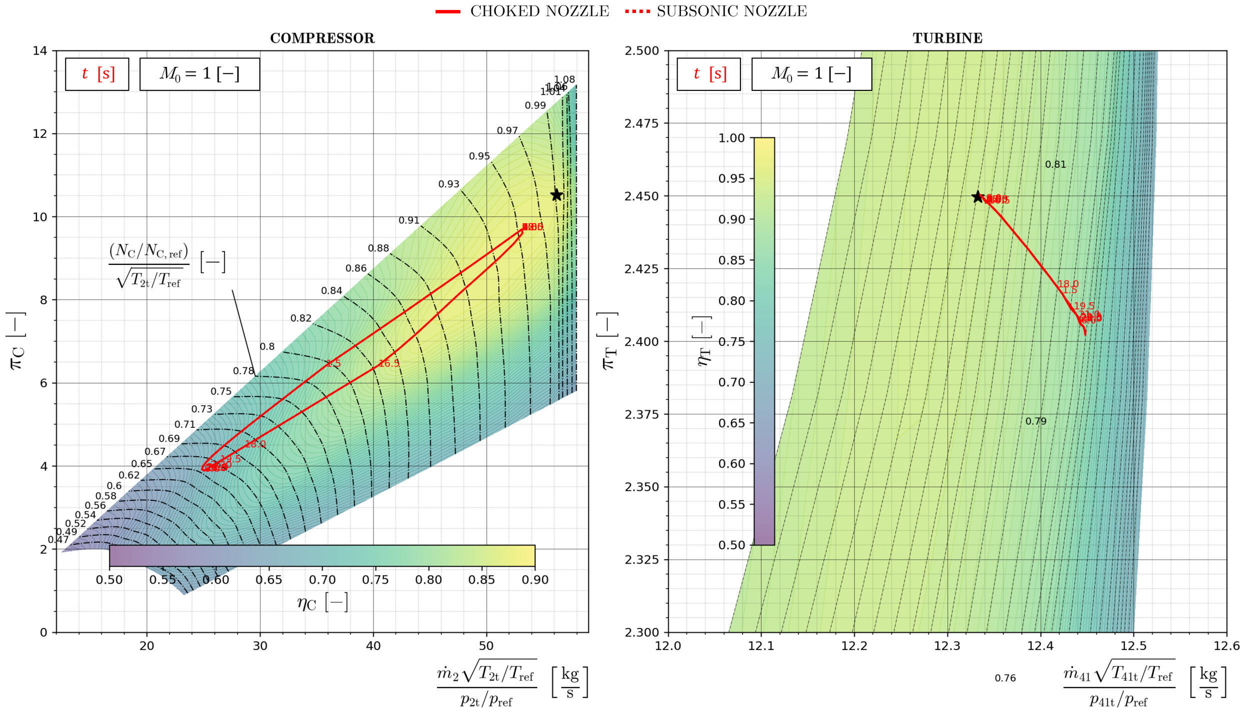

Figure 50: Case 4. Operating Lines in a Single Spool Engine Transient Simulation.

Notice how the formulated transient solver is capable of representing effects that are expected to be observed in the unsteady behavior of single spool turbojet engines. The running lines in transient simulations do not coincide with the steady state ones. This can cause, as profusely mentioned in past sections, the incursion of the operating point in aerodynamically unstable regions in the compressor map, or even cause surge and combustion chamber flame blowout, among others.

Observe how the running lines in these types of engines tend to have a reduced surge margin during acceleration and get closer to the compressor's choke line in deceleration. This is, however, not the case when analyzing dynamics in the LPC and HPC of dual spool engines. These trends will be detailed in forthcoming chapters.

The first studied cases are set to start at a low Mach number to force the nozzle not to be critical during low engine loading stages, that is, in low-valued corrected speed regions of the map. The trend that the running line engages in when accelerating is influenced by the choking of the nozzle, as can be seen when comparing Figure 44 and 46. However, this trend is more influenced by the fact of having a broader difference in the maximum and minimum of the input fuel parameter. Nonetheless, the mechanisms introduced by the nozzle must be taken into account.

An interesting phenomenon can be observed in the evolution of the speed in Figure 43, as well as in Figure 44. Imposing a fuel parameter value is closely related to determining the engine's FAR, rather than setting a value for raw fuel mass flow. This is due to the fact that, apart from f, the rest of the terms that form the fuel parameter $(\eta_{\mathrm{CC}} f L)/(C_{\mathrm{p,c}} T_0)$ can approximately be considered to be constant throughout a maneuver of this kind. When the steady state is reached after an deceleration, it does not return to the initial operating point, albeit it would be expected to do so.

It is clear that controlling the engine through the FAR can lead to bistable points. This behavior is also seen in the characteristic curves. See Figure 32, for example, where the corrected shaft speed function is non-injective with respect to this fuel parameter for a low flight Mach number and low loading regions. More than one value of corrected speed can be achieved through the same fuel parameter, while the transient state dynamics determine how the system will settle down in the steady state.

When considering a high Mach number, the nozzle tends to be choked for the most part of the operation. This leads to the running lines in the turbines concentrating even more around the engine's design point (see Figure 48 and 50). The calculated evolution of the turbine running lines raises strong arguments in favor of the validity of the choked turbine hypothesis made in the analytical solution. In fact, when the nozzle is not choked, the turbine pressure ratio changes significantly more than when it is. This is a feature of the analytical solution, as the total temperature and pressure ratios across the turbine are deemed to be constant when the nozzle is critical and variable otherwise.

These curves have not been represented together mainly due to the difference in starting conditions. Moreover, the above figures would contain too much information that could be difficult to trace for the reader. Thus, different cases have been considered to illustrate the main differences that can be found in unsteady single spool engine behavior.

5.2 Dual Spool Turbojet

After analyzing steady state and transient behavior in a single spool turbojet engine, now the operation of the method is shown for a dual spool turbojet. This includes more complexity and thus, more parameters to be described, although the steady state problem still has 2 DOF as in the case of a single spool.

In the following Table 15 all necessary parameters to describe the engine, at least for the steady state are listed. Note again how many properties will be considered to be equal to the single spool analysis, for a better comparison of both kinds of systems.

Parameter	Value	Parameter	Value
T_{ref} [bar]	288.15	$M_{0,\text{d}}$ [-]	0.8
p_{ref} [bar]	1.01325	$\dot{m}^*_{0,\text{d}}$ [kg/s]	80
$C_{\text{p,c}}$ [J/kg/K]	1,004.5	$\dot{m}^*_{25,\text{d}}$ [kg/s]	23.515
γ_{c} [-]	1.4	$\pi_{\text{LPC,d}}$ [-]	2.74
γ_{h} [-]	1.309	$\pi_{\text{HPC,d}}$ [-]	3.28
$N_{\text{ref,LPC}}$ [rpm]	16,500	$\pi_{\text{HPT,d}}$ [-]	1.682
$N_{\text{ref,HPC}}$ [rpm]	13,216	$\pi_{\text{LPT,d}}$ [-]	1.411
$N_{\text{ref,HPT}}$ [rpm]	6,864	$((\eta_{\text{CC}} f L) \,/\, (C_{\text{p,c}} T_0))_{\text{d}}$ [-]	4.94
$N_{\text{ref,LPT}}$ [rpm]	7,713	b_{25} [-]	0.025
η_{D} [-]	0.98	b_3 [-]	0.05
$\eta_{\text{m,HP}}$ [-]	0.99	$\zeta_{\text{CC,c}}$ [-]	27
$\eta_{\text{m,LP}}$ [-]	0.98	$\zeta_{\text{CC,h}}$ [-]	2
η_{N} [-]	0.97	μ [-]	0.5
A_8 [m^2]	0.1328	f [-]	0.025

Table 15: Properties for the Generic Dual Spool Engine.

The engine OPR has been chosen to be similar to the single spool case. On the other hand, design inlet corrected mass flow $\dot{m}^*_{0,\text{d}}$ and flight Mach number $M_{0,\text{d}}$ in the design point are chosen to be equal to the latter case.

The nozzle throat area A_8 changes in this case to accommodate the steady state running line to pass through the design point in steady conditions. New features, like an intermediate bleed air that is not injected back into the system (b_{25}) are also added, to have an effect on the final solution.

5.2.1 Steady State

Steady state behavior of the dual spool engine is hereby presented, once again, by plotting the engine's running lines and characteristic curves for the general solution devised for this study and the analytic one.

Operating Lines

Operating line results are hereby described, for all components. To reiterate and, although not mentioned at the beginning of this section, generic component performance maps are still being used to model the turbomachinery in the engine. Axial compressor maps from *GSP* are being used.

In fact, the same map is used for the LPC and HPC and for the HPT and LPT, although scaled to ensure a correct coupling. The scaling, along with the modification of some other parameters, like A_8, makes possible to align the steady state running line with the component's design point, indicated with a star in the following Figure 51 and 52.

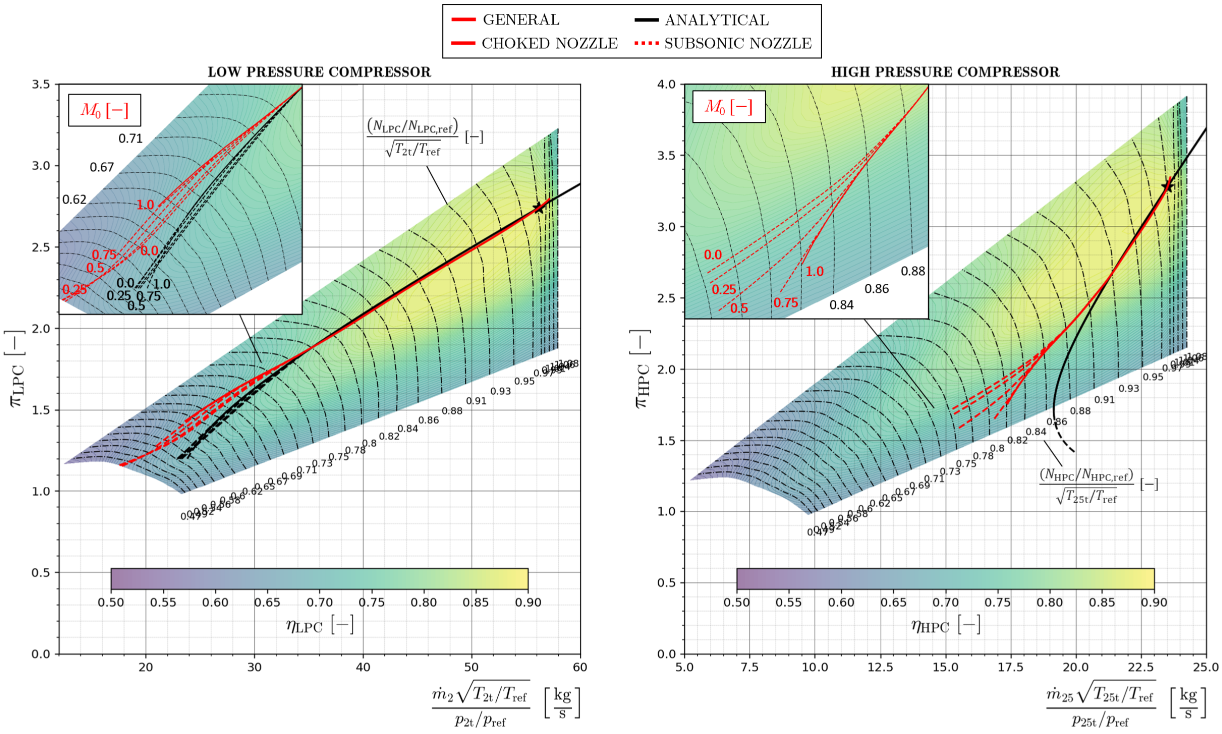

Figure 51: Operating Lines in a Dual Spool Engine Estimated with the General (red) and Analytical Solution (black) for Different Values of Flight Mach Number. LPC (left) and HPC (right).

Consider the proximity of the estimated running line through an analytical analysis with the one calculated by a recursive method employing the performance maps. In the case it is a much better approximation to the problem in both LPC and HPC. Also, the flight Mach number doesn't have a notable effect on the position of the running line, but it is important to calculate when the nozzle will be choked or not (dashed line in Figure 51 and 52.

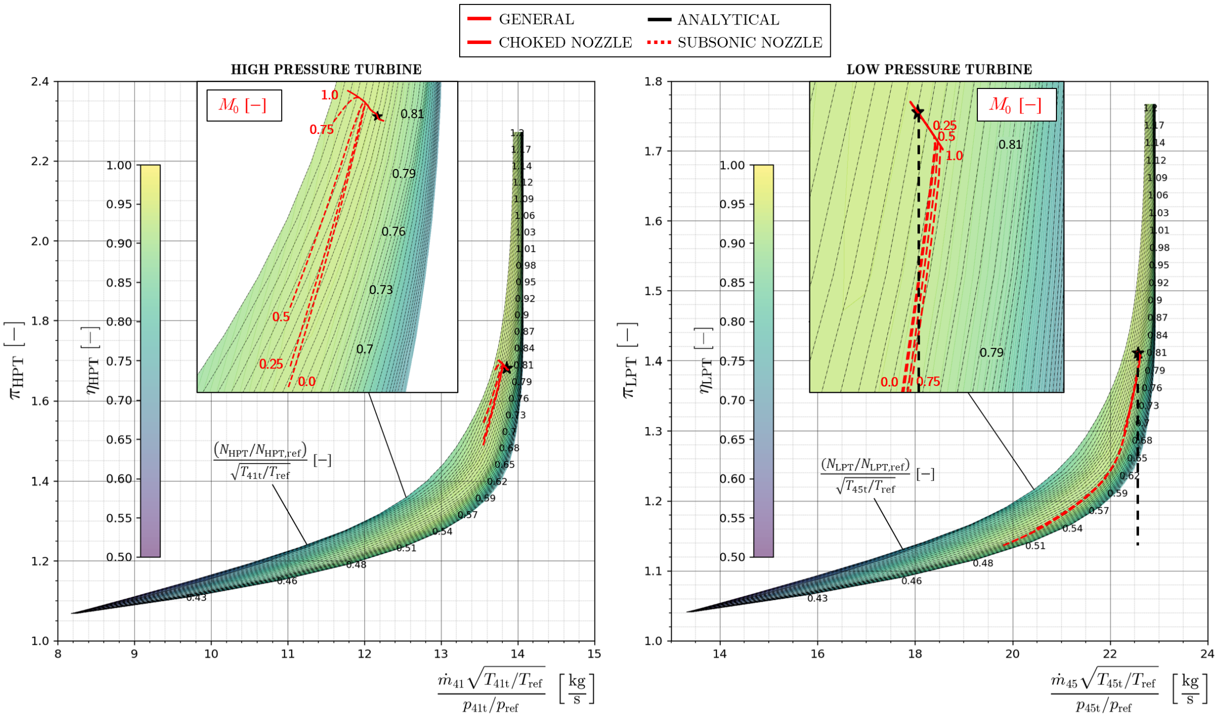

Figure 52: Operating Lines in a Dual Spool Engine Estimated with the General (red) and Analytical Solution (black) for Different Values of Flight Mach Number. HPT (left) and LPT (right).

Nevertheless, and as it happened when calculating a single spool engine, the running line calculated with the general numerical method presented here is much closer to surge effects than the calculated with the analytical, providing more insight into the appearance of undesired destructive effects. Moreover, the running line on the HPC is closer to choked flow aeroelastic instabilities and possible engine lean blowout, phenomena which also have to be taken into account.

In the case of the turbines, the analytical model is far too simple, as it considers that the corrected turbine inlet mass flow in both HPT and LPT is constant during operation. In fact, this model assumes that in the HPT, the turbine total pressure ratio is also constant at all times, so it is not represented in Figure 52, as the analytic running line concentrates in the design point.

This is however not the case, as the running lines vary, like seen in the image. The zone of the map where the lines run is actually concentrated near the design point, making this approximation reasonable to be applied.

Once again, the running line in the LPT covers a much broader region of the performance map, as it happened in the case of a single spool turbojet. This time, although the inlet corrected mass flow is assumed to be constant in the analytical approximation, the LPT total pressure ratio also varies in this model when the nozzle is not critical, which again, observing Figure 52, is a reasonable approximation. Note again the limited effect of the flight Mach number on the running lines in these components.

Characteristic Curves

Steady state characteristic curves in this case are presented for the types of nozzle considered.

- **Convergent Nozzle**

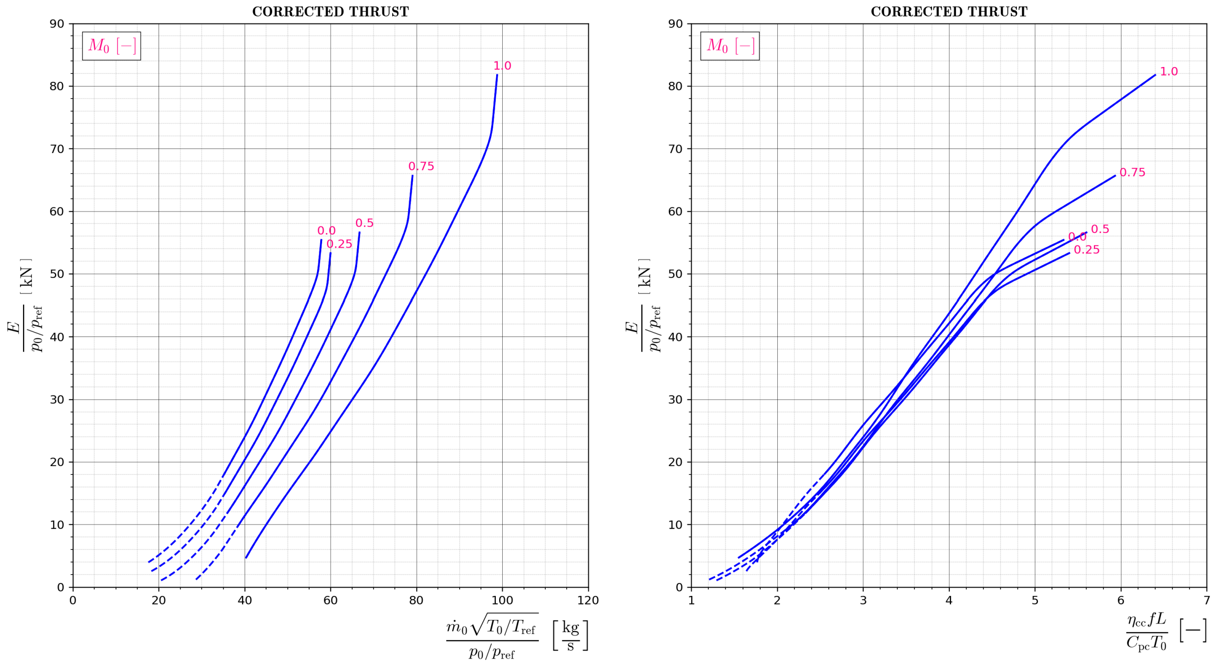

Figure 53: Dual Spool Corrected Thrust vs. Inlet Corrected Mass Flow (left) and Fuel Parameter (right). Convergent Nozzle.

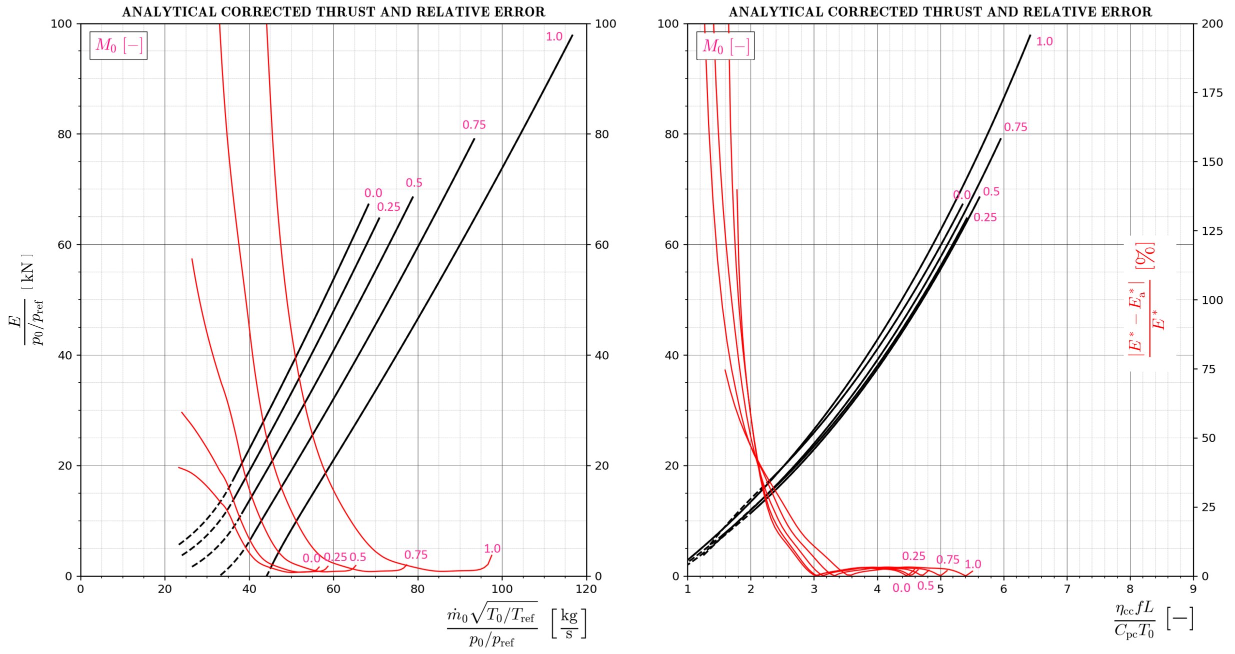

Figure 54: Dual Spool Analytical Corrected Thrust vs. Inlet Corrected Mass Flow (left) and Fuel Parameter (right) Including Error to General Solution. Convergent Nozzle.

Curves regarding both corrected thrust and corrected specific impulse are smoothed by the fact of having to independent couplings in the engine, while they also tend to have a more linear trend. Moreover, there is a clearer coincidence with the analytical solution.

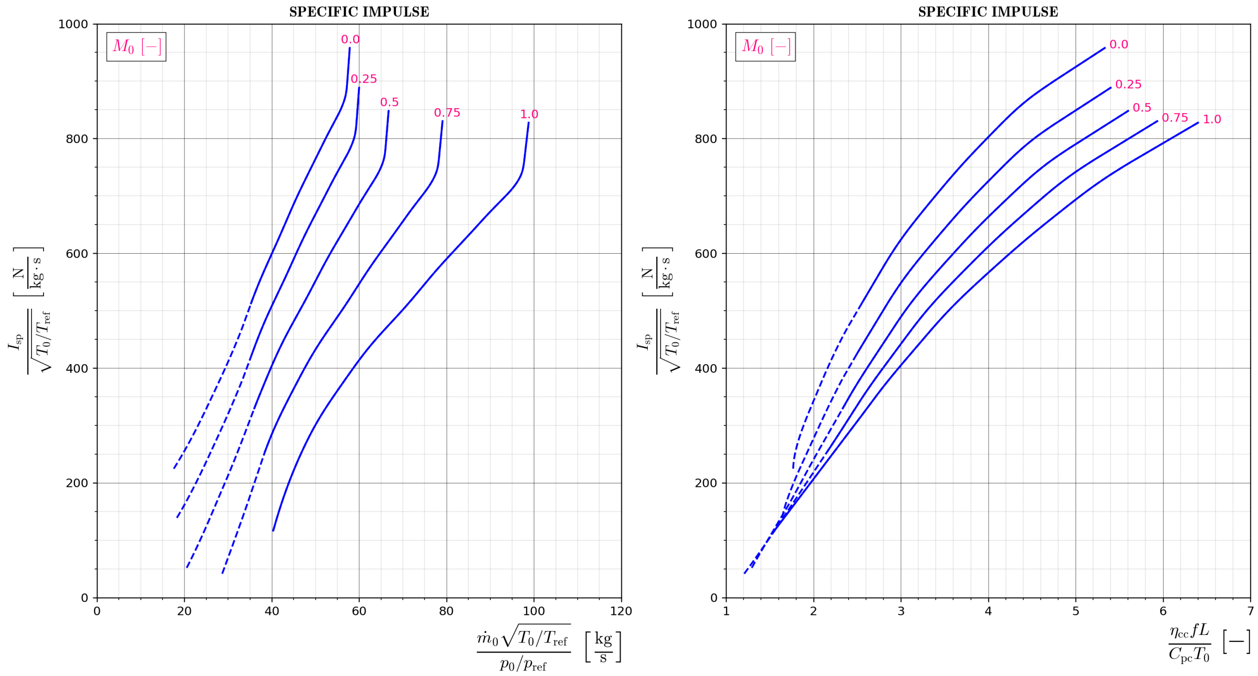

Figure 55: Dual Spool Corrected Specific Impulse vs. Inlet Corrected Mass Flow (left) and Fuel Parameter (right). Convergent Nozzle.

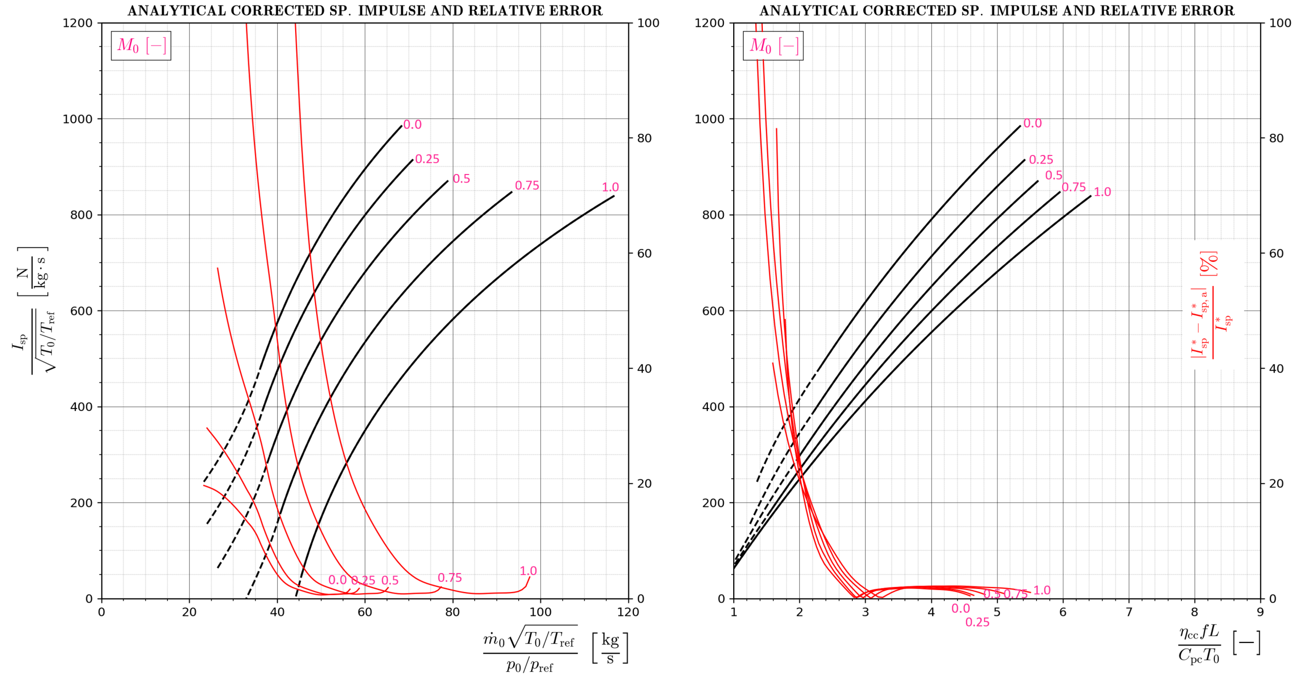

Figure 56: Dual Spool Analytical Corrected Specific Impulse vs. Inlet Corrected Mass Flow (left) and Fuel Parameter (right) Including Error to General Solution. Convergent-Divergent Nozzle.

Corrected TSFC curves are plotted with different scales to better appreciate the trends, but the coincidence with the analytical solution, except in the region where it diverges, is more accused.

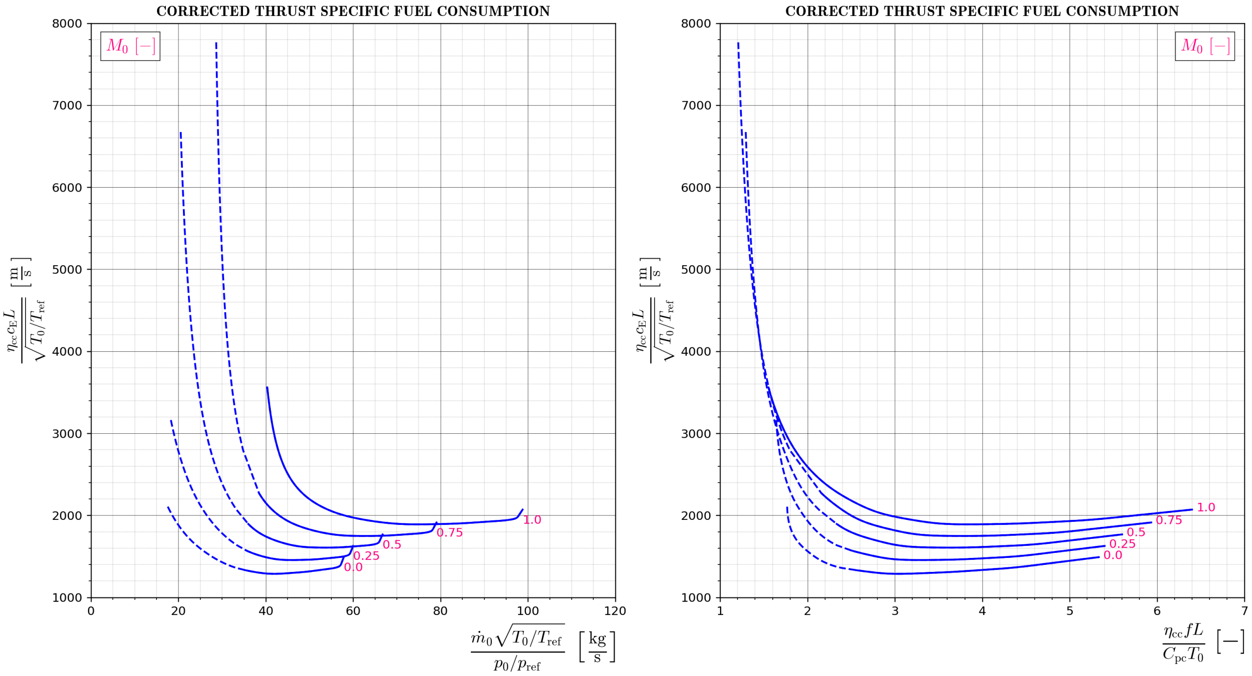

Figure 57: Dual Spool Corrected TSFC vs. Inlet Corrected Mass Flow (left) and Fuel Parameter (right). Convergent Nozzle.

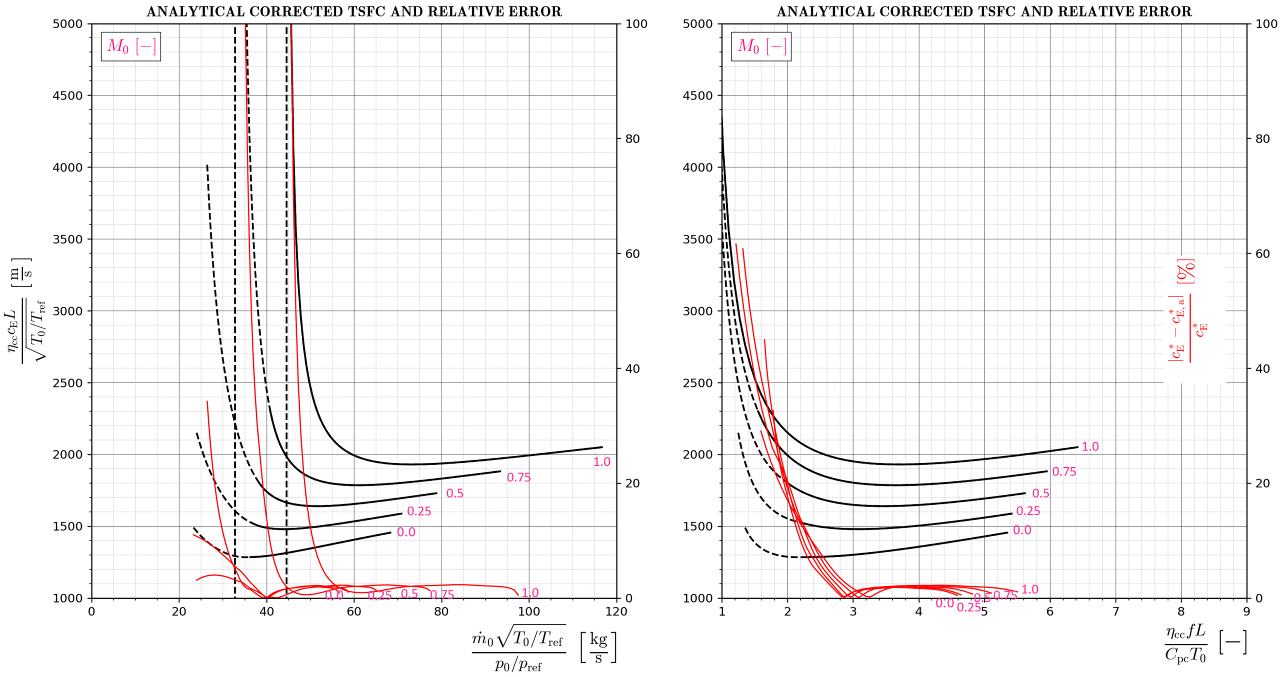

Figure 58: Dual Spool Analytical Corrected TSFC vs. Inlet Corrected Mass Flow (left) and Fuel Parameter (right) Including Error to General Solution. Convergent Nozzle.

Corrected shaft speed curves are plotted once again, now including the high pressure and low pressure sides. Once more, the flight Mach number is not influential when applying a certain fuel parameter into the system in the low pressure side. Thermodynamic ratios, both static and total have a more linear trend, considering a convergent segment.

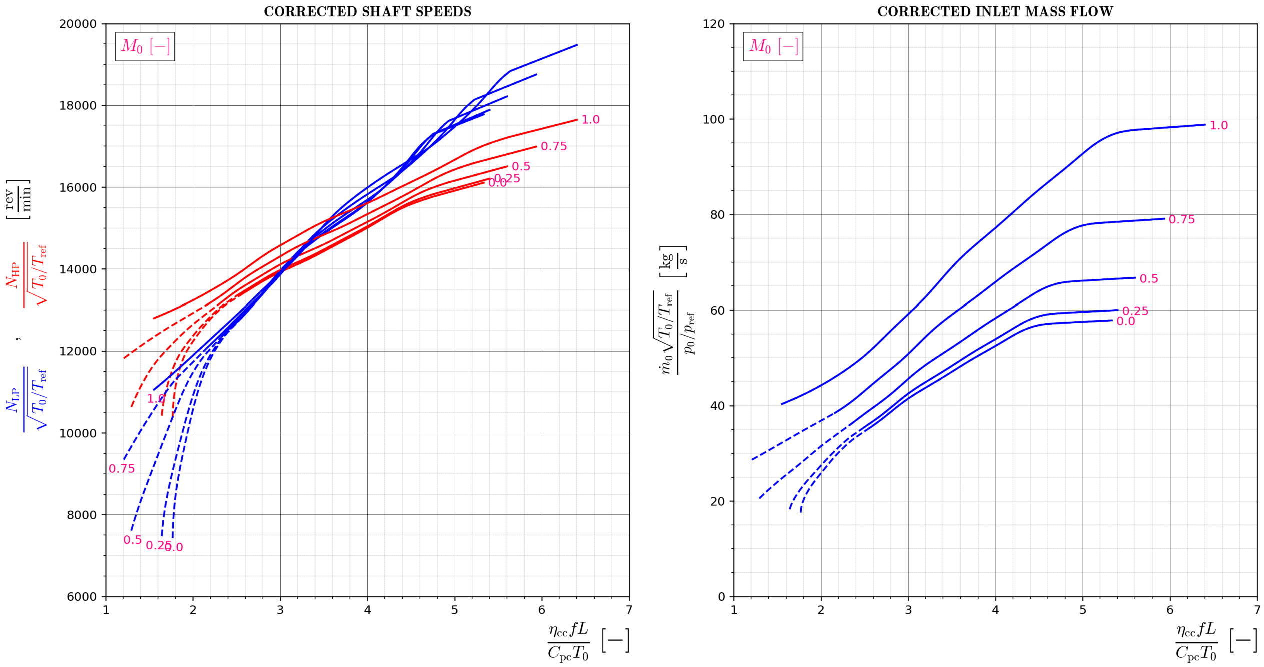

Figure 59: Dual Spool Corrected Low Pressure Shaft Speed and Corrected High Pressure Shaft Speed (left) and Inlet Corrected Mass Flow (right) vs. Fuel Parameter.

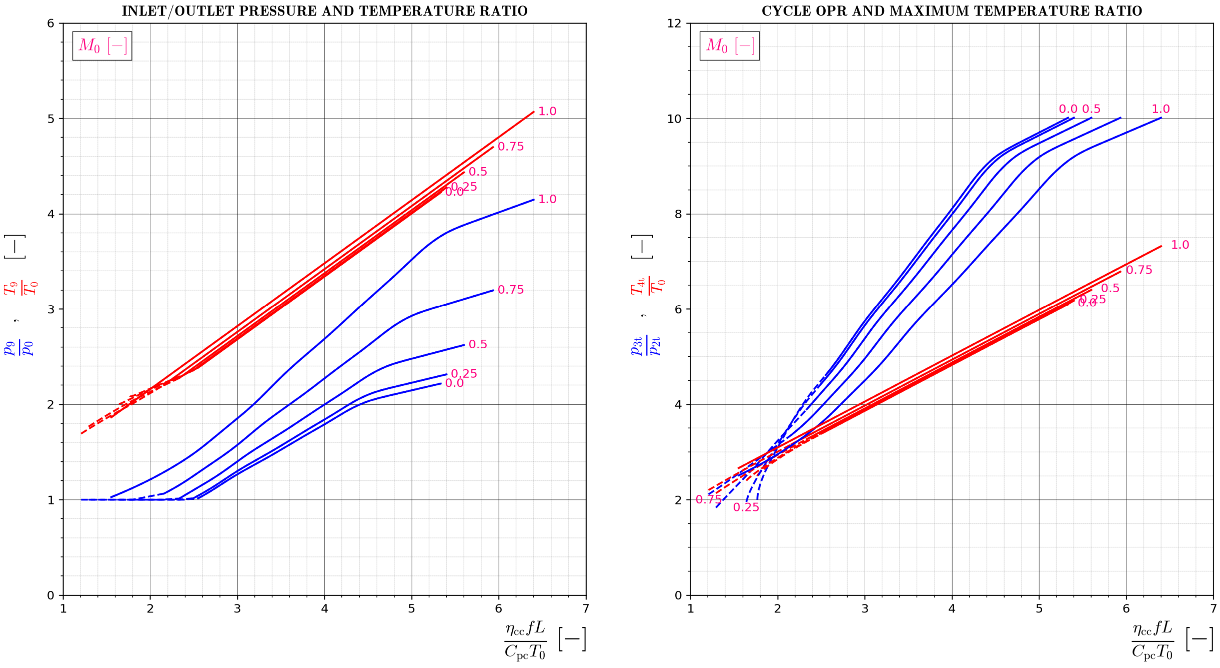

Figure 60: Dual Spool Static Temperature and Pressure Ratio (left) and Maximum Temperature Ratio and OPR (right) vs. Fuel Parameter. Convergent Nozzle.

- **Convergent-Divergent Nozzle**

  A convergent-divergent nozzle is now considered, once more improving the generation of corrected thrust. The trends compared with a convergent segment are steeper in this first case, while the coincidence with the analytical approach keeps being close.

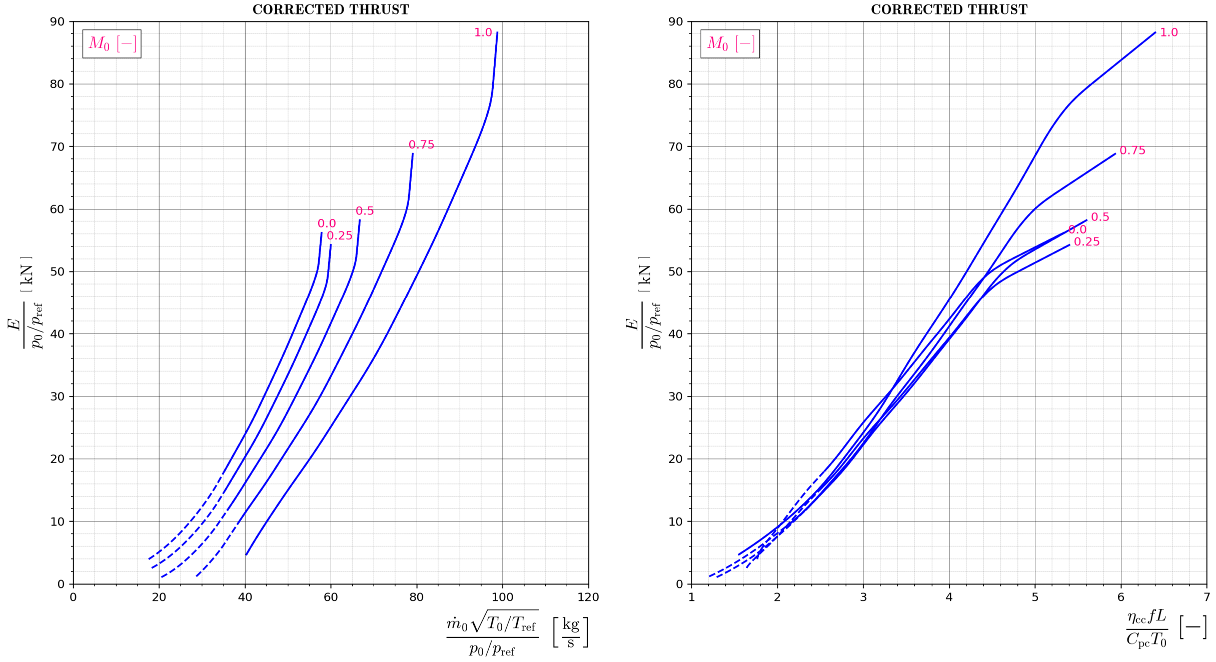

Figure 61: Dual Spool Corrected Thrust vs. Inlet Corrected Mass Flow (left) and Fuel Parameter (right). Convergent-Divergent Nozzle.

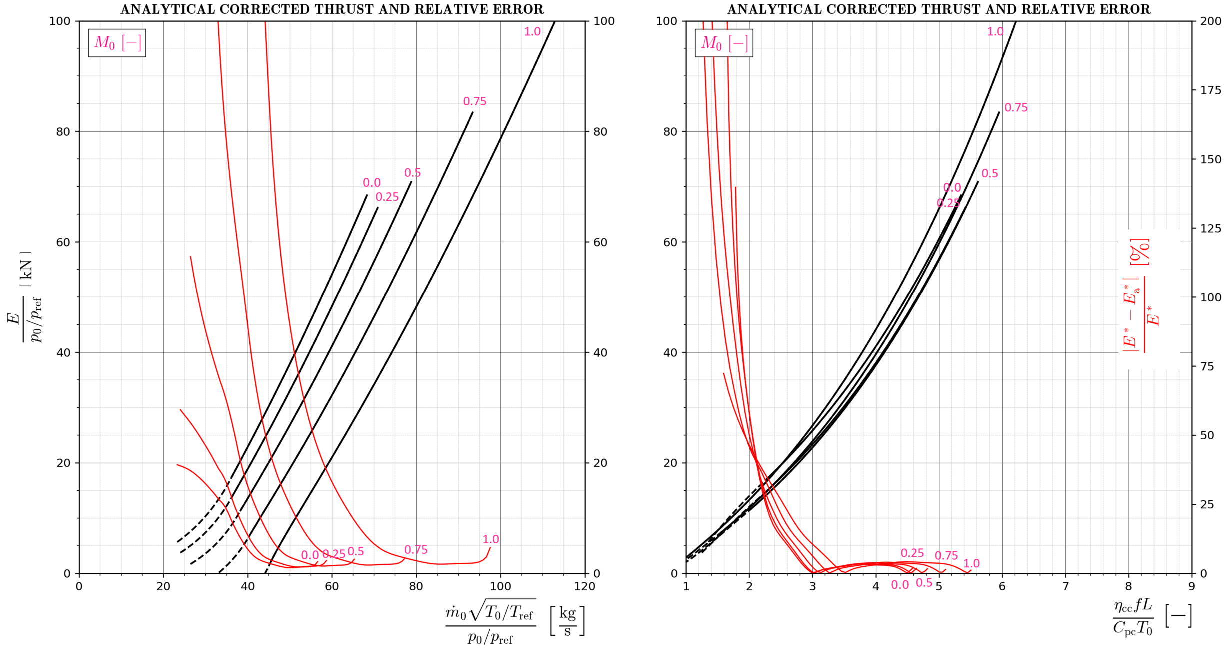

Figure 62: Dual Spool Analytical Corrected Thrust vs. Inlet Corrected Mass Flow (left) and Fuel Parameter (right) Including Error to General Solution. Convergent-Divergent Nozzle.

Corrected specific impulse is higher overall after fitting a convergent-divergent nozzle, both looking at the general and analytical solution. The analytical solution once again adapts well in a broader region than in a single spool with the same type of nozzle.

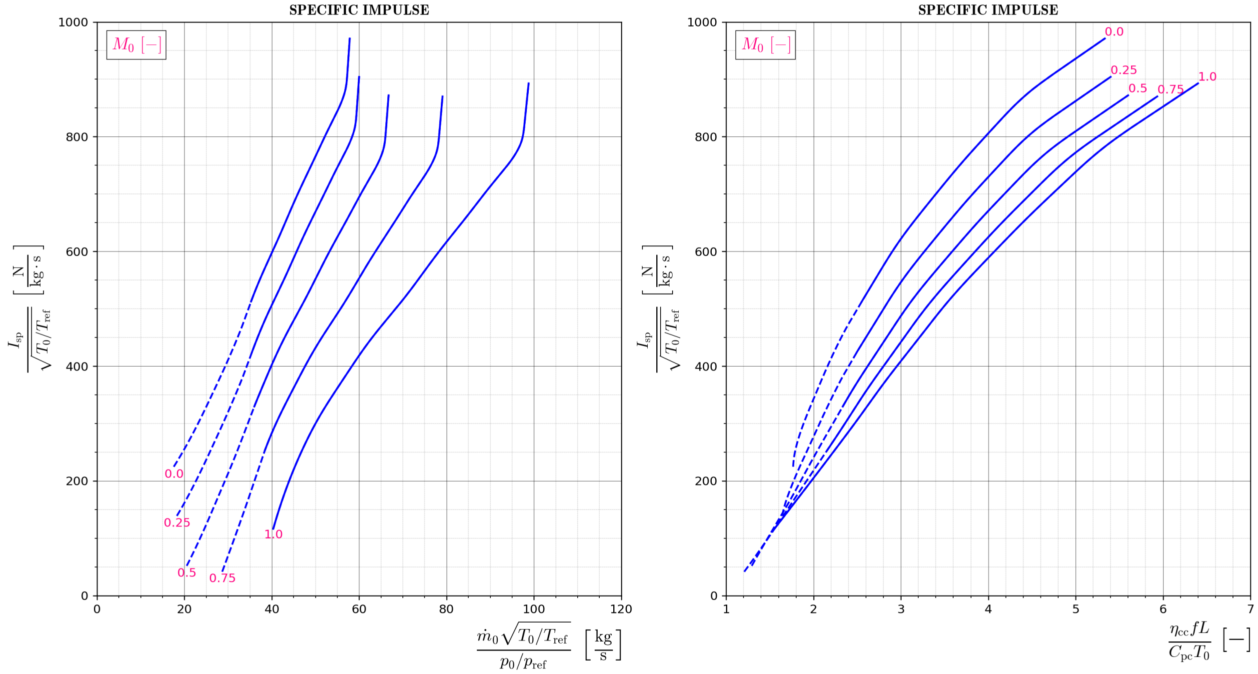

Figure 63: Dual Spool Corrected Specific Impulse vs. Inlet Corrected Mass Flow (left) and Fuel Parameter (right). Convergent-Divergent Nozzle.

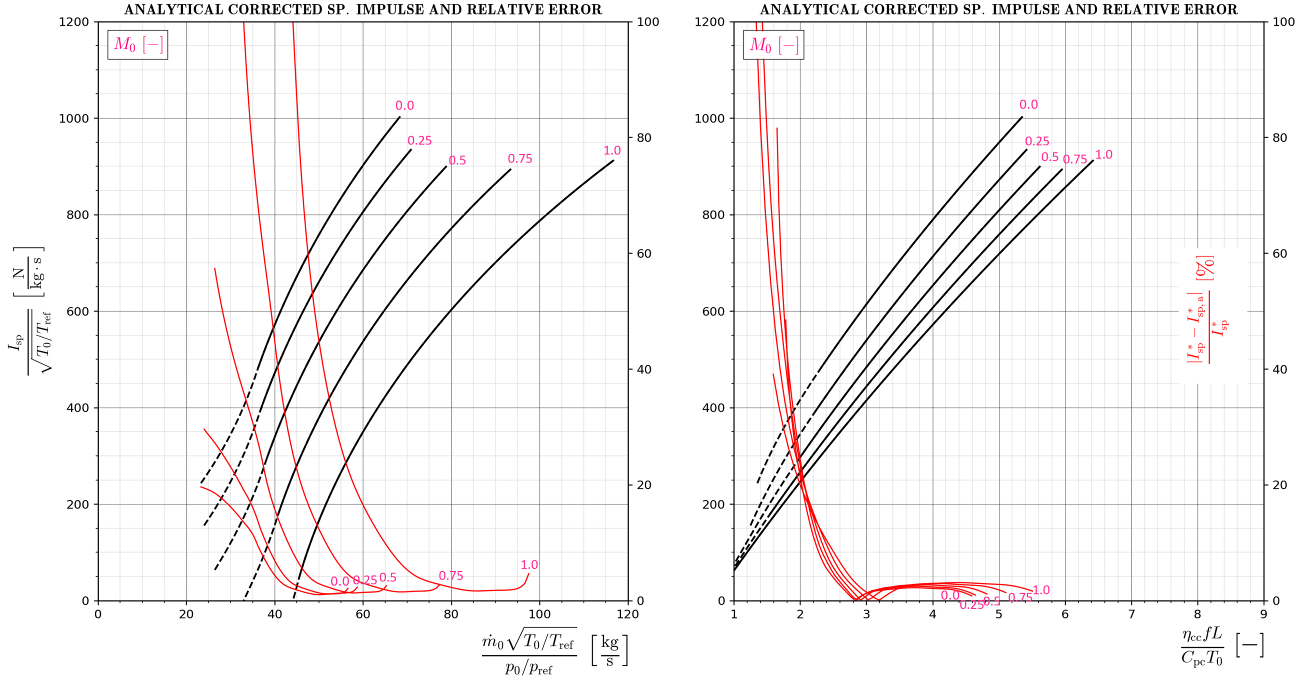

Figure 64: Dual Spool Analytical Corrected Specific Impulse vs. Inlet Corrected Mass Flow (left) and Fuel Parameter (right) Including Error to General Solution. Convergent-Divergent Nozzle.

The corrected TSFC in these types of engines also decreases after fitting a convergent-divergent segment, improving overall efficiency. Note once again that this does not mean that fitting this component can be sufficient for economic viability.

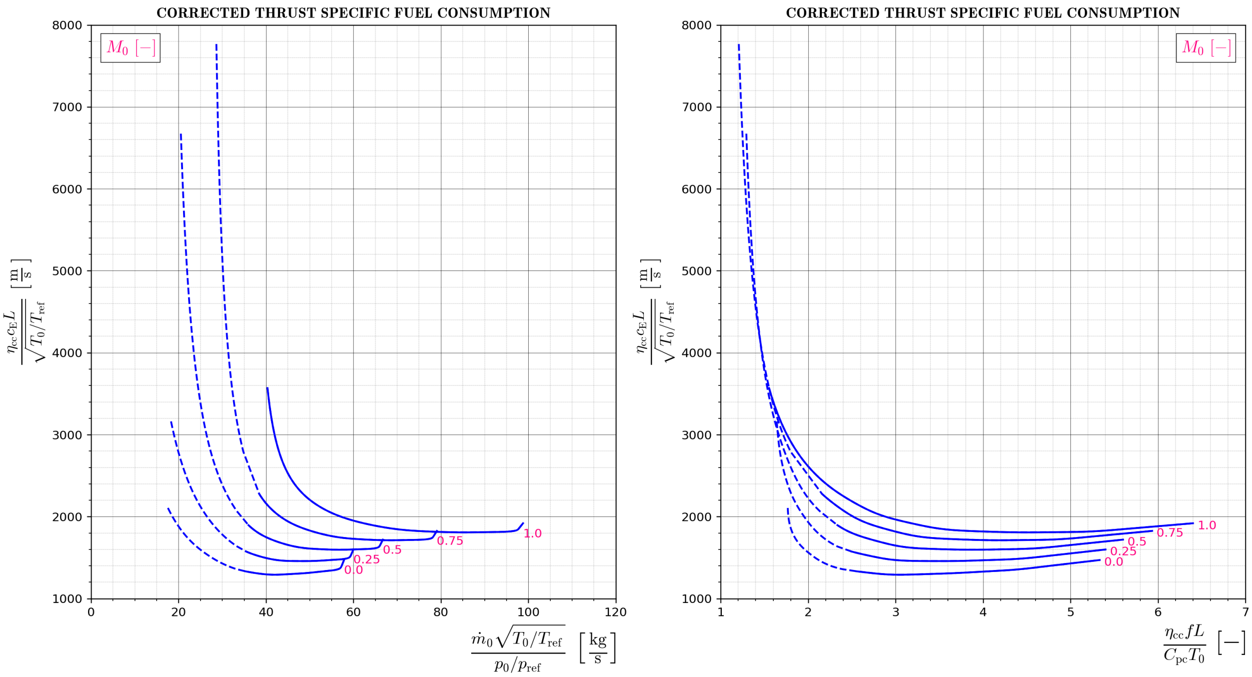

Figure 65: Dual Spool Corrected TSFC vs. Inlet Corrected Mass Flow (left) and Fuel Parameter (right). Convergent-Divergent Nozzle.

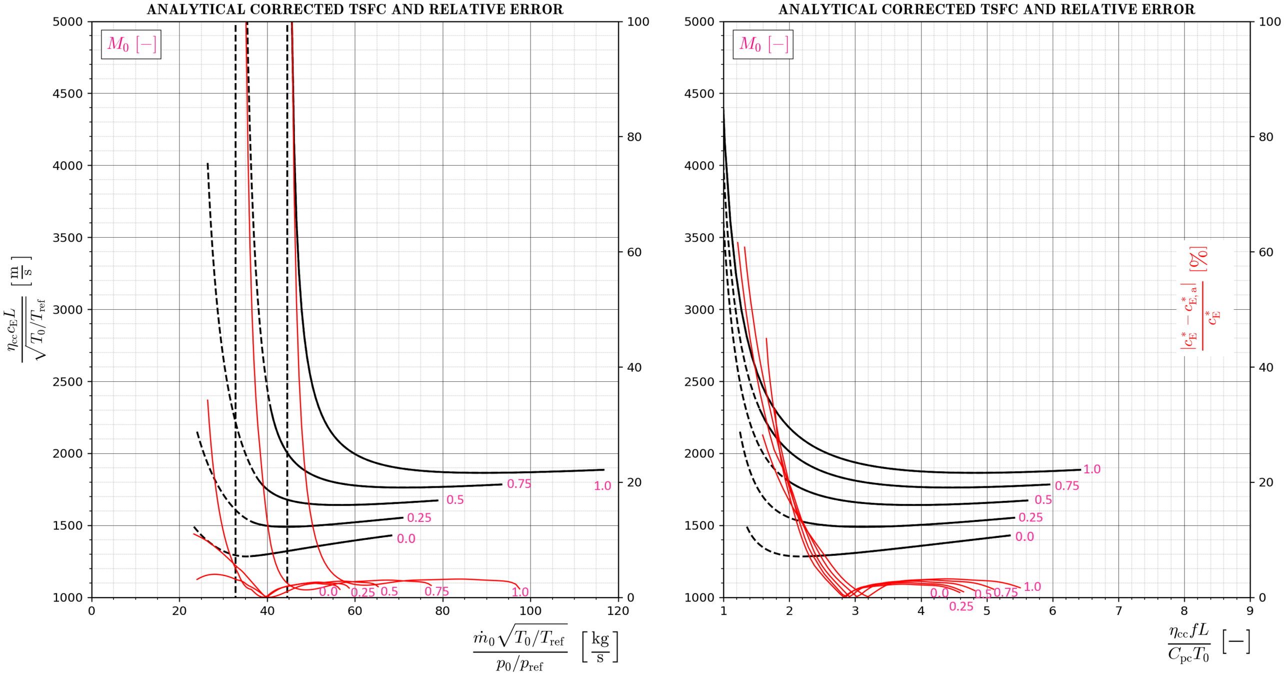

Figure 66: Dual Spool Analytical Corrected TSFC vs. Inlet Corrected Mass Flow (left) and Fuel Parameter (right) Including Error to General Solution. Convergent-Divergent Nozzle.

Note the far better coincidence in this dual spool engine of both M_9 and A_9/A_8. In fact, the area rule is almost perfectly predicted by the analytical approach in almost all operating points.

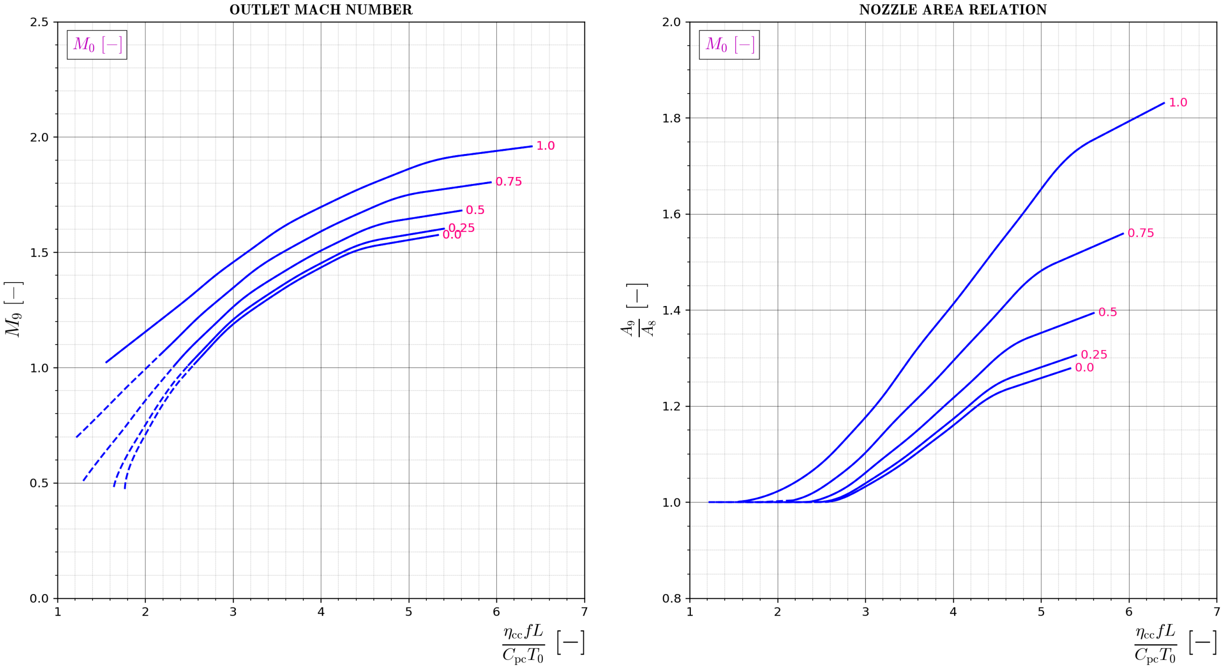

Figure 67: Dual Spool Outlet Mach Number (left) and Nozzle Area Ratio (right) vs. Fuel Parameter.

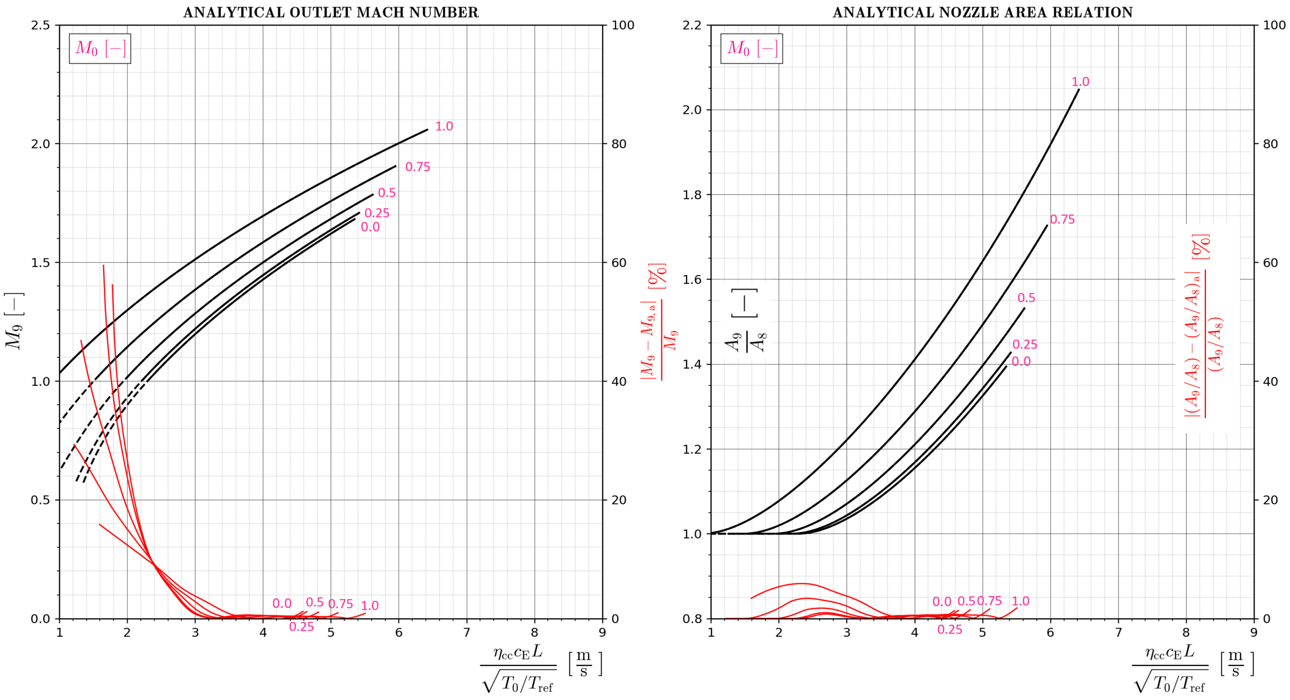

Figure 68: Dual Spool Analytical Outlet Mach Number (left) and Nozzle Area Ratio (right) vs. Fuel Parameter Including Error to General Solution. Convergent-Divergent Nozzle.

Finally, in contrast with Figure 60, the adapted nozzle boundary condition is applied in the case of considering a convergent-divergent nozzle. This can be seen in Figure 69, where $p_9/p_0 = 1$ when the nozzle is not choked and when it is.

Once again both the static temperature ratio and the maximum temperature ratio, along with the OPR, have a quasi-linear trend when plotted against the fuel parameter.

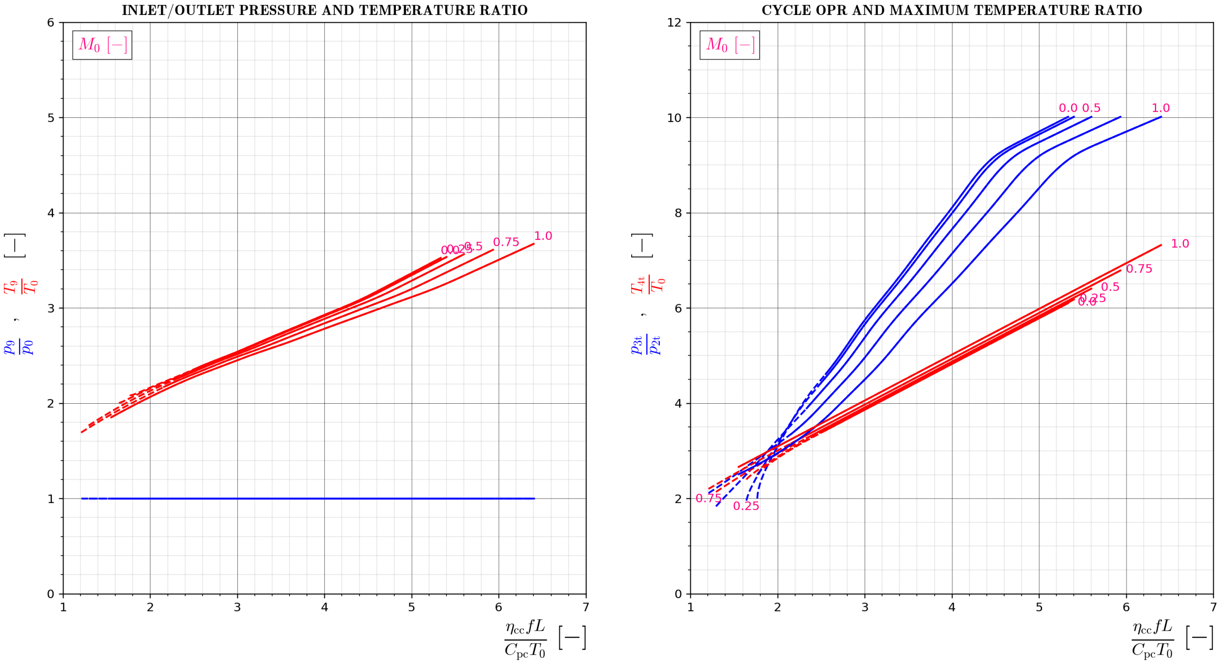

Figure 69: Dual Spool Static Temperature and Pressure Ratio (left) and Maximum Temperature Ratio and OPR (right) vs. Fuel Parameter. Convergent-Divergent Nozzle.

Note that in all these past analyses, there is a region of high temperatures and pressures where the calculated curves by means of performance maps present a change in slope, in a once again almost linear trend. This is also due to the difference in compressor efficiency near the high speed regions (see Figure 51).

A dual spool engine presents similar patterns, compared with a single spool engine, with the found difference of having a smoother steady state behavior. However, note how in Figure 59 overall shaft speeds can be lowered in a dual spool engine, while maintaining similar thrusting and efficiency properties.

This is a fundamental reason for the existence of dual spool engines. The model helps to visualize how they can allow to reduce turbomachinery speed and add more degrees of freedom to the system. This, in turn, avoids the appearance of several problems, like tips reaching relative supersonic speeds, causing destructive effects and plummeting efficiency.

It also allows for a dedicated study of turbomachinery in the low pressure or high pressure side, focusing their design into a narrower range of component speeds, which in the end, can further improve component efficiency because they do not have to adapt to a broader range of working conditions.

5.2.2 Transient

For this dual spool case, again a simple transient state analysis is carried out. This will help to provide evidence for the adequate working principles of the developed tools. The parameters that have been mentioned in Table 15 are also valid for the current analysis. However, new parameters needed for the study of transient phenomena need to be defined.

These new values are gathered in Table 16. The time step Δt and number of points N_{p} now allow the simulation to reach a total time of 20 s. The corrected inertia of the low pressure and high pressure side are again chosen to be a generic values, not referred to any particular existent engine.

Parameter	Value
I^{*}_{LP} [kgm^2]	1.562
I^{*}_{HP} [kgm^2]	0.850
N_{p} [-]	300
Δt [s]	0.067

Table 16: Additional Values for the Dual Spool Transient Simulation.

As done before, 4 different cases will be simulated. The fuel parameter inputs consist of *slam* functions, which allow for the visualization of the transient effects on acceleration and deceleration. *Slam* once again refers to a finite step input of fuel parameter, reaching a maximum (in this case the design value $\left((\eta_{\mathrm{CC}} f L)\,(C_{\mathrm{p,c}} T_0)\right)_{\mathrm{d}}$ shown in Table 15) to return to the same value after a quasi-steady state is reached, which will be the initial fuel parameter ${}^{0}\left((\eta_{\mathrm{CC}} f L)\,(C_{\mathrm{p,c}} T_0)\right)$.

The cases studied here will present different corrected speed initial conditions, for the low pressure and high pressure side, as well as distinct flight Mach numbers, so that effect can be evaluated too, as it greatly affects the appearance of critical conditions in the nozzle. These properties are gathered in Table 17.

Parameter	Case 1	Case 2	Case 3	Case 4
M_0 [-]	0	0.5	0.8	1
${}^{0}\left(N^{*}_{\mathrm{LPC}}\right)$ [-]	0.6	0.6	0.7	0.7

Table 17: Different Cases Considered for the Dual Spool Transient Simulations.

Once again, having a flight Mach number M_0 and a starting corrected relative LPC shaft speed ${}^{0}\left(N^{*}_{\mathrm{LPC}}\right)$, a steady state case is calculated to feed into the system properties like ${}^{0}\left(N^{*}_{\mathrm{HPC}}\right)$ and ${}^{0}\left((\eta_{\mathrm{CC}} f L)\,(C_{\mathrm{p,c}} T_0)\right)$ that allow to start the time-marching in the solver. The time discretization scheme is a forward Euler method. Now, corrected shaft speed in the low pressure and high pressure sides are plotted against the fuel parameter input, together with a visualization of the time evolution of running lines in turbomachinery maps.

- **Case 1**

Case 1 is defined to start with a low LPC relative corrected speed ^{0} (N^*_{LPC}) and low flight Mach number M_0, meaning the nozzle will stay non-critical for an extended period of time after the first moments in acceleration and last moments in deceleration. Notice how this change in fuel parameter greatly affects the response in speed, for both the low pressure and high pressure side. Due mainly to this chosen flight Mach number and fuel parameter input, the corrected speeds of both shafts take the longest time of all the studied cases in order to settle down and achieve a quasi-steady state.

In fact, the suspected main reason behind the low pressure side reaching the quasi-steady state later than the high pressure side is the higher value given to this side's corrected inertia. This is a true statement in general, because many times LPC contain a higher number of stages that are distributed along a greater distance through the engine, increasing this part's inertia.

The engine running lines, as expected in the case of a dual spool turbojet are closer to the compressor choke line in the LPC and the surge line in the HPC when accelerating. On the contrary, in deceleration, the running line in the LPC is the one that approaches the surge line, while the HPC decelerates with a lower component total pressure ratio than in steady state.

The nozzle being critical or not greatly affects the response of the system, in this case changing the trends in deceleration, where the LPC is close to reaching surge. The change in conditions in the nozzle provokes a change in trend, bringing the running line closer to the surge line (see Figure 71).

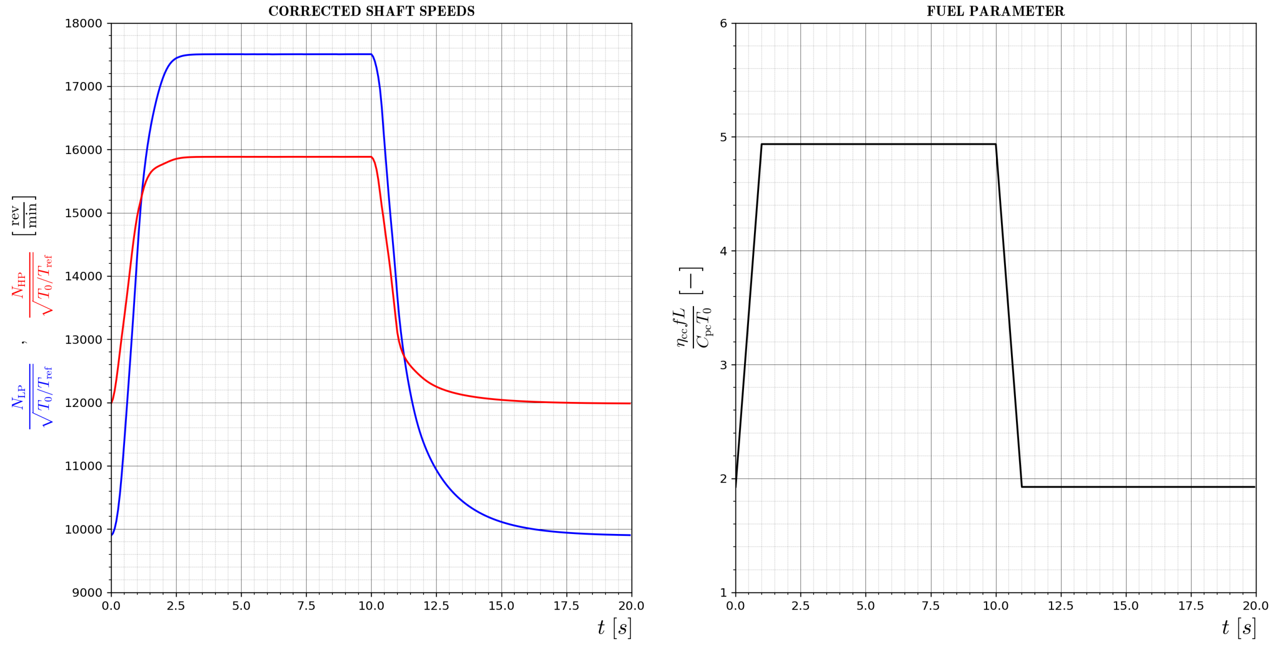
CORRECTED SHAFT SPEEDS

FUEL PARAMETER

Figure 70: Case 1. Corrected Low Pressure Shaft Speed and Corrected High Pressure Shaft Speed (left) and Input Fuel Parameter (right) in a Dual Spool Engine Transient Simulation.

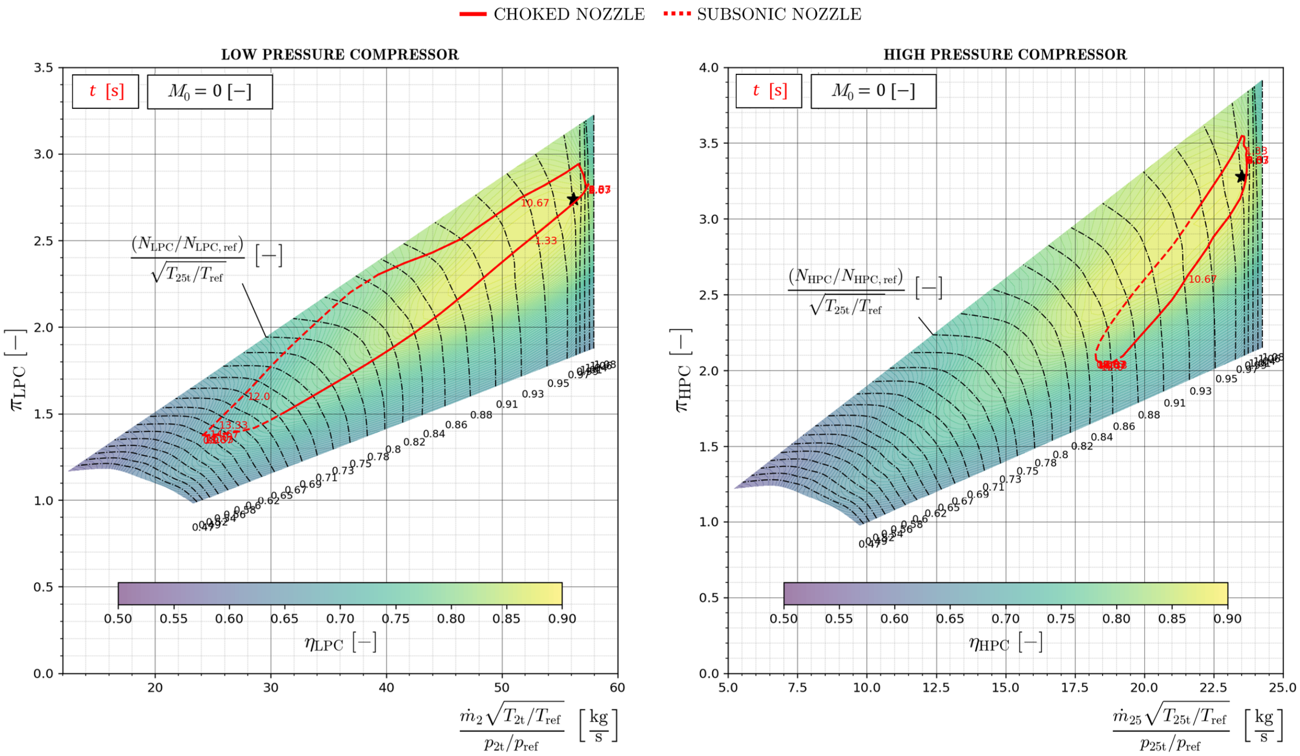

Figure 71: Case 1. LPC (left) and HPC (right) Operating Lines in a Dual Spool Engine Transient Simulation.

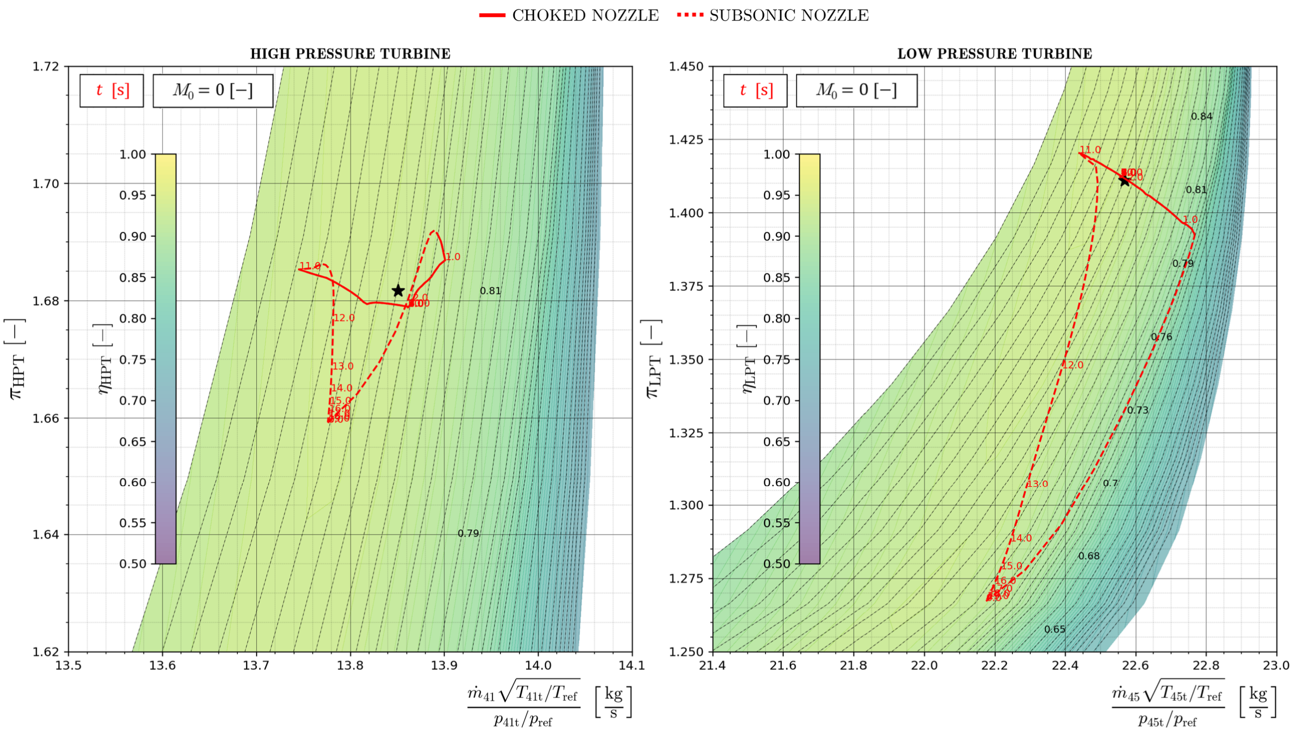

Figure 72: Case 1. HPT (left) and LPT (right) Operating Lines in a Dual Spool Engine Transient Simulation.

- **Case 2**

Case 2 is quite similar to Case 1, this time a higher fight Mach number M_0 is considered, so the initial value of the fuel parameter $^{0}\left(\left(\eta_{\mathrm{CC}} f L\right)\left(C_{\mathrm{p,c}} T_0\right)\right)$ is also higher, which reduced the difference between the maximum and minimum values in the *slam* inputs (see Figure 70).

Similarly, after applying this input, the evolution of the low pressure and high pressure corrected speed varies with respect to Case 1, reaching this time the quasi-steady state quicker.

However, the response is very similar to the last case, being overdamped (not peaking before stabilizing). The running line in both solutions exceeds the design point, as it was devised to be coincident with the steady state line when $M_0 = 0.8$. The peak fuel parameter corresponds to a point further than the design point (see Figure 71 and 74).

The running line in the turbines seems to circle the design point in the HPT in both cases, which supports the hypothesis made in the steady state solution of the analytical approach, in which the corrected HPT inlet mass flow and its total pressure ratio, as well as its total temperature ratio are constant during operation. This is, looking at Figure 72 and 75, also a reasonable assumption.

In fact, for a transient state analytical solution this is generally assumed. However, reiterating, it is not presented here because it is not reasonable enough to assume a constant compressor efficiency during a transient state period unless the change in fuel parameter is mild enough or the corrected inertia is low.

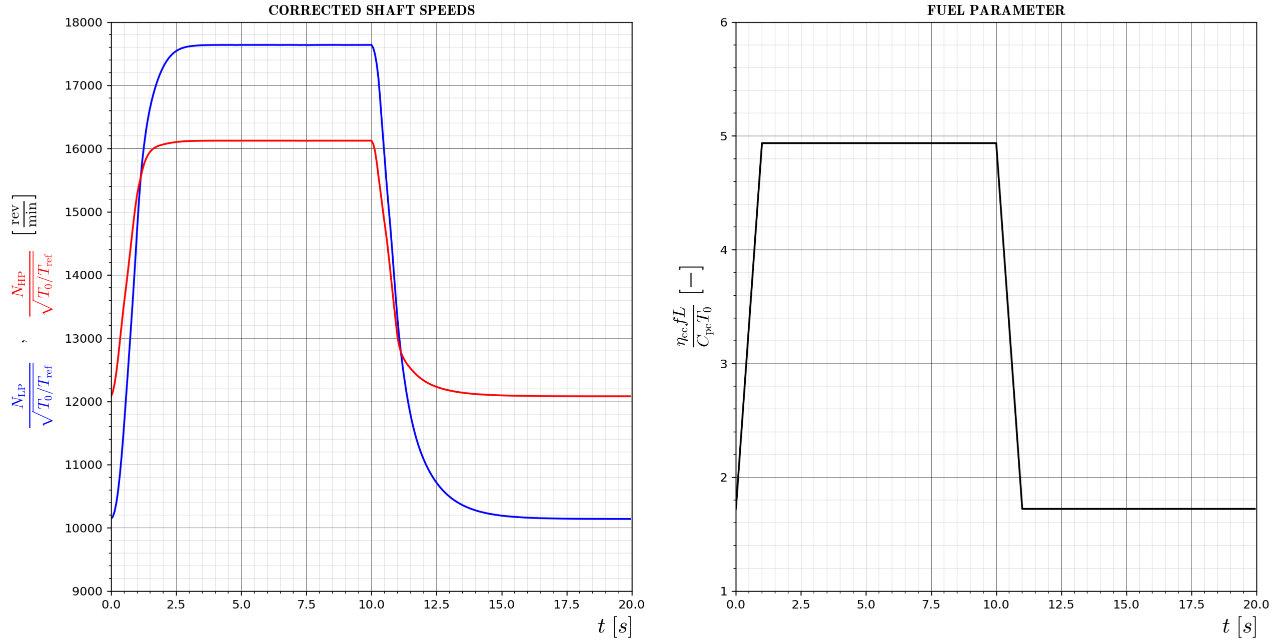

Figure 73: Case 2. Corrected Low Pressure Shaft Speed and Corrected High Pressure Shaft Speed (left) and Input Fuel Parameter (right) in a Dual Spool Engine Transient Simulation.

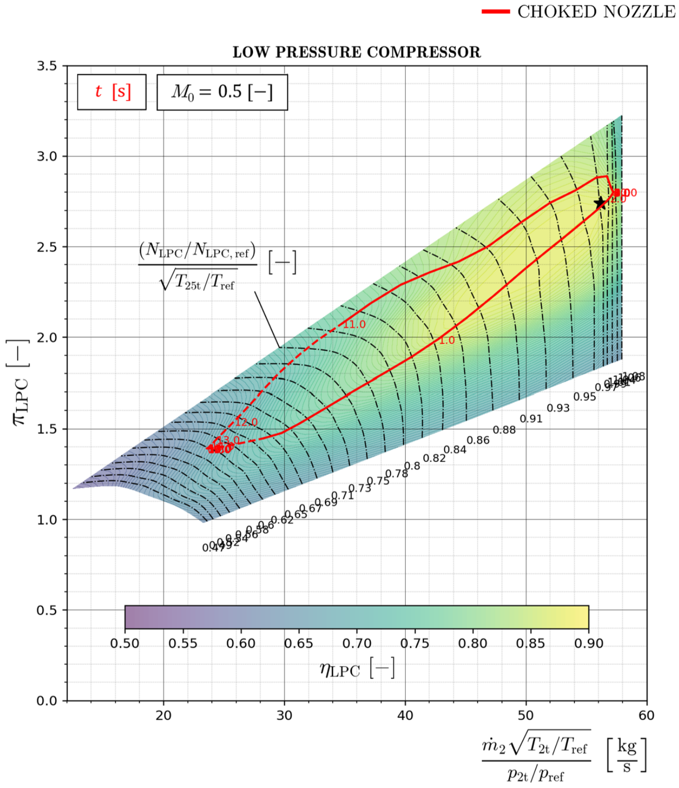

Figure 74: Case 2. LPC (left) and HPC (right) Operating Lines in a Dual Spool Engine Transient Simulation.

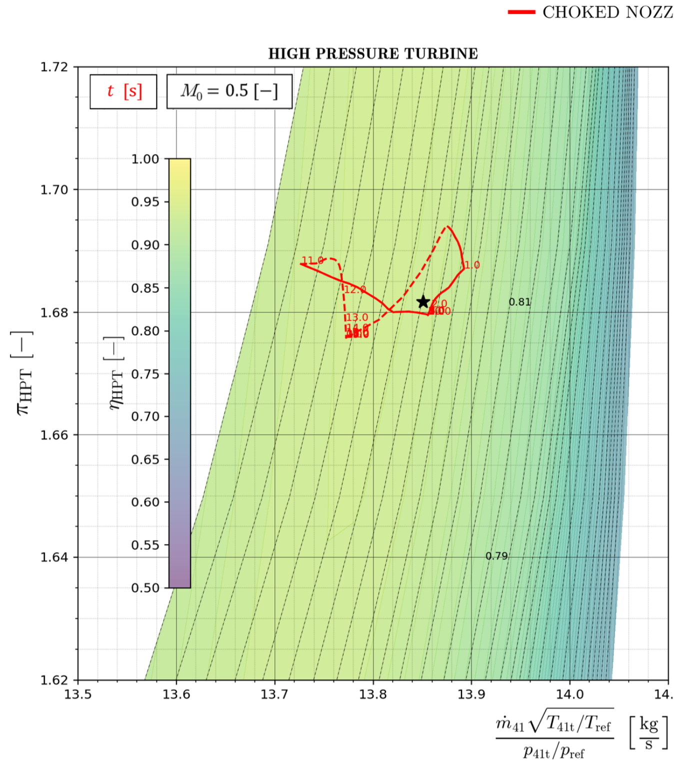

Figure 75: Case 2. HPT (left) and LPT (right) Operating Lines in a Dual Spool Engine Transient Simulation.

- **Case 3**

In Case 3, a faster relative corrected speed in the LPC is chosen as a starting point, limiting more the difference in values of the *slam* input. Note how, once again and as it happened in Case 2, reducing this difference in the maximum and minimum of the forcing term in the differential time evolution relation described in Equation 94 and 93 leads to a shorter settling time overall, which can be seen in Figure 73.

This milder change in the fuel parameter, although still abrupt in time, allows the running line in both compressors to be closer to the steady state operating line, especially in the HPC (see Figure 77), and more notably in the LPT, which is shown graphically in Figure 78.

This variability in the LPT operating line is more pronounced when the nozzle is not choked, so the flight Mach number actually has a great impact in the evolution of the system in regards to the conditions in the LPT. This can especially be seen contrasting Figure 72 and 75 with Figure 78, since in Case 3 the nozzle remains choked during the whole simulated transient state.

The closeness in conditions in the HPC and HPT to the steady state running line is also notable. Now, the quasi-steady state reached after imposing a constant peak fuel parameter corresponding to the design conditions (in this setup $M_0 = M_{0,\mathrm{d}} = 0.8$) leads to the stabilization of the system around the design point, proving that the steady state solution is achieved when letting time be high enough. It also proves the validity of the solver, whose solution in steady state would coincide with this design point, as is to be expected.

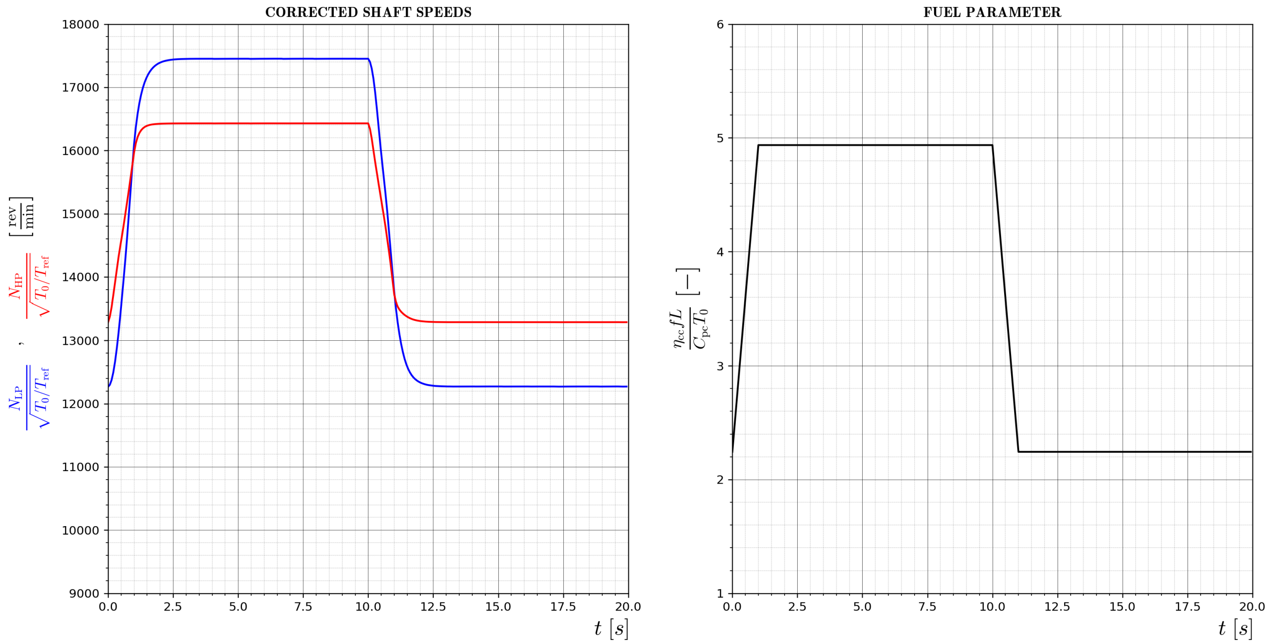

Figure 76: Case 3. Corrected Low Pressure Shaft Speed and Corrected High Pressure Shaft Speed (left) and Input Fuel Parameter (right) in a Dual Spool Engine Transient Simulation.

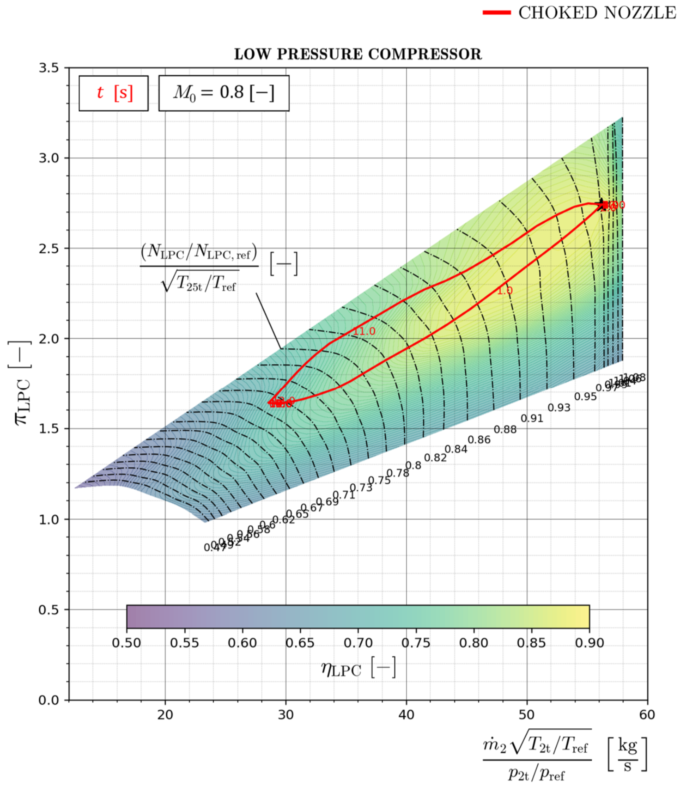

Figure 77: Case 3. LPC (left) and HPC (right) Operating Lines in a Dual Spool Engine Transient Simulation.

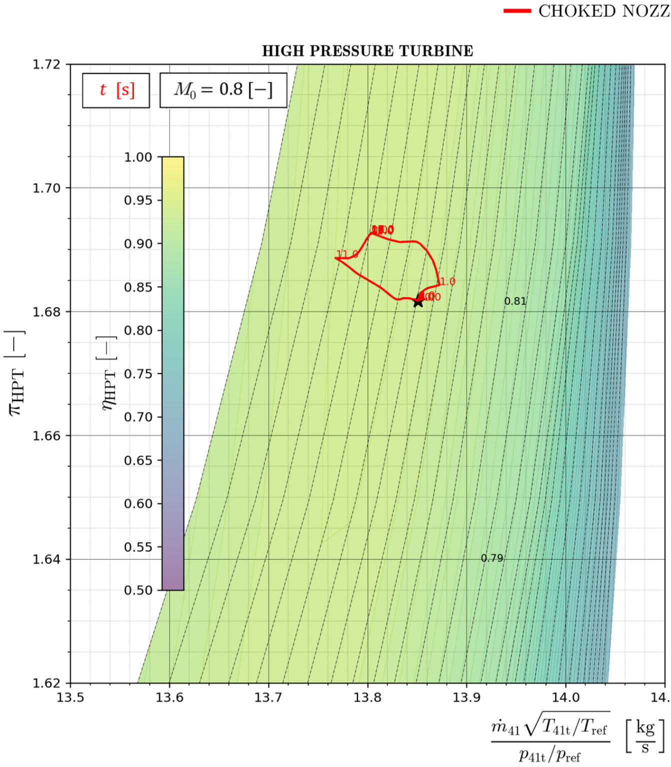

Figure 78: Case 3. HPT (left) and LPT (right) Operating Lines in a Dual Spool Engine Transient Simulation.

- **Case 4**

Finally, Case 4 is tested. It corresponds to a high flight Mach number and relatively high starting LPC relative corrected speed. This definitely ensures that the nozzle is choked throughout the process, as it happened in Case 3. Also, the peak fuel parameter is not high enough to allow the running lines to reach the design point, limiting the settling time even more, as the difference between the lowest and highest point in the fuel parameter input is the smallest of all considered setups. This fact allows the system to stabilize quicker than the rest of tested scenarios. This can be seen in Figure 79, as well as in Figure 80 and 81.

Observe Figure 79. The input function, put together with the output in low pressure and high pressure side corrected shaft speed, suggests that the system is able to follow the input in fuel parameter with more ease than the rest of cases. Lowering the corrected inertia of the system has this effect too, although this is not studied here. The running lines follow the same trend, presenting the smallest differences of all the studied scenarios when put next to the steady state lines, because of this minimal difference in the maximum and minimum fuel parameter input.

In the end, it needs to be mentioned that a dual spool engine behaves very differently from a single spool one in transient states. The running lines, reiterating, can reach surge conditions in the LPC during deceleration and in the HPC during acceleration, while in a single spool engine the surge margin is reduced only when accelerating. This whole study has been carried out without taking into account phenomena such as mass and energy pocketing, which in some cases can be decisive to predict the location of operating lines. However, the majority of times these are deemed to be second order effects.

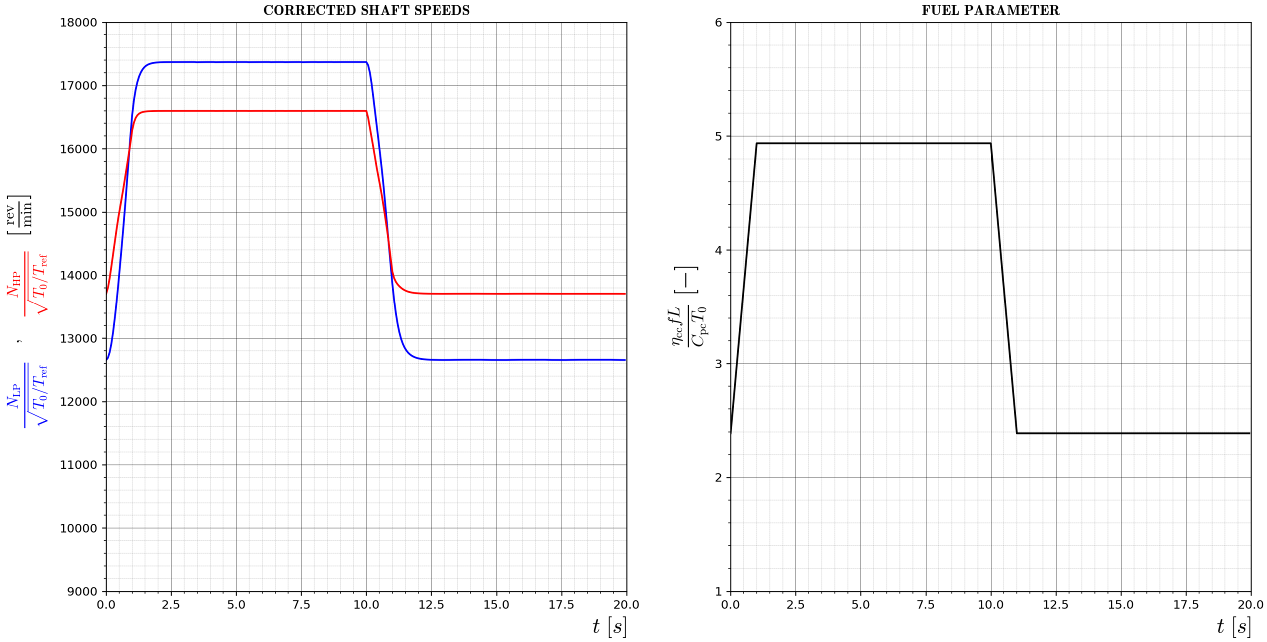

Figure 79: Case 4. Corrected Low Pressure Shaft Speed and Corrected High Pressure Shaft Speed (left) and Input Fuel Parameter (right) in a Dual Spool Engine Transient Simulation.

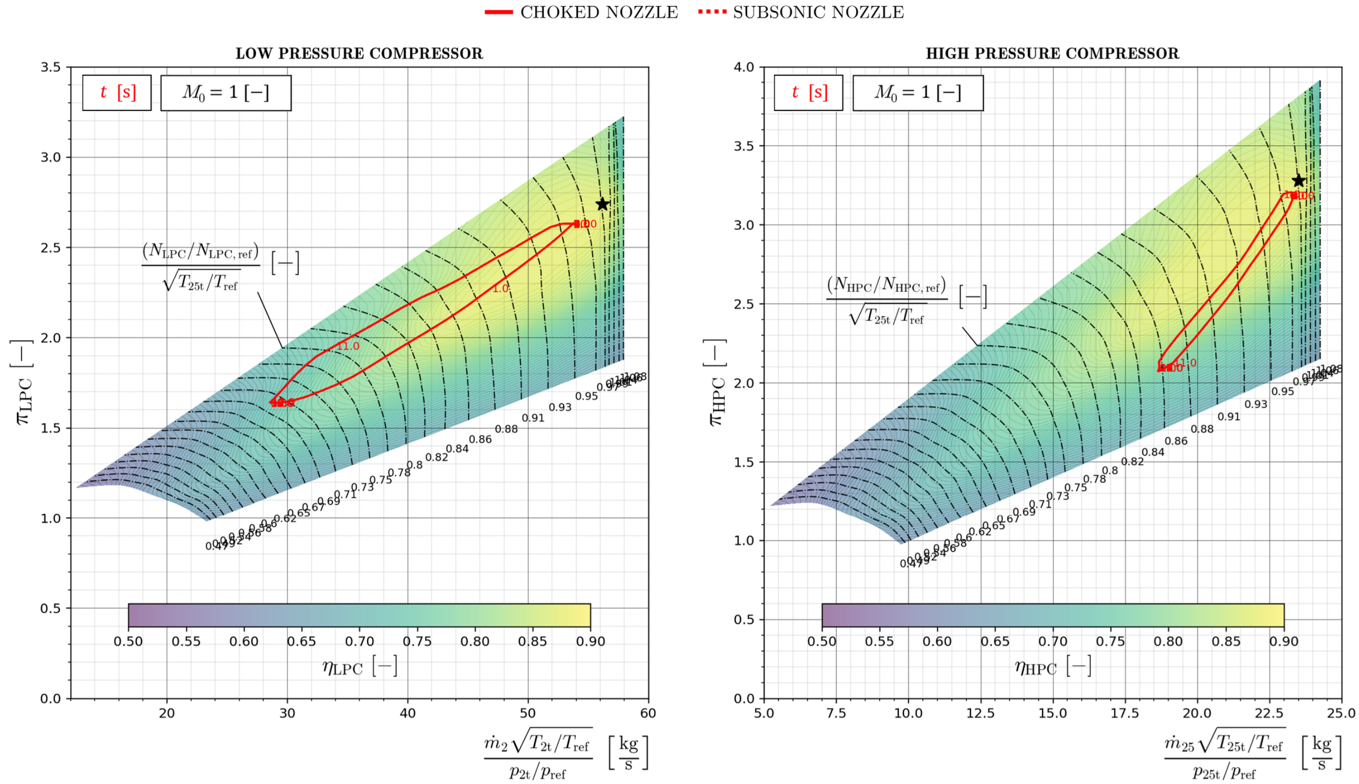

Figure 80: Case 4. LPC (left) and HPC (right) Operating Lines in a Dual Spool Engine Transient Simulation.

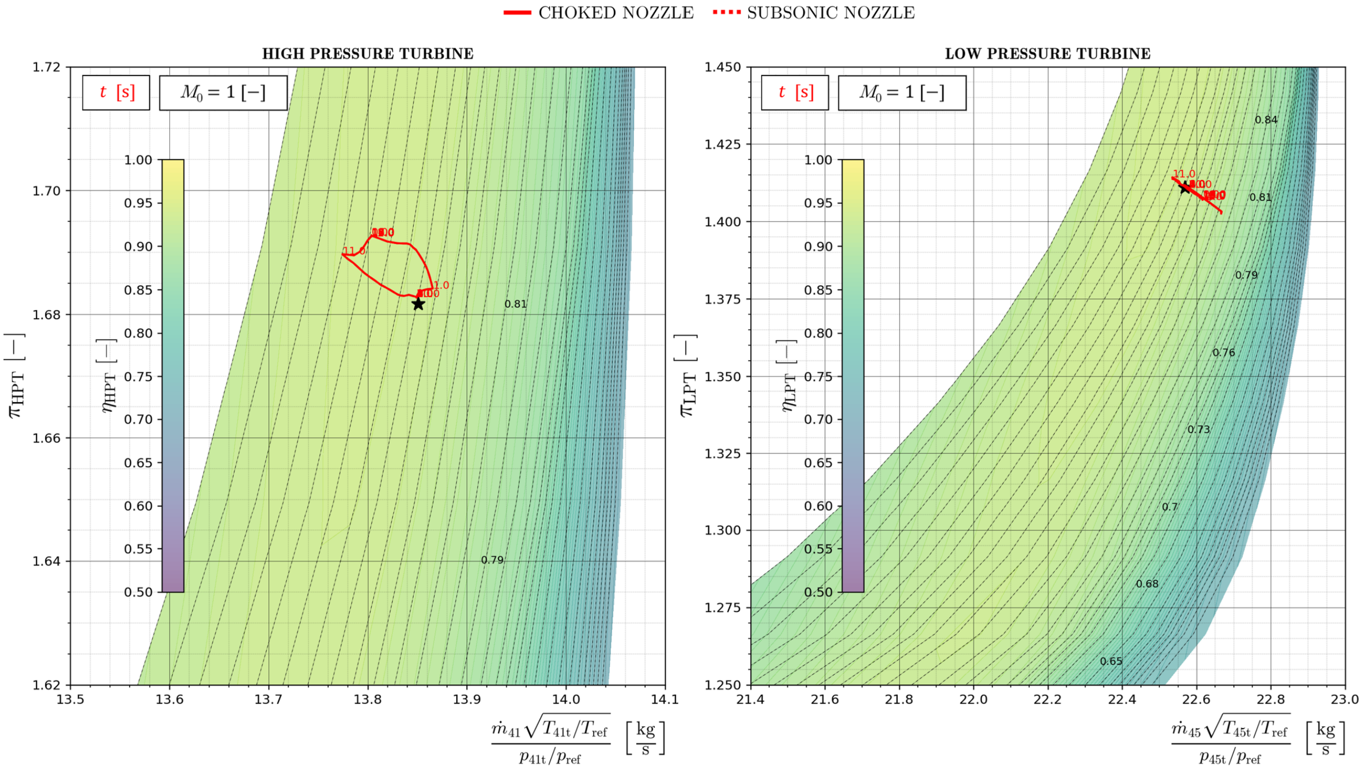

Figure 81: Case 4. HPT (left) and LPT (right) Operating Lines in a Dual Spool Engine Transient Simulation.

6. Kalman Filtering for Transient State Prediction

This section will serve to generate a quick validation process for the transient state solver, employing measurement data from UPV, when implemented along another method that adds more precision to the estimates. This is achieved by combining the modeled states with measurements in an EKF, which is a generalization of a linear quadratic estimator.

In transient state problems, thermocouples generally struggle to adequately follow temperature evolution, as they tend to have a considerable thermal inertia for these applications. There are other inconveniences in the sensor batch. This, together with intrinsic measurement uncertainties and systematic errors in the testing procedure has led to the necessity of mixing theoretical and experimental results with an EKF. In this present study, however, this method was deemed not to be fast enough to be implemented in real time, mainly because of the need of having high relaxation factors in the iterative solution, as well as multiple nested loops. This is an interesting problem to tackle for the multiple benefits it might have, which have been presented in this document's Introduction. It is left as a pending task to be completed in future works, as it requires working on the efficiency of the code.

The notation adopted is of the type $\hat{\mathbf{x}}_{m|n}$, where hat denotes the model estimate and the subindex indicates value after time step m and measurement n. The filter formulated in a general sense, to be later adapted to the engine's notation. In an EKF, this state time marching does not require linearization, unlike in a conventional Kalman Filter. Then, the equation of the filter (Equation 141 in this document) can be used by directly plugging in the values of the time marched estimated state vector $\hat{\mathbf{x}}_{k|k-1}$. The discretization scheme is hence free to be chosen by the user.

6.1 Assumptions

The most important assumptions made in the development of the filter are briefly gathered in the following list, among others that will be commented in due time:

- When updating the estimate with the measurements, the time evolution and measurement functions ($\mathbf{f}$ and $\mathbf{h}$, respectively) are linear in the true and estimated states, together with the control parameter.
- True states and observables differ from the model by including random variables in the form of additive white noise, $\mathbf{w}$ and $\mathbf{v}$, not necessarily gaussian.
- The random processes are, in a statistical sense, wide-sense stationary and ergodic.

6.2 Derivation

To start deriving of the working principles of the implemented EKF, it is necessary to recognize the difference between the true states $\mathbf{x}$ and observables $\mathbf{z}$; which can only be inferred by measurement of the system, and estimated or modeled states $\hat{\mathbf{x}}$ which are predicted by the solvers. These latter can allow to produce an estimation of the measured quantities $\hat{\mathbf{z}}$.

The system's estimated state vector $\hat{\mathbf{x}}$ is expressed in state space. This general representation of the time evolution differential equation of the system (which may be non-linear) ensures generality for any type of IVP. It is put together with the estimation of the measurements $\hat{\mathbf{z}}$:

$$\frac{d\hat{\mathbf{x}}}{dt} = \mathbf{f}(\hat{\mathbf{x}}, \mathbf{u}, t) \tag{117}$$

$$\hat{\mathbf{z}} = \mathbf{h}(\hat{\mathbf{x}}, t) \tag{118}$$

For error correction in the EKF, however, it is necessary to consider the model to be linear. Thus, a linearization process is carried out in both the predicted states and the control vector (denoted as $\mathbf{u}$), simplifying the expression for the evolution of modeled states and measurements. This process takes as an initial point the estimated states in the last iteration of the filter $\mathbf{x}_{k-1|k-1}$ as well as the control vector input at time zero $\mathbf{u}_{k-1}$:

$$\begin{aligned}
\frac{d\hat{\mathbf{x}}}{dt} &= \mathbf{f}(\hat{\mathbf{x}}, \mathbf{u}, t) = \mathbf{f}(\hat{\mathbf{x}}_{k-1|k-1}, \mathbf{u}, t) + \left.\frac{\partial \mathbf{f}}{\partial \hat{\mathbf{x}}}\right|_{\hat{\mathbf{x}}_{k-1|k-1}} \left(\hat{\mathbf{x}}(t) - \hat{\mathbf{x}}_{k-1|k-1}\right) \\
&+ \frac{1}{2}\left(\hat{\mathbf{x}}(t) - \hat{\mathbf{x}}_{k-1|k-1}\right)^T \left.\left(\frac{\partial}{\partial \hat{\mathbf{x}}}\frac{\partial \mathbf{f}}{\partial \hat{\mathbf{x}}}\right)\right|_{\hat{\mathbf{x}}_{k-1|k-1}} \left(\hat{\mathbf{x}}(t) - \hat{\mathbf{x}}_{k-1|k-1}\right) + \cdots \\
&\approx \mathbf{f}(\hat{\mathbf{x}}_{k-1|k-1}, \mathbf{u}, t) + \left.\frac{\partial \mathbf{f}}{\partial \hat{\mathbf{x}}}\right|_{\hat{\mathbf{x}}_{k-1|k-1}} \left(\hat{\mathbf{x}}(t) - \hat{\mathbf{x}}_{k-1|k-1}\right) \\
&\approx \mathbf{f}(\hat{\mathbf{x}}_{k-1|k-1}, \mathbf{u}_{k-1}) + \left.\frac{\partial \mathbf{f}}{\partial \mathbf{u}}\right|_{\hat{\mathbf{x}}_{k-1|k-1}, \mathbf{u}_{k-1}} (\mathbf{u} - \mathbf{u}_{k-1}) \; + \; \left.\frac{\partial \mathbf{f}}{\partial \hat{\mathbf{x}}}\right|_{\hat{\mathbf{x}}_{k-1|k-1}, \mathbf{u}_{k-1}} \left(\hat{\mathbf{x}}(t) - \hat{\mathbf{x}}_{k-1|k-1}\right) \\
&\approx \mathbf{f}(\hat{\mathbf{x}}_{k-1|k-1}, \mathbf{u}_{k-1}) + \left.\frac{\partial \mathbf{f}}{\partial \mathbf{u}}\right|_{\hat{\mathbf{x}}_{k-1|k-1}, \mathbf{u}_{k-1}} \left.\frac{\partial \mathbf{u}}{\partial \boldsymbol{\delta}}\right|_{\boldsymbol{\delta}=\mathbf{0}} \boldsymbol{\delta}_{k-1} \; - \; \left.\frac{\partial \mathbf{f}}{\partial \mathbf{u}}\right|_{\hat{\mathbf{x}}_{k-1|k-1}, \mathbf{u}_{k-1}} \mathbf{u}_{k-1} \; + \; \left.\frac{\partial \mathbf{f}}{\partial \hat{\mathbf{x}}}\right|_{\hat{\mathbf{x}}_{k-1|k-1}, \mathbf{u}_{k-1}} \left(\hat{\mathbf{x}}(t) - \hat{\mathbf{x}}_{k-1|k-1}\right) \\
&= \mathbf{r}_{k-1|k-1} + \mathbf{G}(t)\boldsymbol{\delta}_{k-1} + \mathbf{F}_k \, \hat{\mathbf{x}}(t)
\end{aligned} \tag{119}$$

It has been recognised that, if the state propagation function $\mathbf{f}$ is evaluated at the modeled states $\hat{\mathbf{x}}_{k-1|k-1}$ and control vector $\mathbf{u}_{k-1}$, it need not depend on time, which would mean that the physical model is not changing. A rearrangement of this control vector and control matrix $\mathbf{G}(t)$ can be carried out to simplify this approach, even if it implies including constants as control parameters. Hence, there is a user controlled vector of parameters $\boldsymbol{\delta}$ that influences the forcing terms, and is treated to behave linearly, being $\mathbf{u} = \mathbf{0}$ when $\boldsymbol{\delta} = \mathbf{0}$. An example of user-controlled parameter can be the aforementioned fuel parameter, which greatly influences the rest of thermodynamic states, that act as forcing terms in the IVP.

The Jacobian matrix to evolve to time step k, called $\mathbf{F}_k$, the control matrix $\mathbf{G}(t)$ and additional terms $\mathbf{r}_{k-1|k-1}$ have been shortened for a better comprehensiveness of the derivation. The dependence of $\mathbf{r}_{k-1|k-1}$ on time will be ignored for the rest of the analysis:

$$\mathbf{F}_k = \left.\frac{\partial \mathbf{f}}{\partial \hat{\mathbf{x}}}\right|_{\hat{\mathbf{x}}_{k-1|k-1},\mathbf{u}_{k-1}} \tag{120}$$

$$\mathbf{G}(t) = \left.\frac{\partial \mathbf{f}}{\partial \mathbf{u}}\right|_{\hat{\mathbf{x}}_{k-1|k-1},\mathbf{u}_{k-1}} \left.\frac{\partial \mathbf{u}}{\partial \boldsymbol{\delta}}\right|_{\boldsymbol{\delta}=\mathbf{0}} \tag{121}$$

$$\mathbf{r}_{k-1|k-1} = \mathbf{f}(\hat{\mathbf{x}}_{k-1|k-1}, \mathbf{u}_{k-1}) - \left.\frac{\partial \mathbf{f}}{\partial \mathbf{u}}\right|_{\hat{\mathbf{x}}_{k-1|k-1},\mathbf{u}_{k-1}} \mathbf{u}_{k-1} \quad - \quad \mathbf{F}_k\, \hat{\mathbf{x}}_{k-1|k-1} \tag{122}$$

In an almost identical way of applying the linearization process done in Equation 119, the measurement equation's results to be plugged into the EKF are derived from Equation 118:

$$\begin{aligned}
\hat{\mathbf{z}} = \mathbf{h}(\hat{\mathbf{x}}) &= \mathbf{h}(\hat{\mathbf{x}}_{k-1|k-1}) + \left.\frac{d\mathbf{h}}{d\hat{\mathbf{x}}}\right|_{\hat{\mathbf{x}}_{k-1|k-1}} \Big(\hat{\mathbf{x}}(t) - \hat{\mathbf{x}}_{k-1|k-1}\Big) \\
&+ \frac{1}{2}\Big(\hat{\mathbf{x}}(t) - \hat{\mathbf{x}}_{k-1|k-1}\Big)^T \left.\left(\frac{\partial}{\partial \hat{\mathbf{x}}}\frac{\partial \mathbf{f}}{\partial \hat{\mathbf{x}}}\right)\right|_{\hat{\mathbf{x}}_{k-1|k-1}} \Big(\hat{\mathbf{x}}(t) - \hat{\mathbf{x}}_{k-1|k-1}\Big) + \cdots \\
&\approx \mathbf{h}(\hat{\mathbf{x}}_{k-1|k-1}) + \left.\frac{d\mathbf{h}}{d\hat{\mathbf{x}}}\right|_{\hat{\mathbf{x}}_{k-1|k-1}} \Big(\hat{\mathbf{x}}(t) - \hat{\mathbf{x}}_{k-1|k-1}\Big) = \mathbf{s}_{k-1|k-1} + \mathbf{H}_k \hat{\mathbf{x}}(t)
\end{aligned} \tag{123}$$

Where now the measurement matrix $\mathbf{H}_k$ and a vector of linear independent terms $\mathbf{s}_{k-1|k-1}$, which will be considered independent of time in this analysis. Considering its probable dependence on time does not have an influence in the final solution:

$$\mathbf{H}_k = \left.\frac{\partial \mathbf{h}}{\partial \hat{\mathbf{x}}}\right|_{\hat{\mathbf{x}}_{k-1|k-1}} \tag{124}$$

$$\mathbf{s}_{k-1|k-1} = \mathbf{h}(\hat{\mathbf{x}}_{k-1|k-1}) - \mathbf{H}_k\, \hat{\mathbf{x}}_{k-1|k-1} \tag{125}$$

When estimating reality, the modeled states might include some error in the calculation. This is taken into account by adding a process noise vector $\mathbf{w}(t)$. As mentioned before, it is defined to contain white noise, assuming the difference between true and modeled states is the presence of random uncorrelated variables with zero mean. This process noise is added by the user, generally not directly as will be later described, to tweak the confidence of the filter in the model.

The same is applied to the measurement discrepancy with reality, which to reiterate, is supposed to be also represented by white noise too. The vector that includes this feature is called the measurement noise vector $\mathbf{v}(t)$. True state variables are gathered in the vector $\mathbf{x}$, while true measurements are stored in $\mathbf{z}$.

Performing the aforementioned linearization in Equation 119 and 123, also assumed valid in the case of the true states and observables:

$$\frac{d\mathbf{x}}{dt} = \mathbf{f}(\mathbf{x},\mathbf{u},t) + \mathbf{w}(t) \approx \mathbf{r}_{k-1|k-1} + \mathbf{G}(t)\boldsymbol{\delta}_{k-1} + \mathbf{F}_k\,\mathbf{x}(t) + \mathbf{w}(t) \tag{126}$$

$$\mathbf{z} = \mathbf{h}(\mathbf{x},t) + \mathbf{v}(t) \approx \mathbf{s}_{k-1|k-1} + \mathbf{H}_k\,\mathbf{x}(t) + \mathbf{v}(t) \tag{127}$$

The autocorrelation of the assumed white noise vectors is null when the signal is weighted with itself at different times in the process. This coincidence of time-based autocorrelation and statistic autocorrelation is due to the ergodicity assumption.

The variance of the signal is theoretically infinite in continuous time, not in discrete time where the noise bandwidth is limited and related to the inverse of the time step. It is returned when the function coincides in the cross-correlation operation ($t = 0$). Hence, this is expressed as the following for $\mathbf{w}$:

$$\mathcal{R}_{\mathbf{ww}}(t) = \mathbb{E}\left(\mathbf{w}(\tau)\mathbf{w}^T(\tau - t)\right) = \lim_{T_\mathrm{s}\to\infty}\frac{1}{T_\mathrm{s}}\int_{-T_\mathrm{s}/2}^{T_\mathrm{s}/2}\mathbf{w}(\tau)\mathbf{w}^T(\tau - t)d\tau = \delta(t)\mathbf{Q} \tag{128}$$

Where T_s is the sampling period. The expression $\mathcal{R}_{\mathbf{ww}}$ denotes the autocorrelation of the signal $\mathbf{w}$ and δ is a Dirac delta functional, which integrated over the sampling interval yields an evaluation of the expression inside the integral at time zero.

On the other hand, the matrix $\mathbf{Q}$ contains spectral power densities of the noise components. It is generally considered to be diagonal in Kalman filtering, hence assuming that the random variables that influence the process are uncorrelated between them. The form of $\mathbf{Q}$ becomes obvious when the Wiener-Khinchin theorem is applied, relating the autocorrelation with the spectral power density of the noise by means of a Fourier Transform:

$$\mathcal{S}_{\mathbf{ww}}(\omega) = \mathcal{F}\left\{\mathcal{R}_{\mathbf{ww}}\right\} = \int_{-\infty}^{\infty}\mathcal{R}_{\mathbf{ww}}(\tau)e^{-i\omega\tau}d\tau = \left(\int_{-\infty}^{\infty}\delta(\tau)e^{-i\omega\tau}d\tau\right)\mathbf{Q} = \mathbf{Q} \tag{129}$$

One more remark must be made, as the derivation of the filter requires to define the correlation between this noises. They are deemed to be totally uncorrelated. Thus, it is important to set the value of the following covariance matrices to be the zero matrix, ensuring that the random variables that model these white noises are totally uncorrelated:

$$\mathbb{E}\left(\mathbf{w}\mathbf{v}^T\right) = \mathbb{E}\left(\mathbf{v}\mathbf{w}^T\right) = [\mathbf{0}] \tag{130}$$

To continue with the derivation, the next step is to predict future modeled and true states, taking as starting conditions the instant $k-1$. For this, the Laplace transform is applied, first to the true state evolution in Equation 126, process which will be repeated for Equation 119, but will not be shown here, as it consists of the same steps and involves less terms. Doing so yields the following:

$$\boldsymbol{x}(s) = (s\mathbf{I} - \mathbf{F}_k)^{-1}\left(\mathbf{x}_{k-1} + \boldsymbol{G}(s)\boldsymbol{\delta}_{k-1} + \boldsymbol{r}_{k-1|k-1}(s) + \boldsymbol{w}(s)\right)$$

Where the characters in italics denote the corresponding function's Laplace transform. Applying the inverse Laplace transform to the whole expression, together the convolution theorem, yields the following formula, analytically obtained for a space state linear system.

$$\begin{aligned}\mathbf{x}(t) = e^{t\mathbf{F}_k}\mathbf{x}_{k-1} + \Big(\Big(e^{\tau\mathbf{F}_k} * \mathbf{G}\left(\tau\right)\Big)\left(t\right)\Big)\boldsymbol{\delta}_{k-1} + \Big(e^{\tau\mathbf{F}_k} * \mathbf{r}_{k-1|k-1}\left(\tau\right)\Big)\left(t\right)\\ + \Big(e^{\tau\mathbf{F}_k} * \mathbf{w}\left(\tau\right)\Big)\left(t\right)\end{aligned} \tag{131}$$

Where the term $e^{t\mathbf{F}_k}$ represents the matrix exponential of the quantity $t\mathbf{F}_k$. It has the following expression, related to a Taylor series expansion and the state transition matrix $\mathbf{\Phi}_k$, which represents its truncation:

$$e^{t\mathbf{F}_k} = \sum_{m=0}^{\infty}\frac{t^m}{m!}\mathbf{F}_k^m = \mathbf{I} + t\mathbf{F}_k + \frac{t^2}{2}\mathbf{F}_k^2 + \cdots = \mathbf{\Phi}(t) \approx \mathbf{I} + t\mathbf{F}_k \tag{132}$$

It is usually sufficient to consider a truncation up to the linear term. That will be taken into consideration for the rest of this study because in few cases, when the model is highly non-linear, this has an appreciable effect. Finally, evaluating Equation 131 after a time step Δt yields the predicted real-world state in time-step k, which to reiterate, is differentiated from the model by including white noise, which is also propagated in a convolution with the state transition matrix. This matrix is denoted as $\mathbf{\Phi}_k$ after evaluation.

$$\mathbf{x}_k \approx \mathbf{\Phi}_k\mathbf{x}_{k-1} + \left(\mathbf{\Phi} * \mathbf{G}\right)_k\boldsymbol{\delta}_{k-1} + \Big(\mathbf{\Phi} * \mathbf{r}_{k-1|k-1}\Big)_k + \left(\mathbf{\Phi} * \mathbf{w}\right)_k \tag{133}$$

The convolution is defined in the Laplace sense, where the integrands are considered to be causal functions. If a generic function $\mathbf{f}$, not necessarily vector as expressed here of vector-valued, is convolved with $\mathbf{\Phi}$:

$$\begin{aligned}\left(\mathbf{\Phi} * \mathbf{f}\right)(t) &= \int_0^{\infty}\mathbf{\Phi}(\tau)\mathbf{f}(t-\tau)d\tau = \int_0^{t}\mathbf{\Phi}(\tau)\mathbf{f}(t-\tau)d\tau\\ \Rightarrow\ \left(\mathbf{\Phi} * f\right)_k &= \int_0^{\Delta t}\mathbf{\Phi}(\tau)\mathbf{f}(\Delta t-\tau)d\tau\end{aligned}$$

Since by definition of causal function $f(\tau) = 0\ \forall\tau < 0$. It is evaluated a time step Δt away from the initial moment $k-1$, which corresponds to $t = 0$. Renaming the advanced control matrix $\left(\mathbf{\Phi} * \mathbf{G}\right)_k$, advanced process noise vector $\left(\mathbf{\Phi} * \mathbf{G}\right)_k$, and advanced independent terms the following $\Big(\mathbf{\Phi} * \mathbf{r}_{k-1|k-1}\Big)_k$, for the sake of simplicity throughout the rest of the derivation:

$$\mathbf{G}_k = \int_0^{\Delta t}\mathbf{\Phi}(\tau)\mathbf{G}(\Delta t-\tau)d\tau \tag{134}$$

$$\mathbf{r}_{k|k-1} = \int_0^{\Delta t}\mathbf{\Phi}(\tau)\mathbf{r}_{k-1|k-1}d\tau \tag{135}$$

$$\mathbf{w}_k = \int_0^{\Delta t}\mathbf{\Phi}(\tau)\mathbf{w}(\Delta t-\tau)d\tau \tag{136}$$

Equation 127 and 133 are thus rewritten in considerably simpler expressions, indicated for time step k. They are given in Equation 137 and 138.

$$\mathbf{x}_k \approx \mathbf{\Phi}_k \mathbf{x}_{k-1} + \mathbf{G}_k \boldsymbol{\delta}_{k-1} + \mathbf{r}_{k|k-1} + \mathbf{w}_k \tag{137}$$

$$\mathbf{z}_k = \mathbf{h}(\mathbf{x}_k) + \mathbf{v}_k \approx \mathbf{s}_{k-1|k-1} + \mathbf{H}_k \mathbf{x}_k + \mathbf{v}_k \tag{138}$$

This trend is continued when referring to the model predicted states $\hat{\mathbf{x}}$, before and after the correction due to measurements. In an analogous manner to what has been derived for the true solution, the estimated states and observables are carried through the same process of discretization. Note that the solution given by the process is first transitioned in time. Thus notation-wise, only the first subindices in Equation 139 and 140 are consequently updated:

$$\hat{\mathbf{x}}_{k|k-1} \approx \mathbf{\Phi}_k \hat{\mathbf{x}}_{k-1|k-1} + \mathbf{G}_k \boldsymbol{\delta}_{k-1} + \mathbf{r}_{k|k-1} \tag{139}$$

$$\hat{\mathbf{z}}_{k|k-1} = \mathbf{h}(\hat{\mathbf{x}}_{k|k-1}) \approx \mathbf{s}_{k-1|k-1} + \mathbf{H}_k \hat{\mathbf{x}}_{k|k-1} \tag{140}$$

The filter then acts to make a correction to the predicted state by making use of the estimate error between the measurements and the model. It also ensures that the filtered solution states are unbiased with respect to the true states. This term means that the expected value of the true state $\mathbf{x}_k$ and the predicted state $\hat{\mathbf{x}}_{k|k}$ are the same. If their difference; which represents the error, is seen as a statistic, it has an expected value of zero, being this the reason why it is called unbiased.

The interpretation of the following Equation 141 is not as clear as one may think, because the Kalman gain $\mathbf{K}_k$ still needs to be found. However, its working principle is generally explained as a linear interpolation between the states projected by the model and the anticipated result by attending to measured values:

$$\hat{\mathbf{x}}_{k|k} = \hat{\mathbf{x}}_{k|k-1} + \mathbf{K}_k \left(\mathbf{z}_k - \hat{\mathbf{z}}_{k|k-1} \right) \tag{141}$$

Denote as $\widetilde{\mathbf{x}}_k$ the error between the true and estimate solution after k time steps and measurements. Suppose initially, as a base case, that the filter's initial condition complies with the unbiased process assumption, stated before:

$$\widetilde{\mathbf{x}}_k = \mathbf{x}_k - \hat{\mathbf{x}}_{k|k} \tag{142}$$

$$\mathbb{E}(\mathbf{x}_0 - \hat{\mathbf{x}}_{0|0}) = \mathbb{E}(\widetilde{\mathbf{x}}_0) = \mathbf{0} \tag{143}$$

$$\Rightarrow \ \hat{\mathbf{x}}_{0|0} = \mathbb{E}(\mathbf{x}_0) \tag{144}$$

Suppose that for some $k \in \mathbb{N}$ the assumption $\mathbb{E}(\widetilde{\mathbf{x}}_{k-1}) = \mathbf{0}$ holds true, conforming a weak induction hypothesis. Substitute Equation 137 and 139 for the evolution of states. Note that $\mathbb{E}\left(\mathbf{w}_k\right) = \mathbb{E}\left(\mathbf{v}_k\right) = \mathbf{0}$. Also, apply the linearization of the measurement functions in Equation 138 and Equation 140.

Equation 145 proves that the chosen filtering relation in Equation 141 approximately respects the unbiased estimator condition, if the initialization is adequate enough and if the functions behave in an almost linear way. The induction step for the mean error in time k consequently reads the next expression:

$$\begin{aligned}
\mathbb{E}(\widetilde{\mathbf{x}}_k) = \mathbb{E}\left(\mathbf{x}_k - \hat{\mathbf{x}}_{k|k}\right) &\approx \mathbb{E}\left(\mathbf{\Phi}_k\left(\mathbf{x}_{k-1} - \hat{\mathbf{x}}_{k-1|k-1}\right) - \mathbf{K}_k\left(\mathbf{h}(\mathbf{x}_k) - \mathbf{h}(\hat{\mathbf{x}}_{k|k-1}) + \mathbf{v}_k\right) + \mathbf{w}_k\right) \\
&= \mathbf{\Phi}_k\mathbb{E}\left(\mathbf{x}_{k-1} - \hat{\mathbf{x}}_{k-1|k-1}\right) - \mathbf{K}_k\left(\mathbb{E}\left(\mathbf{h}(\mathbf{x}_k) - \mathbf{h}(\hat{\mathbf{x}}_{k|k-1})\right) + \mathbb{E}\left(\mathbf{v}_k\right)\right) + \mathbb{E}\left(\mathbf{w}_k\right) \\
&\approx \mathbf{\Phi}_k\mathbb{E}\left(\mathbf{x}_{k-1} - \hat{\mathbf{x}}_{k-1|k-1}\right) - \mathbf{K}_k\mathbf{H}_k\mathbb{E}\left(\mathbf{x}_k - \hat{\mathbf{x}}_{k|k-1}\right) \\
&\approx \mathbf{\Phi}_k\mathbb{E}\left(\mathbf{x}_{k-1} - \hat{\mathbf{x}}_{k-1|k-1}\right) - \mathbf{K}_k\mathbf{H}_k\mathbf{\Phi}_k\mathbb{E}\left(\mathbf{x}_{k-1} - \hat{\mathbf{x}}_{k-1|k-1}\right) - \mathbf{K}_k\mathbf{H}_k\mathbb{E}\left(\mathbf{w}_k\right) \\
&= \left(\mathbf{I} - \mathbf{K}_k\mathbf{H}_k\right)\mathbf{\Phi}_k\mathbb{E}(\widetilde{\mathbf{x}}_{k-1}) \\
&= \mathbf{0}
\end{aligned} \tag{145}$$

Then, it is necessary to define one of the fundamental parameters in the EKF, the filter's covariance matrix after k time steps and k measurements $\mathbf{P}_{k|k}$. It has the following expression, again making use of Equation 137. 138, 139 and 140:

$$\begin{aligned}
\mathbf{P}_{k|k} &= \mathbb{E}\left(\widetilde{\mathbf{x}}_k\widetilde{\mathbf{x}}_k^T\right) = \mathbb{E}\left(\left(\mathbf{x}_k - \hat{\mathbf{x}}_{k|k}\right)\left(\mathbf{x}_k - \hat{\mathbf{x}}_{k|k}\right)^T\right) \\
&\approx \mathbb{E}\Big(\Big(\left(\mathbf{I} - \mathbf{K}_k\mathbf{H}_k\right)\left(\mathbf{\Phi}_k\widetilde{\mathbf{x}}_{k-1} + \mathbf{w}_k\right) - \mathbf{K}_k\mathbf{v}_k\Big)\Big(\left(\mathbf{I} - \mathbf{K}_k\mathbf{H}_k\right)\left(\mathbf{\Phi}_k\widetilde{\mathbf{x}}_{k-1} + \mathbf{w}_k\right) - \mathbf{K}_k\mathbf{v}_k\Big)^T\Big) \\
&= \left(\mathbf{I} - \mathbf{K}_k\mathbf{H}_k\right)\left(\mathbf{\Phi}_k\mathbb{E}\left(\widetilde{\mathbf{x}}_{k-1}\widetilde{\mathbf{x}}_{k-1}^T\right)\mathbf{\Phi}_k^T + \mathbb{E}\left(\mathbf{w}_k\mathbf{w}_k^T\right)\right)\left(\mathbf{I} - \mathbf{K}_k\mathbf{H}_k\right)^T + \mathbf{K}_k\mathbb{E}\left(\mathbf{v}_k\mathbf{v}_k^T\right)\mathbf{K}_k^T \\
&= \left(\mathbf{I} - \mathbf{K}_k\mathbf{H}_k\right)\left(\mathbf{\Phi}_k\mathbf{P}_{k-1|k-1}\mathbf{\Phi}_k^T + \mathbf{Q}_k\right)\left(\mathbf{I} - \mathbf{K}_k\mathbf{H}_k\right)^T + \mathbf{K}_k\mathbf{R}_k\mathbf{K}_k^T \\
&= \left(\mathbf{I} - \mathbf{K}_k\mathbf{H}_k\right)\mathbf{P}_{k|k-1}\left(\mathbf{I} - \mathbf{K}_k\mathbf{H}_k\right)^T + \mathbf{K}_k\mathbf{R}_k\mathbf{K}_k^T
\end{aligned} \tag{146}$$

The process noise covariance matrix $\mathbf{Q}_k$ has been defined. A relation between it and the spectral power density process noise needs to be derived. In it, the expected value operator is slipped inside of the following integral sign, acquiring a continuous time meaning [22]:

$$\begin{aligned}
\mathbf{Q}_k = \mathbb{E}\left(\mathbf{w}_k\mathbf{w}_k^T\right) &= \mathbb{E}\left((\mathbf{\Phi} * \mathbf{w})_k(\mathbf{\Phi} * \mathbf{w})_k^T\right) = \mathbb{E}\left((\mathbf{\Phi} * \mathbf{w})_k(\mathbf{w}^T * \mathbf{\Phi}^T)_k\right) \\
&= \mathbb{E}\left(\int_0^{\Delta t}\int_0^{\Delta t}\mathbf{\Phi}(\tau_1)(\mathbf{w}(\Delta t - \tau_1)\mathbf{w}^T(\Delta t - \tau_2))\mathbf{\Phi}(\tau_2)d\tau_1 d\tau_2\right) \\
&= \int_0^{\Delta t}\int_0^{\Delta t}\mathbf{\Phi}(\tau_1)\mathbb{E}(\mathbf{w}(\Delta t - \tau_1)\mathbf{w}^T(\Delta t - \tau_2))\mathbf{\Phi}(\tau_2)d\tau_1 d\tau_2
\end{aligned}$$

$\mathbf{Q}_k$ is related to the process noise spectral power density matrix $\mathbf{Q}$, after the continuous time autocorrelation is taken inside of the integral, noting that the variance of the continuous time process white noise signal $\mathbf{w}$ infinite.

The Dirac delta resultant from Equation 128 is of the form $\mathbb{E}(\mathbf{w}(\Delta t - \tau_1)\mathbf{w}^T(\Delta t - \tau_2)) = \delta(\tau_1 - \tau_2)\mathbf{Q}$. Integrating in τ_1 and then, changing $\tau_2 \rightarrow \tau$ yields the final form for $\mathbf{Q}_k$:

$$\mathbf{Q}_k = \int_0^{\Delta t} \mathbf{\Phi}(\tau)\mathbf{Q}\mathbf{\Phi}^T(\tau)d\tau \tag{147}$$

Where $\mathbf{Q}$ is not assumed to depend on time because of the statistically wide-sense stationary behavior of the noise. In Equation 146, $\mathbf{R}_k$ is the Measurement Noise Covariance Matrix. Both $\mathbf{Q}_k$ and $\mathbf{R}_k$ are parameters to be estimated by the user and fed into the filter, paying attention to the processes' or measurements' confidence at instant k. Because the expected value is taken in discrete time, the covariance between all random variables is bounded, unlike theoretical full-bandwidth continuous time white noise.

$$\mathbf{R}_k = \mathbb{E}(\mathbf{v}_k\mathbf{v}_k^T) \tag{148}$$

$\mathbf{R}_k$ is generally taken to be diagonal. If the variances are located in the principal directions, then additive random variables that affect measurement are not correlated. This does not imply a general independence, but it instead their linear independence. Finally, the time advanced filter covariance matrix $\mathbf{P}_{k|k-1}$ is given by the formula:

$$\mathbf{P}_{k|k-1} = \mathbf{\Phi}_k\mathbf{P}_{k-1|k-1}\mathbf{\Phi}_k^T + \mathbf{Q}_k \tag{149}$$

The last requisite for the filter is to minimize the mean squared error between the true and estimated states. This is done by finding the k-th step Kalman gain $\mathbf{K}_k$ to allow so. The mean square error is related to the trace of the covariance matrix $\mathbf{P}_{k|k}$. Hence, the quantity to minimize is expressed as:

$$\begin{aligned} \mathbb{E}\left(\|\mathbf{x}_k - \hat{\mathbf{x}}_{k|k}\|^2\right) &= \mathbb{E}\left(\widetilde{\mathbf{x}}_k^T\widetilde{\mathbf{x}}_k\right) = \operatorname{tr}\left(\mathbf{P}_{k|k}\right) \\ &= \operatorname{tr}\left(\left(\mathbf{I} - \mathbf{K}_k\mathbf{H}_k\right)\mathbf{P}_{k|k-1}\left(\mathbf{I} - \mathbf{K}_k\mathbf{H}_k\right)^T\right) + \operatorname{tr}\left(\mathbf{K}_k\mathbf{R}_k\mathbf{K}_k^T\right) \end{aligned} \tag{150}$$

Finding the minimum requires taking the matrix gradient to the above expression and setting the result to equal the zero vector. Applying trace derivative rules with respect to a column vector defined matrix yields:

$$\begin{aligned} \frac{\partial \operatorname{tr}(\mathbf{P}_{k|k})}{\partial \mathbf{K}_k} &= -2\left(\mathbf{I} - \mathbf{K}_k\mathbf{H}_k\right)\mathbf{P}_{k|k-1}\mathbf{H}_k^T + 2\mathbf{K}_k\mathbf{R}_k = \mathbf{0} \\ \Rightarrow \mathbf{K}_k &= \mathbf{P}_{k|k-1}\mathbf{H}_k^T\left(\mathbf{H}_k\mathbf{P}_{k|k-1}\mathbf{H}_k^T + \mathbf{R}_k\right)^{-1} \end{aligned} \tag{151}$$

Where the found value of $\mathbf{K}_k$ is called the optimal Kalman gain, as it minimizes the variance between the noise-affected true states and the filter estimate ones. Thus, an unbiased quadratic error minimizing filter is achieved. The last step of the derivation consists on obtaining an expression for $\mathbf{P}_{k|k}$ after finding the optimum value for the gain.

To achieve this, suffices to plug in the optimal value of $\mathbf{K}_k$ into the description of the evolution of $\mathbf{P}_{k|k}$ (see Equation 146). After expanding and substituting Equation 151 into the last term, the cancellation of the last two follows:

$$\mathbf{P}_{k|k} = \mathbf{P}_{k|k-1} - \mathbf{K}_k\mathbf{H}_k\mathbf{P}_{k|k-1} - \mathbf{P}_{k|k-1}\mathbf{H}_k^T\mathbf{K}_k^T + \mathbf{K}_k\left(\mathbf{H}_k\mathbf{P}_{k|k-1}\mathbf{H}_k^T + \mathbf{R}_k\right)\mathbf{K}_k^T$$

$$\Rightarrow\ \mathbf{P}_{k|k} = \left(\mathbf{I} - \mathbf{K}_k\mathbf{H}_k\right)\mathbf{P}_{k|k-1} \tag{152}$$

It is thus necessary to plug in the found optimal Kalman gain $\mathbf{K}_k$ in Equation 141 as well as having information about the method's covariance matrix $\mathbf{P}_{k|k}$ obtained through this linearization step. Then $\hat{\mathbf{x}}_{k|k}$ is found and the observables can also be updated in consequence to $\hat{\mathbf{z}}_{k|k} = \mathbf{h}(\hat{\mathbf{x}}_{k|k})$ with the estimate, although this is not necessary for the process. Figure 82 schematizes the block diagram for the EKF:

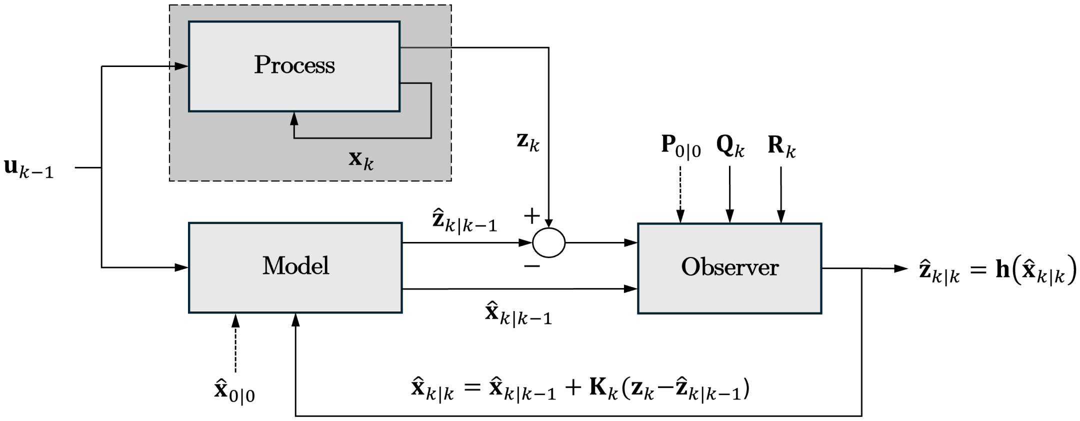

Figure 82: Block Diagram for the EKF.

As a summary, the filter requires the estimation of the continuous state transition matrix $\mathbf{\Phi}$, which requires knowledge about the Jacobian matrix of the differential equation $\mathbf{F}_k$. $\mathbf{H}_k$ is also required, see Equation 151 and 152. On another hand, there are several values that need to be estimated by the user of the EKF. They are gathered in the following list:

- The process noise spectral power density matrix $\mathbf{Q}$ or, in order to avoid considering the spectral behavior of the simulated white noise, directly impose the process noise covariance matrix $\mathbf{Q}_k$, respecting its possible anatomy.
- The measurement noise covariance matrix in each iteration k, namely $\mathbf{R}_k$. Reiterating, it is generally considered to be diagonal, as many sensors do not introduce errors on consequent measurements. This, however, might be the case of a sensor interfering in the internal flow of an engine and contaminating subsequent measurements.
- The initial value of the filter covariance matrix $\mathbf{P}_{0|0}$ also needs to be given. The speed in which the filter settles down depends strongly on the chosen value of $\mathbf{P}_{0|0}$.
- The initial condition of the IVP, stated as $\hat{\mathbf{x}}_{0|0}$ in the Kalman filtering process. To respect the non-bias condition of the filter, a value respecting the condition $\hat{\mathbf{x}}_{0|0} = \mathbb{E}\left(\hat{\mathbf{x}}_0\right)$ needs to be imposed.

6.3 Application to the Current Problem

In the current transient state problem for the laboratory-scale *AMT Netherlands Olympus HP* used for the validation the EKF will be tested. Several parametric studies will be conducted, to test what the response of the filter is in each of the cases. For the current case, the state $\hat{\mathbf{x}}_{k|k}$ that evolves in time through a differential equation is the shaft corrected speed, a scalar. The number of measured observables is hereby denoted as n_z. Table 18 summarizes the dimension of some features in the filter:

Parameter	**Dimensions**
$\hat{\mathbf{x}}$	1 x 1
$\mathbf{F}$	1 x 1
$\mathbf{\Phi}$	1 x 1
$\mathbf{H}$	n_z x 1
$\mathbf{K}$	1 x n_z
$\mathbf{P}$	1 x 1
$\mathbf{Q}$	1 x 1
$\mathbf{R}$	n_z x n_z

Table 18: Parameter Dimensions in the Implemented EKF.

The time evolution function $\mathbf{f}$ is given in Equation 55. The Jacobian matrix $\mathbf{F}$ is numerically approximated in each time step by calculating the numerical derivative after imposing the adequate fuel parameter, which is the control input $\mathbf{u}_{k-1}$. The measurement Jacobian matrix $\mathbf{H}$ is also approximated numerically, by acknowledging that the measurement function $\mathbf{h}$ is given by the solution method itself for many of the observables. Additional parameters of the *Olympus* engine need to be supplied. These include the corrected inertia [19], a predicted state starting point and time discretization parameters of a forward Euler method. Table 10, used for steady state validation, together with Table 19 totally define the problem.

Parameter	**Value**
I^* [kgm^2]	$2 \cdot 10^{-5}$
$\hat{\mathbf{x}}_{0\|0}$ [rpm]	60,000
$\mathbf{P}_{0\|0}$ [rpm^2]	10,000
N_p [-]	309
Δt [s]	0.02

Table 19: Additional Values for the Kalman Filter Simulation.

The fuel parameter input has a slightly different definition from the one given in past analyses, but the method has been corrected to deal with it. It is supposed to be exact, meaning that no uncertainties are present in its definition. This control term was obtained from the measurements in the UPV test rig. It has the form of a *slam* input:

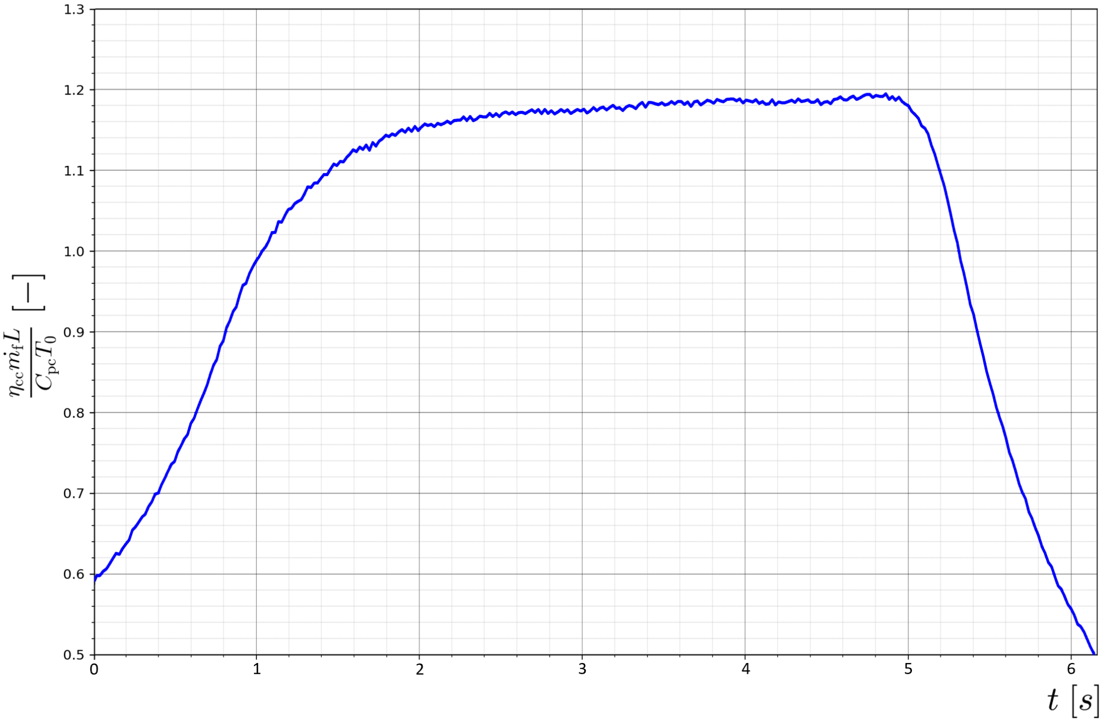

Figure 83: Modified Fuel Parameter Input in the EKF Algorithm.

3 different and simple studies will be carried out. These studies will serve to validate the proposed filtered transient model, when adjusting the estimations to the measurements. First of all, there is a need of evaluating the response of the filter when there is a change in the proportion of process noise compared to measurement noise.

Thus, a first study will focus on varying the process noise spectral power density matrix $\mathbf{Q}$ with a constant measurement noise covariance matrix $\mathbf{R}_k$. The second study will consist on inferring the influence of adding or subtracting measured variables in the system. Then, as mentioned, in third place there will be a brief investigation about the degree of $\mathbf{\Phi}$. This is summarized in Table 20.

	Case 1	**Case 2**	**Case 3**
Description	Parametric study in $\mathbf{Q}$	Measurement study	Truncation of $\mathbf{\Phi}$
No. of Observables	2	7	2
Degree of $\mathbf{\Phi}$	2	2	1

Table 20: Description of the EKF Studied Cases.

As will be made clear in following steps, the transient behavior of the system does not at all adjust to what could be expected from a single spool engine. In acceleration the compressor total pressure ratio appears to be lower than in deceleration. This can be produced by numerous reasons, including the following:

- **Sensor Systematic Errors**

  If a sensor is returning inexact readings due to, for example, a bad placement or usage wear, it can affect the determination of other parameters, like in this case the corrected inlet mass flow. It is measured according to the nozzle calibration curve presented in Figure 24.

- **Combustion Beyond CC**

  Delay in combustion in transient maneuvers is a common feature in the *Olympus HP*. It can greatly affect measurements and the operation of components. The model is incapable of predicting chemical equilibrium heat addition outside of the combustion chamber.

- **Low Inertia Effects**

  Since the axis inertia is very low, the time it takes the engine to adapt to changes is quick in consequence. This can lead to higher order transient effects, not only heat or mass pocketing, that are coming into play.

The state transition matrix $\mathbf{\Phi}$ will generally be truncated up to the quadratic term, except when studying the effect of truncating it even more. Thus, noting that $\mathbf{\Phi}$ and $\mathbf{Q}$ are scalars, while performing the integration in Equation 147 for obtaining $\mathbf{Q}_k$ in the quadratic case:

$$\begin{aligned}\mathbf{Q}_k &= \mathbf{Q}\int_0^{\Delta t}\left(1+\mathbf{F}_k\tau+\frac{1}{2}\mathbf{F}_k^2\tau^2\right)^2 d\tau \\ &= \mathbf{Q}\left(\Delta t+\mathbf{F}_k\left(\Delta t\right)^2+\frac{2}{3}\mathbf{F}_k^2\left(\Delta t\right)^3+\frac{1}{4}\mathbf{F}_k^3\left(\Delta t\right)^4+\frac{1}{20}\mathbf{F}_k^4\left(\Delta t\right)^5\right)\end{aligned} \tag{153}$$

The measurement noise covariance matrix $\mathbf{R}_k$ will be considered constant in time. The 2 measurements included for all cases except Case 2 are $\dot{m}_0^*$, and $p_{3\mathrm{t}}/p_0$. The noises are, as explained, considered to be uncorrelated between them, forging a diagonal matrix:

$$\mathbf{R}_k = \begin{pmatrix} 2\cdot 10^{-1} & 0 \\ 0 & 8\cdot 10^{-2}\end{pmatrix} \quad \forall k \in \{0,1,2,...,N_\mathrm{p}\} \tag{154}$$

These presented values for $\mathbf{Q}_k$ and $\mathbf{R}_k$ will be valid for the majority of cases stated in Table 20. $\mathbf{R}_k$ in Equation 154 has multiple units, all of them expressed in the International System of Units (SI). Nonetheless, if in the following studies there is a variation of any of these formulae, it will be noted in each subsequent case. Note how the entry related to temperature ratio is given a higher variance in comparison with the pressure ratio.

- **Case 1**

For this first case 4 different values for the process noise spectral power density are tested. They will differ between them by a large amount, so these quantities are better measured in logarithmic units, more specifically decibel watts, denoted as dBW. The case of having no process noise correspond to $-\infty$ dBW.

Having a high value of the process noise drives the filter to stick to what the measurements are indicating, thus the prediction should be more similar to the observed values. This can be seen as the case when plotting the filtered compressor operating lines, where the measurements in UPV test rig are also indicated.

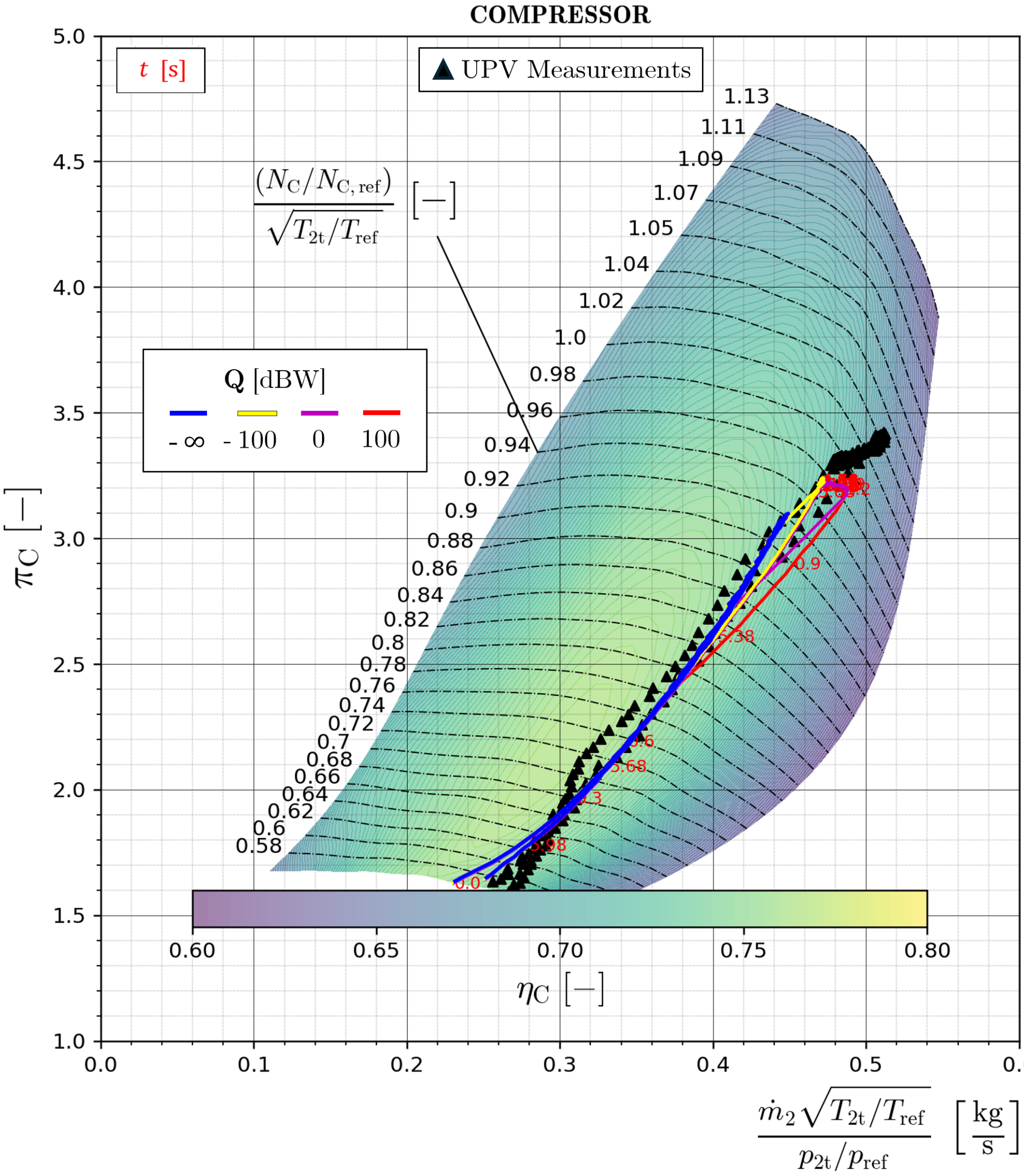

Figure 84: Filtered Compressor Operating Lines along Evolution for Different Values of Process Noise Spectral Power Density Including UPV Test Rig Measurements.

Note in Figure 84 how the measurements obtained in the UPV test rig predict the reversal of the operating line when plotted onto the compressor map. To reiterate, this is not the expected behavior, so the model struggles to follow the solution.

In fact, when no process noise is added (blue curve in Figure 84), the filter adapts to the transient general solution model that has been devised in this work, without the perceptible contribution of the measurements. On the contrary, when measurements are highly taken into account (high process noise) the filtered results are able to follow this trend, where the operating line transits a higher compressor total pressure ratio in deceleration, rather than in acceleration.

If the evolution of the predicted corrected speed and corrected thrust are followed, the filter produces abrupt changes in the time evolution, very quickly commuting from following the model to following the measurements. Observe Figure 85:

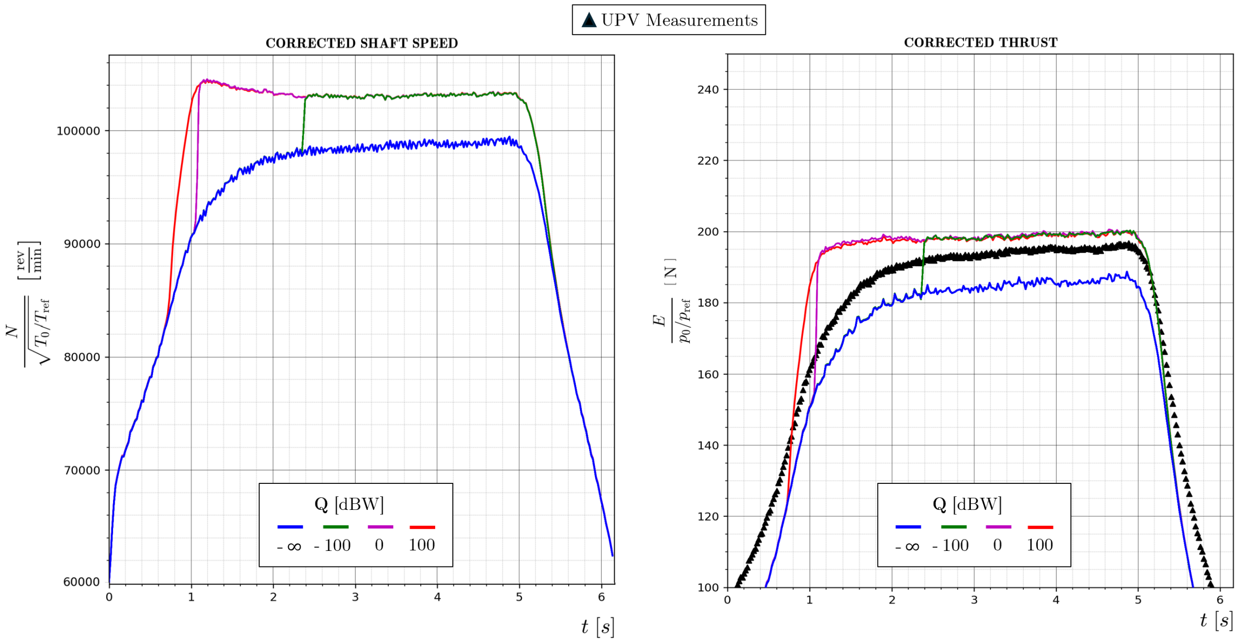

Figure 85: Filtered Corrected Shaft Speed (left) and Filtered Corrected Thrust (right) Time Evolution for Different Values of Process Noise Spectral Power Density.

This can caused by multiple reasons. It is believed that, due to the model having a considerable systematic error in comparison to the measurements, sudden changes in the evolution are necessary to adequately follow the trend. Perhaps the value of the inertia must be tweaked to allow for a better representation of the observables, or even increasing the uncertainty in measurements and considering more of them (Case 2). Recall that the discrepancy between true states and measurements with the estimated ones is assumed to have the form of white noise. The error between the pure model observables and the real measurements is absolutely not consistent with this hypothesis.

This jump is delayed the more the model is trusted, so the power spectral density of the process noise can help tweak the confidence of the filter in the model. Notice how for $\mathbf{Q} \to -\infty$ dBW, the model is completely trusted and no jump towards the measured values are present.

- **Case 2**

  In this case 5 more measurements are added to the model, enriching the existing information. The 7 total possible measurements in this case are, respectively: $\dot{m}_0^*$, $T_{3\mathrm{t}}/T_0$, $p_{3\mathrm{t}}/p_0$, $p_{4\mathrm{t}}/p_{3\mathrm{t}}$, $T_{5\mathrm{t}}/T_0$, $p_{5\mathrm{t}}/p_0$ and E^*. Now, the full measurement covariance matrix has size 7x7, being constant in time and diagonal:

$$\mathbf{R}_k = \begin{pmatrix} 2\cdot10^{-1} & 0 & 0 & 0 & 0 & 0 & 0 \\ 0 & 2\cdot10^{-1} & 0 & 0 & 0 & 0 & 0 \\ 0 & 0 & 8\cdot10^{-2} & 0 & 0 & 0 & 0 \\ 0 & 0 & 0 & 1\cdot10^{-1} & 0 & 0 & 0 \\ 0 & 0 & 0 & 0 & 2\cdot10^{-1} & 0 & 0 \\ 0 & 0 & 0 & 0 & 0 & 8\cdot10^{-2} & 0 \\ 0 & 0 & 0 & 0 & 0 & 0 & 10 \end{pmatrix} \quad \forall k \in \{0, 1, 2, ..., N_{\mathrm{p}}\} \tag{155}$$

  The process noise spectral power density **Q** considered in this case will be 100 dBW (or 10^{10} rpm^2/s^3, in natural units). Alluding to units, albeit Equation 155 has multiple entries with certain units, all variances will be considered to expressed in SI terms, allowing to be compatible with the presented procedures. Given this setup, observe the reduction in the value of the (scalar) covariance matrix:

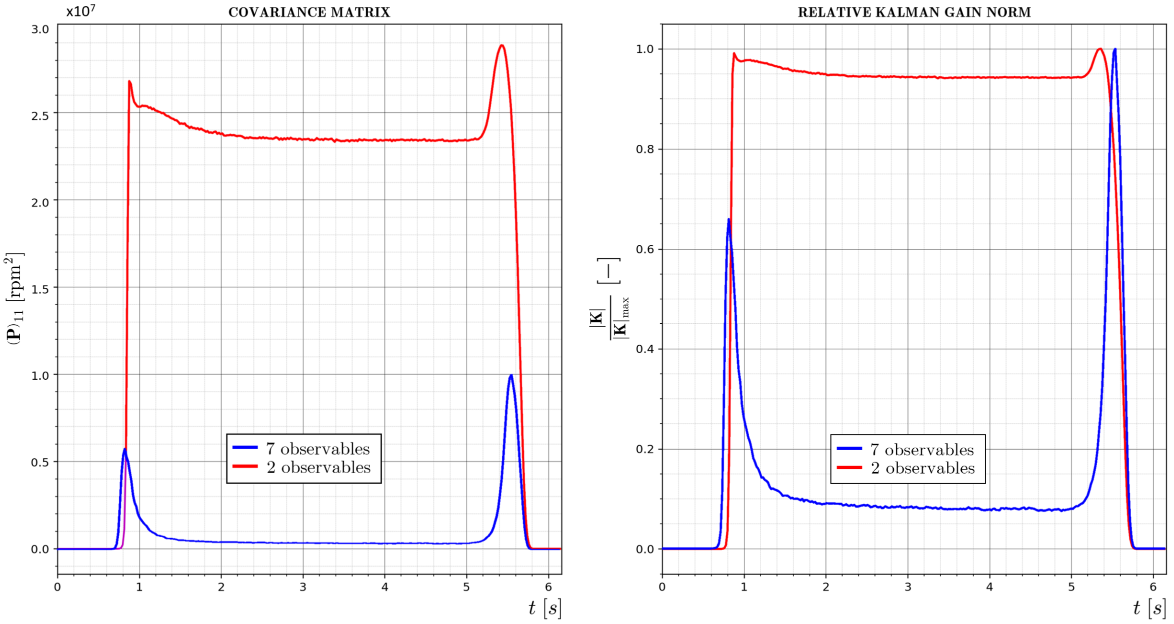

Figure 86: Filter Covariance Matrix (left) and Relative to Maximum Kalman Gain Norm (right) Time Evolution for Different Number of Observables.

Note how the optimal Kalman gain is linked to the evolution of the covariance matrix (recall Equation 152), as both peak at the end of the acceleration and at the start of the deceleration.

This might be an indicator of the failure of the model predicting the response of the engine variables after the *slam* input. Note that the systematic error between the measurements and the model forces the Kalman gain to be high in those instants.

Considering 7 observables not only makes the model gain stability and precision by feeding more information about the system, but also in this case has helped reduce the variance between measurements and model. Observe in Figure 87 how the running line is not as forced to be balanced with imposed measurement values as before, in Case 1 (see also Figure 84).

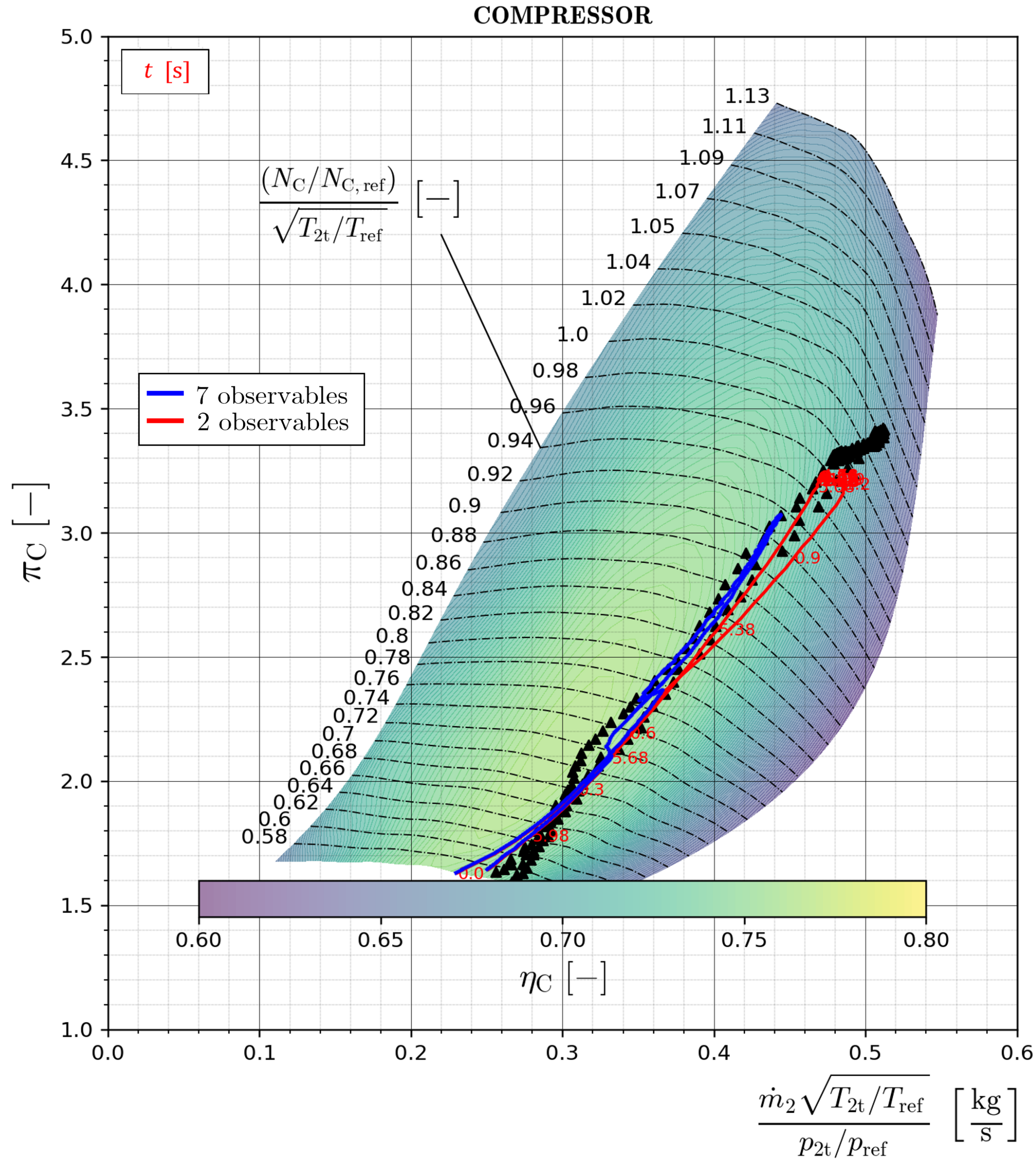

Figure 87: Filtered Compressor Operating Lines for Different Number of Observables Including UPV Test Rig Measurements.

Note in Figure 88 how adding more observables to the filter can absolutely modify the outcome of the process, as the model tends to adapt to a broader set of parameters with their respective noisiness.

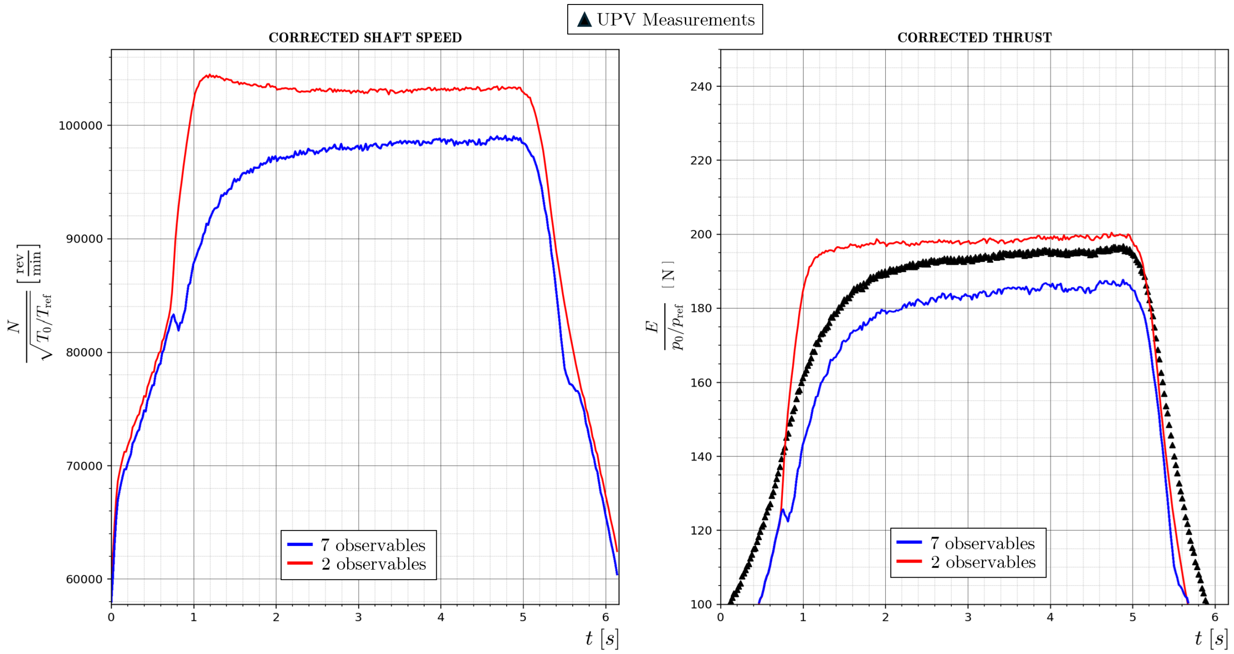

Figure 88: Filtered Corrected Shaft Speed (left) and Filtered Corrected Thrust (right) Time Evolution for Different Number of Observables.

In Case 1, the system tried to adapt to measurements of inlet corrected mass flow $\dot{m}_0^*$ and pressure ratio between the compressor exit and ambient, p_{3t}/p_0. Now, the filter tries to adapt the solution to many more parameters that make up the thermodynamic system. To reiterate, these are $\dot{m}_0^*$, T_{3t}/T_0, p_{3t}/p_0, p_{4t}/p_{3t}, T_{5t}/T_0, p_{5t}/p_0 and E^*, measured in laboratory conditions in the UPV test rig.

The further addition of observables is a way of providing certainty that, if some sensor readings are not accurate, the model will still be functioning adequately. Moreover, although the measurements are noisy (and generally that noise is not compatible with the definition of white noise), adding more information generally allows for a more precise model. This happens to be the case of the current simulation.

Observe the fact that both the estimated corrected shaft speed and model thrust are lower than initially predicted with just the 2 aforementioned observables. Moreover, the filter acts when the covariance matrix stabilizes, causing the predicted variables to present an unforeseen peak at the start of the acceleration. This feature can be seen in Figure 87 and 88.

An interesting line of action in these investigations could be addressing the filter's initialization. An inexact initial estimate of the covariance matrix can act on firstly obtained results. It is affecting the outcomes shown in these 3 cases with almost total sureness. However, it is considered that the information provided in these 3 brief studies is sufficient for a description of the application of the EKF to the transient problem.

- **Case 3**

  Now the state transition matrix is taken to be linear in $t\mathbf{F}_k$, leading to the following expression for evaluating the process noise covariance matrix in instant k:

$$\mathbf{Q}_k = \mathbf{Q}\int_0^{\Delta t}\left(1+\mathbf{F}_k\tau\right)^2 d\tau = \mathbf{Q}\left(\Delta t + \mathbf{F}_k\left(\Delta t\right)^2 + \frac{1}{3}\mathbf{F}_k^2\left(\Delta t\right)^3\right) \tag{156}$$

  Given $\mathbf{Q} = 100$ dBW, as in the last case, the running line over the compressor is better suited to the 2 used measurements, at least initially. This should not be the case, as adding more terms to $\mathbf{\Phi}$ improves the accuracy of the error propagation.

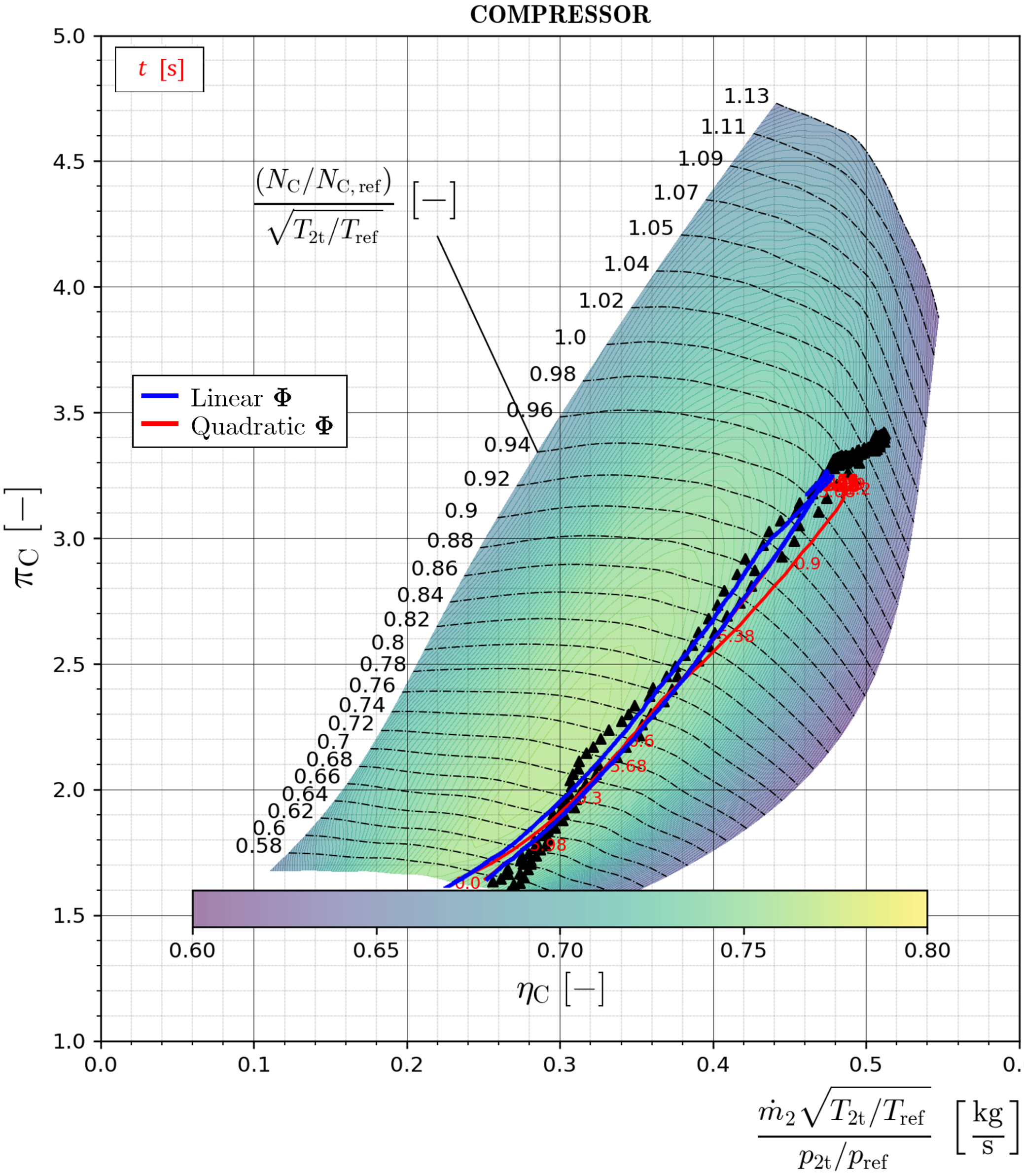

Figure 89: Filtered Compressor Operating Lines for Different Truncations of the State Transition Matrix Including UPV Test Rig Measurements.

Finally, it is recognized that imposing a linear estimate for the state transition matrix somehow delays the response of the filter when initializing the covariance matrix in the same value given in Table 19, as well as using the same initial estimated state and time marching step.

This can be observed when plotting the estimated evolution of the system's shaft corrected speed and corrected thrust. Notice how at the end of the *slam* maneuver the degree of $\mathbf{\Phi}$ becomes irrelevant.

This is irrelevance in precision is the reason why, for most systems that are not extremely non-linear, it is a common practice to truncate up to the linear term. Of course this applies if the time step is low enough, otherwise the evolution of most systems would not be linear in time anymore.

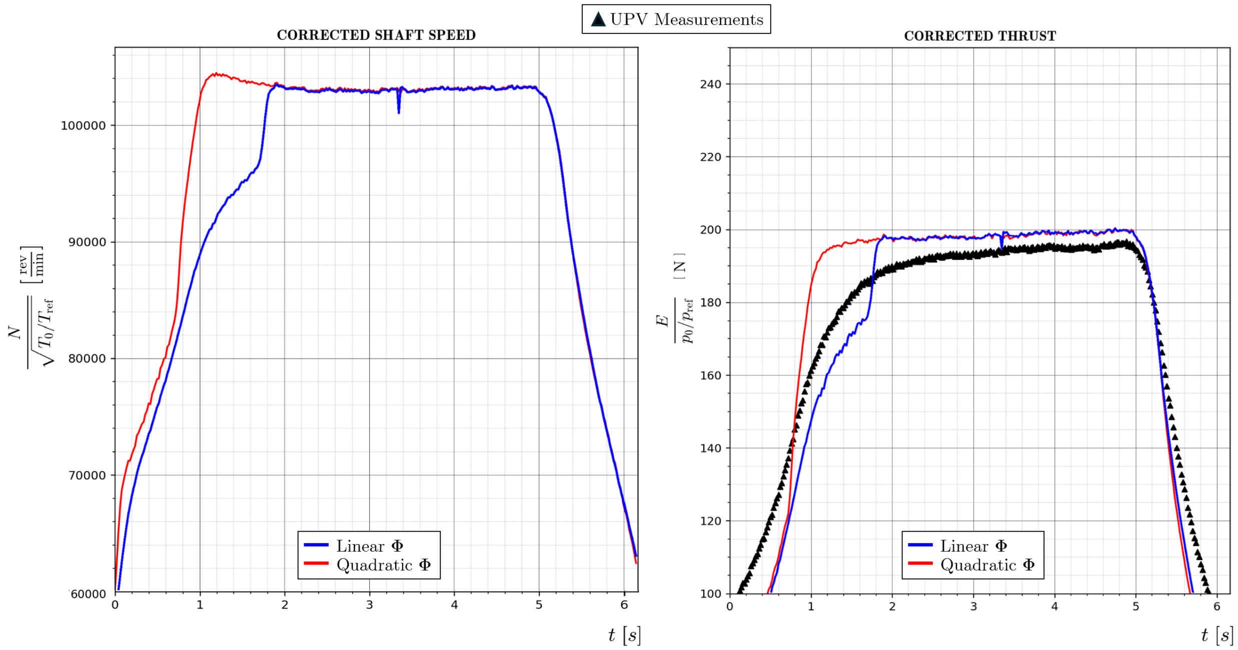

Figure 90: Filtered Corrected Shaft Speed (left) and Filtered Corrected Thrust (right) Time Evolution for Different Truncations of the State Transition Matrix.

This delay in the response of the filter might be due to an increase in the time that it takes for the system's covariance matrix to enter a settled state. As updating the filter's covariance matrix in time requires the state transition matrix (see Equation 149) as an intermediate step, this might be affecting the speed in which $\mathbf{P}$ transitions from a user-defined heuristic value to the actual estimate of the method.

There are applications where a good initialization of the EKF is fundamental for accurate predictions. If the filter needs to be multiple time rebooted because of, for example, a loss of accuracy or the eventual lack of sensor reading; and the characteristic times of the physical phenomena that the observer describes are low, then providing a good estimate of initial estimated state $\hat{\mathbf{x}}$ and filter's covariance matrix $\mathbf{P}_{0|0}$ is critical. To reiterate, no description will be provided about initialization techniques regarding the algorithms in this work.

7. Conclusions

To conclude this work, some remarks must be made. To start off, it is essential to acknowledge the importance of off-design and transient behavior in ICEs. The extent of this study has been limited to turbojet engines, which have been chosen for being one of the most common airbreathing ICEs in modern day for transonic and supersonic military applications. As explained before, their components are generally very sensitive to the system's operating point. The off-design and transient behavior of jet engines, hence, poses numerous safety and efficiency concerns that have to be taken into account in design as well as during testing, operation, maintenance or engine prognostics and health monitoring.

A general method of solution to these problems has been presented for two different typologies, the single spool and dual spool turbojet. It involves considering turbomachinery performance maps in a simplified 0-D thermodynamic approach. Moreover, it requires resorting to the use of certain algorithms and strategies to achieve a numerical solution. The employment of performance maps can allow to predict the appearance of undesired destructive effects. This makes it a useful tool for the predesign phase.

The developed tools have been first validated with a laboratory-scale single shaft engine for the steady state case, yielding close estimates between the model and the several consulted sources that have tested the device. The nozzle has been calibrated in the UPV test rig. A dedicated study on this component shed light on the necessity of quantifying two-dimensional flow effects that invalidated the one-dimensional flow model initially proposed.

Along with the main core of this work, namely the general solution, an analytical method has also been derived in order to provide means of comparing and, to a certain extent, validating the generated models. This solution is certainly simpler than the former, in regards to its formulation and implementation. After this, to illustrate engine behavior in steady and transient states, a study involving generic parameters and performance maps has been performed. Engine characteristic curves and operating lines have been obtained and compared with the analytical solution. Results showed excellent agreement near the engine's design point, which is to be expected as the analytical approach is a linearization of the system in this region. It has been proven not to be a recommendable tool for predicting off-design behavior outside of this range of applicability.

To end this work, the Kalman Filter tool has been presented, described and implemented using test results for the *AMT Netherlands Olympus HP* obtained in UPV. This optimal observer provides a generally more accurate description of the time evolving system by combining the current model with the measurements. It allowed the models to adapt to unexpected trends. Some tests have been performed on it. A pending task for future studies is improving the efficiency of the coded algorithms. A quicker code could allow implementing the filter in real time, adding in consequence more utility to the EKF as an internal state estimator.

8. Specifications

This chapter summarizes the specifications followed in the project. Given the nature of the project, the applicable regulation is Real Decreto 488/1997 (April 14th) [23], as most of the study involved the use of computer devices. The regulation establishes minimum safety and health requirements for workers using equipment that includes display screens, which is why it is relevant to this study.

It provides an explicit and broad definition for the applicable workstation type, including the display equipment, input device, associated software, office accessories, seating, work surface, and even the immediate work environment.

According to the regulation, because of the characteristics of the workstations, there are risks regarding electrical security, illumination, noise, thermal conditions, and fatigue. The responses to these risks are covered in the following sections, which summarize the aspects of the equipment needed, the work environment, and the hardware and software requirements.

8.1 Equipment

The regulation provides guidelines for screens, input devices, desks and office chairs to mitigate some of the existing risks. Screens should have clear, adjustable displays without glare, and keyboards should be tiltable and separate from the screen for comfort. Desks must allow flexible equipment placement, and chairs should be stable, adjustable, and provide proper support.

8.2 Environment

The regulation outlines other guidelines for environmental factors to ensure safety and mitigate risks in the workstation. Workspaces must be spacious enough to allow workers to change positions and move comfortably during their tasks. Illumination with general and task-specific lighting must provide sufficient brightness without causing glare or reflections on screens. The positioning of light sources, such as windows and artificial lights, should avoid glare and reflections on the display. Besides, workstations should include adjustable window coverings to control natural light and prevent excessive brightness.

The regulation also addresses other environmental factors such as noise, heat, emissions, and humidity. Noise generated by equipment in the workstation should be minimized to avoid distracting workers. Similarly, equipment should not produce excessive heat that could cause discomfort. Electromagnetic radiation should be reduced to ensure worker safety. An acceptable humidity level in the workspace is also recommended for a suitable working environment.

8.3 Hardware and software

Another aspect is for workers to have access to the necessary tools, precisely adequate hardware and software, to complete their tasks efficiently. It is essential to provide the right technological resources to meet the project's objectives.

For this specific project, the equipment has to handle the demands of the tasks, including the implementation of numerical methods. It is only compatible with the programming language Python. Table 21 summarizes the characteristics of the computer used for the tasks, as well as Python's version and most important libraries.

Hardware	
Personal Computer	**HP Spectre x360** [24]
Processor	Intel® Core™ Ultra 7 155H
Memory	32 GB LPDDR5x-7467 MHz
Storage	2 TB
Graphics	Integrated SoC
Ports	1 USB Type-A (10Gbps), 2 Thunderbolt™ 4 (40Gbps), Headphone/microphone combo
Wireless	Intel® Wi-Fi 7 BE200, Bluetooth® 5.4

Software	
Python version	Python 3.9.7
Plot library	Matplotlib
Math libraries	Numpy, scipy

Table 21: Hardware and Software Specifications.

9. Budget

The present chapter summarizes an estimate of the project's costs. It considers the derived costs from three different categories: a cost regarding the human labor invested in the development of the study, a cost for the materials and hardware that were used for the completion of the work, and a cost for the required software licenses. The sources for the cost estimation for each category are specified in the following sections, and a summary of the project's total cost is provided at the end of the chapter.

9.1 Labor cost

The human resources required for the study were an engineer and a professor. Both workers invested an amount of time whose cost was estimated with two fixed rates measured in euros per hour. The rates were determined for a junior engineer and a professor using a popular job portal [25], averaging 15 €/hour and 30 €/hour, respectively. The entire project was divided into several tasks, including a documentation phase, the algorithm conceptualization, the code and algorithm implementation, results validation, and summary report generation. Table 22 provides a detailed breakdown of the labor cost considering these rates, as well as the division of the tasks throughout the project.

Task	Role	Rate [€/hour]	Hours	Total cost [€]
Documentation	Engineer	15	30	450
Algorithm conceptualization	Engineer	15	80	1200
Code and algorithm implementation	Engineer	15	160	2400
Results validation	Engineer	15	40	600
Summary report generation	Engineer	15	120	1800
Project supervision	Professor	30	20	600
				7050 €

Table 22: Labor Cost Summary.

9.2 Hardware cost

Another essential element of the cost corresponds to the allocated budget for the necessary materials, which includes mainly a turbine that was leveraged for the experimental results of the study and a personal computer.

The turbine is an AMT Netherlands Olympus model [26], which was purchased and managed by the UPV. The personal computer is an HP Spectre x360 [24], which was purchased in 2021. The cost of both components has been attached in Table 23. It considers the full price of the turbine instead of a fraction corresponding to the current project, as no information regarding other studies is known to the author. As for the personal computer, the years of use have been accounted for when assigning the cost, dividing the initial total price of 1, 799.10 € by the three years of use.

Component	**Cost [€]**
Computer	599.7 €
AMT Netherlands Olympus	8, 643.37 €
	9, 243.07 **€**

Table 23: Hardware Cost Summary.

9.3 Software cost

There was no cost derived from the software used in this project, as it was built entirely on Python, a free, open-source programming language. The programming tasks were done with the free version of Visual Studio Code. The final report was elaborated using LaTeX through the free plan of `www.overleaf.com`.

9.4 Total cost

Table 24 summarizes the total cost of the project, adding the sums for the labor costs and hardware and software costs, as well as a standard industry benefit of a 6 %. The total cost amounts to 14, 273.26 € excluding the Value Added Tax (VAT), or a total **17, 270.65** € including taxes.

Concept	**Cost [€]**
Labor	7050
Hardware	9, 243.07
Software	0
Industry benefit (6 %)	977.58
Total cost (No VAT)	14, 273.26
Total cost	**17, 270.65**

Table 24: Total Cost Summary.

Bibliography

[1] Piqueras Cabrera, P. Notes on aircraft propulsion. Departamento de Máquinas y Motores Térmicos (Universidad Politécnica de Valencia), 2021.

[2] Mattingly, J. D. *Elements of Propulsion. Gas Turbines and Rockets.* American Institute of Aeronautics and Astronautics (Education Series), second edition, 2006.

[3] Greitzer, E. M. Surge and rotating stall in axial flow compressors. *Journal of Engineering for Gas Turbines and Power*, 1976.

[4] Astarita, T. et al. Some experimental investigations on gas turbine cooling performed with infrared thermography at Federico II. *International Journal of Rotating Machinery*, 2015.

[5] Morris, S. C., Corke, T. Aero-mechanical coupling in a high-speed compressor. Technical report, Department of Aerospace and Mechanical Engineering University of Notre Dame. Hessert Laboratory for Aerospace Research, 2007.

[6] López Juárez, M. Notes on aeroengines testing and certification. aeroengine sub-systems. Departamento de Máquinas y Motores Térmicos (Universidad Politécnica de Valencia), 2023.

[7] Richter, H. *Advanced Control of Turbofan Engines.* Springer, 2011.

[8] Thornock, R.L., Brown, E.F. An experimental study of compressible flow through convergent-conical nozzles, including a comparison with theoretical results. *Journal of Fluids Engineering*, 1971.

[9] López Juste, Gregorio. Banco de Ensayos de Turborreactores de Flujo Único de Aeromodelos para Prácticas de Laboratorio en la E.T.S.I. Diseño, UPV. Technical report, Laboratorio de Propulsión, Universidad Politécnica de Madrid, 2007.

[10] EUROCONTROL. Aviation outlook 2050. https://www.eurocontrol.int/article/aviation-outlook-2050-air-traffic-forecast-shows-aviation-pathway-net-zero-co2-emissions. Last visited: 22/08/2024.

[11] Bares Moreno, P., García Tíscar, J. Notes on off-design performance of aeroengines. Departamento de Máquinas y Motores Térmicos (Universidad Politécnica de Valencia), 2023.

[12] Zhao, J., Wang, Y., Luo, Y., Zhang, X. A vibration damping analysis method of turbine blade shroud dampers based on a given eigen-mode. In *ASME 2018 International Design Engineering Technical Conferences and Computers and Information in Engineering Conference*, November 2, 2018.

[13] Boyle, R. J., Agricola, L. M., Parikh, A. H., Ameri, A. A., Nagpal, V. K. Shrouded cmc rotor blades for high pressure turbine applications. In *ASME TURBO EXPO 2018: Turbine Technical Conference and Exposition*, June 15-19, 2018.

[14] Pellissier, V., Rodríguez, E., Meunier, G. Method for Determining Relaxation Factor for Modified Newton-Raphson Method for Non-linear Systems. Technical report, International Compumag Society, 2011.

[15] Ilhem, J. Theoretical-experimental Study of the Combustion Chamber of a Laboratory-scale Jet Engine . Master's thesis, Universidad de Jaén, 2023.

[16] Leylek, Z. An Investigation into Performance Modelling of a Small Gas Turbine Engine. Technical report, Australian Government Department of Defence, 2012.

[17] López Juste, G., Velazquez, A., Montañés, J.L. Micro-Jet Test Facility for Aerospace Propulsion Engineering Education. *International Journal of Engineering Education*, 2009.

[18] Bakalis, Diamantis P., Stamatis, Anastassios G. Data Analysis and Performance Model Calibration of a Small Turbojet Engine. *Proceedings of the Institution of Mechanical Engineers, Part G. Journal of Aerospace Engineering*, 2011.

[19] Lichtsinder, M., Levy, Y. Jet Engine Model for Control and Real-Time Simulations. Technical report, Faculty of Aerospace Engineering, Technion-Israel Institute of Technology, 2006.

[20] Ekincy, S. *Surrogate Model Based System Identification and Control of Gas Turbine Engines*. PhD thesis, Middle East Technical University, 2019.

[21] Vannoy, S., Cadou, C. Performance Characterization of a Small Turbojet Engine Platform for an Engine-Integrated Solid Oxide Fuel Cell System. Technical report, University of Maryland, 2015.

[22] Mohinder, S. Grewal. Kalman Filters. Technical report, California State University, 2009.

[23] Agencia Estatal Boletín Oficial del Estado. Real Decreto 488/1997, de 14 de abril, sobre disposiciones mínimas de seguridad y salud relativas al trabajo con equipos que incluyen pantallas de visualización. https://www.boe.es/buscar/act.php?id=BOE-A-1997-8671. Last visited: 01/09/2024.

[24] HP.com. Hp spectre x360 14-eu0004ns convertible touch laptop. https://www.hp.com/es-es/shop/product.aspx?id=9D0K0EAopt=ABEsel=NTB. Last visited: 01/09/2024.

[25] Talentcom Portal. Average salary for Engineer in Spain, 2024. https://es.talent.com/salary?job=ingeniero. Last visited: 01/09/2024.

[26] DreamWorksRC. AMT NL Olympus HP Engine. https://dreamworksrc.com/product/amt-nl-olympus-hp-engine/. Last visited: 01/09/2024.

Appendix I: AMT Netherlands Compressor Map and Datasheet

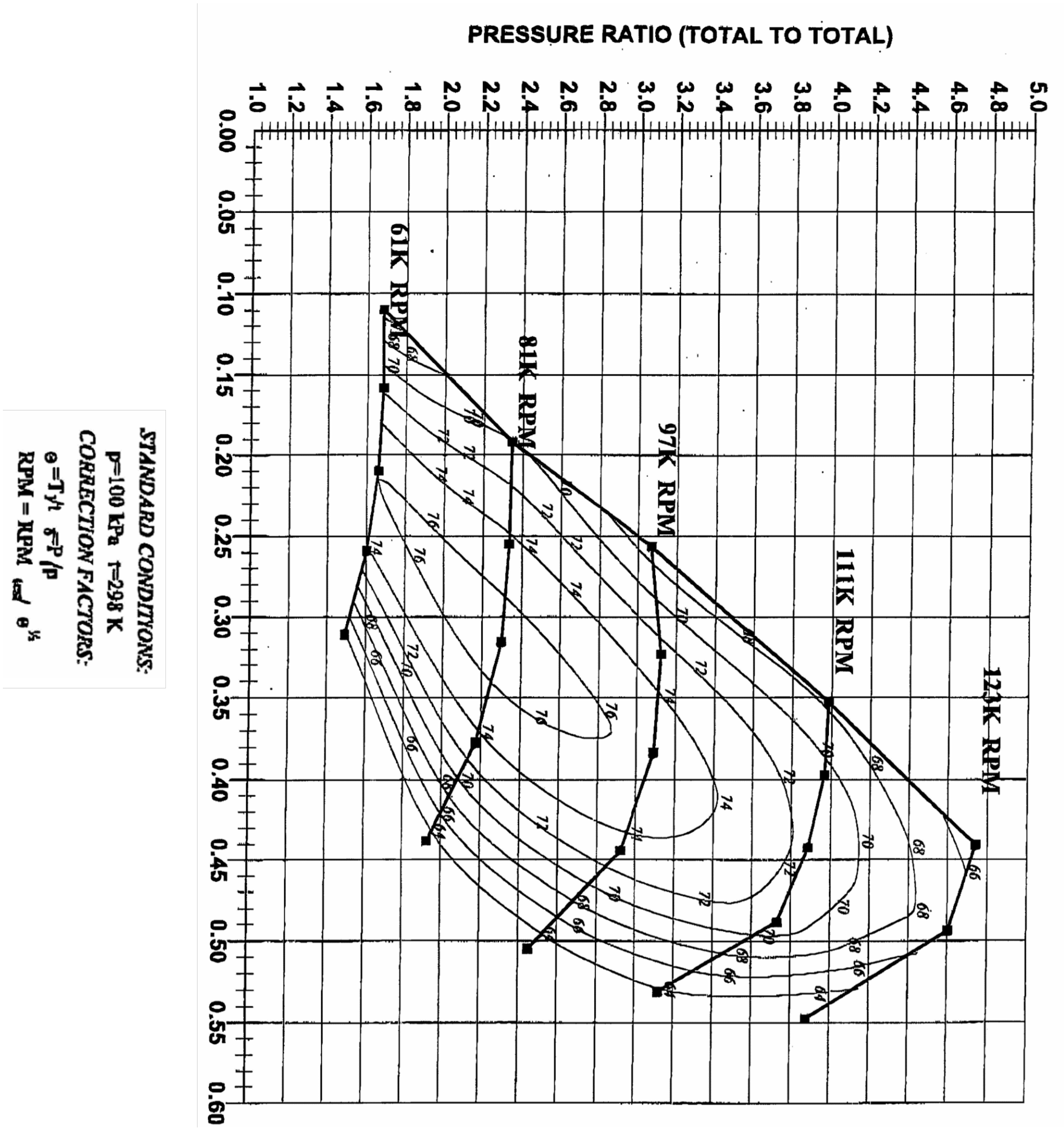

AMT Netherlands b.v.
Heistraat 89
NL-5701 HJ Helmond
Netherlands/Holland

Tel: int+31 492 545801
Fax: int+31 492 550379
Http: //www.amtjets.com
Email: email@amtjets.com

June 2009

Olympus HP gas-turbine.

	E-start system	Air-start system
Diameter	131 mm	131 mm
Length	384 mm	273 mm
Turbine weight	2850 gram	2475 gram
System weight *	3795 gram	3150 gram
Thrust @ max. rpm	230 N	230 N
Thrust @ min. rpm	13 N	13 N
Maximum RPM	108,500	108,500
Idle RPM	36,000	36,000
Pressure ratio @ max. rpm	3,8 :1	3,8 :1
Mass flow @ max. rpm	450 gr/sec.	450 gr/sec.
Normal EGT	700 ºC	700 ºC
Maximum EGT	750 ºC	750 ºC
Fuel consumption @ max. rpm	640 gr/min.	640 gr/min.
Fuel	JP-4/petroleum/Jet A1	
Oil	4,5% aeroshell 500 mixed with fuel.	

* System airborne weight. (complete system)
Engine, ECU, pump, battery, thermo sensor, mounting straps.

All data at STP **S.T. P.** : Standard Temp. & Pressure
Temperature : 15 Degrees Celsius / 59 Degrees Fahrenheit
Pressure : 1013 Mbar / 29.91 in

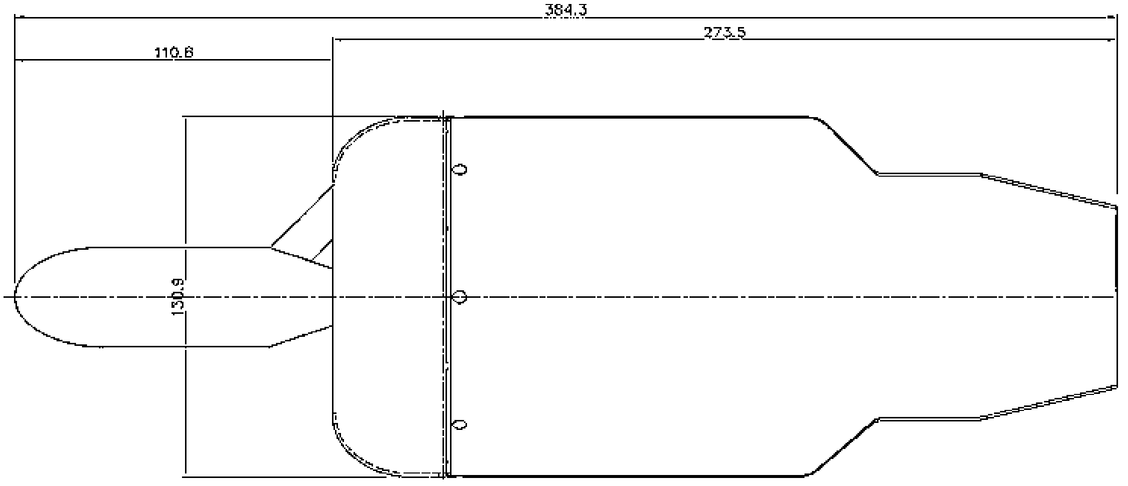

Appendix II: Relation with the SDGs

SDG	**High**	**Medium**	**Low**	**Does Not Apply**
SDG 1. End poverty.				x
SDG 2. Zero hunger.				x
SDG 3. Good health and well-being.				x
SDG 4. Quality education.				x
SDG 5. Gender equality.				x
SDG 6. Clean water and sanitation.				x
SDG 7. Affordable and clean energy.				x
SDG 8. Decent work and economic growth.				x
SDG 9. Industry, innovation, and infrastructure.		x		
SDG 10. Reduced inequalities.				x
SDG 11. Sustainable cities and communities.				x
SDG 12. Responsible consumption and production.				x
SDG 13. Climate action.				x
SDG 14. Life below water.				x
SDG 15. Life on land.				x
SDG 16. Peace, justice, and strong institutions.				x
SDG 17. Partnerships for the goals.				x

Table 25: Degree of Relation of the Work with the Sustainable Development Goals (SDGs).

Table 25 shows the degree of relation of the present study with the SDG framework. Due to the technical nature of the project, which focuses mainly on developing and validating a numerical model for a jet engine, there is no strong alignment with any of the proposed goals according to their definition. However, there is a medium degree of relation with SDG 9 of Industry, innovation and infrastructure, mainly through its target 9.5 for enhancing scientific research and upgrading industrial sectors' technological capacities, since the study and its results can be leveraged for further research.